Coupling Nitrogen-Vacancy Centers in Diamond to Fiber-based Fabry-Pérot Microcavities

Hanno S. Kaupp

München 2017

Coupling Nitrogen-Vacancy Centers in Diamond to Fiber-based Fabry-Pérot Microcavities

Hanno S. Kaupp

Dissertation
an der Fakultät für Physik
der Ludwig–Maximilians–Universität
München

vorgelegt von
Hanno S. Kaupp
aus Tübingen

München, den 18.07.2017

Erstgutachter: Prof. Dr. Theodor W. Hänsch
Zweitgutachter: Prof. Dr. David Hunger
Tag der mündlichen Prüfung: 27.10.2017

Meiner Familie

Das Staunen ist eine Sehnsucht nach Wissen.

Thomas von Aquin

Zusammenfassung

Diese Arbeit erforscht die Kopplung der Fluoreszenz von Stickstoff-Fehlstellen-Zentren (NV-Zentren) in Diamant mit durchstimmbaren optischen Mikroresonatoren bei Umgebungsbedingungen, insbesondere im Regime der Purcell Verstärkung. Hierzu benutzen wir faserbasierte, offen zugängliche Fabry-Pérot Resonatoren, die für hohe Finesse und ultrakleine Modenvolumen optimiert sind. Verschiedene, komplementäre Bereiche der Resonatorverstärkung werden untersucht.

Ein erstes Experiment basiert auf einem Resonator mit hoher Finesse und dielektrischen Spiegeln. Das Skalierungsverhalten der Purcell Verstärkung wird ausführlich ausgewertet, indem man sowohl das Modenvolumen des Resonators ($V = 16 - 600\,\mu m^3$) als auch dessen Güte ($Q = 6 \cdot 10^3 - 2 \cdot 10^6$) über einen weiten Bereich verändert. Die spektrale Leistungsdichte der Emission kann durch den Resonator um einen Faktor von bis zu 300 überhöht werden. Das gesamte Leistugsvermögen dieses Resonators kann mit schmalbandigen Emittern ausgenutzt werden, deren Emissionslinienbreite kleiner als die Linienbreite des Resonators ist. Dies ist ein vielversprechender Ansatz für die Umsetzung von schmalbandigen Einzelphotonenquellen mit durchstimmbarer Wellenlänge und für die Erzeugung ununterscheidbarer Einzelphotonen bei Umgebungsbedingungen. Jedoch bleibt die Lebenszeit der Emission für breitbandige Emitter, wie dem NV-Zentrum bei Raumtemperatur, in dieser Anordnung nahezu unbeeinflusst.

Um eine Veränderung der Lebenszeit und durch den Purcell-Effekt verstärkte Einzelphotonenemission direkt zu beobachten, stellen wir Faserresonatoren mit silberbeschichteten Spiegeln und ultrakleinen Modenvolumen, bis hinab zu $V = 1.0\,\lambda^3 = 0.34\,\mu m^3$, her. Wir demonstrieren resonatorverstärkte Fluoreszenzbildgebung, die das Auffinden und Untersuchen von verschiedenen einzelnen NV-Zentren mit einem Resonator erlaubt. Der Purcell-Effekt wird über eine gesteigerte Aufsammlung der Fluoreszenz nachgewiesen, mit einer Rate von bis zu $1.6 \cdot 10^6$ Photonen pro Sekunde von einzelnen NV-Zentren und außerdem durch die abstimmbare Veränderung der Emissionslebenszeit, entsprechend einem effektiven Purcell Faktor von bis zu 2. Des Weiteren untersuchen wir ein vorteilhaftes Regime, in dem der Diamant Nanokristall selbst eine zusätzliche Einschränkung der optischen Mode bewirkt, die sich mit der Mode des Fabry-Pérot Resonators verbindet und Modenvolumen unter $1\lambda^3$ ermöglicht. Simulationen ergeben effektive Purcell Faktoren von bis zu 11 für NV-Zentren und von bis zu 63 für Silizium-Fehlstellen-Zentren, wodurch das große Potenzial für helle Einzelphotonenquellen und für effizientes Spin-Auslesen bei Umgebungsbedingungen aufgezeigt wird.

Abstract

This thesis investigates the coupling of the fluorescence of nitrogen-vacancy (NV) centers in diamond to tunable optical microresonators at ambient conditions, in particular in the regime of Purcell enhancement. We use fiber-based, open-access Fabry-Pérot cavities optimized for high finesse and ultra-small mode volume. Different regimes of cavity enhancement are studied that are complementary to each other:

A first experiment relies on a high-finesse cavity with dielectric mirrors. The scaling laws of Purcell enhancement are explicitly demonstrated by a large-range variation of both the cavity mode volume ($V = 16 - 600\,\mu\text{m}^3$) and the quality factor ($Q = 6 \cdot 10^3 - 2 \cdot 10^6$). We detect an enhancement of the emission spectral density by up to a factor of 300. The full potential of this resonator can be exploited with emitters having a linewidth which is narrower than the resonance linewidth of the cavity. This concept holds promise for the implementation of wavelength-tunable, narrow-band single-photon sources as well as the generation of indistinguishable single-photons at ambient conditions. However, for broad-band emitters like the NV center at room temperature, the emission lifetime is not affected noticeably in this configuration.

In order to directly observe lifetime changes and Purcell-enhanced single-photon emission, we manufacture fiber-based cavities with silver-coated mirrors having ultra-small mode volumes, as small as $V = 1.0\,\lambda^3 = 0.34\,\mu\text{m}^3$. We demonstrate cavity-enhanced fluorescence imaging, which allows to locate and analyze several single NV centers with one cavity. The Purcell effect is evidenced by an enhanced fluorescence collection of up to $1.6 \cdot 10^6$ photons per second from single-NV centers and a tunable variation of the emission lifetime corresponding to an effective Purcell factor of up to 2. We furthermore investigate a beneficial regime of optical confinement where the Fabry-Pérot cavity mode is combined with additional mode confinement by the diamond nanocrystal itself, enabling sub-λ^3 mode volumes. We perform simulations that predict effective Purcell factors of up to 11 for NV centers and of up to 63 for silicon-vacancy centers, revealing a great potential for bright single-photon sources and efficient spin readout at ambient conditions.

Contents

1. Introduction

A wealth of fascinating phenomena and important applications like photosynthesis or lasing are based on the elementary interplay between light and matter. At the submicroscopic level, light is modeled as a stream of photons emitted and absorbed from quantum emitters with discrete energy states. There has thus been a large interest to study the interaction of light and matter at its most fundamental level where a single photon interacts with a single quantum system. An approach that allows to isolate the quantum dynamics of this interaction is the coupling of an individual quantum systems to an optical resonator. Intriguingly, the radiative behavior of the coupled emitter-cavity system can be fundamentally different from that of the uncoupled components. For instance, a spontaneously emitted photon is kept within the cavity and can be reabsorbed by the emitter. Due to its simplicity, the idealized system of a single quantum emitter interacting with a single resonator mode is particularly suited for comparison with theory. The experimental realization of this elementary model in cavity quantum electrodynamics (CQED) can thus be seen as a testbed for fundamental physics [1, 2, 3, 4]. The work of Nobel prize winner S. Haroche, who established an impressive illustration of quantum physics at the single-particle level, may serve as a bright example [5].

Besides the textbook character of these experiments, coupling of a single quantum system to a cavity holds a lot of promise for a technological breakthrough. The excellent control of microscopic systems that has been achieved may serve to process information by harnessing quantum mechanical phenomena, like superposition and entanglement [6]. Indeed, the new perspective of quantum information processing (QIP) bears great potential to surpass existing concepts based on classical physics, some believe even in the decade to come [7]. A well-known example is the factoring of prime numbers that can be performed much more efficiently on a quantum computer using Shor's algorithm compared to applying classical methods [8]. Moreover, quantum cryptography, enabling theoretically safe data transfer, has already taken the step into first practical applications [9, 10]. As these instances may demonstrate, QIP may give direction to science, technology and eventually society.

Due to their beneficial properties, resonators play a crucial role for the realization of QIP. In a nutshell, resonators provide the recirculation of photons at a certain, resonant wavelength, for instance, by reflecting them at a set of mirrors. An embedded quantum system can therefore experience multiple interaction events with one and the same photon before it gets lost, leading to an overall enhanced light-matter interaction. Thus, resonators allow for the ultimate coherent control of single quanta of light and matter. While the coherent coupling of light and matter represents a rather fragile state, a more robust regime, governed by the Purcell effect [11], proves beneficial with respect to practical applications. In the Purcell regime, the cavity serves to enhance the radiation of an

embedded emitter into a particular mode. As a consequence, Purcell enhancement can be exploited to build efficient single-photon sources for quantum computing and cryptography [12, 13, 14, 15, 16], or to implement an efficient interface between photons and the internal degrees of freedom of the quantum system, like the electron spin [17, 18]. It might also boost the sensitivity of sensing applications. For example, electromagnetic field sensing based on optically detected magnetic resonance (ODMR) [19, 20], would directly benefit from a cavity-enhanced collection efficiency leading to an increased optical signal.

All essential requirements for the physical implementation of QIP have been clearly formulated by D. P. DiVincenzo in 2000. However, it proves difficult to find suitable quantum systems that suffice all prerequisites simultaneously. Additionally, practical considerations play a crucial role. While trapped atoms or ions constitute well-isolated model systems, they require a tour de force of experimental effort. Solid-state-based systems, like quantum dots, molecules or color centers in diamond circumvent this issue at the cost of interacting with the embedding matrix. The hereby induced accelerated decoherence often results in the total loss of quantum properties at ambient conditions requiring cryogenic cooling, which limits the field of application. The nitrogen-vacancy center (NV) in diamond is a remarkable exception, preserving longlived quantum coherence of spin degrees of freedom up to room temperature. This color center consists of a nitrogen atom substituting a carbon atom and an adjacent lattice vacancy embedded into the diamond matrix. Giving rise to bound, discrete electronic states, it may act as an artificial atom and basis for QIP, i.e. a quantum bit (qubit). In fact, the NV center can serve all essential building blocks necessary for QIP [21, 22, 23]: It provides a quantum memory, quantum logic gates, and the possibility for the transfer of quantum information. Furthermore, spin-photon entanglement and the operation as single-photon source is feasible. Diamond fabrication techniques provide a way to build scalable systems consisting of interconnected nanophotonic devices [24, 25]. Whether diamond, sometimes denoted an "engineer's best friend", will be processed as successfully as silicon in the semiconductor industry one day, is surely an exciting question.

A critical factor for all applications based on the NV center is the efficiency that can be achieved for the exchange of quantum information from its electron spin, to the emitted photons, i.e. from the stationary, to the flying qubit. Thus, the efficient optical readout and manipulation of the electron spin is of paramount importance. However, due to the large refractive index of diamond, total internal reflection limits the collection efficiency of NV centers in bulk material to only about 3%. Furthermore, the color center's level structure comprises a set of vibronic states, yielding a broad emission spectrum. Only about 4% of the fluorescence is emitted into the so-called zero phonon line (ZPL), allowing for coherent optical interaction with the electron spin at cryogenic temperatures. Coupling of NV centers to optical microcavities provides an elegant way to overcome the involved deficiencies. Exploiting the Purcell effect, the emission rate and spectrum can be optimized, and the photons can be efficiently channeled into a well-collectable optical mode.

The enhancement of the spontaneous emission rate of an emitter coupled to a cavity

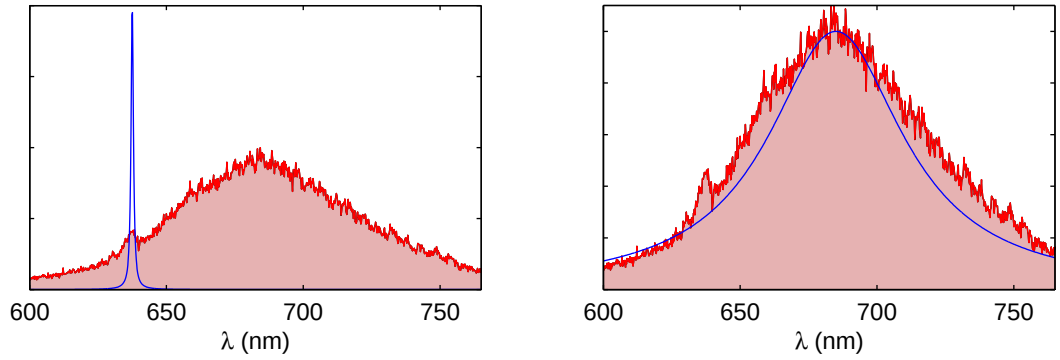

(a) (b)

Figure 1.1.: Spectral representation of the two profitable regimes of coupling of an NV center (red) to a microcavity resonance (blue): (a) Cryogenic ZPL-coupling to a cavity with high quality factor (b) Room-temperature coupling with an ultra-low mode volume cavity with moderate quality factor

scales with the ratio of the cavity quality factor to the cavity mode volume. Furthermore, it depends on the overlap of the emission spectrum and the cavity resonance [26, 27]. Thus, the effective Purcell enhancement of the fluorescence of NV centers coupled to cavities is constrained to two main regimes (see Fig. 1.1) [28].

- At cryogenic temperatures, when the ZPL narrows and approaches its Fourier limit [29], cavities with a high quality factor provide a way to considerably enhance the ZPL transition, holding promise for coherent spin-photon interfaces with large efficiency. According to the involved rates, the strong coupling regime of CQED seems in reach [30, 31, 32].

- On the contrary, at room temperature, where the quality factor of the emitter, inferred from the broad emission spectrum is merely on the order of 10, only ultra-small mode volumes provide significant Purcell factors, accompanied with near unity collection efficiency [33], yielding large overall count rates. NV centers coupled to cavities with ultra-small mode volume could thus serve as bright single-photon sources, efficient quantum memories [34, 35, 36, 37, 38], or sensors [39, 40, 41, 42, 20, 43, 44, 45] at ambient conditions. Increasing the quality factor of the cavity increases the spectral purity of the emitted photons, but does not affect the overall rate of collected photons.

The desire to improve the coupling of photons to continuously decreasing quantities of matter gave rise to the implementation of miniaturized low-loss cavities [46]. A wealth of advanced cavity designs is therefore available, among them Fabry-Pérot, whispering gallery mode (WGM) [47], and photonic crystal (PC) [48] resonators. A particularly promising approach makes use of the micromachined and mirror coated end facets of

optical fibers forming a Fabry-Pérot cavity [49, 50, 51, 52, 53, 54, 55, 56, 57]. This so called fiber Fabry-Pérot cavity (FFPC) contains a tunable, easily accessible, open mode volume of microscopic dimensions, while dielectric coatings provide the possibility for ultra-low-loss mirrors, at the same time. As a benchmark of their superior quality, the coherent coupling of single atoms and photons has been realized [58, 59]. Apart from the excellent coupling that can be achieved, FFPCs exhibit a series of favorable practical features: The cavity mode is readily fiber coupled for further communication, the cavity design compact and robust, making FFPCs well compatible with diverse, complex experimental environments. The option to easily and reversibly tune and stabilize the cavity length is a great advantage compared to monolithic architectures. Moreover, by scanning the cavity fiber over a sample mirror, different emitters can be investigated with enhanced sensitivity inside the cavity [60, 61, 62, 63]. This is a unique characteristic of this type of resonator design.

Owing to their versatility combining ultra-small mode volumes with customized mirrors, allowing for moderate or extremely low loss, FFPCs are well-suited for dealing with the demands of both regimes of interest for NV center coupling. By applying nanodiamonds (NDs) to one of the cavity mirrors, the NV centers can be easily coupled to the cavity mode, without introducing large loss. Advantageously, NV centers in diamond nanocrystals exhibit larger photon count rates than when embedded in bulk material, because total internal reflection is irrelevant for NDs of sub-wavelength diameters [64]. However, the spontaneous emission rate is slightly lowered, due to the reduced effective refractive index of the surrounding medium [65, 66]. The spectral and spin properties of NV centers in NDs are usually considered inferior to that of ultra-pure, low-strain, single-crystal, bulk diamond, regarding the broadening of the ZPL [67, 68] and the spin coherence times [69]. However, recent progress shows that similar quality can be achieved for artificially produced nanocrystals [70, 71]. Due to their easy integration, NDs coupled to Fabry-Pérot cavities bear potential for scalable quantum computing [72].

This work is devoted to the investigation of NV centers in NDs coupled to FFPCs at room temperature (see Fig. 1.2):

- In a first study, a high finesse FFPC with dielectric mirrors is applied to enhance the phonon sideband fluorescence of NV centers [31]. The scaling behavior of the Purcell enhancement is explicitly demonstrated by varying both the mode volume and the quality factor over a large range. This experiment provides a direct evaluation of the Purcell factors achievable with a FFPC at low temperature, where the ZPL can be narrower than the cavity linewidth. This approach may also serve as a wavelength-tunable, narrow-band single-photon source.

- In a complementary approach, we developed micro-resonators enabling ultra-small mode volumes down to $1.0\,\lambda^3$, which is novel for the FFPC design [73]. These cavities use silver-coated mirrors similar to the microcavities described in [74, 75, 76, 77]. Purcell enhanced single-photon emission is demonstrated and the direct modification of the spontaneous emission lifetime by the cavity is observed. For the

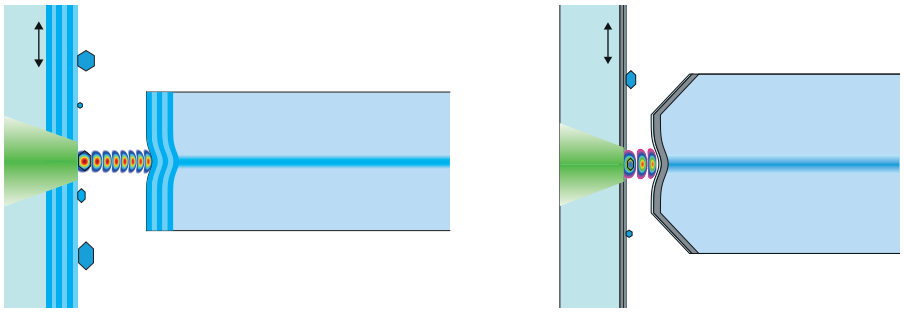

(a) (b)

Figure 1.2.: Schematic drawing of NV center coupling to FFPCs with (a) dielectric low-loss mirrors and (b) silver mirrors and ultra-low mode volume.

first time, large total photon count rates were achieved with this concept. Furthermore, cavity-enhanced fluorescence images are recorded. Numerical simulations indicate that a new regime of light confinement can be achieved where a ND in a Fabry-Pérot cavity provides additional mode confinement. In this regime, the Purcell factor can be dramatically increased holding promise for bright single-photon sources, as well as efficient spin readout and manipulation at ambient conditions.

The coupling of NV centers to micro- and nanocavities has been studied on the basis of a large variety of concepts, summarized[1] in Tab. 1. Apart from Fabry-Pérot type cavities [78, 31, 79, 80], different geometries of WGM[2] [81, 82, 83, 84, 85, 86, 87, 88, 89, 90], and PC cavities [91, 92, 93, 94, 95, 96, 97, 18, 98, 99, 100] have been investigated. On the one hand, direct fabrication of WGM or PC cavities into single crystal diamond is technically demanding, but allows optimal coupling to NV centers with the best available spectral properties until now. On the other hand, hybrid approaches, relying on non-diamond cavity materials like gallium phosphide (GaP), are easier to manufacture, owing to established fabrication methods. Positioning of the NV center with respect to the field maximum of the cavity is however non-ideal. With the advance of diamond fabrication, hybrid cavities will presumably be outpaced. Sub-λ^3 mode volumes have been realized with PC cavites, just slightly below the values that have been demonstrated for FFPC with metallic mirrors (this work). The ease of tuning, the collection efficiency and customized mirror coatings speak for the latter, the integrated design with the potential for scaling to diamond photonic networks for the former. The largest Purcell factors have been achieved for the ZPL coupled to PC cavities at cryogenic temperatures, just like most experiments have been performed in this regime, where the overall rate of collected photons is usually small. Experiments that give rise to large photon rates at ambient conditions, like in this work, are scarce. Single-photon sources for quantum cryptogra-

[1] The silicon-vacancy (SiV) defect constitutes another promising color center in diamond. It has been added to the list and will be introduced later.

[2] Among the common geometries are spheres, toroids, disks, and rings

phy and high-precision sensing applications would highly profit from their realization. The NV's broad emission spectrum spanning over roughly 100 nm at room temperature is not problematic for these applications, opposed to the majority of QIP concepts, requiring indistinguishable photons. Single photons are crucial for a multitude of schemes within QIP. For example, quantum computing is feasible using only linear optical components, like beam splitters, phase shifters, photo-detectors, and single-photon sources [101, 102, 103, 104]. Owing to the vital significance of single-photon sources, this topic will be discussed more thoroughly in the next chapter.

This thesis is organized in the following chapters: Chapter 2 illuminates the topic of single-photon creation. The introduction comprises a short historical outline, an illustration of the connection to the field of QIP, and a specification of an ideal single-photon source. Next, different types of single-photon sources will be reviewed, including a discussion of the NV center. Finally, criteria to determine the quality of real single-photon sources are given. Chapter 3 and 4 encompass the theoretical basics about Fabry-Pérot cavities and emitter-cavity coupling, respectively. In the following, the practical implementation of the experiment is discussed. Chapter 5 highlights the features of FFPCs and gives a detailed insight into their fabrication. Chapter 6 describes the experimental setup and preparation, followed by a section about characterization measurements. Chapter 7 provides the results of the coupling of NV centers to dielectric high-finesse cavities and ultra-small mode volume cavities with silver coating. Chapter 8 finishes with a conclusion and outlook.

Authors	Year	Type	Cavity architecture	V (λ^3)	Q_{exp} (Q_{th})	C_{exp} (C_{th})	T (K)	CR (s^{-1})	Ref.
Albrecht *et al.*	2013	FP	FFPC with ND			(0.01)	300	770 (3.7 k)	[78, 32]
this work	2013	FP	FFPC with ND	47	2 M	0.06 (0.05)	300		[31]
Albrecht *et al.*	2014	FP	FFPC with ND	22.7			300		[79]
Johnson *et al.*	2015	FP	Focused ion beam milled microcavity with ND	4.7	3 k (3 k)	1.40	77	15 k	[80]
this work	2016	FP	FFPC with ND	1.0	42	2.0 (11)	300	1.6 M	[73]
Schietinger *et al.*	2008	WGM	Polysterene microsphere with ND		5.5 k				[81]
Gregor *et al.*	2009	WGM	Toroidal microcavity with ND		500 k				[82]
Santori *et al.*	2010	WGM	Silica microdisk with ND coupled to tapered fiber	90	2-3 k	(1)	17		[85]
Barclay *et al.*	2009	WGM	GaP microdisc on SCD substrate	18	(9 k)	(17)			[83, 84]
Barclay *et al.*	2011	WGM	GaP ring nanocavity supported by SCD	3	3 k (10 M)	6.3 (6.7-12)	6		[86]
Fu *et al.*	2011	WGM	GaP-diamond hybrid microcavity		4.9 k (35 k)	4.2 (13)	10		[87]
Faraon *et al.*	2011	WGM	Microring in SCD	17-32	4 k (1 M)	11 (9-18)	<10		[88]
Hausmann *et al.*	2012	WGM	Ring resonator coupled to opt. waveguide in SCD		2.5 k (12.6 k)		300		[89]
Faraon *et al.*	2013	WGM	Diamond microring resonator in SCD	15	5.5 k	12 (29)	< 10		[90]
Wolters *et al.*	2010	PC	GaP PC L3 cavity with ND	0.75	600	12 (61)	300		[91, 105]
Van der Saar *et al.*	2011	PC	GaP PC S1 cavity with ND		(3.8 k)	25 (100)	300		[93]
Englund *et al.*	2010	PC	GaP PC L3 cavity over PMMA layer with ND	0.74	610 (6 k)	7 (62)	300	1 M	[92]
Faraon *et al.*	2012	PC	PC L3 cavity in SCD	0.88	3 k (6 k)	70 (250)	<10	30 k	[94]
Hausmann *et al.*	2013	PC	Nanobeam in SCD membrane	3.7	1.6 (10 k)	7 (34)	4	15 k	[95]
Lee *et al.*	2014	PC	Nanobeam in SCD, sandwiched by Bragg mirrors	0.47	7 k (24 k)	26 (3.9 k)	4.5		[96]
Li *et al.*	2015	PC	Nanobeam in SCD	1.05	1.7 k (600 k)	62 (123)	18		[97, 18]
Riedrich-Möller *et al.*	2015	PC	PC M1 cavity in SCD membrane, NV implantation	1.1	160 (1.2 k)	0.7 (0.7)	10		[100]
Riedrich-Möller *et al.*	2011	PC	SiV center coupled to PC M7 cavity in SCD	1.5	450 (11.8 k)	(20)	300		[98]
Riedrich-Möller *et al.*	2011	PC	SiV center coupled to Nanobeam in SCD	0.7	700 (600 k)		300		[98]
Riedrich-Möller *et al.*	2014	PC	SiV center coupled to PC M7 cavity in SCD	1.7	430	5 (20)	300		[99]
Sipahigil *et al.*	2016	PC	Nanobeam in SCD, SiV implantation	2.5	7.2 k	2.0	4	15 k	[106]

Table 1.1: List of experiments with NV centers coupled to micro- and nanocavities, quoting mode volume V, experimental (theoretical) quality factor Q_{exp} (Q_{th}) and Purcell factor C_{exp} (C_{th}), temperature T, saturated count rate CR. Abbreviations: Fabry-Pérot (FP), whispering-gallery mode (WGM), photonic crystal (PC), nanodiamond (ND), gallium phosphide (GaP), single crystal diamond (SCD), silicon-vacancy (SiV)

Die ganzen 50 Jahre bewußter Grübelei haben mich der Antwort der Frage
"Was sind Lichtquanten" nicht näher gebracht.
Heute glaubt zwar jeder Lump, er wisse es, aber er täuscht sich...

Albert Einstein in einem Brief an Michele Besso aus dem Jahre 1951

2. Single-photon sources

A major driver for the coupling of a single quantum system to an optical microcavity is the realization of efficient single-photon sources. Single photons play a key role in the fast growing field of quantum information science, where quantum-mechanical behavior is harnessed to develop conceptually new ways of processing, communicating or encoding information. As shown in Fig. 2.1, the increasing interest is also reflected in the growing number of publications per year containing the term "single-photon source".

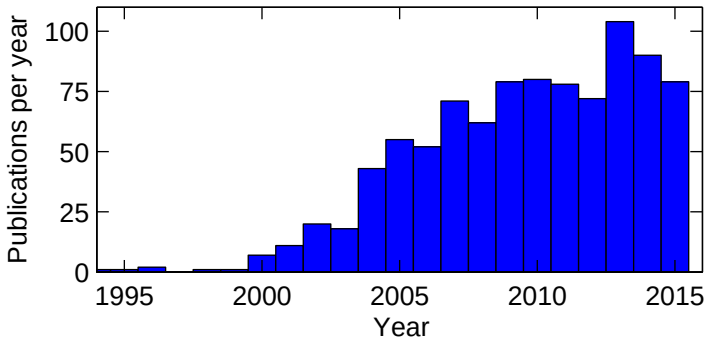

Figure 2.1.: Publications per year containing the exact term "single-photon source"

This chapter gives a broad overview of the topic of single-photon sources to be able to compare our approach based on the NV center to concepts relying on other quantum emitters. We start with some historical remarks about the photon as the quantum of the electromagnetic field. A short introduction into quantum information processing follows and in this context, the main applications of single photons are sketched. In the next paragraph, we describe the features of an ideal single-photon source. After this introductory part, different implementations of single-photon sources are discussed in more detail, among them attenuated laser pulses, spontaneous parametric down conversion, atomic systems, and solid-state systems. For the latter, we lay the focus on color centers in diamond and in particular on the NV center. At last, some common parameters used to characterize the performance of real single-photon sources are specified.

2.1. Introduction

The early days

The thorough investigation of light contributed to our today's understanding of the universe in a way that cannot be underestimated. Its puzzling nature has been subject to continuous debates. The two main points of view of the early days may be represented by two prominent physicists of the 17th century. On the one hand, Isaac Newton's idea of light was governed by a corpuscular theory, as he stated in his *Hypothesis of Light* in 1675. Christiaan Huygens, on the other hand, believed in light being a wave, as set forth in his *Treatise on Light* in 1690. While both hypotheses had their strong and weak points they gave the impression of being incompatible with each other. So when James Clerk Maxwell formulated the powerful, then not so classical theory of electromagnetic radiation in 1865 [107], the wave picture seemed to prevail.

In 1900 Max Planck presented a formula to the German Physical Society, describing the electromagnetic radiation emitted by a black body in thermal equilibrium, which became famous as Planck's law [108]. For its derivation he postulated that the energy transfer between oscillators and the electromagnetic field did not occur continuously, but in discrete energy packets. Retrospectively, this is often denoted the birth hour of quantum physics. However, at that time Planck could not anticipate the full consequences of his assumption. Stimulated by Planck's work and unresolved experimental findings, Albert Einstein published an explanation for the photoelectric effect in 1905, which was based on a particle-like character of light [109]. He claimed that

> "[...] when a light ray expands from a point in space, the energy is not distributed continuously over an ever increasing space, but it consists of a finite number of energy quanta localized at points in space, which move without division and which can only be absorbed and created as a whole."[1]

The quantum of energy in which he believed, is now known as the *photon*, the elementary particle of the electromagnetic field. Curiously enough the expression photon was coined more than twenty years later by physical chemist Gilbert N. Lewis, even though his idea of the photon was incompatible with Einstein's light quantum [110].

Planck's and Einstein's studies on electromagnetic radiation contributed decisively to an exceptionally fruitful scientific period in the beginning of the 20th century that gave

[1] The explicit quote in German reads:

> "Es scheint mir nun in der Tat, daß die Beobachtungen über die "schwarze Strahlung", Photolumineszenz, die Erzeugung von Kathodenstrahlen durch ultraviolettes Licht und andere die Erzeugung bez. Verwandlung des Lichtes betreffende Erscheinungsgruppen besser verständlich erscheinen unter der Annahme, daß die Energie des Lichtes diskontinuierlich im Raume verteilt sei. Nach der hier ins Auge zu fassenden Annahme ist bei Ausbreitung eines von einem Punkte ausgehenden Lichtstrahles die Energie nicht kontinuierlich auf größer und größer werdende Räume verteilt, sondern es besteht dieselbe aus einer endlichen Zahl von in Raumpunkten lokalisierten Energiequanten, welche sich bewegen, ohne sich zu teilen und nur als Ganze absorbiert und erzeugt werden können."

rise to the revolutionary quantum theory and in particular quantum electrodynamics. Ironically, the photoelectric effect as Einstein described it, does not require a quantum mechanical treatment of the light field, but can be explained within the frame of a semiclassical model, assuming that the surface can only absorb and emit light in energy quanta, while the electromagnetic radiation is a classical field [111]. In fact, semiclassical theory would have been sufficient to explain a large part of phenomena originally expected to be connected to photons. A clear proof for the particle-like nature of light was given by J. F. Clauser in 1974, by measuring photon pair coincidence rates behind two beam splitters [112]. He stated:

> "That a photon is not split in two by a beam splitter is certainly "old hat", and it may seem surprising that we have gone to the effort to test this prediction experimentally. What is in fact much more surprising is that evidently no such experimental test has heretofore been performed, and such tests are clearly of great importance."

It was the first demonstration of sub-Poissonian photon statistics, and a striking evidence for the quantum mechanical description of light. The underlying measurement principle is simple but conclusive. Single photons impinge one by one on a 50:50 beam splitter, with a detector positioned behind each output arm, a configuration named after R. Hanbury Brown and R. Q. Twiss, commonly abbreviated as HBT setup [113]. A semiclassical treatment, for which the photons are replaced by a weak field, does not contradict coincident events on both detectors, as the detection probability is proportional to the square of the electric field. In contrast, within a quantum theory of light, single photons can naturally not be detected simultaneously in both outputs. The inhibition of coincidences serves as a proof for the non-classical character of light and especially for effects like photon antibunching.

In 1976 H. J. Carmichael *et al.* [114], as well as H. J. Kimble *et al.* [115] theoretically predicted photon antibunching in the resonance fluorescence of two-level atoms and proposed a direct measurement in order to test quantum electrodynamics. One year later, H. J. Kimble *et al.* demonstrated this distinctive nonclassical effect for the first time by observing the fluorescence of sodium atoms with an HBT setup [116]. As valuable insight into the fundamentals of single-photon sources, they explicitly noticed that

> "[...] the atom, having emitted a photon at time t, is unable to radiate again immediately after having made a quantum jump back to the lower state. The quantum nature of the radiation field and the quantum jump in emission, which are of course inextricably connected, are therefore both manifest in these photoelectric correlation measurements."

In another striking experiment in 1987, F. Diedrich and H. Walther showed both photon antibunching and a sub-Poissonian probability distribution of the photon number by analyzing the photon correlation of the fluorescence of single trapped ions [117]. Being able to store an ion for up to 10 minutes emitting a stream of photons one by one, their device came already closer to an ideal single-photon source. With these remarkable

proofs, the HBT setup became a standard in quantum optics for testing the purity of single-photon sources. The early investigations, focusing on the fundamental aspects of the quantum nature of light, have paved the way to a diverse and vivid field of promising implementations of single photons.

The age of quantum information processing

Photons propagate at the speed of light and can be transmitted via existing optical fiber networks. Quantum bits (qubits) of information can be encoded easily in its degrees of freedom, e.g. polarization, timing or spatial mode. Thus, they seem to be an ideal choice to transmit information and to serve as "flying qubits" for quantum information processing (QIP) [118, 119, 120, 104]. In spite of its still modest success, QIP holds a lot of promise to outperform classical concepts one day [6]. One case in point is the factoring of prime numbers that can be performed much faster by running Shor's algorithm on a quantum computer than attacking the problem classically [8]. This poses a potential danger for the encrypted data transfer based on the frequently used RSA cryptosystem, named after its inventors R. L. Rivest, A. Shamir and L. Adleman. New concepts for perfectly safe data transfer based on quantum mechanical effects are therefore of fast-growing interest. Single-photon sources play a crucial role for both quantum computing, as well as quantum cryptography and a wealth of other QIP concepts.

In 2001, E. Knill, R. Laflamme and G. J. Milburn showed that efficient quantum computation is feasible with linear optics only, based on single-photon sources, beam splitters, phase shifters and photo detectors [101, 103]. This seminal work meant a dramatic simplification compared to previous proposals. However, the indispensable indistinguishability of the photons is still a demanding task, especially when working with solid-state single-photon sources. At the same time, the implementation of the first quantum cryptography protocol developed by C. Bennett and G. Brassard in 1984 (BB84) [121] also benefits from true single-photon sources, compared to applying attenuated laser pulses, for instance [122]. Surprisingly, as one of few exceptions within QIP, the photons do not have to be indistinguishable, in this case. Quantum cryptography, as arguably one of the most advanced disciplines, has taken the step into commercialization[2] and public life[3].

The unconditional[4] security of quantum cryptographic protocols, such as BB84, is based on true random numbers. Within the Copenhagen interpretation of quantum mechanics, objective randomness is believed a matter of fact. For instance, the exact point in time of the spontaneous emission of a photon by an atom is not governed by an objective reason and therefore random and unpredictable. Quantum random number generators exploit such processes. Once again, single photons impinging on a 50:50 beam splitter

[2] Among the companies offering solutions around quantum key distribution are ID Quantique, MagiQ Technologies, QuintessenceLabs, SeQureNet

[3] In 2007, in the Swiss national election, the canton of Geneva transmitted ballot results to the capital using quantum encryption technology.
http://web.archive.org/web/20071209214958/http://www.technewsworld.com/story/59793.html

[4] The attribute *unconditional* is subject for debate.

prove beneficial to this end. Since it is not predictable for a certain particle, which output it will end up in, single-photon sources serve well to produce true random numbers [123, 124, 125]. Besides quantum cryptography, random numbers are valuable for statistical methods like Monte-Carlo simulations, gambling or computer game technology.

Furthermore, single photons are crucial for many concepts in the context of entanglement. This peculiarity of quantum physics represents one of the most interesting effects to be harnessed for QIP. By analyzing the implications of entanglement in 1935, A. Einstein, B. Podolsky and N. Rosen doubted that quantum mechanics could be a complete theory [126] and speculated about local hidden variables. Almost 30 years later, in 1964, J. S. Bell proposed that this issue could unexpectedly be resolved by performing a measurement [127]. He deduced an inequality (Bell's inequality) that proves true for any local realistic theory, while it is violated by quantum mechanics. Since then, many groups have accepted the challenge to show a violation [128, 129, 130, 131, 132, 133, 134, 135, 136, 137, 138], with the latest success in 2015 by three different groups, having closed all significant loopholes simultaneously and therefore ruling out local hidden variables and all local realistic theories [139, 140, 141].

As a side note, entangled photon pairs produced by parametric down-conversion were also the basis for the first experimental verification of quantum teleportation by Bouwmeester *et al.* in 1997 [142]. In contrast to these experiments of philosophical momentousness, entanglement can also be of use in everyday life. In 2004, the first bank transfer via quantum cryptography relying on entangled photons [143] was demonstrated by a collaboration around the group of A. Zeilinger in Vienna[5].

As all of these examples may demonstrate, single photons are an ubiquitous element in QIP and have taken the step into first commercial products. After this short summary of the diverse fields of application, the key parameters of single-photon sources are briefly introduced. A more detailed characterization follows in Section 2.3.

The ideal single-photon source

The perfect device emits exactly one photon at a desired point in time, i.e. deterministically, into a well-defined, collectable spatio-temporal mode with an arbitrarily large repetition rate, the subsequently emitted photons being indistinguishable from each other [144]. Indistinguishable photons have identical polarization, as well as spectral and temporal envelope. In reality however, deviations from this ideal behavior are inevitable and depend on the particular source type. Several parameters quantifying the deficiencies provide a better comparability to each other. The emission efficiency of a source is given by the ratio of usable single photons per initiated emission cycle, typically including extraction or filtering loss. However, note that different definitions are in use, as well. The second-order correlation function at zero time delay $g^{(2)}(0)$ is the figure of merit for the inhibition of undesired multi-photon events and sometimes referred to as single-photon purity. It is determined with an HBT setup. The closer its value drops to zero, the smaller the probability that more than a single photon is emitted within one

[5] https://web.archive.org/web/20150211032846/http://www.secoqc.net/downloads/pressrelease/Banktransfer_english.p

cycle, i.e. ideally $g^{(2)}(0) = 0$. The indistinguishability of a pair of photons is tested by exploiting the Hong-Ou-Mandel effect: Two indistinguishable photons, each entering one of the input ports of a 50:50 beamsplitter, will always exit together through one of the two output ports. These concepts will be discussed in more detail in Section 2.3. In some cases, a tradeoff between different parameters might be unavoidable. Imagine a source emitting photons that are per se not lifetime limited, i.e. the photons are distinguishable. However, by spectral filtering, a sub-group of indistinguishable photons can be selected at the cost of a decreased efficiency.

2.2. Source types

A few different concepts for single-photon creation have been come up with. The most important approaches will be briefly discussed here, including probabilistic sources based on faint laser pulses or spontaneous parametric down-conversion, as well as deterministic sources relying on true single-emitter systems like atoms, ions, molecules, color centers in diamond and quantum dots. Several publications offer a more detailed insight into the field in general [145, 146, 147, 144, 148] or focus on solid-state-based [149], diamond-based [150, 151], or quantum dot-based sources [152, 153]. The latter exhibit a particular diversity of material systems, often withstanding more general statements. Therefore, the discussion is restricted to the subgroup of semiconductor quantum dots, here.

2.2.1. Faint laser pulses

Faint laser pulses serve as a technically simple and in many cases satisfying approximation to single-photon sources and are therefore still among the most common choices. Because the photon number in a coherent state follows Poisson statistics, the probability of having more than one photon per pulse scales with the average photon number. As a result, the suppression of multi-photon events is borne by the overall brightness or efficiency. And a decent single-photon purity is only achieved if most of the pulses do not contain any photon at all. This is an intrinsic drawback of this concept. In 2007, weak coherent pulses have for example been applied for the demonstration of free-space quantum key distribution over 144 km by T. Schmitt-Manderbach *et al.* [154].

2.2.2. Spontaneous parametric down-conversion

Another major scheme relies on the creation of correlated pairs of single photons in a three-wave mixing process in a crystal with $\chi^{(2)}$ nonlinearity [155, 156]. In order to obtain single photons, one of the photons is detected, heralding the existence of its partner in another channel that can be used for experiment. These so-called heralded single-photon sources are based on spontaneous parametric down-conversion (SPDC), where the photon of a pump laser is converted into two photons under the constraints of energy and momentum conservation, determining the relation between the involved wave vectors and frequencies. This relation is also known as phase-matching condition.

Advantageously, the down-converted photons thus exhibit a high directionality. However, the spatial modes the photon pairs are guided in are usually multi-mode cones around the pump beam that are not straightforward to collect. Due to limited tuning possibilities of the dispersion of the commonly applied crystals, the phase matching conditions can often be met only for a particular wavelength region. Furthermore, the bandwidth usually ranging from some nanometers to some ten nanometers is rather broad [146]. Periodic poling constitutes an effective method to design crystals providing phase matching for customized situations [157, 158]. Another approach coping with the phase matching issue is based on a whispering gallery mode resonator. Photon pairs are efficiently generated in two defined resonator modes enabling wavelength tuning over 100 nm and a controllable bandwidth $\leq 13\,\mathrm{MHz}$ [159].

Even though the conversion efficiency for SPDC is very low ($10^{-7} - 10^{-11}$, [146]) and the creation process is random in time, heralded single-photon sources represent a practicable and powerful technique [160]. Obviously, as probabilistic sources following Poisson statistics, they suffer from the inherent compromise between inhibition of multi-photon events and brightness, just like faint laser pulses. Advantageously, since the arrival of the single photons is heralded, one can efficiently gate the associated experiments. The main benefit of SPDC however is the intrinsic potential to create two photons that exhibits correlations in time, energy, polarization, momentum or angular momentum and as a result, photon pairs that can be entangled in one or more of their observables [161]. For example, in 2007, R. Ursin *et al.* used polarization-entangled photons produced by SPDC to demonstrate entanglement-based, free-space quantum key distribution over 144 km [162].

2.2.3. Atomic systems

2.2.3.1. Atomic cascades

Pairs of polarization-entangled photons can also be created in some atomic cascades. However, SPDC has largely replaced this method to prepare correlated photon pairs, because of their much easier operation and superior brightness. An atomic cascade was harnessed in the pioneering Bell test experiments by S. J. Freedman and J. F. Clauser in 1972 [128, 163] and A. Aspect *et al.* in 1981/82 [164, 129]. In this process, photon pairs at wavelengths $\lambda_1 = 551\,\mathrm{nm}$ and $\lambda_2 = 423\,\mathrm{nm}$ are emitted and at a rate of $5 \cdot 10^7\,s^{-1}$ was reported [165]. This atomic cascade was also the basis for a beautiful illustration of the wave-particle duality of light by Grangier *et al.* in 1986 [166]. By sending one of the photons onto a beam splitter (the other one is used as a gate trigger), the anti-correlation of photodetections on both outputs and therefore the single-particle behavior was demonstrated. In this case, the photon does not split in two. On the contrary, the wave nature became apparent, by building a Mach-Zehnder interferometer around the beam splitter and recording the number of counts in dependence of the path difference between the two interferometer arms. The observed interference contrast was excellent, a visibility of almost 99% was achieved, making a pure wave explanation tempting. The explanation of both experiments in combination requires quantum mechanics, of course.

2.2.3.2. Atoms and ions

Due to their comparatively easy technical feasibility, probabilistic concepts like faint laser pulses or photon pairs produced by SPDC still have a wide scope within quantum optics. However, these sources produce a Poisson distribution of photons with a non-negligible probability to obtain more than a single photon per pulse. Alternatives based on fundamentally different processes are therefore desirable. In this respect, deterministic sources offer the advantage to provide exactly one photon on-demand, mainly[6] from single-emitter systems like single atoms, ions, molecules, color centers in diamond, semiconductor quantum dots or quantum wells [167]. In spite of the peculiarities of each system, their operation principle is similar. Much simplified, the system is first excited into a higher level by an external excitation pulse from where it decays radiatively to a lower level under the emission of a single photon. Because the system has to be recycled into the excited state before it can re-emit another photon, it can never create more than one photon at a time and hence constitutes a true, on-demand single-photon source. Conceptually as simple as intriguing, operating a single quantum system can prove difficult in practice. Especially, the trapping and cooling of single atoms or ions demands a tour de force of experimental effort. An outstanding advantage of once isolated atomic systems is that the same element will universally exhibit identical properties. Fourier-limited, indistinguishable photons can be produced [168, 169, 170, 171, 172]. Scaling atomic systems is in principle possible, but technically challenging and does not seem practicable for large numbers today. Multi-photon events are normally negligible.

By coupling a single emitter to an optical cavity, the tractability of the system is further increased and the emission can be efficiently channeled into an engineered spatio-temporal output mode [33, 173]. Especially atoms strongly coupled to an optical cavity provide a way to deterministically generate single photons on demand with well-controllable properties, e.g. their pulse shape is predefined by a steerable input pulse, when a stimulated Raman process drives an adiabatic passage (STIRAP) [174, 175, 176, 177, 178, 179, 180, 181]. Establishing coherent light-matter interaction is also an important step towards quantum networks, requiring a reversible exchange of quantum states between flying and stationary qubits [182, 120, 183, 184, 185]. Limiting factors are the finite trapping time of neutral atoms on the order of several minutes, as well as a variation in the atom cavity-coupling strength due to fluctuations of the position of the atom.

In contrast, ions can be trapped for an almost infinite amount of time, variations in the coupling strength are negligible [186]. By long-term coupling of single calcium ions to a cavity, single photons with an exactly defined pulse shape and timing have been produced [173, 187]. But until now, the strong-coupling regime of cavity quantum electrodynamics, has only been reached for neutral and not for charged particles, because it has proven difficult to combine ion traps with cavities with small mode cross sections. Furthermore, the single-photon efficiency decreases with a larger cavity length, i.e. there is a general tradeoff between the efficiency and emission rate. The ion trap community is therefore putting a lot of effort into the realization of small-mode-volume, high-finesse

[6] For the more exotic case of ensemble-based systems consult [144] and references therein.

cavities compatible with their traps, in order to increase the coupling strength. Fiber-based Fabry-Pérot cavities seem to be a promising tool to this end [188, 189, 190, 191]. A calcium ion trapped in between two optical fibers operating as single-photon source has already been demonstrated [189].

Even though efficiencies of several tens of percent have been reported [173, 181], the overall rate of single photons detected from atoms and ions is still moderate and usually considerably below $1 \cdot 10^5\, s^{-1}$ [187, 180].

2.2.4. Solid-state sources

Compared to atomic systems, emitters in the solid state, like molecules or color centers in diamond, offer the advantage of being already trapped in a host matrix. Because trapping and laser cooling is irrelevant, the technical overhead is reduced dramatically. This is however at the cost of detrimental effects caused by interactions with the embedding medium: First of all, phonons influence the level scheme of the emitter's electronic states, as a result of motional coupling to the lattice. Furthermore, spectral diffusion due to charge fluctuations in the environment or magnetic field noise from neighboring nuclear spins can lead to a significant deterioration of the emission properties. As a result, the fluorescence emission spectrum of a solid-state quantum emitter may be considerably broader than the Fourier-transform limited linewidth that is inferred from the spontaneous emission lifetime.

The consequences of the interaction of a quantum emitter with lattice vibrations is now briefly sketched. A more detailed picture of phonon coupling is given below. Transitions to an excited electronic state are spread over a wide range of frequencies, because of accompanying vibrational excitations. Upon the relaxation from the lowest vibrational level of the excited electronic state to one of the multiple vibrational states of the ground state, fluorescence is emitted. The latter is therefore distributed over several transitions yielding a broad emission spectrum. The transition from the lowest vibrational level of the excited to the lowest vibrational level of the ground state, does not involve any phonons and is therefore denominated zero-phonon line (ZPL). The so-called phonon side band (PSB) consists of transitions from the vibrational ground state of the excited level into higher vibrational levels of the ground state, which are red-shifted with respect to the ZPL. The intensity ratio emitted into the ZPL is referred to as Debye-Waller factor. The emission linewidth of the ZPL is ultimately limited by the long lifetime of the excited state, which is often in the nanosecond regime. However, at room temperature, the line is considerably broader. At cryogenic temperatures it can get narrow and ultimately approach its Fourier limit to provide indistinguishable photons. On the contrary, the linewidths of the PSB transitions remain much broader, since they are determined by the lifetime of the vibrations, which are on the order of some picoseconds.

Unlike systems based on single atoms, solid-state emitters exhibit inhomogeneous broadening resulting from individual properties due to local variations in the embedding matrix. This general deficiency can be addressed by tuning techniques, for example to overlap the ZPLs of two remote systems in order to generate indistinguishable photons.

2.2.4.1. Molecules

In 1992, for the first time, antibunching in the fluorescence emission of an emitter in the solid state, namely a molecule of pentacene in a p-terphenyl host, was demonstrated by T. Basche *et al.* [192]. Originally requiring cryogenic temperatures [193, 194, 195], the emission of single photons from single molecules at room temperature has also been shown [196, 197, 198, 60]. At liquid helium temperature, organic molecules in crystalline hosts exhibit a good photostability (several days reported), as well as lifetime limited ZPLs [146]. The ZPL emission of single molecules has been harnessed to produce indistinguishable photons from one [199], or even two remote sources that were electrically tuned via the Stark effect to achieve perfect spectral overlap [200, 201, 202]. The photostability is a major issue for molecules at room temperature. Even though, it can be on the order of some hours in certain cases [60], it usually takes only a few seconds of illumination with typical excitation intensities to destroy a chemically stable dye in a polymer matrix [146].

2.2.4.2. Color centers in diamond

Color centers in diamond originate from defects in the carbon lattice like vacancies, substitutional or interstitial impurities that give rise to localized, discrete electronic states within the wide bandgap (5.5 eV) of its diamond host. The electronic level structure and photophysical characteristics are similar to that of molecules. However, concerning the photo stability, color centers outperform molecules by far, because of the superior mechanical rigidity of the diamond lattice and the good chemical protection it provides. Due to its large refractive index ($n = 2.4$), total internal reflection severely limits the collection efficiency of color centers embedded in bulk diamond. This problem is readily circumvented for diamond nanocrystals, enabling a much larger collection efficiency [64]. Typical crystal diameters range from a few ten to one or two hundred nanometers. However, as a result of the lower effective refractive index of the medium surrounding the emitter, its fluorescence lifetime is increased yielding a smaller photon emission rate [65, 66]. Utra-pure, low strain diamond is still difficult to obtain in the form of nanocrystals. Thus, color centers in nanodiamonds do usually not exhibit the good spectral and spin properties achievable with bulk diamond samples. If the use of bulk diamond is indispensable, solid immersion lenses can improve the collection by about one order of magnitude [203, 204, 205, 206, 207]. Even though hundreds of color centers in diamond have been reported, only few are well understood and amenable to a larger field of research. Among the stable single-photon emitters at room temperatures [151, 208] are the nitrogen-vacancy (NV) center, silicon-vacancy (SiV) center, the nickel-nitrogen complex (NE8) [209, 210, 211], or the recently emerged germanium-vacancy center [212, 213].

The nitrogen-vacancy center

The NV center is a point defect in diamond with C_{3v} symmetry consisting of a substitutional nitrogen atom (N) with an adjacent lattice vacancy (V), as shown in Fig. 2.2(a). It

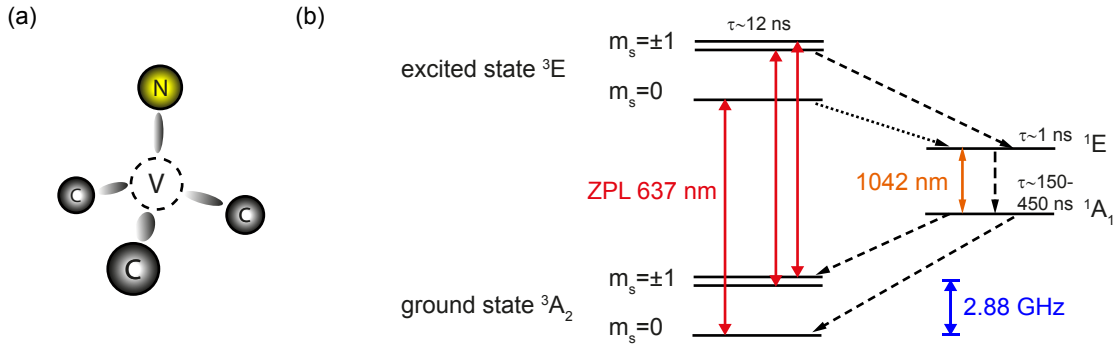

Figure 2.2.: (a) Structure of the NV center in the diamond lattice given by a substitutional nitrogen atom (N) and a lattice vacancy (V) between the nearest neighbor carbon atoms (C). (b) Schematic of the electronic structure of the NV center. Radiative transitions are indicated by solid arrows, weak and strong non-radiative transitions by dotted and dashed arrows, respectively [216, 217, 215].

exists in two charge states. The main focus of research is on the the negatively charged NV^-, while its neutral variant NV^0 is of minor interest. In this work, for the sake of brevity, the expression NV center refers to the negative charge state. One can distinguish between the charge states by detection of the optical zero-phonon lines at 637 nm (NV^-) and 575 nm (NV^0), respectively. The subsequent presentation of the NV center will be limited to its basic characteristics, referring to two extensive reviews [214, 215] and references therein, for a deeper insight.

The NV center is the by far most investigated color center and was the first to be addressed not only in an ensemble but individually [218, 219]. In the year 2000, its potential as single-photon emitter was confirmed using a bulk diamond sample [220, 221, 222], noting that

> "Color centers are included in a solid matrix, are easy to handle, and appear to be good candidates for realizing single-photon sources for quantum cryptography. We should obtain the ultimate efficiency for such a source by coupling the emitting dipole to a microcavity, so it will emit light in a single mode." [220]

The photostability of the NV center is excellent, it does not suffer from photobleaching or fluctuation of the emission spectrum [218]. However, the fluorescence is emitted into a broad spectrum originating from a strong PSB and spans over almost 100 nm peaking at a wavelength of around 690 nm. Due to the stiffness of the diamond lattice, the ZPL at wavelength of 637 nm is still visible at room temperature. This is in general not the case for molecules. The intensity fraction emitted into the ZPL is small, the Debye-Waller factor is only around 0.04. The broadening mechanism of the ZPL will be discussed in more detail below.

In bulk diamond of type Ib, emission lifetimes of 12.9 ns and 11.6 ns were found for natural and synthetic samples, respectively [223]. A saturated fluorescence intensity for a single NV center of $1.7 \cdot 10^7$ photons per second at an excitation intensity of 2.4 MWcm^{-2} has been reported, about 2% of which had been collected [218]. Collected photon rates of several $1 \cdot 10^5\, s^{-1}$ can be achieved with the help of solid immersion lenses [203, 204, 207] or nanophotonic structures [224, 225, 226, 227, 228].

A quantum efficiency (QE) close to unity has often been assumed for NV centers in bulk diamond [218]. However, values of 0.7 to 0.8 were observed for shallow-implanted NV centers in a recent measurement [229] that was following a scheme similar to the original Drexhage experiment [230, 231]. A QE of 0.7 valid for bulk samples had already been proposed to partially explain measurements of the fluorescence decay rate of NV centers in diamond nanocrystals [232].

Nanodiamonds

Diamond nanocrystals can also host NV centers and in particular single emitters, as was first shown in 2001 [64, 233]. The fluorescence emission behavior of NV centers in nanodiamonds (NDs) is modified by the nano-environment [64, 66]. First of all, due to the subwavelength dimensions of the diamond surrounding, the photons are not subject to total internal refraction, resulting in a significantly larger extraction efficiency compared to bulk diamond. Furthermore, the fluorescence lifetime is affected by the modified local density of states (LDOS). Chew analytically evaluated the spontaneous emission rates of dipoles inside spherical dielectric particles, which may serve as first approximation [65]: For a particle in air having a radius much smaller than the transition wavelength, the LDOS is lowered by a factor of $9/\left(n^2+2\right)^2$. This corresponds to a reduction of the transition rate by a factor of $\Gamma_{\mathrm{ND}}/\Gamma_{\mathrm{Bulk}} = 9/n\left(n^2+2\right)^2$ compared to the rate in the bulk material with equivalent refractive index n, independent of the dipole location. As a result, the lifetime is increased dramatically for emitters in NDs, which implies a lower fluorescence yield. A better picture can be obtained by evaluating the transition rate as a function of the diameter of the spherical particle with FDTD simulations [66]. The results indicate, that the emission rate is continuously suppressed with decreasing particle size. A superimposed oscillating behavior presumably originates from interference effects of the electric field within the sphere. A clear exposition of the involved effects can be found in [234] where the dependence of the spontaneous emission rate on the size and shape of a dielectric environment has also been systematically studied with europium ions embedded in dielectric nanospheres.

In practice, the shape of diamond nanocrystals is typically irregular, giving rise to a broad distribution of spontaneous emission rates. Reported lifetimes of NV centers in nanocrystals with a mean size of 60 nm produced from high-pressure high-temperature (HPHT) diamond are on the order of 23 ns [235]. The lifetime has also been measured for different ND sizes indicating that non-radiative decay emerges for small NDs with sizes on the order of some ten nanometers [236, 66]. This effect is expressed by a reduced QE. For NV centers in NDs with a mean size of 100 nm, measurements yielded a wide distribution

of QEs ranging from 0.1 to 0.9, while QEs between 0 and 0.2 are proposed for 25 nm crystals [232]. Embedding NDs in an air-like silica areogel allows to study the emission behavior of NV centers with negligible contribution from the surrounding environment. The mean lifetime of such a sample is increased with respect to NDs prepared on glass coverslips and a mean QE of ~ 0.7 has been reported [237]. It has also been shown that the excitation intensity may affect the QE, which dropped from near unity to around 0.5 with increasing power for 50 nm NDs [238].

Electronic structure

The level scheme of the electronic structure, as understood until now [216, 217, 215], is shown in Fig. 2.2(b). The ground state $^3A_2$ is a spin triplet, with a zero-magnetic-field splitting between the $m_s = 0$ and $m_s = \pm 1$ sublevels of 2.88 GHz. The excited state ^3E is also a spin triplet having a measured lifetime of 12.9 ns and 11.6 ns for natural and synthetic bulk diamond, respectively [223]. Two intermediate singlet states $^1A_1$ and ^1E have been proposed that give rise to a radiative transition in the near infrared at 1042 nm[7] [239, 216]. However, the reported lifetime of only 0.9 ns for the upper singlet ^1E points at a predominantly non-radiative decay [216]. The lower state $^1A_1$ is metastable with a temperature-dependent lifetime ranging from about 150 to 450 ns [240, 216, 241]. According to the current point of view, the non-radiative decay from the spin sub-levels of the excited state ^3E to the intermediate state ^1E is slower for $m_s = 0$ than for $m_s = \pm 1$. Furthermore, the non-radiative decay from the intermediate state $^1A_1$ back to the spin sub-levels of the ground state $^3A_2$ is similar for the sub-levels. Effectively, this leads to a polarization into the $m_s = 0$ sub-level after a few optical cycles. The NV center is thus amenable to optical spin-polarization into the "bright" sub-level $m_s = 0$ and its spin state can be read out optically by the amount of detected fluorescence. It is quite exceptional for a solid-state system to serve as spin-photon interface at room temperature. This is also the basis for optically detected magnetic resonance (ODMR) experiments and has, for instance, lead to the demonstration of nanoscale sensing of temperature [43, 44, 45], as well as magnetic [39, 40, 41, 242, 20] and electric [42] fields at ambient conditions.

Another remarkable feature of this color center is the very long coherence time of the ground state electron spin of up to $T_2 = 1.8$ ms for isotopically engineered diamond at room temperature [69], which can be seen as a result of the stiffness of the diamond lattice. The reported dephasing time is actually the longest ever observed in solid-state systems and enables to control the coupling with close by electron and nuclear spins [243, 244, 36]. This qualifies the NV center as quantum memory [34, 35, 36, 37, 38] at ambient conditions and it may ultimately serve as a building block for quantum networks [245, 21, 24, 22, 23].

Vibrational structure - phonon sideband

Like many other solid-state systems, color centers in diamond are exposed to distinctive electron-phonon coupling. As a result, their emission and absorption spectra are often

[7] In [239], a wavelength of 1046 nm was reported, which was however a misprint according to [216].

shaped by phonon sidebands (PSBs). First insight into the effect of lattice vibrations on the emission and absorption behavior can be gained within the simple Huang-Rhys model that considers only a single mode of vibration, in place of the quasi-continuum of modes encountered in diamond. Within this model, the displacement of the nucleus between the equilibrium positions of the corresponding electronic states is taken as the normal coordinate. In the Born-Oppenheimer approximation, the quantum mechanical state is described with the help of electronic and vibrational potentials that are decoupled from each other, the latter being approximated by a harmonic potential of the normal coordinate. The nuclear equilibrium positions of the electronic ground and excited state are often not identical but deviate by δQ from each other, as shown in Fig. 2.3(a). According to the Franck-Condon principle, the most likely transitions are, however, found for the same nuclear configuration of the involved states. In general, the transition probabilities are proportional to the square of the overlap of the vibrational wave functions where the overlap integrals are the so-called Franck-Condon factors.

The influence of lattice vibrations is now discussed by starting with the Huang-Rhys model closely following the review of Davies [246]. The model system consists of one ground and one excited state that both couple to a single mode of vibration. The vibrational potential of the electronic ground state is approximated by a harmonic potential,

$$V_\mathrm{g} = \frac{1}{2} m\omega^2 Q^2, \tag{2.1}$$

with the mass of the mode m, its angular frequency ω, and its instantaneous displacement from the equilibrium position Q. The potential of the excited state can be formulated by

$$\begin{aligned} V_\mathrm{e} &= E_\mathrm{e} + \frac{1}{2} m\omega^2 Q^2 + aQ + bQ^2 \\ &= E_\mathrm{e} + \left(\frac{1}{2} m\omega^2 + b\right)\left(Q + \frac{a}{m\omega^2 + 2b}\right)^2 - \frac{a^2}{2m\omega^2 + 4b}, \end{aligned} \tag{2.2}$$

where a and b constitute the linear and quadratic electron-phonon coupling factors of the excited state. The vibrations of the excited state may thus be centered around a new equilibrium position and have another frequency compared to the ground state. Defining the displacement from the ground state equilibrium by

$$\delta Q \equiv -\frac{a}{m\omega^2 + 2b}, \tag{2.3}$$

the new mode frequency by

$$\Omega \equiv \sqrt{\omega^2 + 2b/m}, \tag{2.4}$$

and the relaxation energy, coming along with the modified nuclear configuration by

$$E_\mathrm{r} \equiv \frac{a^2}{2m\omega^2 + 4b}, \tag{2.5}$$

the excited state potential adopts the simple form

$$V_\mathrm{e} = E_\mathrm{e} - E_\mathrm{r} + \frac{1}{2} m\Omega^2 \left(Q - \delta Q\right)^2 . \tag{2.6}$$

Since the frequency changes are small for diamond, one may set $\omega = \Omega$ for now.

The wave function of the defect states can be written as the product of the electronic state and the vibrational state, i.e. the nth state of the harmonic oscillator. For instance, the state with minimal energy is the product of the electronic ground state $\phi_\mathrm{g}(r, Q)$ with the zeroth harmonic oscillator state $\chi_0(Q)$:

$$\psi_0(r, Q) = \phi_\mathrm{g}(r)\chi_0(Q). \tag{2.7}$$

The slight dependence of the electronic state on the atomic position Q is neglected. The probability of an optical transitions from the ground state to the excited electronic state $\phi_\mathrm{e}(r)$ and the nth vibrational state $\chi_n(\delta Q)$ is then proportional to the square of the integral

$$\int\int \mathrm{d}r\mathrm{d}Q\phi_\mathrm{e}^\star(r)\chi_n^\star(Q - \delta Q)D\phi_\mathrm{g}^\star(r)\chi_0^\star(Q), \tag{2.8}$$

with the electric dipole operator D. The assumption that the integral over the electronic states and the dipole operator is independent of the displacement coordinate Q is known as Condon approximation:

$$\int \mathrm{d}r\phi_\mathrm{e}^\star(r)D\phi_\mathrm{g}^\star(r) \int \mathrm{d}Q\chi_n^\star(Q - \delta Q)\chi_0^\star(Q). \tag{2.9}$$

It is usually justified by an energy difference of the electronic states that is large enough to prevent mixing of the electronic states by the vibration, i.e. the electronic states are independent of Q. This is also expected for the dipole operator, since the diamond lattice does not contain ionic charges that could generate modifications of the local electric fields as a result of vibrations. Given that the first integral has a certain value that can be obtained experimentally from the radiative transition lifetime, the focus is on the second integral. The so-called Franck-Condon factors are defined as

$$M_{0n} = \int \mathrm{d}Q\chi_n^\star(\delta Q)\chi_0(Q). \tag{2.10}$$

The harmonic oscillator states χ then yield

$$|M_{0n}|^2 = \frac{\mathrm{e}^{-S}S^n}{n!}, \tag{2.11}$$

with the Huang-Rhys factor

$$S = a^2/2m\hbar\omega^3 = E_\mathrm{r}/\hbar\omega. \tag{2.12}$$

According to Eq. 2.11, the relative intensities of the optical transition to the excited states $\phi_\mathrm{e}\chi_n$, $n = 0, 1, 2, ...$, follow a Poisson distribution with the mean phonon number S, as shown for $S = 2.6$ and $n = 0, 1, ..., 6$ in Fig. 2.3(b).

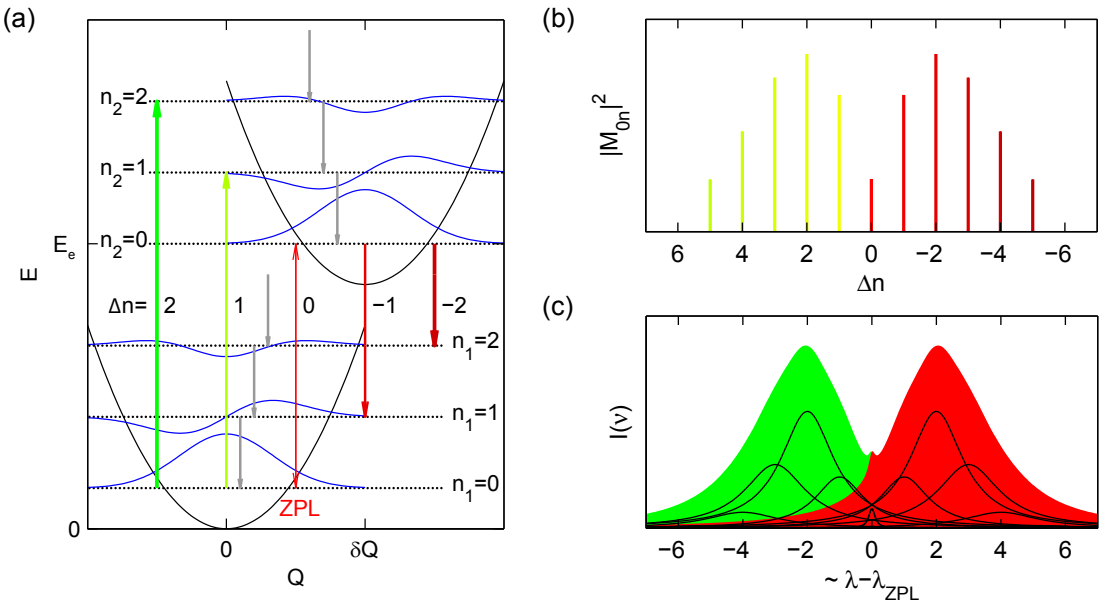

Figure 2.3.: (a) Schematic of the Huang-Rhys model in the Franck-Condon approximation. The ground and excited states are given by harmonic potentials of the nuclear displacement coordinate Q (black lines) and comprise equally spaced vibrational sublevels, whose nuclear wavefunctions are shown, as well (blue lines). The nuclear equilibrium position of the electronically excited state is shifted by δQ. Multiple optical transitions between the vibronic leveles are indicated by the colorful arrows pointing upwards and downwards, corresponding to absorption and emission of photons, respectively. Additional non-radiative decay between vibrational sublevels is indicated by the gray arrows pointing downwards. (b) Franck-Condon factors for absorption (green) and emission (red), in the case of a single vibrational mode. (c) More realistic model of the absorption (green) and emission (red) spectrum for a continuum of phonon modes. The bandshape of the n-phonon sideband can be determined from the one-phonon spectrum.

For temperatures $T > 0\,\mathrm{K}$, vibrational levels of the electronic ground state become excited. The sum of all transitions between vibrational states with the same quantum numbers (i.e. $\phi_\mathrm{g}\chi_n \rightarrow \phi_\mathrm{e}\chi_n$,) form the zero-phonon line (ZPL). Thus, the ZPL consists of several lines separated by $\hbar(\Omega - \omega)$. These are, however, not observable due to the coupling to a continuum of modes, as discussed below. The transitions with $\Delta n \geq 1$ create phonon sidebands (PSBs), which are shifted to lower energies with respect to the ZPL in the photoluminescence spectrum. The nth PSB is at a photon energy of

$$h\nu_{0n} = E_\mathrm{e} - E_r + n\hbar\omega. \tag{2.13}$$

The energy of the electronic ground state E at the equilibrium position $Q = 0$ can be expressed as

$$E_\mathrm{e} = \frac{\sum_{n=0}^{\infty} |M_{0n}|^2 \, h\nu_{0n}}{\sum_{n=0}^{\infty} |M_{0n}|^2}. \tag{2.14}$$

In this simple model, for equal vibration frequencies $\omega = \Omega$ and assuming that the system starts in the lowest vibrational level of the ground state, the absorption and the emission spectrum are simply mirrored at the ZPL with respect to each other.

The Hung-Rhys factor S is also a measure for the fraction of the transition probability of the ZPL

$$S = \ln\left(\sum_{n=0}^{\infty} |M_{0n}|^2 \,/\, |M_{00}|^2\right), \tag{2.15}$$

and can thus be estimated from the photoluminescence or the absorption spectrum of a color center. For the NV center, a Huang-Rhys factor of $S = 3.73$ and an energy of the vibrational mode of $\hbar\omega = 65\,\mathrm{meV}$ have been reported [246]. The maximum of the emission spectrum is located around $\nu_\mathrm{max} = \nu_\mathrm{ZPL} + S \cdot \hbar\omega$.

So far, the coupling of the electronic state to a single vibrational mode has been discussed. However, defects in diamond are typically coupled to a continuum of vibrational modes. For a more realistic description, the model is now refined with little effort, by considering a sum of N vibration modes. Under the restriction of linear electron-phonon coupling, Eqs. 2.1 and 2.2 yield

$$V_\mathrm{g} = \frac{1}{2}\sum_{i=1}^{\infty} m_i\omega_i^2 Q_i^2, \tag{2.16}$$

$$\begin{aligned} V_\mathrm{e} &= E_\mathrm{e} + \frac{1}{2}\sum_{i=1}^{\infty} m_i\omega_i^2 Q_i^2 + \sum_{i=1}^{\infty} a_i Q_i \\ &= E_\mathrm{e} + \frac{1}{2}\sum_{i=1}^{\infty} m_i\omega_i^2 \left(Q_i + \frac{a_i}{m_i\omega_i^2}\right)^2 - \frac{1}{2}\sum_{i=1}^{\infty} \frac{a_i^2}{m_i\omega_i^2}. \end{aligned} \tag{2.17}$$

All modes of vibration in the potential sum are independent of each other. Thus, the vibronic wavefunction can be factorized into

$$\psi_\mathrm{e}(r, Q_1, Q_2, ..., Q_N) = \phi_\mathrm{e}(r) \prod_{i=1}^{N} \chi_i^{n_i}(\delta Q_i), \tag{2.18}$$

where each vibrational mode $\chi_i^{n_i}$ can be excited into any state n_i, and $\delta Q_i = Q_i - a_i/m_i\omega_i^2$. As shown later, it is useful to form a sum over individual Huang-Rhys factors for each mode:

$$S = \sum_{i=1}^{N} S_i, \tag{2.19}$$

$$S_i = \frac{a_i^2}{2\hbar\omega_i^3 m_i}, \tag{2.20}$$

where the relaxation energy of the ith mode equals $S_i\hbar\omega$.

In the one-phonon sideband, only a single vibrational mode is excited . This quantum of excitation can be in any of the N modes. In this case, the Franck-Condon factors for exciting exclusively the ith mode is given by

$$M_{01}^i = \int \mathrm{d}Q_1 \chi_1^{0\star}(Q_1)\chi_1^0(\delta Q_1)... \int \mathrm{d}Q_i \chi_i^{0\star}(Q_i)\chi_i^1(\delta Q_i)... \int \mathrm{d}Q_N \chi_N^{0\star}(Q_N)\chi_N^0(\delta Q_N), \tag{2.21}$$

which can be abbreviated as

$$\left|M_{01}^i\right|^2 = S_i \exp(-S_i) \prod_{j\neq i} \exp(-S_j) = S_i \mathrm{e}^{-S}. \tag{2.22}$$

Making use of this result, the total relative intensity of the one-phonon sideband reads

$$|M_{01}|^2 = \sum_i \left|M_{01}^i\right|^2 = \mathrm{e}^{-S} \sum_i S_i = S\mathrm{e}^{-S}. \tag{2.23}$$

In analogy, the calculations for an n-phonon sideband yield

$$|M_{0n}|^2 = \frac{S^n \mathrm{e}^{-S}}{n!}, \text{ with } \sum_{n=0}^{\infty} |M_{0n}|^2 = 1. \tag{2.24}$$

Note, that this equation is formally equivalent to the case of a single mode of vibration, Eq. 2.11. All vibrational modes are independent of each other. Consequently, the case for n phonons, absorbing at a frequency ν from the ZPL can be expressed by the case for $(n-1)$ phonons absorbing at $(\nu - x)$ plus one more phonon at a frequency x. Thus, the bandshape of the n-phonon sideband $I_n(\nu)$ can be evaluated recursively from the one-phonon bandshape $I_1(\nu)$

$$I_n(\nu) = \int_0^{\omega_m} dx I_1(x) I_{n-1}(\nu - x), \text{ for } n > 1, \tag{2.25}$$

with the maximum vibrational frequency ω_m. This is an important outcome, since the complete PSB is obtained, if S and the one-phonon bandshape $I_1(\nu)$ are known. Due to the evaluation by convolution, the bandshape gets increasingly broader for higher order phonon modes, as indicated in Fig. 2.3(c). Note that the bandshape ($I_n(\nu)$) is a

transition probability. An absorption spectrum is obtained by multiplying the bandshape by the photon frequency ν, and by ν^3 for the luminescence spectrum, respectively.

Davies *et al.* made use of the linear model to describe the optical spectrum of the NV center [247, 248]. Electronic ground state modes with a vibrational energy of around 67 meV were found to interact particularly strongly with the excited electronic state. Therefore, the Huang-Rhys model, considering a single mode of vibration only, serves well to understand the electron-phonon coupling mechanism of the NV center. For a deeper insight into the vibronic structure of the NV center, one may refer to the good overview by Doherty *et al.* [215] or consult ab initio studies, e.g. by Gali *et al.* [249].

Broadening mechanism of the zero-phonon line

The broadening of the ZPL of the NV center is caused by two main effects [32]: Dephasing of the optically excited state attributed to the dynamic Jahn-Teller effect [246] and spectral diffusion due to a time-dependent Stark-shift, which is originating from a fluctuating electric environment [67, 250].

The excited state of the NV center ^3E is an orbitally degenerate doublet (E_x,E_y), which is coupled to a doubly degenerate vibrational mode (e) resulting in a classic $E \otimes e$ Jahn-Teller system. The coupled vibronic system yields three configurations with minimal energy [251]. If the phonon energy is not enough to overcome the energy barrier between these minima, the system will remain in one of the minima. This is the static Jahn-Teller effect. In contrast, the dynamic Jahn-Teller effect corresponds to the situation where the phonon energy is large enough to induce dynamic tunneling processes through the barrier. For the NV center, the local energy minima are separated by a barrier of only 10 meV and, while the calculated energy of the local vibration mode is 71 meV [251], such that frequent tunneling is expected.

In other words, vibrations may induce transitions between E_x and E_y by a two-phonon Raman process [29]. This Raman relaxation reduces the electronic lifetime of both states E_x and E_y giving rise to dephasing of the optical transition and a broadening of the ZPL. Based on first-principle calculations and an analysis of the vibronic interaction model, Abtew *et al.* derived the temperature-dependent dephasing rate of the ZPL [251], which is in very good agreement with measurements by Fu *et al.* [29]. The data was obtained with a $\langle 111 \rangle$-oriented type IIa natural diamond sample with a low NV center density. The calculated linewidth of the ZPL is given by

$$\gamma(T) = \gamma_0 + 2W(T), \tag{2.26}$$

where $\gamma_0 = 2\pi \cdot 16.2\,\mathrm{MHz}$ and

$$W(T) = \frac{8\pi}{\hbar} \left(\frac{\Omega}{2\pi^2 \hbar^3 v_\mathrm{s}^3} \right)^2 C^4 (k_\mathrm{B}T)^5 I_4 \left(\frac{\hbar\omega_\mathrm{D}}{k_\mathrm{B}T} \right), \tag{2.27}$$

with the Debye integral $I_4(y) = \int_0^y \mathrm{d}x \left[x^4 e^x / (e^x - 1)^2 \right]$ for an appropriately chosen cutoff energy (Debye energy), here $\hbar\omega_\mathrm{D} = 50\,\mathrm{meV}$, the sound velocity in diamond $v_s = 1.2 \cdot$

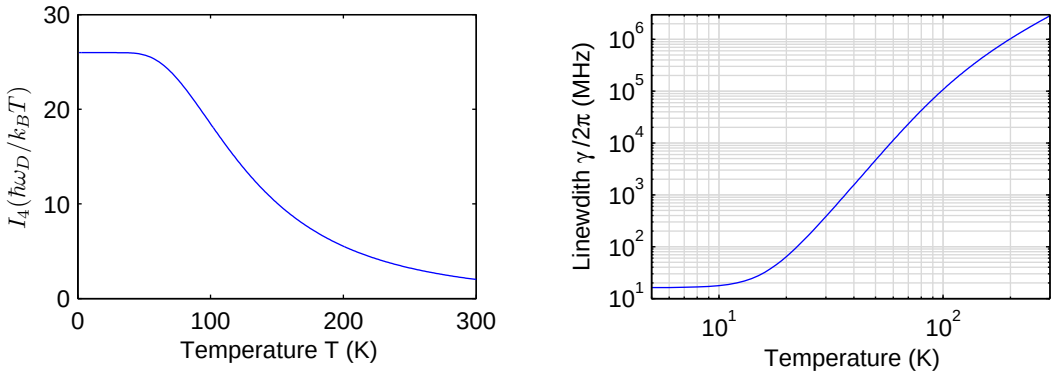

(a) (b)

Figure 2.4.: (a) Debye intgral $I_4(\hbar\omega_D/k_BT)$ for $\hbar\omega_D = 50\,\mathrm{meV}$ (b) Calculated linewidth of the the ZPL closely reproducing measurements by Fu *et al.* [29]

$10^4\,\mathrm{m}s^{-1}$, and the volume of the diamond unit cell $\Omega = \left(8r/\sqrt{(3)}\right)^3$, with a radius $r = 200\,\mathrm{pm}$ (see Fig. 2.4(a)). The coupling constant C is given by $C = F/\omega_0\sqrt{2M}$, with the vibronic coupling constant $F = 0.74\,\mathrm{eV\AA}^{-1}$ at the phonon energy $\hbar\omega_0 \approx 70\,\mathrm{meV}$, and the mass of the carbon atom M. In the low temperature limit, the Debye integral results in $I_4(\infty) = 4\pi^4/25$.

The characteristic temperature scaling of the linewidth $\gamma/2\pi$ is shown in Fig. 2.4(b). While it is close to its spontaneous emission lifetime limit of 13 MHz for temperatures below about 10 K, the linewidth scales approximately with T^5 in the intermediate temperature range for $10\,\mathrm{K} \lesssim T \lesssim 100\,\mathrm{K}$. At room temperature, dephasing increases the linewidth to a few THz.

In summary, the optically excited state of the NV center is subject to the dynamic Jahn-Teller effect. The induced dynamic population transfer results in dephasing and homogeneous broadening of the ZPL at finite temperatures. To date, this seem to be the dominant contribution to electron-phonon coupling.

It is commonly accepted that spectral diffusion originates from a varied DC Stark-shift, which is caused by a fluctuating electrostatic environment. It becomes manifest by inhomogeneously broadened emission lines, as a result of random jumps of the emission wavelength. These jumps occur on a timescale much faster than the recording time of a spectrum leading to a ZPL with Gaussian shape. The spectral diffusion time was measured for nanocrystals milled from high-quality type Ib bulk diamond with sizes between 30 and 100 nm. At cryogenic temperatures ($T = 5 - 20\,\mathrm{K}$) it amounts to a few microseconds [250]. Changes of the local electrostatic field of NV centers are attributed to nearby charge traps [252] and impurities that can be ionized by the excitation laser. In diamond, substitutional nitrogen constitutes the predominant impurity with an optical ionization energy of 2.2 eV [253]. Note that, excitation light at a wavelength $\lambda = 532\,\mathrm{nm}$

has a photon energy of 2.33 eV and can therefore ionize nearby nitrogen atoms. In conclusion, spectral diffusion can be reduced by using an excitation wavelength low enough to prevent ionization of nitrogen [254]. NV centers located close to the surface may also suffer from spectral diffusion induced by charge traps arising from surface defects. NV center in small NDs or shallow centers created by implantation are especially susceptible in this regard.

The Stark shift of the excited state of an NV center caused by a single elementary charge at a distance of 10 nm may be as large as several hundreds of GHz [250, 67, 255]. In return, the Stark shift can also be harnessed to tune [67, 252] or stabilize [255] the spectral position of the ZPL. In general, the degree of spectral diffusion critically depends on the quality of the diamond sample and in particular on the amount of substitutional nitrogen. For nitrogen-rich type Ib NDs the linewidth of the ZPL may be on the order of 0.5 nm, corresponding to spectral diffusion of several hundreds of GHz [250]. However, in spite of spectral diffusion and spin-nonconserving transitions, linewidths as small as 16 MHz, i.e. close to the lifetime limit, have been observed in milled, synthetic, high-pressure high-temperature, type Ib nanocrystals at cryogenic temperatures, as well [68]. The abundance of NV centers with these superior properties in such a sample is probably extremely low. Linewidths of a few hundred MHz have been reported for ultra-pure synthetic IIa bulk diamond with a nitrogen concentration below 5 ppb, which was grown by chemical vapor deposition [254]. Linewidths as low as 16.2 MHz were measured for a natural IIa diamond sample with low NV density, which is again close to the lifetime limit [29].

In short, spectral diffusion stems from a DC Stark shift, which is induced by a variation of the local electric field. These fluctuations are caused by nearby impurities like substitutional nitrogen and charge traps. Thus, the ZPL experiences a broadening that can be as large as several hundreds of GHz. To my understanding, the dominant broadening mechanism of the ZPL at room temperature is however dephasing due to the Jahn-Teller effect followed by spectral diffusion.

At cryogenic temperatures, the generation of indistinguishable photons from two remote NV centers has been accomplished [256, 257]. In order to achieve the spectral overlap between the two ZPLs, the NV centers were electrically tuned by inducing a DC Stark shift. Quantum entanglement between an emitted photon and the spin of the center is feasible [258]. Furthermore, by entanglement swapping [259], indistinguishable photons originating from two remote NV centers serve to transfer the entanglement to their spins [260]. This technique also lead to the first realization of a loop-hole free Bell test [139]. However, for this approach, the rate of successfully established entanglement events is still low (about $1\,h^{-1}$) compared to systems relying on SPDC, representing statistically more significant proofs [140, 141].

The silicon-vacancy center

The SiV center is formed by introducing a silicon atom into the diamond lattice replacing two carbon atoms. It is located along the $\langle 111 \rangle$ direction in between two lattice sites in

a so-called split-vacancy configuration [261, 262, 263, 264]. In contrast to the NV center, the linear electron-phonon coupling at room temperature is weak. Thus its fluorescence is predominantly emitted into the sharp ZPL located around 740 nm [24], with a Debye-Waller factor of around 0.7. A linewidth below 1 nm at room temperature has been observed [265, 266]. Even though the excited state lifetime is on the order of only 1 ns, the brightness is in general not superior to that of the NV center [267, 268, 208], because its quantum efficiency is lower. Values between 0.05 [269] and 0.63 [270, 99] have been reported with a dependence on the temperature [271] and the sample preparation method. Early attempts where single SiV centers were produced by ion implantation into bulk natural diamond, showed photo count rates of only around $1 \cdot 10^3\, s^{-1}$ [267, 150]. Alternatively, single SiV centers can be found in diamond grown by chemical vapor deposition (CVD) techniques. In this process, silicon is often etched from the reactor walls and in-situ incorporated into the diamond lattice[8]. Nanodiamonds produced from low-stress, single crystalline CVD films yield single-photon count rates exceeding $1 \cdot 10^5\, s^{-1}$ [268]. Even larger values, of up to $6 \cdot 10^6\, s^{-1}$, have been reported for randomly oriented NDs and oriented heteroepitaxial nano-islands grown on iridium films [265, 266, 270]. The authors assume that the high brightness is not exclusively due to the larger collection efficiency on the reflective iridium substrate, but points to a slightly improved quantum efficiency. Photo bleaching and blinking limits the group of fully photostable emitters to about 20-30% [270]. The ZPLs have a spectral width of only 1.3 ± 0.4 nm, but exhibit a broad distribution ranging from 730 to 750 nm, probably owing to variable stress in the NDs [266]. The temperature-dependent (5-295 K) ZPL fine structure, line shift and widths have been investigated in detail for single SiV centers in CVD NDs on iridium, as well as an ensemble of SiV centres in a high-quality, low-stress, homoepitaxial diamond film [272]. While most of the single SiV centers showed an emission linewidth between 25 and 160 GHz at 5 K, due to phonon broadening in the presence of impurities and additional spectral diffusion, individual fine structure components of the ensemble exhibited values down to 9 GHz. Recently, the underlying electron-phonon interactions have also been studied thoroughly [273]. Combining the large collection efficiency typical of NDs with the advantageous spectral emission properties of homoepitaxial diamond films would be a great leap towards the realization of bright sources of indistinguishable single photons. This issue can for example be addressed by photonic structures, directly fabricated in high-quality diamond embedding individual color centers [225]. For instance, Purcell enhancement has been shown for SiV centers coupled to photonic crystal cavities fabricated in single crystal diamond, enabling mode volumes on the order of λ^3 [98, 99, 106].

Remarkably, in low-strain bulk diamond at 4 K, multiple intrinsically identical, single-photon emitting SiV centers have been observed, a novelty for solid-state systems [274]. The collectable single-photon rates are on the order of some $1 \cdot 10^5\, s^{-1}$. Since the nearly transform-limited linewidths did not show spectral diffusion, it was possible to demonstrate the creation of indistinguishable photons from two separated SiV centers in a Houng-Ou-Mandel interference test without the need of tuning [275]. First steps towards

[8] Because silicon is much less abundant in natural diamond, the detection of silicon impurities also serves to indicate the synthetic origin of a diamond sample.

accessing and manipulating the spin of the SiV center have been successfully undertaken [276, 277, 278]. In contrast to the NV center, these experiments are restricted to cryogenic temperatures, however.

2.2.4.3. Quantum dots

Quantum dots (QDs) are nanoscale structures in semiconductors that give rise to an energy quantization as a consequence of a strong spatial confinement of conduction-band electrons or/and valence-band holes. In contrast to quantum wells and quantum wires, being confined in one, respectively two dimensions, QDs exhibit a full three-dimensional confinement. Different fabrication techniques and thus, a large variety of systems exist. Here, we focus on epitxial semiconductor QDs that prove as stable, bright and pure (low $g^{(2)}(0)$) single-photon emitters at cryogenic temperatures. The electronic confinement is obtained by creating a nanometer-sized island of one semiconductor within another, the latter having a larger band gap. When an electron is optically or electrically [167, 279] excited from the valence to the conduction band, a hole remains in the valence band. If the electrons and holes are originally excited to higher levels, they usually experience fast non-radiative relaxation into their lowest states and can form an exciton trapped to the QD. Recombination of the electron in the ground state of the conduction band with the hole in the valence band can occur radiatively under the emission of a photon. The lifetime is typically on the order of 1 ns. Besides the exciton, multi-particle states combining different numbers of electrons and holes exist, for example the biexciton, involving two electrons and two holes. As a consequence, the observed photoluminescence spectrum consists of multiple emission lines for above-band excitation. In order to observe single photons, one transition has to be spectrally isolated, for instance by a simple external bandpass filter or by an optical cavity.

On the basis of CVD or molecular-beam epitaxy, self-assembled QDs can be grown. A very common approach is the Stranski-Krastanov mode applied to the semiconductors indium arsenide (InAs) and gallium arsenide (GaAs) [280]. When InAs is deposited on GaAs, strain arises due to the lattice mismatch of the two crystalline materials. Only the so-called wetting layer, about one or two monolayers thick, still constitutes a smooth film matching the underlying crystal lattice. In further layers, self-assembled islands start to form reducing the overall strain. Their thickness ranges from 4 to 7 nm, their diameter from 20 to 40 nm [147]. Finally, a capping layer of GaAs is applied. The level structure and therefore the emission characteristics of the QDs is strongly correlated to the particular size, shape and the mixture of InAs and GaAs of such an island. Because these parameters are slightly different for each QD, the emission wavelengths of an ensemble exhibits a large inhomogeneous broadening, i.e. they are widely spread. The possible emission wavelength for this material combination spans from 850 to 1000 nm. Furthermore, the location of the structures is not predefined. Techniques to achieve site-controlled QD growth however exist, an important step towards scalable systems (see [281, 153] and references therein).

Just like color centers in bulk diamond, QDs in GaAs, having a refractive index of 3.8, suffer from a reduced collection efficiency as a result of total internal reflection. Mi-

crocavities, directly fabricated around the QDs, can serve to channel the emission into a well-collectable mode and Purcell-enhance the emission rate to overcome this shortcoming. A very common approach relies on planar distributed Bragg reflector (DBR) microcavities [282, 283, 284, 285, 286, 287, 288, 289, 290, 291]. Alternating, optical quarter-wavelength-thick layers of high and low refractive index, usually GaAs ($n = 3.8$) and AlAs ($n = 3.0$), serve to longitudinally confine an optical mode. A one optical wavelength thick spacer layer of GaAs in between the DBR system hosts the InAs islands at its center. Lateral confinement is achieved by etching pillars or microposts out of the layer system. Because of the large refractive index contrast with the surrounding medium (usually air), total internal reflection proves beneficial, in this case. A larger number of layer pairs beneath the QD ensures that most of the light is coupled out of the top of the pillar, allowing for a high extraction efficiency. Mode volumes on the order of λ^3 and below, and quality factors of some $1 \cdot 10^3 - 1 \cdot 10^4$ provide a large coupling strength, enabling coherent light-matter interaction.

A wealth of seminal experiments have been performed with QDs. A good idea of their potential can already be obtained by primarily considering the subgroup of In(Ga)As/GaAs QDs typically operating at temperatures of a few Kelvin. Starting around the year 2000, a number of QD-based single-photon sources were reported, among them QDs embedded in microdisk resonators [292] and pillar microcavities [285, 286], or without cavity [293]. Furthermore, QDs have also been successfully coupled to photonic crystal cavities [294]. In 2001, an electrically driven single-photon source was demonstrated by integrating QDs into a conventional semiconductor light-emitting diode, as a step towards better practicality [279]. Remarkably, the polarization, the oscillator strength, and the energy of the optical transitions in a single QD can be tuned with a DC voltage [295]. Quantum key distribution based on a QD single-photon turnstile was realized [122]. By means of optical or electrical excitation, indistinguishable photons originating from one and the same QD [296, 297, 15] or even from two remote systems can be produced [298, 299]. For a single QD, the strong coupling regime of cavity quantum electrodynamics has been reached [287, 288], photon blockade [300], and resonantly driven coherent oscillations have been demonstrated [301, 302], just like the onset of lasing in the strong coupling regime [303]. Highly efficient single-photon sources based on a QD in a photonic nanowire [13] and a micropillar cavity [291] have been implemented, providing collected photon count rates of several $1 \cdot 10^5\, s^{-1}$. Moreover, entangled photon pairs can be produced [304, 305, 306, 307], even with a high degree of indistinguishability $I > 0.8$ and a large efficiency $\epsilon > 0.8$ at the same time [290]. A teleportation protocol has been experimentally demonstrated [308].

As this far-from-complete overview may illustrate, semiconductor QDs are a promising tool for QIP. Advanced semiconductor device technology allows their artificial growth and integration into miniaturized monolithic cavities, in order to tailor the light-matter interactions to multiple requirements. However, a major drawback is their weak carrier confinement that requires operation at cryogenic temperatures. Even though other QD systems providing single photons at room temperature are being explored [309], the lack of long spin coherence times still sets a noteworthy limit to their field of application.

2.2.4.4. Carbon Nanotubes

Optically excited single-photon emission from single-wall carbon nanotubes (CNTs) at low temperatures ($< 25\,\mathrm{K}$) was shown in the near infrared by Högele *et al.* in 2008 [310]. It was attributed to Auger processes inhibiting multi-photon generation to some degree and the existence of localized excitons. However, it has not been completely resolved, why CNTs behave like single-photon emitters. One possible explanation is based on the assumption of extremely well-localized excitons due to an individual state with lowered energy. The latter might be caused by a distortion of the environment of the CNT, e.g. by doping. In 2015, room-temperature, fluctuation-free single-photon emission in the near infrared has been shown by Ma *et al.* [311]. Here, single-wall CNTs had been incorporated into a SiO2 matrix, giving rise to the creation of solitary oxygen dopants. Only recently, the potential for electrical excitation of semi-conducting CNTs for single-photon emission has been investigated under cryogenic conditions by Khasminskaya *et al.* [312]. In this approach, the CNTs serve as single-photon emitters and provide the electrical lead at the same time. The emitted photons are directly coupled into an optical waveguide for efficient light collection.

2.2.5. Summary

It is fair to say that to date no single concept is able to satisfy all requirements on an ideal single-photon source at once. Especially practical considerations, like scalability or operability at ambient conditions represent major obstacles for many approaches that exhibit excellent properties otherwise. The NV center in diamond stands out, because apart from providing single photons, it may serve as quantum memory and spin-photon interface. Its quantum mechanical functionality is preserved up to room temperature and diamond nano-engineering has the potential to enable scalable systems [313, 314, 243, 36, 315, 316]. The phonon-induced broad emission spectrum represents a major downside. However, by coupling the NV center to an ultra-small mode volume cavity with low finesse, its entire emission spectrum can be Purcell-enhanced, to allow for a large brightness and near-unity collection efficiency.

2.3. Characterization

2.3.1. Saturation behavior

We introduce a simple model to gain basic understanding about the saturation behavior and the efficiency of single color centers that behave like emitting dipoles with strongly damped coherence at room temperature. The system consists of two discrete energy levels and an additional mode continuum of higher levels, such that it can be driven non-resonantly. The ground state $|1\rangle$ is separated by the energy $h\nu_0$ from the excited state $|2\rangle$, as shown in Fig. 2.5(a). Excitation into higher levels of the continuum is achieved by illumination with a laser with frequency $\nu_L > \nu_0$, when an excitation photon is absorbed. From the higher levels the system relaxes nonradiatively and very fast into the excited

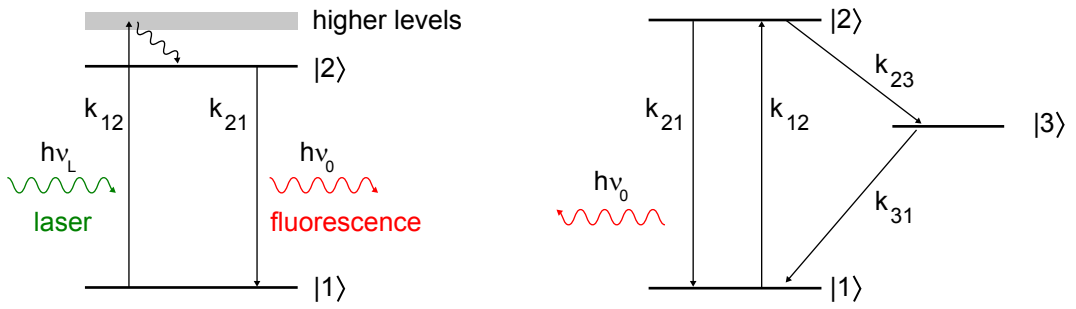

(a) (b)

Figure 2.5.: (a) Two-level scheme with continuum of higher levels (b) Three-level scheme involving the additional metastable state $|3\rangle$.

state $|2\rangle$. From here it decays radiatively into the ground state $|1\rangle$ by spontaneous emission of a photon with frequency ν_0. Before the system can re-emit another photon, it has to be recycled into the excited level. Since this is connected with a certain time delay, the system may act as single-photon source.

For a negligible relaxation time from the higher levels to the excited state, the pump rate coefficient k_{12} is proportional to the excitation laser power P_{ex},

$$k_{12} = aP_{\mathrm{ex}}, \tag{2.28}$$

with the constant of proportionality a. The optical transition featuring the fluorescence of the color center is characterized by the rate k_{21}. The populations of the involved levels ρ_1, ρ_2 sum up to unity,

$$\rho_1 + \rho_2 = 1. \tag{2.29}$$

If coherences are not considered, the population dynamics are governed by rate equations:

$$\begin{pmatrix} \dot{\rho}_1 \\ \dot{\rho}_2 \end{pmatrix} = \begin{pmatrix} -k_{12} & k_{21} \\ k_{12} & -k_{21} \end{pmatrix} \cdot \begin{pmatrix} \rho_1 \\ \rho_2 \end{pmatrix}. \tag{2.30}$$

Pumping with a continuous wave laser results in reaching a steady state when $\dot{\rho}_1 = \dot{\rho}_2 = 0$. Equations 2.29 and 2.30 yield the equilibrium population of the excited state

$$\rho_2(t \to \infty) = \frac{k_{12}}{k_{12} + k_{21}}. \tag{2.31}$$

The photon emission rate $R = k_{21}\rho_2$ is determined with the help of Equs. 2.28 and 2.31,

$$R(P_{\mathrm{ex}}) = \frac{k_{21}P_{\mathrm{ex}}}{P_{\mathrm{ex}} + k_{21}/a} = \frac{k_{21}P_{\mathrm{ex}}}{P_{\mathrm{ex}} + P_{\mathrm{sat}}}, \tag{2.32}$$

with the saturation power $P_{sat} = k_{21}/a$. As a consequence, the emission rate increases approximately linearly with the excitation power for $P_{ex} \ll P_{sat}$, whereas it converges to k_{21} for $P_{ex} \gg P_{sat}$. This behavior is well-known as saturation. From the point of view of this simple model, the emission rate is only limited by the intrinsic decay rate from the excited to the ground state k_{21}. The brightness of a single-photon source is then directly determined by the decay rate or alternatively the fluorescence lifetime $1/k_{21}$ of the optical transition.

The saturated emission rate serves as indicator for the intrinsic brightness of a source. It is independent of the excitation power and expresses the maximally obtainable rate of single-photons

$$R_\infty = R(P_{\text{ex}} \to \infty) = k_{21}. \tag{2.33}$$

This basic model gives insight into the physical process of saturation and provides a parameter to compare the brightness of single-photon sources. The exact electronic level structure of an emitter is often not of primary interest and the simplification is appropriate in this context. However, the simple model inherently fails in explaining phenomena connected to additional levels like metastable states. Also known as "shelving states", these states can trap an electronic excitation for a certain time span and degrade the brightness of the source. Note that the decay via the metastable state does not contribute to the fluorescence. In order to gain understanding about the related phenomena, the model is extended by an intermediate level $|3\rangle$ that represents a metastable state (see Fig. 2.5(b)) [221]. Like before, coherences are assumed to be damped fast, such that they do not play a role. Two additional transitions are now considered. First, the decay from the excited state $|2\rangle$ to the metastable state $|3\rangle$ with the rate k_{23}. Second, the decay from the metastable state $|3\rangle$ to the ground state $|1\rangle$ with rate k_{31}. Even though, a transition from the shelving state to the excited state is in principal possible, "deshelving" is omitted, here for simplicity[9]. Population dynamics are then governed by the following rate equations

$$\begin{pmatrix} \dot{\rho}_1 \\ \dot{\rho}_2 \\ \dot{\rho}_3 \end{pmatrix} = \begin{pmatrix} -k_{12} & k_{21} & k_{31} \\ k_{12} & -k_{21} - k_{23} & 0 \\ 0 & k_{23} & -k_{31} \end{pmatrix} \cdot \begin{pmatrix} \rho_1 \\ \rho_2 \\ \rho_3 \end{pmatrix}. \tag{2.34}$$

Analytically resolving this set of equations yields the steady state population of the excited level

$$\rho_2(t \to \infty) = \frac{k_{12}}{(1 + \frac{k_{23}}{k_{31}})k_{12} + k_{21} + k_{23}}. \tag{2.35}$$

The emission rate as a function of the excitation power is then given by

$$R(P_{\text{ex}}) = \frac{\xi k_{21} P_{\text{ex}}}{P_{\text{ex}} + P_{\text{sat}}}, \tag{2.36}$$

[9] After deshelving back to the excited state, relaxation to the ground state would give rise to another photon that may influence the saturation behavior and the $g^{(2)}$-function.

with

$$\xi = \frac{1}{1 + \frac{k_{23}}{k_{31}}} \tag{2.37}$$

and

$$P_{\text{sat}} = \xi(k_{21} + k_{23})/a, \tag{2.38}$$

in analogy to the calculus of the previous model. The factor ξ can be interpreted as the time ratio the system is cycling through the fluorescence transition from $|1\rangle$ to $|2\rangle$. The brightness or saturated emission rate of the source is then modified to

$$R_\infty = \xi k_{21}. \tag{2.39}$$

Obviously, the brightness decreases with an increasing ratio k_{23}/k_{31}. Even for small transition rates into the shelving state k_{23}, the brightness can be diminished considerably, if $k_{31} \ll k_{23}$. Cycling through long-lived metastable states is thus disadvantageous for the realization of bright single-photon sources. In contrast, the brightness approaches the value of the two-level model k_{21} for $\xi \to 1$, i.e. $k_{23}/k_{31} \to 0$.

2.3.2. The second-order correlation function

Correlation functions are used to quantify the degree of coherence of electromagnetic fields. The first order correlation function $g^{(1)}$ quantifies the ability of two electric fields to interfere and can be determined experimentally with a Michelson interferometer, for instance. Note that $g^{(1)}$ is only related to the spectrum and fields with the same spectral properties cannot be distinguished from their first-order degree of coherence. The second-order correlation function $g^{(2)}$ correlates intensities instead of amplitudes [317, 318, 150]. Knowledge about the latter reveals whether a light field requires classical or quantum mechanical description and can prove single-emitter behavior.

In classical theory, a temporal second-order correlation function is given by

$$g^{(2)}(\tau) = \frac{E^*(t)E^*(t+\tau)E(t+\tau)E(t)}{\langle E^*(t)E(t)\rangle\langle E^*(t+\tau)E(t+\tau)\rangle} = \frac{\langle I(t)\cdot I(t+\tau)\rangle}{\langle I(t)\rangle^2}, \tag{2.40}$$

where $E(t)$ and $E(t)^*$ are the time dependent electric field amplitude and its complex conjugate, $I(t)$ is the average intensity, τ a time delay and $\langle\,\rangle$ denotes a statistical average, in this case an average over a long time interval. According to the Cauchy-Schwartz inequality, the average intensities at two different points in time t_1, t_2 satisfy

$$2I(t_1)I(t_2) \leq I(t_1)^2 + I(t_2)^2. \tag{2.41}$$

This relation can be used to prove that

$$\left\{\frac{I(t_1) + I(t_2) + ... + I(t_N)}{N}\right\}^2 \leq \frac{I(t_1)^2 + I(t_2)^2 + ... + I(t_N)^2}{N}, \tag{2.42}$$

which can be abbreviated as

$$\langle I(t)\rangle^2 \leq \langle I(t)^2\rangle. \tag{2.43}$$

In combination with Eq. 2.40 this results in

$$g^{(2)}(0) \geq 1. \tag{2.44}$$

Equation 2.41 can be furthermore used to derive

$$\begin{aligned} &\{I(t_1)I(t_1+\tau)+...+I(t_N)I(t_N+\tau)\}^2 \\ \leq\ &\left\{I(t_1)^2+...+I(t_N)^2\right\}\left\{I(t_1+\tau)^2+...+I(t_N+\tau)^2\right\}, \end{aligned} \tag{2.45}$$

where the summations on the right side will be equal for measurement series that are sufficiently long and numerous. Finally this yields

$$\langle I(t)I(t+\tau)\rangle \leq \langle I(t)^2\rangle, \tag{2.46}$$

or more compact

$$g^{(2)}(\tau) \leq g^{(2)}(0). \tag{2.47}$$

In summary, for classical fields, the second-order correlation function never exceeds its value at $\tau = 0$ and is always larger or equal to 1. Thermal or coherent light satisfy these relations. When $g^{(2)}(\tau) < g^{(2)}(0)$ for $\tau < \tau_c$, there are more photon correlations for times shorter than the correlation time τ_c. Photons preferentially arrive together in bunches rather than stochastically. This phenomenon named *photon bunching* is observed for thermal light, for instance. The violation of one of the relations 2.44 or 2.47 is used to prove the *nonclassical* character of an investigated field. For example, when $g^{(2)}(\tau) > g^{(2)}(0)$ more photon pairs are detected with larger rather than shorter time differences, which is the opposite effect called *photon antibunching*. Furthermore, fields can be classified as *sub-Poissonian*, *Poissonian* and *super-Poissonian*, for which $g^{(2)}(0) < 1$, $g^{(2)}(0) = 1$ and $g^{(2)}(0) > 1$, respectively. Note that sub-Poissonian statistics and antibunching are in general distinct effects and the respective definitions should not be confused [319].

By way of example, the second-order correlation function of three classical light sources are quoted from [318]. Coherent light fields of a single frequency, produced by lasers, for instance, are the most simple case:

$$g^{(2)}_{\mathrm{coh}}(\tau) = 1. \tag{2.48}$$

The constant value indicates that there is no time correlation among the photons. In contrast, the photons of thermal light fields originating from a large number of independent emitters tend to bunch. For thermal sources with a Lorentzian or Gaussian frequency distribution stemming from collision-, respectively Doppler-broadening, it can be shown that

$$g^{(2)}_{\mathrm{Lorentz}}(\tau) = 1 + \mathrm{e}^{-2\gamma|\tau|} \tag{2.49}$$

$$g^{(2)}_{\mathrm{Gauss}}(\tau) = 1 + \mathrm{e}^{-\delta^2\tau^2}. \tag{2.50}$$

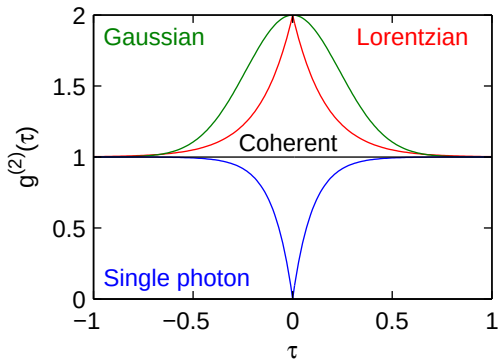

Figure 2.6.: Second-order correlation function for different types of light sources: Single photons (blue), coherent light (black), and thermal sources with a Gaussian (green) or a Lorentzian (red) frequency distribution.

Here, $g^{(2)}(0) = 2$ and $g^{(2)}(\tau \to \pm\infty) = 1$, such that thermal sources can be categorized as super-Poissonian and bunched. All three examples are plotted in Fig. 2.6, together with the second-order correlation function of an ideal single-photon source. The latter cannot be obtained within classical theory.

The transition from a classical to a quantum mechanical treatment is achieved by expressing the electric field by an operator

$$\hat{E}(t) \propto \hat{a}e^{-i\omega} + \hat{a}^\dagger e^{i\omega}, \tag{2.51}$$

with the common photon destruction and creation operators $\hat{a}^\dagger(t)$ and $\hat{a}(t)$ that obey the relations

$$\hat{a}^\dagger|n\rangle = \sqrt{n+1}|n\rangle \tag{2.52}$$

$$\hat{a}|n\rangle = \sqrt{n}|n-1\rangle. \tag{2.53}$$

Here, $|n\rangle$ represents a Fock or number state and contains precisely n photons. The second-order correlation function translates to

$$g^{(2)}(\tau) = \frac{\langle \hat{a}^\dagger(t)\hat{a}^\dagger(t+\tau)\hat{a}(t+\tau)\hat{a}(t)\rangle}{\langle \hat{a}^\dagger(t)\hat{a}(t)\rangle^2}. \tag{2.54}$$

For the derivation, consult, for instance [150].

For all number states with $n \geq 1$, it can be shown that

$$g^{(2)}(0) = \frac{\langle n(n-1)\rangle}{\langle n\rangle^2} = 1 - \frac{1}{n} \tag{2.55}$$

holds true. A field containing a single photon results in $g^{(2)}(0) = 0$. This is in contradiction with Eq. 2.44 and indicates that the field is of non-classical origin. Since $g^{(2)}(0) > 0$ for all fields containing more than a single photon, the second-order correlation function

serves as a standard for the purity of a single-photon source. A measurement resulting in $g^{(2)}(0) < 0.5$ reveals single-photon emission. Alternatively, Eq. 2.55 provides an estimate for the number of emitters in an ensemble.

The complete second-order correlation function can be evaluated by normalizing the population $\rho_2(t)$ to $\rho_2(t \to \infty)$ [221]. The basic model without metastable state that was introduced in the previous paragraph yields [150]

$$g^{(2)}(\tau) = 1 - \mathrm{e}^{-|\tau|/\tau_0}, \tag{2.56}$$

with

$$\tau_0 = \frac{1}{k_{12} + k_{21}}. \tag{2.57}$$

As expected, antibunching already emerges even for this most simple treatment, as displayed by the clear dip at $\tau = 0$, as shown in Fig. 2.6. The time constant τ_0 determines the time delay between the generation of two consecutive photons.

Things get more subtle when the three-level model is applied [150], resulting in

$$g^{(2)}(\tau) = 1 + c{\cdot}\mathrm{e}^{-|\tau|/\tau_1} - (1 + c){\cdot}\mathrm{e}^{-|\tau|/\tau_2}, \tag{2.58}$$

where

$$c = \frac{1 - \tau_1 k_{31}}{k_{31}(\tau_1 - \tau_2)}, \tag{2.59}$$

$$\tau_{1,2} = 2/(A \pm \sqrt{A^2 - 4B}), \tag{2.60}$$

and

$$A = k_{12} + k_{21} + k_{23} + k_{31} \tag{2.61}$$

$$B = k_{12}k_{23} + k_{12}k_{31} + k_{21}k_{31} + k_{23}k_{31}. \tag{2.62}$$

The second order correlation function of the three-level system is shown in Fig. 2.7. Note that both antibunching at $\tau = 0$, as well as correlated emission around the antibunching dip is possible. To illustrate the influence of the additional state, we show two more examples where the transition rates to and from the shelving level are modified, while the rates connected to the optical transition are kept constant. For a small probability to decay into and stay in the shelving state, i.e. small values of k_{23}/k_{31} and k_{31}, the $g^{(2)}$-function is similar to that of the more simple model (see Fig. 2.6). This is confirmed by a brightness close to unity. With an increasing ratio k_{23}/k_{31}, the probability to stay in the shelving state grows, going along with a decrease of the brightness. Interestingly, correlated emission arises in this case, since $g^{(2)}(\tau) > 1$ around the antibunching dip. The smaller k_{31}, the longer the time delays around $\tau = 0$, for which the emission is correlated, before $g^{(2)}(\tau) \to 1$.

The second-order correlation function does not only provide information about the number of emitters, but may also give insight into the level scheme. To this end, the $g^{(2)}$- function is first measured for different excitation powers and then fitted with a

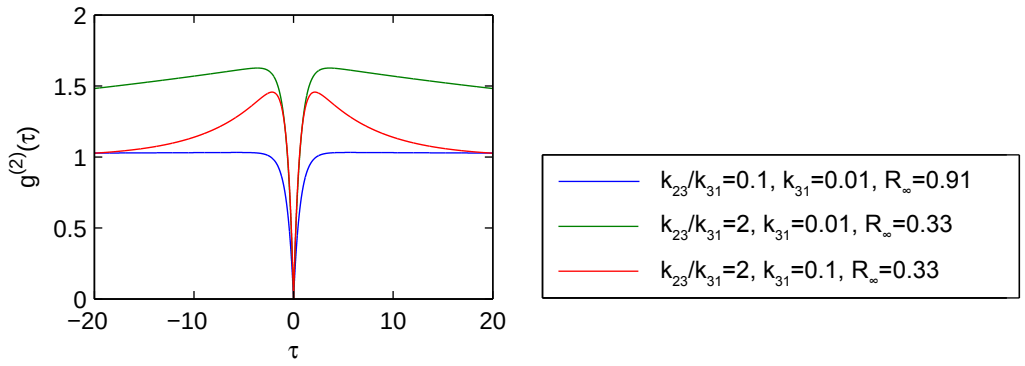

Figure 2.7.: Examples for the second-order correlation function $g^{(2)}(\tau)$ of the three-level model for different values of k_{23} and k_{31} resulting in a modified brightness R_∞ (see legend). The rates $k_{12} = 0.5$ and $k_{21} = 1$ are in common for all curves.

function that has been derived from an assumed level scheme. The fit allows to extract the in general power-dependent transition rates between the individual levels [320]. Furthermore the source brightness of color centers can be inferred from $g^{(2)}(\tau)$.

The second-order correlation function is now routinely measured in a HBT setup. Originally applied in the field of astronomy to measure the angular diameter of radio stars in 1954 [321], the concept has been quickly transferred to the visible range [113].

2.3.3. Indistinguishability

Ideally, spontaneous emission from resonantly driven two-level systems provides bandwidth-limited, i.e. perfectly indistinguishable photons with the same coherent wave packets at identical frequencies and polarization. However, the indistinguishability of real sources is degraded because of three main reasons. First, the interaction of the system with a fluctuating environment leads to a gradual loss of the phase and thus to a spectral broadening of the emission. The dephasing or decoherence time T_2 is given by [322]

$$\frac{1}{T_2} = \frac{1}{2T_1} + \frac{1}{T_2^*}, \tag{2.63}$$

with the fluorescence lifetime T_1, and T_2^* defining pure dephasing processes induced by interactions with the bath. The full-width at half-maximum (FWHM) frequency linewidth is then determined by

$$\delta\nu = \frac{1}{2\pi T_1} + \frac{1}{\pi T_2^*}. \tag{2.64}$$

The minimal, Fourier-transform-limited linewidth is only attained in the absence of pure dephasing, $T_2^* \to \infty$. Comparison of the spontaneous emission lifetime with the emission

linewidth, or alternatively with the decoherence time gives a direct measure for the spectral quality of emitted photons [296].

Second, the emission process can be subject to a timing jitter, e.g. when the excitation scheme involves higher states that must initially relax to the upper level of the fluorescent transition [323]. Third, the emission line may spectrally scatter on a slower timescale, known as spectral diffusion. This is for example caused by charge fluctuations in the local environment [250].

The degree of indistinguishability of two photons can be directly tested on the basis of the Hong-Ou-Mandel effect: Two indistinguishable photons impinging on a 50:50 beam splitter, one on each input port, always exit *pairwise* from one of the output ports. Placing one photo detector at each output arm, no coincident events are registered for perfectly indistinguishable photons. This quantum mechanical effect is based on the bosonic nature of photons and can be explained qualitatively by the superposition of the four possible photon paths through the beam splitter. When one photon is transmitted while the other is reflected, two photons end up in the same output arm. Otherwise, i.e. when both photons are either transmitted or reflected, there is one photon in each output. Due to a relative phase shift, the latter two paths cancel out for indistinguishable particles, which can be interpreted as destructive interference. However, if the two photon wavepackets do not perfectly overlap, there is a non-vanishing probability for the two photons to leave the beam splitter through different output ports. This probability is given by

$$p = (1 - I)/2, \tag{2.65}$$

with the degree of indistinguishability

$$I = \frac{\left\langle \left| \int \mathrm{d}\omega s_1(\omega) s_2^*(\omega) \right|^2 \right\rangle}{\left(\int \mathrm{d}\omega \langle |s(\omega)|^2 \rangle \right)^2}, \tag{2.66}$$

where $s_i(\omega)$ is the spectral envelope functions for two single photons and $\langle\,\rangle$ denotes the ensemble average over $s_i(\omega)$ [147]. Alternatively, the parameter may be expressed by [324, 322]

$$I = \frac{T_2}{2T_1} = \frac{\gamma}{\gamma + \gamma^*}, \tag{2.67}$$

with the population decay rate

$$\gamma = 1/T_1, \tag{2.68}$$

and the pure dephasing rate

$$\gamma^* = 2/T_2^*. \tag{2.69}$$

The relation to the FWHM linewidth can then be written as

$$2\pi\delta\nu = \gamma + \gamma^*. \tag{2.70}$$

In 1987, C. K. Hong, Z. Y. Ou and L. Mandel were the first to demonstrate the two-photon interference effect with photon pairs produced by spontaneous parametric down-conversion [325, 326]. In order to overlap the photons optimally, they displaced the beam splitter by various small distances, while they recorded the coincidence count rate of two photo detectors placed in each of its output arms. The distinct dip they recorded in this way was a clear signature of the almost perfect overlap they had achieved.

This concept has become a benchmark to test the indistinguishability of photons, just like an HBT interferometer is used to check whether a source really emits single photons one by one. Apart from photon pairs produced by spontaneous parametric down-conversion [325, 327, 328], the generation of indistinguishable photons has been demonstrated for a few other systems, among them trapped atoms [168, 169] and ions [170, 172, 329]. While atomic systems are natural sources for indistinguishable photons, solid-state systems are in general more challenging in this respect. As a result of the discussed coupling to the phonon bath, the photons are per se not Fourier-transform-limited at room temperature. Additionally, due to variations of the embedding medium, individual systems are inherently dissimilar with each other and do usually not provide photons with identical properties. This problem is often addressed by simply searching for sufficiently similar systems, by tuning techniques, or more elegantly, by coupling the emitters to microcavities. Indistinguishable photons have been obtained from Nitrogen-Vacancy centers in diamond [256, 257], quantum dots [296, 298, 299, 15], and molecules [199, 202]. Silicon-Vacancy centers in synthetic, ultrapure, low-strain diamond exhibiting intrinsically identical spectral properties constitute a remarkable exception among emitters in the solid state [274, 275].

3. Fabry-Pérot cavities and multilayer coatings

Optical resonators serve to confine and store light at a particular resonant frequency, in the most common case by reflecting photons multiple times at a set of mirrors. They have a vast field of application. For instance, the amplification of light in lasers is realized by embedding a gain medium into an optical resonators, providing the optical feedback. A particularly simple and successful resonator geometry is based on two opposing mirrors, denominated as Fabry-Pérot cavity after French physicists Charles Fabry and Alfred Pérot [330].

In this chapter, the fundamentals of Fabry-Pérot cavities are introduced based on the textbook of Saleh and Teich [331] and the master thesis of M. Mader [332]. First insight into the conditions for light confinement is gained by modeling the light field inside the cavity as standing wave and later as a traveling wave bouncing back and forth between two planar mirrors. The most important cavity parameters are obtained within these simple approaches. Consecutively, the spatial intensity distribution within a Fabry-Pérot cavity with curved mirrors is discussed in the form of Gaussian and Hermite-Gaussian resonator modes, providing a more precise treatment.

Thus far, the mirrors have been treated as abstract optical elements with constant reflectivity. In reality, cavity mirrors are often distributed Bragg reflectors consisting of multiple layers of alternating materials with high and low refractive index. Deeper insight into the optical response of such a multilayer coating system is gained with the help of the matrix calculation method [333]. The fundamentals of this concept are introduced, along with the theoretical framework necessary for the simulation of layered media. Note that this method enables the simulation of a complete Fabry-Pérot cavity composed of two mirrors with an intermediate air spacer layer, as well.

3.1. Fabry-Pérot cavities

3.1.1. Fundamental cavity parameters

A resonator mode is a field distribution that reproduces itself after one round trip inside an optical resonator (excluding power loss). First of all, the modes of a cavity consisting of two opposing parallel, planar, and lossless mirrors are investigated. The modes sustained by such a resonator are found by following an intuitive argumentation, first. A more rigorous treatment is given below.

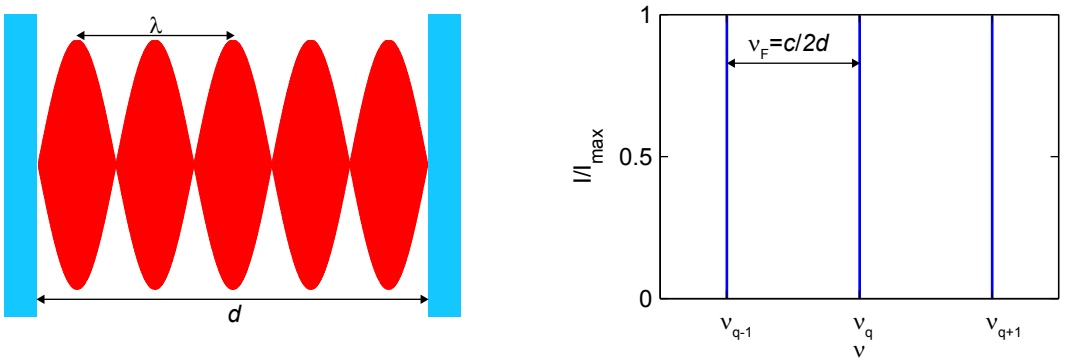

(a) (b)

Figure 3.1.: (a) A standing wave (red) inside a Fabry-Pérot cavity with length d, as an example of a stable resonator mode. In this case, the resonance condition $d = 5 \cdot \lambda/2$ is fulfilled. (b) Sharp resonator modes (blue) separated by the free spectral range ν_F for a resonator with perfect mirrors ($\mathcal{F} = \infty$).

Standing wave treatment

Assuming that the electric field amplitude vanishes at the mirror surfaces, allows only light waves whose half wavelength and integer multiples thereof are equal to the resonator length. If the two mirrors are placed at a distance d, as shown in Fig. 3.1(a), stable resonator modes thus fulfill the resonance condition

$$d = q \cdot \frac{\lambda_q}{2}, \tag{3.1}$$

with the longitudinal mode order $q = 1, 2, ...$ and the wavelengths λ_q. Alternatively, this expression can be formulated in the frequency domain as

$$\nu_q = q \cdot \frac{c}{2d}, \tag{3.2}$$

with the frequency ν_q, and the speed of light c (or more general, the speed of light in the medium embedded between the mirrors). Not only a single mode, but several consecutive modes are supported by the cavity, as illustrated in Fig. 3.1(b). The frequency difference of two neighboring cavity modes is constant for a given cavity length and denominated the free spectral range (FSR):

$$\nu_\mathrm{F} = \frac{c}{2d}. \tag{3.3}$$

This relation serves to experimentally determine the cavity length from the resonance positions. Often, it is also convenient to directly apply the wavelengths of two neighboring resonances located at λ_1 and $\lambda_2 > \lambda_1$ to estimate the cavity length by

$$d = \frac{\lambda_1 \lambda_2}{2(\lambda_2 - \lambda_1)}. \tag{3.4}$$

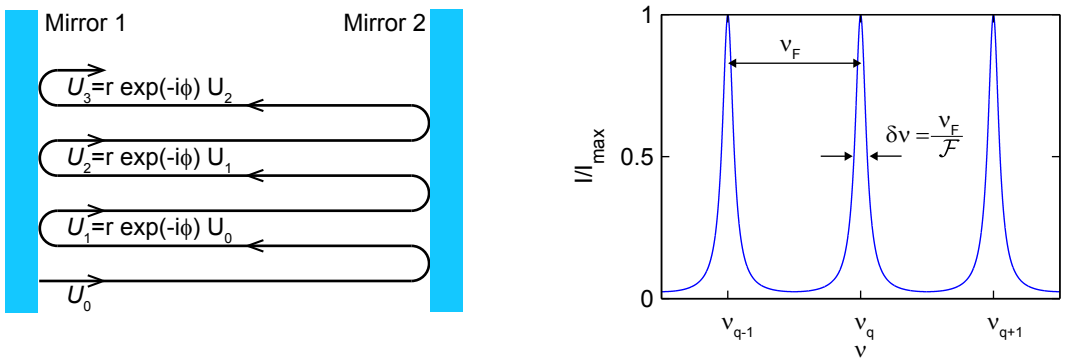

(a) (b)

Figure 3.2.: (a) Schematic of a wave bouncing back and forth between the two mirrors of a Fabry-Pérot cavity. The complex amplitude U_m experiences a phase shift ϕ after each round trip. (b) Neighboring resonant modes separated by the free spectral range ν_F. The resonance width $\delta\nu$ is determined by the cavity finesse, here, $\mathcal{F} = 10$.

Note that the distance of two adjacent modes in the wavelength domain is however not constant, but depends on the wavelength.

Traveling wave treatment

As a more thorough alternative to the intuitive derivation, the resonator modes can be identified by investigating a wave bouncing back and forth between the mirrors. Upon reflection at each (ideal) mirror, the wave experiences a phase shift of π, adding up to 2π, or effectively 0, for both mirrors. Consequently, in order to reproduce itself, the phase shift of the wave after a single round trip of propagation, i.e. after traveling the distance $2d$, must be a multiple of 2π:

$$\phi = k2d = 4\pi\nu d/c = q \cdot 2\pi,\ q = 1, 2, ..., \tag{3.5}$$

with the wave number $k = 2\pi/\lambda$. In short, this relation is expressed as

$$kd = q\pi. \tag{3.6}$$

It is equivalent to Eq. 3.1 and provides the resonance frequencies, as well.

So far, ideal mirrors without loss have been treated. The imposed strict resonance condition is however relaxed for real mirrors with finite reflectivity. It can be derived by expressing the total wave U as a sum of an infinite number of partial waves U_m, $m = 0, 1, 2, ...$, where U_0 is the complex amplitude of an introduced monochromatic plane wave, U_1 represents the wave after the first round trip, U_2 after the second round trip, and so forth, as shown in Fig. 3.2(a). Since the original wave and therefore its successors

are assumed monochromatic, all waves coexist. Due to loss that is introduced upon each reflection at the mirrors or by the embedded medium, the so-called phasors U_m are not of equal magnitude, but are reduced by a round trip amplitude attenuation factor r after each cycle. Hence, $U_1 = hU_0$, with $h = r\mathrm{e}^{-i\phi}$, $U_2 = hU_1$, etc.. The resulting wave U is obtained by adding up the infinite amount of complex amplitudes[1]

$$U = U_0 + U_1 + U_2 + ... = U_0 + hU_0 + h^2U_0 + ... = U_0(1 + h + h^2 + ...) = U_0/(1-h). \quad (3.7)$$

The power inside the cavity is then given by

$$P = |U|^2 = \frac{|U_0|^2}{|1 - r\mathrm{e}^{-i\phi}|^2} = \frac{P_{\max}}{1 + (2\mathcal{F}/\pi)^2 \sin^2(\phi/2)}, \quad (3.8)$$

with

$$P_{\max} = \frac{P_0}{(1-r)^2}, \quad (3.9)$$

where $P_0 = |U_0|^2$ is the power of the initial wave. Furthermore,

$$\mathcal{F} = \frac{\pi\sqrt{r}}{1-r} \quad (3.10)$$

is known as the cavity finesse, the figure of merit to describe the overall resonator loss. In most cases, the spectral response of the resonator is of interest, reformulation of Eq. 3.8 yields

$$P = \frac{P_{\max}}{1 + (2\mathcal{F}/\pi)^2 \sin^2(\pi\nu/\nu_{\mathrm{F}})} = \frac{P_{\max}}{1 + (2\mathcal{F}/\pi)^2 \sin^2(2\pi d/\lambda)}, \quad (3.11)$$

as shown in Fig. 3.2(b). This function comprises cavity resonance at

$$\nu_q = q \cdot \nu_{\mathrm{F}},\ q = 1, 2, ..., \quad (3.12)$$

as has already been derived before. If the cavity finesse is large, i.e. $\mathcal{F} \gg 1$, the width (FWHM) of the resonance peaks is given by

$$\delta\nu \approx \frac{\nu_{\mathrm{F}}}{\mathcal{F}} \quad (3.13)$$

or alternatively, in the wavelength domain by

$$\delta\lambda \approx \frac{\lambda^2}{2d\mathcal{F}}, \quad (3.14)$$

i.e. the width gets more and more narrow with increasing finesse.

The cavity finesse is directly related to the cavity loss. If there is no additional loss inside the cavity (see below), the round trip amplitude attenuation factor r is given by

$$r = \sqrt{R_1 R_2}, \quad (3.15)$$

[1] For the derivation, the geometric series for $n \to \infty$ has been applied: $\sum_{m=0}^{n-1} ax^m = a\frac{1-x^n}{1-x}$, for $x \neq 1$.

with the reflectivity of the two mirrors

$$R_i = r_i^2 = 1 - T_i - L_i, \text{ for } i = 1, 2. \tag{3.16}$$

Here, T_i stands for the mirror transmission and L_i for the total loss of each mirror, for example caused by absorption A_i or scattering S_i. Scattering loss is related to the surface roughness of the mirror and can by approximated by [334]

$$S \approx (4\pi\sigma_{\text{rms}}/\lambda)^2, \tag{3.17}$$

where σ_{rms} is the root mean square (rms) roughness and λ is the wavelength of the incident light.

An exact expression of the Finesse follows from Eqs. 3.10 and 3.15

$$\mathcal{F} = \frac{\pi \left(R_1 R_2\right)^{1/4}}{1 - \left(R_1 R_2\right)^{1/2}}. \tag{3.18}$$

For large mirror reflectivities, i.e. $R_i \to 1$ and thus $r \to 1$, Eq. 3.10 can be approximated by[2]

$$\mathcal{F} \approx \frac{\pi}{1 - r} \approx \frac{2\pi}{T_1 + L_1 + T_2 + L_2}. \tag{3.19}$$

This relation is often applied to estimate the finesse that can be achieved with a set of characterized mirrors. Additional round trip loss inside the cavity L_{add} further reduces the finesse to

$$\mathcal{F} \approx \frac{2\pi}{T_1 + L_1 + T_2 + L_2 + 2L_{\text{add}}} = \frac{2\pi}{L_{\text{tot}}}, \tag{3.20}$$

with the the total loss given by

$$L_{\text{tot}} = 2L_{\text{add}} + \sum_i T_i + L_i = 2L_{\text{add}} + \sum_i T_i + A_i + S_i. \tag{3.21}$$

Another important parameter is the probability with which a photon leaves the cavity through one of the mirrors. It is determined by

$$p(T_i) = \frac{T_i}{T_1 + T_2 + L_1 + L_2}. \tag{3.22}$$

Now, the intensity fraction T transmitted through the cavity is briefly discussed in analogy to the previous derivation of the intra-cavity intensity. An incident plane wave with complex amplitude U_i and power P_i impinges on the cavity and bounces back and forth multiple times between the mirrors, as shown in Fig. 3.3. The wave U_t with power P_t is transmitted through the cavity. The transmission is defined as $T = P_t/P_i$. The

[2] Using a Taylor expansion of first order $\sqrt{1-x} \approx 1 - x/2$

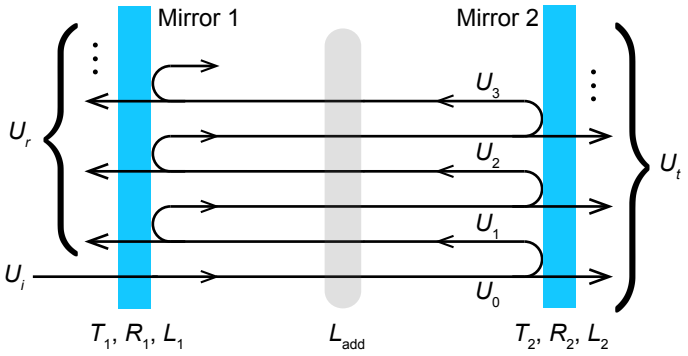

Figure 3.3.: Multiple reflections of a light wave between two resonator mirrors

transmitted power is inferred from the transmission through the second mirror and the total power inside the resonator $P_t = T_2 P$. Moreover, the initial power P_0 relates to the incident power P_i as $P_0 = T_1 P_i$. Together, this yields $P_t/P_i = T_1 T_2 \cdot P/P_0$. Applying Eq. 3.11, the transmission of a Fabry-Pérot resonator as a function of the frequency is obtained:

$$T(\nu) = \frac{T_{\max}}{1 + (2\mathcal{F}/\pi)^2 \sin^2(\pi\nu/\nu_{\mathrm{F}})}. \tag{3.23}$$

The maximal transmission on resonance is given by

$$T_{\max} = \frac{T_1 T_2}{(1-r)^2} \approx \frac{4T_1 T_2}{(T_1 + L_1 + T_2 + L_2)^2}, \tag{3.24}$$

where the approximation is valid for large mirror reflectivities. The power P_r of the reflected wave U_r can be derived in an analogous manner. The peak power inside the resonator is given by

$$P_{\max} \approx 4T_1 P_i \left(\frac{F}{\pi}\right)^2. \tag{3.25}$$

As an alternative to the cavity finesse, the quality factor Q is a common figure of merit of resonators. In general, it is defined as the total stored energy inside a resonator divided by the energy loss per cycle. For an optical cavity this results in

$$Q = \frac{\nu_0}{\delta\nu}, \tag{3.26}$$

with the resonance frequency ν_0 and the resonance width $\delta\nu$ (FWHM). Unlike the cavity finesse, the quality factor is not constant, but depends on the cavity length

$$Q = \frac{\nu_0}{\nu_F} \cdot \mathcal{F} = \frac{d}{\lambda/2} \cdot \mathcal{F} = q \cdot \mathcal{F}. \tag{3.27}$$

Furthermore, the photon lifetime inside the resonator τ_{p} is connected to the quality factor via [335]

$$Q = 2\pi\nu_0\tau_{\mathrm{p}}. \tag{3.28}$$

3.1.2. Gaussian resonator modes

Several fundamental cavity parameters have been derived on the basis of a plane parallel cavity and planar monochromatic waves traveling back and forth between the mirrors. However, this simple treatment fails in explaining the spatial intensity distribution and exact resonance frequencies inside Fabry-Pérot cavities with curved mirrors. Spherical mirrors support Gaussian beams as resonator modes, as shown subsequently. In paraxial approximation, Gaussian beams are solutions of the Helmholtz equation under the constraints the spherical geometry of the mirrors impose.

The complex amplitude U of a Gaussian beam is a function of the axial and radial distance z and $\rho = \sqrt{x^2 + y^2}$, given by

$$U(\rho, z) = A_0 \left(\frac{w_0}{w(z)} \right) \exp \left[-\frac{\rho^2}{w(z)^2} \right] \exp \left[-ikz - ik\frac{\rho^2}{2R(z)} + i\zeta(z) \right], \tag{3.29}$$

with the mode radius

$$w(z) = w_0 \sqrt{1 + \left(\frac{z}{z_0} \right)^2}, \tag{3.30}$$

the wavefront curvature

$$R(z) = z + \frac{z_0^2}{z}, \tag{3.31}$$

and the Gouy phase

$$\zeta(z) = \arctan \left(\frac{z}{z_0} \right), \tag{3.32}$$

which will become important later. For each axial distance from the beam waist z, the intensity

$$I(\rho, z) = I_0 \left(\frac{w_0}{w(z)} \right)^2 \exp \left[\frac{-2\rho^2}{w(z)^2} \right], \tag{3.33}$$

follows a Gaussian distribution in the transverse xy-plane, explaining the denomination as Gaussian beam. The wavefront curvature is maximal at an axial distance know as the Rayleigh range

$$z_0 = \frac{\pi w_0^2}{\lambda}. \tag{3.34}$$

The minimal beam radius w_0 is found at $z = 0$ and $w(z)$ grows in both directions with increasing axial distance from the beam waist (see Fig. 3.4(a)).

In order to be sustained by the resonator, the wavefront curvature of a cavity mode has to match the mirror radii. Only then the Gaussian beam can reproduce itself and represents a stable mode, given that the phase also retraces itself (see below). Now, the Gaussian beam is determined, which satisfies the geometrical condition for a resonator with spherical mirrors having radii R_1 and R_2 that are spaced by the distance d, as illustrated in Fig. 3.4(b). The origin of the z-axis is defined at the position of the beam waist, which has to be determined still. The mirrors are located at the positions z_1 and

$$z_2 = z_1 + d, \tag{3.35}$$

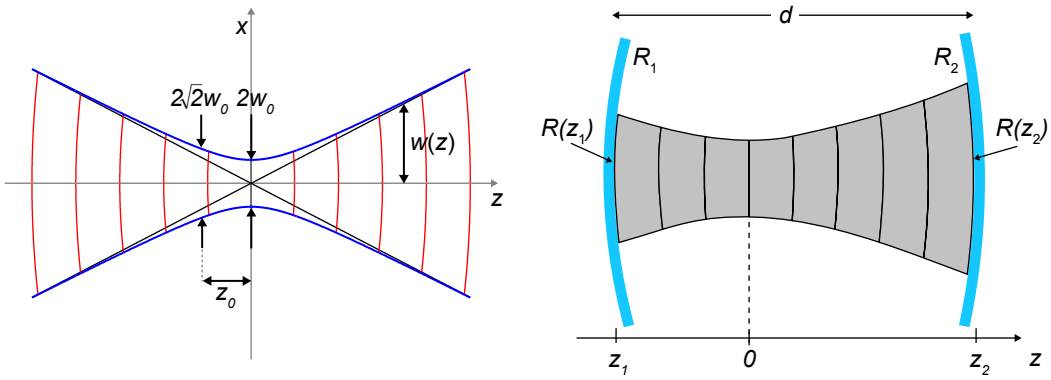

(a) (b)

Figure 3.4.: (a) Gaussian beam defined by the waist w_0, or alternatively the Rayleigh range z_0. The outer shape of the beam (blue line), the spherical wavefronts (red), and the tangents the beam approaches for large values of z are shown. (b) Schematic of a Gaussian beam whose wavefronts match the curvature of the spherical cavity mirrors.

respectively. The mirror positions on the z-axis are chosen such that the radius of curvature of the beam matches the radii of the mirrors R_1 at z_1, and R_2 at z_2. The convention for the signs for the radii has to considered carefully. For concave mirrors, the radii of curvature are negative, $R_i < 0$. However, the beam radius of curvature is defined to be positive for $z > 0$ and negative for $z < 0$, resulting in $R_1 = R(z_1)$ and $-R_2 = R(z_2)$. Thus, the following relations have to be fulfilled:

$$R_1 = R(z_1) = z_1 + \frac{z_0^2}{z_1}, \tag{3.36}$$

$$-R_2 = R(z_2) = z_2 + \frac{z_0^2}{z_2}. \tag{3.37}$$

Combining Eqs. 3.35, 3.36, and 3.37, results in

$$z_1 = \frac{-d(R_2 + d)}{R_2 + R_1 + 2d} \tag{3.38}$$

and

$$z_0^2 = \frac{-d(R_1 + d)(R_2 + d)(R_2 + R_1 + d)}{(R_2 + R_1 + 2d)^2}. \tag{3.39}$$

Once, the location of the beam center, as well as its Rayleigh range z_0 is determined, all necessary information about the beam is known.

To assure that the established solution constitutes a Gaussian beam, the Rayleigh range z_0 has to be real. The stability condition $z_0 > 0$ yields

$$0 \leq \left(1 + \frac{d}{R_1}\right)\left(1 + \frac{d}{R_2}\right) \leq 1. \tag{3.40}$$

Plane-concave cavities

The most important resonator geometry of this work consists of one concave mirror with a radius of curvature $|R_1| = R$ and one planar mirror with $R_2 = \infty$. Since this is simply a special case of the already discussed cavities with two concave mirrors, the relevant parameters are found straightforward from Eqs. 3.35, 3.38, and 3.39: $z_1 = -d$, $z_2 = 0$, and $z_0 = \sqrt{Rd - d^2}$. From Eq. 3.34 the minimal $1/e^2$ beam radius is obtained

$$w_0^2 = \lambda/\pi \cdot \sqrt{Rd - d^2}. \tag{3.41}$$

The latter is located directly on the planar mirror. The beam radius on the concave mirror (the mirror on the machined fiber) results from Eq. 3.30 and is given by

$$w_\mathrm{m} = w_0 \sqrt{1 + \left(\frac{\lambda d}{\pi w_0^2}\right)^2}. \tag{3.42}$$

The stability condition Eq. 3.40 requires that the the cavity length is shorter than the radius of curvature of the concave mirror: $0 \leq d \leq R$.

The mode volume of a plane-concave cavity is given by

$$V = \frac{\int \mathrm{d}^3 r \left|\vec{E}(\vec{r})\right|^2}{\max \left|\vec{E}(\vec{r})\right|^2} = \frac{\pi}{4} \cdot w_0^2 d = \frac{\lambda}{4} d^2 \sqrt{\frac{R}{d} - 1}. \tag{3.43}$$

Resonance frequencies

So far, it has been shown that the Gaussian beam can be a mode of a resonator with spherical mirrors, if the wavefronts match the mirror surfaces. It is furthermore necessary that the phase reproduces itself after each round trip. The phase of the Gaussian beam is given by Eq. 3.29

$$\phi(\rho, z) = kz - \zeta(z) + \frac{k\rho^2}{2R(z)}. \tag{3.44}$$

Since the phase is identical on all points on the spherical wavefront, as well as on the mirror surface, it is sufficient to restrict the analysis to the optical axis $\rho = 0$. Here, $\phi(0, z) = kz - \zeta(z)$ and the phase retardation with respect to a plane wave is given by the Gouy phase $\zeta(z)$. At the mirror positions z_1 and z_2

$$\phi(0, z_1) = kz_1 - \zeta(z_1), \tag{3.45}$$

$$\phi(0, z_2) = kz_2 - \zeta(z_2). \tag{3.46}$$

After each round trip, the total phase change accumulates to

$$\Delta\phi = 2\left[\phi(0, z_2) - \phi(0, z_1)\right] = 2k(z_2 - z_1) - 2\left[\zeta(z_2) - \zeta(z_1)\right] = 2kd - 2\Delta\zeta, \tag{3.47}$$

with $\Delta\zeta = \zeta(z_2) - \zeta(z_1)$. The beam reproduces itself, if the phase change $\Delta\phi$ after one round trip is an integer multiple of 2π, i.e. $\Delta\phi = q \cdot 2\pi$, $q = 0, \pm 1, \pm 2, \ldots$. Applying the

common definitions of the wave number $k = 2\pi\nu/c$ and the free spectral range $\nu_\mathrm{F} = c/2d$, the resonance condition reads

$$\nu_q = q\nu_\mathrm{F} + \frac{\Delta\zeta}{\pi}\nu_\mathrm{F}. \tag{3.48}$$

These are the resonance frequencies of a resonator with spherical mirrors. The frequency spacing of neighboring modes, the free spectral range, is identical to that of the plane parallel cavity. However, a constant offset that depends on the mirror curvature is added.

In addition, an advanced formulation of the optical cavity length d follows from Eq. 3.48 by insertion of the free spectral range $\nu_\mathrm{F} = c/2d$ (Eq. 3.3):

$$d = \left(q + \frac{\Delta\zeta}{\pi}\right)\frac{c}{2\nu_q} = \left(q + \frac{\Delta\zeta}{\pi}\right)\frac{\lambda_q}{2}. \tag{3.49}$$

3.1.3. Hermite-Gaussian resonator modes

The Gaussian beam is not the only mode supported by a resonator with spherical mirrors. In fact, there is a whole family of modes, that satisfy the Helmholtz equation under the corresponding boundary conditions. The Hermite-Gaussian beam has the same wavefront as the Gaussian beam, only its amplitude distribution is different. Thus, all Hermite-Gaussian beams constitute stable resonator modes, given that their phase reproduces itself after one round trip in the resonator.

The complex amplitude $U_{l,m}$ and the intensity distribution $I_{l,m}$ of the Hermite-Gaussian beam with the transverse mode order (l, m) are given by

$$\begin{aligned} U_{l,m}(x,y,z) =& A_{l,m}\left(\frac{w_0}{w(z)}\right)\mathrm{G}_l\left[\frac{\sqrt{2}x}{w(z)}\right]\mathrm{G}_m\left[\frac{\sqrt{2}y}{w(z)}\right] \\ &\cdot\exp\left[-ikz - ik\frac{\rho^2}{2R(z)} + i(l+m+1)\zeta(z)\right] \end{aligned} \tag{3.50}$$

and

$$I_{l,m}(x,y,z) = |A_{l,m}|^2\left(\frac{w_0}{w(z)}\right)^2\mathrm{G}_l^2\left[\frac{\sqrt{2}x}{w(z)}\right]\mathrm{G}_m^2\left[\frac{\sqrt{2}y}{w(z)}\right], \tag{3.51}$$

respectively. Here $A_{l,m}$ is a constant and $\mathrm{G}_l(u) = \mathrm{H}_l(u)\exp\left(-u^2/2\right)$, for $l = 0, 1, 2, ...$, is the Hermite-Gaussian function of order l with the Hermite polynomial $H_l(u)$. For instance, for $l = 0$ $H_0(u) = 1$ and the Hermite Gaussian beam of 0th order $I_{0,0}$ is equivalent to the Gaussian beam. The phase of the Hermite-Gaussian beam depends on the mode order:

$$\phi(0,z) = kz - (l+m+1)\zeta(z). \tag{3.52}$$

In analogy to the previous argumentation, the resonance frequencies result in

$$\nu_{q,l,m} = q\nu_\mathrm{F} + (l+m+1)\frac{\Delta\zeta}{\pi}\nu_\mathrm{F}, \tag{3.53}$$

with the longitudinal or axial mode order q and the transverse mode order (l, m). In the lateral intensity distribution, l and m correspond to the number of nodes along the x and y axis, respectively. A few properties of the resonance frequencies of Hermite-Gaussian resonator modes are summarized:

- The longitudinal mode spacing for a given transverse mode (l, m) is still given by the free spectral range: $\nu_{q+1,l,m} - \nu_{q,l,m} = \nu_\mathrm{F}$
- Transverse modes with the same sum $l + m$ have identical resonances frequencies
- For a given longitudinal mode q, different transverse modes (l, m) and (l', m') exhibit a frequency spacing determined by

$$\nu_{q,l,m} - \nu_{q,l',m'} = (l - l' + m - m')\frac{\Delta\zeta}{\pi}\nu_\mathrm{F}. \tag{3.54}$$

  Since the Gouy phase difference $\Delta\zeta$ is related to the mirror radii, higher order transverse modes serve to directly obtain information about the mirrors.

3.2. Simulation of multilayer systems with the matrix calculation method

To understand or optimize the behavior of cavity mirrors, the simulation of optical coatings is an important ingredient. These coatings usually consist of multiple layers of different materials. By adjusting the thicknesses and refractive indices of these layers the spectral behavior of the mirror can be designed to large extent. The spectral response (reflectivity, transmission, absorption) of a multilayer coating, as well as the field distribution within the layer system is efficiently evaluated with a matrix calculation method where each layer is represented by a characteristic matrix. The product of all these matrices describes the entire layer stack and allows to calculate the characteristics parameters of the mirror. The introduction of an air spacer layer in between two such mirror stacks enables the simulation of a complete cavity, as well. The thickness of the spacer layer, which represents the mirror distance, can then be varied to predict the spectral position of the cavity resonances for different cavity lengths, for instance.

This section introduces the basics of the matrix method closely following the text book of Furman and Tikhonravov [333]. Starting with Maxwell's equations, the relations defining the electromagnetic field in a stratified medium are presented, first. Based on these findings, the derivation of the matrix method is sketched. Finally, the relevant equations are given that allow to evaluate the mirror reflectivity, transmission and absorption, as well as the electromagnetic field at an arbitrary position within the coating stack.

Electromagnetic field in a layered medium

A multilayer coating can be modeled as a stack of plane-parallel, isotropic layers of infinite extent in the dimensions parallel to the layer boundaries embedded between two

homogeneous, semi-infinite, isotropic media (outer space and substrate). The permittivity ϵ and conductivity σ of the individual layers are then a function of one spatial coordinate normal to the layer boundary. Consider a plane electromagnetic wave traveling in the first medium towards the first layer. At the boundary, the plane wave will party be reflected back into the first medium and partly be transmitted into the second one. The assumption of infinite lateral dimensions is valid, since the wavelength is much smaller than the lateral extension of the layers and the overall thickness of the coating stack. In addition, the embedding media and the layers are assumed to be non-magnetic (magnetic permeability $\mu = \mu_0$) and without space charges. Under these conditions, the Maxwell equations (in cgs units) within the medium read

$$\Delta \times \vec{\mathcal{E}} = -\frac{1}{c}\frac{\partial \vec{\mathcal{H}}}{\partial t}, \quad \Delta \times \vec{\mathcal{H}} = \frac{\epsilon}{c}\frac{\partial \vec{\mathcal{E}}}{\partial t} + \frac{4\pi\sigma}{c}\vec{\mathcal{E}}, \tag{3.55}$$

with the speed of light c and the electric and magnetic vectors $\vec{\mathcal{E}}$ and $\vec{\mathcal{H}}$. Within a layer, the permittivity ϵ and the conductivity σ are continuous, and $\vec{\mathcal{E}}$ and $\vec{\mathcal{H}}$ satisfy Eqs. 3.55. At the layer boundaries, i.e. at the discretion points of ϵ and σ, the tangential components of $\vec{\mathcal{E}}$ and $\vec{\mathcal{H}}$ have to be continuous. If the field is excited by an incoming plane wave, the evaluation of the electric and magnetic fields in a stratified medium can be reduced to the solution of the simplified Maxwell equations 3.55, obeying these boundary conditions.

The space variable z is chosen normal to the layer boundaries pointing to the outer space. The incoming wave shall be plane and monochromatic with frequency ω. The fields are expressed by

$$\vec{\mathcal{E}} = \vec{E}e^{i\omega t}, \quad \vec{\mathcal{H}} = \vec{H}e^{i\omega t}, \tag{3.56}$$

such that $\vec{E}$ and $\vec{H}$ are depending only on spatial variables and the definition of the time dependence $e^{i\omega t}$ is in accordance with a complex refractive index with a negative imaginary part. Eqs. 3.55 can then be further simplified to

$$\Delta \times \vec{E} = -ik\vec{H}, \quad \Delta \times \vec{H} = ik\tilde{\epsilon}(z)\vec{E}, \tag{3.57}$$

with the common definition of the wave number $k = 2\pi/\lambda$, the vacuum wavelength of the incident wave $\lambda = c/2\pi\omega$, and the complex permittivity

$$\tilde{\epsilon} = \epsilon - i\frac{4\pi\sigma}{c}, \tag{3.58}$$

which is a function of z, here.

The electromagnetic field is decomposed into an S-component ($\vec{E}$ normal to plane of incidence) and a P-component ($\vec{E}$ parallel to plane of incidence) and the coordinate system is aligned such that the x-axis is normal to the plane of incidence and the y-axis is lying within this plane, as shown in Fig. 3.5(a). The angle of the incoming (outgoing) wave with respect to the z-axis is γ_a (γ_s), the permittivity of the outer space (substrate) is ϵ_a (ϵ_s). The equations valid for the S- and P-components can now be derived from Eqs. 3.57.

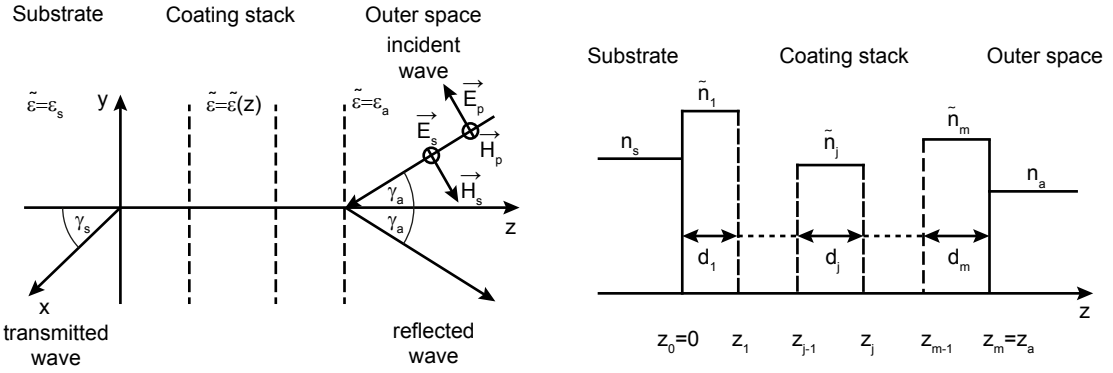

(a) (b)

Figure 3.5.: (a) Electromagnetic field vectors for S- and P-polarization. (b) Sketch of a coating stack with m layers.

S-polarization: The electromagnetic fields can be expressed as

$$\vec{E} = \begin{pmatrix} u(z) \\ 0 \\ 0 \end{pmatrix} e^{ik\alpha y},\ \vec{H} = \begin{pmatrix} 0 \\ -v(z) \\ \alpha u(z) \end{pmatrix} e^{ik\alpha y}, \tag{3.59}$$

and the functions $u(z)$ and $v(z)$ are defined by the differential equations

$$\frac{\mathrm{d}u}{\mathrm{d}z} = ikv, \quad \frac{\mathrm{d}v}{\mathrm{d}z} = ik\left[\tilde{\epsilon}(z) - \alpha^2\right] u, \tag{3.60}$$

with

$$\alpha = \sqrt{\epsilon_\mathrm{a}}\sin(\gamma_\mathrm{a}) = \sqrt{\epsilon_\mathrm{s}}\sin(\gamma_\mathrm{s}), \tag{3.61}$$

which represents Snell's law being valid for absorbing media ($\epsilon_\mathrm{s} = \tilde{\epsilon}_\mathrm{s}$), as well. These differential equations follow from the simplified Maxwell's equations. Within an individual layer, where ϵ and σ, and thus the complex permittivity $\tilde{\epsilon}(z)$ are continuous, Eqs. 3.60 are valid. At the layer boundaries, where ϵ and σ take discrete values, the tangential components of the electromagnetic fields have to be continuous, implying the continuity of $u(z)$ and $v(z)$.

P-polarization: In analogy, the electromagnetic field is given by

$$\vec{E} = \begin{pmatrix} 0 \\ u(z) \\ -\frac{\alpha}{\tilde{\epsilon}(z)} v(z) \end{pmatrix} e^{ik\alpha y},\ \vec{H} = \begin{pmatrix} v(z) \\ 0 \\ 0 \end{pmatrix} e^{ik\alpha y}, \tag{3.62}$$

with $u(z)$ and $v(z)$ satisfying

$$\frac{\mathrm{d}u}{\mathrm{d}z} = ik\left[1 - \frac{\alpha^2}{\tilde{\epsilon}(z)}\right] v, \quad \frac{\mathrm{d}v}{\mathrm{d}z} = ik\tilde{\epsilon}(z)u, \tag{3.63}$$

where α is still defined by Eq. 3.61.

Altogether, Eqs. 3.59-3.63 constitute the mathematical framework for the description of electromagnetic fields in stratified media. For normal incidence, i.e. $\alpha = 0$, both polarization-cases are equal.

Matrix calculation method

Based on the quoted relations, a matrix calculation technique can now be applied to evaluate the electromagnetic field inside a multilayer coating with little effort. The layer stack is assumed to consists of a finite number m of homogeneous isotropic layers, as sketched in Fig. 3.5(b). The numbering of the layers starts at the substrate. Their right boundaries are positioned at $z_1, z_2, ...$, where the last coordinate $z_m = z_\mathrm{a}$ defines the border of the coating to the outer medium, which is equal to the total thickness of the coating stack. The geometrical thicknesses of the layers are given by $d_1, d_2, ...$, with the corresponding complex refractive indices $\tilde{n}_1, \tilde{n}_2, ...$ The substrate and the outer space have refractive indices n_s and n_a, respectively, which are typically, but not necessarily real. The complex refractive index, which is the parameter commonly used in practice, is related to the complex permittivity by

$$\tilde{n}^2 = \epsilon. \tag{3.64}$$

For each homogeneous layer, the electromagnetic field is determined by the previously given equations. For the S-polarization, and the jth layer, the corresponding equations read

$$\frac{\mathrm{d}u}{\mathrm{d}z} = ikv, \quad \frac{\mathrm{d}v}{\mathrm{d}z} = ik\left[\tilde{n}_j^2 - \alpha^2\right] u, \tag{3.65}$$

which can be transformed into a single differential equation of second order

$$\frac{\mathrm{d}^2u}{\mathrm{d}z^2} + k^2(\tilde{n}_j^2 - \alpha^2)u = 0. \tag{3.66}$$

The definition of the wave propagation angle in the jth layer

$$\alpha = \tilde{n}_j \sin\gamma_j = n_\mathrm{a} \sin\gamma_\mathrm{a}, \tag{3.67}$$

which is again based on Snell's law, allows for further simplification of Eq. 3.66:

$$\frac{\mathrm{d}^2u}{\mathrm{d}z^2} + (k\tilde{n}_j \cos\gamma_j)^2 u = 0. \tag{3.68}$$

For absorbing media, γ_j is complex. The latter differential equation has two linear independent solutions that can be chosen as

$$u_1(z) = \cos\left[k\tilde{n}_j \cos\gamma_j (z - z_{j-1})\right], \tag{3.69}$$

$$u_2(z) = \sin\left[k\tilde{n}_j \cos\gamma_j (z - z_{j-1})\right], \tag{3.70}$$

where z_{j-1} is the left boundary of the jth layer. Their linear combination yields the general solution of Eq. 3.68:

$$u(z) = c_1 \cos\left[k\tilde{n}_j \cos\gamma_j (z - z_{j-1})\right] + c_2 \sin\left[k\tilde{n}_j \cos\gamma_j (z - z_{j-1})\right]. \tag{3.71}$$

Choosing $z = z_{j-1}$, yields $c_1 = u(z_{j-1})$. To determine the second prefactor, $u(z)$ is differentiated with respect to z. Setting $z = z_j$ once more, results in $k\tilde{n}_j \cos\gamma_j c_2 = u'(z - z_j)$. By making use of Eq. 3.65, this can be written as $c_2 = iv(z - z_j)/\tilde{n}_j \cos(\gamma_j)$. Eventually, the solution of the original differential equation of second order 3.68 in the jth layer reads

$$u(z) = u(z_{j-1}) \cos\left[k\tilde{n}_j \cos\gamma_j (z - z_{j-1})\right] + iv(z - z_{j-1}) \sin\left[k\tilde{n}_j \cos\gamma_j (z - z_{j-1})\right] / \tilde{n}_j \cos\gamma_j. \tag{3.72}$$

When combining the derivative of $u(z)$ with Eq. 3.65 one finds

$$v(z) = i\tilde{n}_j \cos\gamma_j u(z_{j-1}) \sin\left[k\tilde{n}_j \cos\gamma_j (z - z_{j-1})\right] + v(z_{j-1}) \cos\left[k\tilde{n}_j \cos\gamma_j (z - z_{j-1})\right]. \tag{3.73}$$

Note, that the latter two formulas allow to determine the tangential components of the electric and magnetic field vectors at an arbitrary position within the jth layer.

For $z = z_j$, these relations simplify to

$$\begin{aligned} u(z_j) &= u(z_{j-1}) \cos\phi_j + (i/q_j) v(z_{j-1}) \sin\phi_j, \\ v(z_j) &= iq_j u(z_{j-1}) \sin\phi_j + v(z_{j-1}) \sin\phi_j, \end{aligned} \tag{3.74}$$

with the definitions

$$\phi_j = k\tilde{n}_j \cos\gamma_j d_j, \quad d_j = z_j - z_{j-1}, \quad q_j = \tilde{n}_j \cos\gamma_j, \tag{3.75}$$

where ϕ_j is the so-called angular phase thickness of the jth layer. As a result, the field at the boundary of the jth layer is completely defined by the field at the other boundary. And because the function $u(z)$ and $v(z)$ are continuous at the boundaries between the layers, the field can be recalculated from the boundary at the substrate $z = z_0$ to the boundary to the outer space $z_m = z_\mathrm{a}$. This allows to evaluate the complete field in the stratified medium.

An elegant representation of Eqs 3.74 is the matrix form

$$\begin{pmatrix} u \\ v \end{pmatrix}_{z=z_j} = M_j \begin{pmatrix} u \\ v \end{pmatrix}_{z=z_{j-1}}, \tag{3.76}$$

with the characteristic matrix of the jth layer

$$M_j = \begin{pmatrix} \cos\phi_j & (i/q_j)\sin\phi_j \\ iq_j \sin\phi_j & \cos\phi_j \end{pmatrix}. \tag{3.77}$$

The field at the outer medium follows from the field at the substrate via

$$\begin{pmatrix} u \\ v \end{pmatrix}_{z=z_\mathrm{a}} = M_m M_{m-1} \ldots M_1 \begin{pmatrix} u \\ v \end{pmatrix}_{z=0}. \tag{3.78}$$

The characteristic matrix of a complete multilayer coating is the product of the individual characteristic matrices in order from the outer space towards the substrate

$$M = M_m M_{m-1} ... M_1, \tag{3.79}$$

with

$$M = \begin{pmatrix} m_{11} & m_{12} \\ m_{21} & m_{22} \end{pmatrix}. \tag{3.80}$$

Once the characteristic matrix M has been evaluated, the amplitude transmission and reflection coefficients t and r, and the power transmission and reflectivity T and R can be obtained from the relations

$$t(k) = \frac{2q_a}{q_a m_{11} + q_s m_{22} + q_a q_s m_{12} + m_{21}}, \tag{3.81}$$

$$r(k) = \frac{q_a m_{11} - q_s m_{22} + q_a q_s m_{12} - m_{21}}{q_a m_{11} + q_s m_{22} + q_a q_s m_{12} + m_{21}}, \tag{3.82}$$

$$T = \frac{q_\mathrm{s}}{q_\mathrm{a}} \left| \frac{E_T}{E_A} \right|^2 = \frac{q_s}{q_a} |t|^2, \quad R = \left| \frac{E_R}{E_A} \right|^2 = |r|^2, \tag{3.83}$$

with the necessary definitions for S- and P-polarization (analogous calculation) listed in Table 3.1. E_A, E_T and E_R are the amplitudes of the tangential components of the electric field vector of the incident, transmitted and reflected waves.

Polarization	q_s	q_a	q_j	ϕ_j
S	$n_\mathrm{s} \cos\gamma_j$	$n_\mathrm{a} \cos\gamma_\mathrm{a}$	$\tilde{n}_j \cos\gamma_j$	$\phi_j = k\tilde{n} \cos\gamma_j d_j$,
P	$n_\mathrm{s} / \cos\gamma_j$	$n_\mathrm{a} / \cos\gamma_\mathrm{a}$	$\tilde{n}_j / \cos\gamma_j$	$k = 2\pi/\lambda$

Table 3.1.: Calculation parameters for S- and P-polarization

Absorption stemming from layers with complex refractive indices can be inferred from the law of energy conservation

$$A = 1 - R - T. \tag{3.84}$$

Furthermore, the matrix method provides an easy way to evaluate the electromagnetic field in the layer stack. As already presented for the S-component, the field at an arbitrary position inside the jth layer is given by Eqs. 3.72 and 3.73. The derivation of the P-component follows in analogy. Both cases can be written in the combined form

$$\begin{aligned} u(z) &= u(z_{j-1}) \cos\left[k\tilde{n}_j \cos\gamma_j (z - z_{j-1})\right] + (i/q_j) v(z - z_{j-1}) \sin\left[k\tilde{n}_j \cos\gamma_j (z - z_{j-1})\right], \\ v(z) &= i q_j u(z_{j-1}) \sin\left[k\tilde{n}_j \cos\gamma_j (z - z_{j-1})\right] + v(z_{j-1}) \cos\left[k\tilde{n}_j \cos\gamma_j (z - z_{j-1})\right], \end{aligned} \tag{3.85}$$

where q_j is defined by Table 3.1. To obtain the entire field distribution from these formulas, it is necessary to relate $u(z_{j-1})$ and $u(z_{j-1})$ to the field amplitude of the incident field. If E is the tangential component of the electric field vector of the incoming

wave for S- or P-polarization, the transmitted wave is given by $u(0) = tE$ and $v(0) = q_s u(0) = q_s tE$. Making use of the characteristic matrices the electromagnetic field at the boundary $z = z_{j-1}$ can then be expressed by

$$\begin{pmatrix} u(z_{j-1}) \\ v(z_{j-1}) \end{pmatrix} = M_{j-1} ... M_1 \begin{pmatrix} 1 \\ q_s \end{pmatrix} tE. \tag{3.86}$$

4. Emitter-cavity coupling

In the previous chapter, the key parameters of optical resonators have been discussed on the basis of Fabry-Pérot cavities. In this chapter, the interaction of light and matter inside a resonator is investigated. The strong and the weak coupling regime of cavity quantum electrodynamics will be introduced by means of a single two-level atom coupled to a cavity, in accordance with the text book of Fox [336]. While phenomena like Rabi oscillations become manifest in the strong coupling regime, the modification of the spontaneous emission rate characterizes the weak coupling regime, which is the relevant domain for this work. The Purcell factor, as the figure of merit for the enhancement of the spontaneous emission rate by a cavity, will be derived for three different cases following Meldrum *et al.* [27]: The bad cavity and the bad emitter regime are simply two important special cases of the general treatment, discussed subsequently. At last, a more elaborate rate model for the coupling of solid state emitters suffering from dissipation and dephasing is briefly sketched, in accordance with the theoretical description of Auffeves *et al.* [337, 338, 26, 322].

4.1. Introduction

Consider a two-level atom inside a cavity. If one of the cavity modes is tuned into resonance with the transition frequency of the atom, a resonant exchange of photons between the atom and the cavity can occur and hence the interaction between the atom and the cavity photons can be modified. The relative strength of this interaction is given by the following fundamental parameters:

- the coherent atom-photon coupling rate g_0,
- the photon decay rate of the cavity κ, and
- the non-resonant decay rate γ of the atom.

While the coupling rate g_0 characterizes the coherent transfer of excitation between the atom and the cavity field, the cavity decay rate κ and the decay rate of the atom γ account for dissipative processes.

In general, decoherence and phase relaxation lead to a broadening of the optical transition [26]. These effects are particularly strong for emitters in the solid state that are inherently coupled to a surrounding matrix. Decoherence-induced broadening is, for instance, caused by phonon-assisted processes or spectral diffusion. In turn, spectral diffusion can be simply modeled as an additional pure dephasing channel, if it happens

on a timescale that is much shorter than the spontaneous emission time. In a simplified treatment,

- the pure dephasing rate γ^*

may thus be used to capture the broadening processes encountered when working with artificial atoms [338, 26, 322].

The strong-coupling limit is reached when the coherent coupling rate g_0 is the by far largest rate, i.e. $g_0 \gg \max(\kappa, \gamma, \gamma^*)$. Here, the interaction between the atom and the photons occurs on a faster time scale than the irreversible processes. Thus, the emitted photon can be reabsorbed by the atom before it gets lost from the cavity mode. This represents a reversible process.

On the contrary, in the weak coupling regime, the coupling rate is much smaller than at least one of the other rates, i.e. $g_0 \ll \max(\kappa, \gamma, \gamma^*)$. Here, the emission process is irreversible like in free-space spontaneous emission. However, the emission rate can still be modified by the cavity. For a closer analysis, the different rates are now addressed in detail. Note that in cavity quantum electrodynamics the rates are usually expressed as the half-width at half-maximum (HWHM) angular frequency[1], while in laser physics full-width at half maximum (FWHM) frequencies are common.

At first, the coherent atom-photon coupling rate is discussed. The atom interacts with the vacuum field existing within the cavity, as a result of zero-point fluctuations of the electromagnetic field. The electric dipole interaction determines the interaction energy between the atom and the vacuum field

$$\Delta E = |\mu_{12} \mathcal{E}_{\mathrm{vac}}| \,, \tag{4.1}$$

with the electric dipole transition matrix element $\mu_{12} = -e\langle g\,|x|\,e\rangle$. Here, $|g\rangle$ denotes the ground state and $|e\rangle$ the excited state of the two-level system, not to be confused with the elementary charge e. The magnitude of the vacuum field is given by[2]

$$\mathcal{E}_{\mathrm{vac}} = \left(\frac{\hbar\omega}{2\epsilon_0 V}\right)^{1/2}, \tag{4.2}$$

where $\omega = 2\pi\nu_0$ is the angular frequency of the mode, V the cavity mode volume, and ϵ_0 the vacuum permittivity. By identifying the interaction energy ΔE with $\hbar g_0$, the coupling rate is obtained:

$$g_0 = \left(\frac{\mu_{12}^2 \omega}{2\epsilon_0 \hbar V}\right)^{1/2}. \tag{4.3}$$

[1] In parallel, FWHM angular frequencies are in use, which is quite confusing, at times.

[2] Noting that the time-averaged energy contribution of the electric and the magnetic fields are the same, the magnitude of the electric field can be inferred from the zero point energy per mode: $2 \times \int \frac{1}{2}\epsilon_0 \mathcal{E}_{\mathrm{vac}}^2 \mathrm{d}V = \frac{1}{2}\hbar\omega$

The coupling strength is therefore proportional to the dipole moment μ_{12}, the transition frequency, and the inverse cavity mode volume. If an ensemble of N atoms is coupled to the cavity, the overall coupling rate scales as

$$g = \sqrt{N} g_0. \tag{4.4}$$

The photon decay rate of the cavity κ (HWHM) is defined by the resonance width of the cavity and is therefore directly connected to the finesse, the quality factor (Eq. 3.26) and the photon lifetime (Eq. 3.28):

$$\kappa \equiv \frac{2\pi\delta\nu}{2} = \frac{\pi c}{2d\mathcal{F}} = \frac{\pi\nu_0}{Q} = \frac{1}{2\tau_\mathrm{p}}. \tag{4.5}$$

Thus, the larger the quality factor of the cavity, the smaller the photon decay rate.

In free space, the spontaneous decay rate of an ideal emitter with a Fourier-limited linewidth is related to its radiative lifetime τ_r by

$$\gamma_0 = 1/2\tau_\mathrm{r}.$$

The non-resonant decay rate inside a cavity γ is influenced by different factors: First of all, the atom may decay via another transition, emitting a photon at a frequency, which is detuned with respect to the cavity resonance. This case corresponds to a breakdown of the approximation of the atom as a two-level system. Furthermore, the atom may emit a photon at the resonant frequency of the cavity, but in a direction that does not overlap with a cavity mode, meaning that it is again non-resonant. This process is characterized by the cavity geometry. A simple estimation of the spontaneous emission rate out the side of the cavity is for example given by [339]

$$\gamma_\mathrm{out} = \gamma_0 \left[1 - \frac{3\Delta\Omega}{8\pi}\right], \tag{4.6}$$

with the total solid angle subtended by the cavity mirrors at the position of the atom $\Delta\Omega$. This approximation is valid for an atom placed at the center of a cavity, with its dipole aligned at right angles to the cavity axis and $\Delta\Omega \ll 4\pi$. At last, the atom can also be scattered from the excited to another state and the decay may then be non-radiative, i.e. without the emission of any photon at all.

4.2. Strong coupling regime

The Jaynes-Cummings model was the first purely quantum mechanical approach treating the interaction of a two-level atom with a single quantized mode of a cavity field. It was introduced by Edwin Jaynes and Fred Cummings in 1963, in order to compare the quantum theory of radiation to the semi-classical description, where only the atom is quantized, but the electromagnetic radiation is a classical field [340, 341]. The two-level system can either be in the ground state $|g\rangle$ with energy $E = 0$ or in the excited state

$|e\rangle$ with energy $E = \hbar\omega_0$, where ω_0 is the angular resonance frequency of the atom. The Hamiltonian for the mere atom is thus given by $H_\mathrm{a} = \hbar\omega_0\sigma^+\sigma^-$, with the creation and annihilation operators of the atom $\sigma^+ = |e\rangle\langle g|$ and $\sigma^- = |g\rangle\langle e|$, respectively. In analogy, the electromagnetic field inside the cavity is expressed by the bosonic creation and annihilation operators for photons: $H_\mathrm{c} = \hbar\omega_\mathrm{c} a^\dagger a$, with the angular photon frequency ω_c. The number operator $a^\dagger a$ is the observable that counts the number of photons n. The corresponding energy eigenvalues of the cavity field are thus given by $E_\mathrm{c} = \hbar\omega_\mathrm{c} n$. Finally, the interaction between the atom and the cavity field is addressed. In the rotating wave approximation the interaction Hamiltonian comprises only two terms: $H_\mathrm{int} = \hbar g_0 \left(a^\dagger\sigma^- + \sigma^+ a\right)$. These terms correspond to the relaxation of the atom into the ground state, while a photon is created at the same time and vice versa, the annihilation of a photon, while the atom is transferred from the ground into the excited state. It is the coupling constant $g_0 \in \mathbb{R}^+$ that determines the coupling strength between the atom and the cavity field. The integral system is then expressed by the sum of all introduced terms, known as Jaynes-Cummings Hamiltonian:

$$H_\mathrm{JC} = \hbar\omega_0\sigma^+\sigma^- + \hbar\omega_\mathrm{c} a^\dagger a + \hbar g_0(a^\dagger\sigma^- + \sigma^+ a). \tag{4.7}$$

The Jaynes-Cummings model still serves as a theoretical basis for the investigation of light-matter interactions in the the strong coupling regime. Since this regime plays a minor role for this work, the Jaynes-Cummings model is not treated in more detail, here and we refer the interested reader to the text books [5, 317]. Only the main characteristics of the strong coupling regime are briefly addressed.

The strong coupling regime is characterized by a coupling rate g_0 exceeding the cavity decay rate κ, the non-resonant decay rate of the atom γ, and the pure dephasing rate γ^*. A photon that is emitted into a resonant mode may then bounce back and forth between the mirrors and be reabsorbed by the atom, before it gets lost, representing a reversible process. The coupled system dynamics are governed by a coherent exchange of the excitation between the atom and the cavity field mode. This interplay leads to an oscillatory energy exchange known as *vacuum Rabi oscillations*. The so-called *vacuum Rabi frequency* $\Omega = 2g_0$ determines the oscillation rate. The system spends half of the oscillation time in the state $|e, 0\rangle$ (atom excited, no photon in cavity field mode), and the state $|g, 1\rangle$ (atom in ground state, one photon in cavity field mode), respectively. The new stationary eigenstates, known as *dressed states*, are a linear superposition of the excitation of the cavity and the atom. In the resonant case, they are given by $|\pm\rangle = [|e, 0\rangle \pm i|g, 1\rangle] / \sqrt{2}$. During the periods of oscillation, energy is leaking to the environment with a rate γ and to the cavity radiation modes with a rate κ [147]. Consequently, energy dissipation happens at the overall rate $1/2\gamma + 1/2\kappa$. Note that increasing the coupling rate enhances the frequency at which energy is exchanged between the atom and the cavity field, but does not influence the fraction of energy dissipated in the form of photons.

The experimental realization of the strong coupling regime calls for cavities with small mode volumes to increase the coupling rate g_0 and high quality factors to decrease the cavity decay rate κ. All other dissipative rates connected to dephasing and non-resonant emission need to limited to a minimum. As well, the cavity must not support more than

a single mode, which is resonant with the emitter. These demands are very challenging and require a tour de force of experimental commitment. The efforts towards reaching this goal have been nicely summarized in the Noble lecture of S. Haroche [4]. Further reviews of the topic can be found in [1, 342, 343, 3].

Pioneering work in realizing the strong coupling regime with single atoms was performed in H. Walthers group where the so-called one-atom maser was developed in the mid-1980s [344, 345, 3]. Microwave transitions of Rydberg atoms were coupled to a high-Q superconducting cavity. Some years later, strong coupling was also observed in the optical domain [346, 347, 348].

4.3. Weak coupling regime and Purcell effect

Weak coupling is characterized by an atom-cavity coupling rate g_0 much smaller than the cavity decay rate κ, the non-resonant decay rate of the emitter γ, or the pure dephasing rate γ^*, which can be particularly large for emitters in the solid-state. A photon emitted by the atom escapes from the atom-cavity system, before it can be reabsorbed by the atom. Consequently, the interaction is not coherent and the emission process is irreversible, like in free space. However, the cavity is able to modify the density of states the photons can decay into. As a result, the radiative emission rate can be enhanced or suppressed compared to free space. The excited state spontaneous emission rate is thus not constant, but may be controlled by means of a cavity.

In the weak coupling regime, perturbation theory serves well to describe the atom-cavity interaction. Fermi's golden rule is used to first calculate the spontaneous emission rate in free-space, followed by the one in a single-mode cavity. Based on these results, the Purcell factor [11] characterizing the effect of the cavity is finally introduced.

4.3.1. Free-space spontaneous emission

The transition rate for the spontaneous emission in free space can be calculated with the help of an atom inside a cavity, whose mode volume is large enough to have a negligible physical effect on the atom. In this case, the cavity just serves as a mathematical trick to simplify the calculation. According to Fermi's golden rule the transition probability per unit time is given by

$$W_{\mathrm{fs}} = \frac{2\pi}{\hbar^2} \left|M_{12}\right|^2 \rho(\omega), \tag{4.8}$$

with the transition matrix element M_{12} and the density of states of the cavity $\rho(\omega)$. For photon modes in free space, the density of states is given by[3]

$$\rho(\omega) = \frac{\omega^2 V}{\pi^2 c^3}, \tag{4.9}$$

[3] See for example Appendix C in [336]

with the large cavity mode volume V and the speed of light c. Assuming electric dipole interaction, the matrix element can be written as

$$M_{12} = \langle \vec{p} \cdot \vec{\mathcal{E}} \rangle, \tag{4.10}$$

where $\vec{p}$ is the electric dipole. In free space, the electric field $\mathcal{E}$ is equal to the vacuum field $\mathcal{E}_{\mathrm{vac}}$ given by Eq. 4.2. Averaging over all orientations of the atomic dipole with respect to the field direction results in

$$M_{12}^2 = \frac{1}{3}\mu_{12}^2 \mathcal{E}_{\mathrm{vac}}^2 = \frac{\mu_{12}^2 \hbar\omega}{6\epsilon_0 V}. \tag{4.11}$$

Altogether, Fermis Golden Rule (Eq. 4.8) yields the free-space transition probability

$$W_{\mathrm{fs}} \equiv \frac{1}{\tau_{\mathrm{r}}} = \frac{\mu_{12}^2 \omega^3}{3\pi\epsilon_0 \hbar c^3}, \tag{4.12}$$

with the radiative lifetime τ_{r}. The volume V cancels out, as expected. Remember that for an ideal emitter with a Fourier-limited linewidth

$$\tau_{\mathrm{r}} = 1/2\gamma_0,$$

where γ_0 respresents the natural linewidth (HWHM). Making use of the latter relations, the coupling constant (Eq. 4.3) can also be expressed as

$$g_0 = \sqrt{\frac{3c\lambda^2\gamma_0}{4\pi V}}. \tag{4.13}$$

4.3.2. Spontaneous emission of an emitter in a cavity and the Purcell effect

Now, the modified emission rate of an emitter inside a cavity is investigated in the weak coupling limit. To this end, Fermi's Golden Rule is applied, in the compared to Eq. 4.8 more general form

$$W_{\mathrm{cav}} = \frac{2\pi}{\hbar} \int_0^\infty |M_{12}(\omega)|^2 \, \rho(\omega)\Lambda(\omega)\mathrm{d}\omega. \tag{4.14}$$

Here, M_{12} is the transition matrix element and $\rho(\omega)$ and $\Lambda(\omega)$ are the densities of states of the cavity and the emitter, respectively. The extension with $\Lambda(\omega)$ needs to considered only, when the width of the emitter's emission spectrum becomes comparable to or larger than that of the cavity resonance. For the usually sharp emission spectra of atoms, $\Lambda(\omega)$ reduces to a branching ratio for the typical case of multiple optical transitions. In a more rigorous treatment, the evaluation of the transition rate can be categorized into three different cases [27]:

1. If the emitter spectrum is much more narrow than the cavity resonance spectrum, the emitter density of states can be approximated by a delta function in frequency: $\Lambda(\omega) = \delta(\omega - \omega_0)$. This regime is known as bad cavity regime, since the cavity loss is the limiting factor, i.e. $\kappa > \gamma + \gamma^* \gg g_0$.

2. If the cavity resonance is much more narrow than that of the emitter spectrum, the cavity density of states is treated as a delta function $\rho(\omega) = \delta(\omega - \omega_{\mathrm{cav}})$. This regime is usually denoted the bad emitter regime, $\gamma + \gamma^* > \kappa \gg g_0$.

3. If the spectral width of both emitter and cavity resonance are comparable, the integral in Eq. 4.14 accounting for $\rho(\omega)$ and $\Lambda(\omega)$ needs to be carried out.

As already mentioned, the first case corresponds to the standard text book example of a two-level atom inside a cavity. Even though, it cannot be directly applied to the experiments of this work, it serves well to introduce the concept. The latter two cases represent the theoretical basis of NV centers coupled to high- and low-finesse cavities, respectively.

1. Bad cavity regime

Now the focus is on a narrow-band emitter, such as an atom, inside a single-mode cavity, meaning that there is only one cavity mode close to a single atomic transition frequency. Of course more than a single resonator mode exists. However, all other modes are assumed to be far from resonance and thus negligible. The density of states of the emitter $\Lambda(\omega) = \delta(\omega - \omega_0)$ is then approximated by a delta function centered at the emission frequency ω_0 and Fermi's Golden Rule takes the simple form of Eq. 4.8. The cavity mode is assumed to have an angular frequency ω_{c} and a linewidth $\kappa = \pi\delta\nu$ (HWHM), which is connected to the quality factor of the cavity according to Eq. 3.26 by

$$Q = \frac{\omega_{\mathrm{c}}}{2\kappa}. \tag{4.15}$$

The density of states of the cavity can be modeled as a Lorentzian function

$$\rho(\omega) = \frac{1}{\pi\kappa} \frac{\kappa^2}{(\omega - \omega_{\mathrm{c}})^2 + \kappa^2}, \tag{4.16}$$

satisfying the condition that there is only one resonant mode

$$\int_0^\infty \rho(\omega) = 1. \tag{4.17}$$

At the angular transition frequency of the atom $\omega = \omega_0$, Eq. 4.16 reads

$$\rho(\omega_0) = \frac{1}{\pi\kappa} \frac{\kappa^2}{(\omega_0 - \omega_{\mathrm{c}})^2 + \kappa^2} \tag{4.18}$$

and on resonance, i.e. $\omega_0 = \omega_{\mathrm{c}}$, simplifies to

$$\rho(\omega_0) = \frac{1}{\pi\kappa} = \frac{2Q}{\pi\omega_0}. \tag{4.19}$$

In analogy to the free-space case, the electric dipole matrix element is given by Eq. 4.10 yielding

$$M_{12}^2 = \xi^2 \mu_{12}^2 \mathcal{E}_{\mathrm{vac}}^2 = \xi^2 \frac{\mu_{12}^2 \hbar\omega}{2\epsilon_0 V}, \tag{4.20}$$

with the normalized dipole orientation factor

$$\xi = \frac{\left|\vec{p}\cdot\vec{\mathcal{E}}\right|}{|\vec{p}|\left|\vec{\mathcal{E}}\right|}. \tag{4.21}$$

For a randomly oriented dipole in free space $\xi^2 = 1/3$.

Inserting Eqs. 4.18 and 4.20 into Fermi's Golden Rule (Eq. 4.14), results in the spontaneous emission rate inside the cavity:

$$W_{\mathrm{cav}}(\omega_0) = \frac{2}{\hbar\epsilon_0}\mu_{12}^2 \xi^2 \frac{Q}{V} \frac{\kappa^2}{(\omega_0 - \omega_{\mathrm{c}})^2 + \kappa^2}. \tag{4.22}$$

The Purcell factor C can then be defined by comparing W_{cav} to the free-space transition probability (Eq. 4.12)

$$C = \frac{W_{\mathrm{cav}}}{W_{\mathrm{fs}}} = \frac{\tau_{\mathrm{r,fs}}}{\tau_{\mathrm{r,cav}}}, \tag{4.23}$$

which takes the general form

$$C = \frac{3}{4\pi^2}\left(\frac{\lambda}{n}\right)^3 \frac{Q}{V} \cdot \xi^2 \frac{\kappa^2}{(\omega_0 - \omega_{\mathrm{c}})^2 + \kappa^2}. \tag{4.24}$$

Here, $c/\omega = \lambda/2\pi$ has been used, λ being the free-space wavelength of the photons and n the refractive index of the medium inside the cavity. On resonance and for ideally oriented dipoles, the Purcell factor may reach its maximal value

$$C_0 = \frac{3}{4\pi^2}\left(\frac{\lambda}{n}\right)^3 \frac{Q}{V}, \tag{4.25}$$

as illustrated for different examples in Fig. 4.1(a). Insertion of the expressions for the cavity quality factor (Eq. 3.27) and the mode volume (Eq. 3.43) of a plane-concave Fabry-Pérot cavity yields the dependence on the cavity finesse $\mathcal{F}$ and mode radius w_0:

$$C_0 = \frac{6}{\pi^3}\left(\frac{\lambda}{n}\right)^2 \frac{\mathcal{F}}{w_0^2}. \tag{4.26}$$

Furthermore, the coherent coupling rate g_0 (Eq. 4.13), the cavity decay rate κ (Eq. 4.5) and the free-space spontaneous emission rate γ_0, allow a simple expression of the ideal Purcell factor:

$$C_0 = \frac{g_0^2}{\kappa\gamma}. \tag{4.27}$$

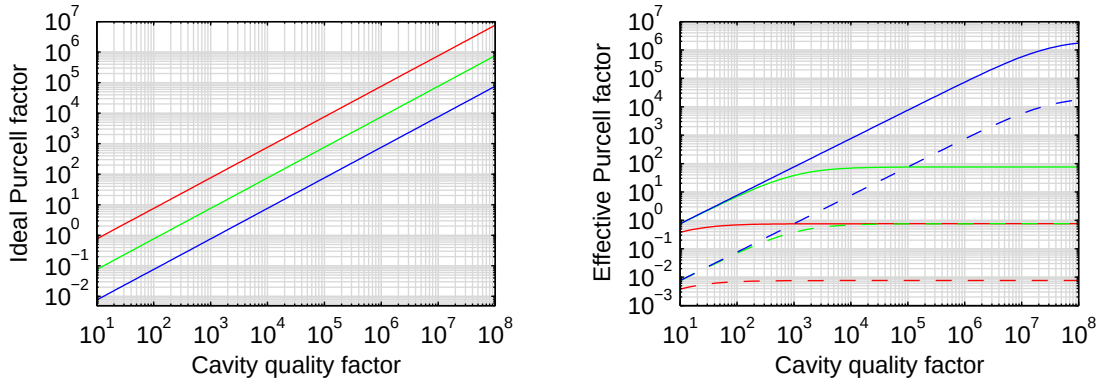

(a) (b)

Figure 4.1.: (a) Ideal Purcell factor C_0 as a function of the cavity quality factor Q_{cav} for different mode volumes V: $1\,\lambda^3$ (red), $10\,\lambda^3$ (green), $100\,\lambda^3$ (blue). (b) Effective quality factor C_{eff} as a function of the cavity quality factor Q_{cav} for different mode volumes V: $1\,\lambda^3$ (full lines), $100\,\lambda^3$ (dashed lines) and emitter quality factors Q_{em}: 10 (red), 1000 (green), $3 \cdot 10^7$ (blue), as an estimation for the NV and SiV center at ambient conditions and the ZPL of the NV center at cryogenic temperature, respectively.

Equation 4.25 had already been derived by E. M. Purcell in 1946 for nuclear magnetic moment transitions at radio frequencies coupled to resonant electrical circuits [11]. The modification of the transition rate of an emitter inside a cavity is now known as Purcell effect and the Purcell factor is a common figure to determine the strength of the resulting change. For example, for a Purcell factor of one, the spontaneous emission rate is doubled and 50% of the photons are emitted into the cavity mode, i.e. as many as would be emitted into the entire solid angle in free space. In order to achieve large Purcell factors, cavities with a large quality factor and a small mode volume are required within this description. Furthermore, the cavity should be tuned into resonance with the atomic transition and the dipole should be aligned with the cavity mode. In summary, enhanced emission inside a resonant cavity can be seen as a result of an increased density of modes the atom can decay into. In contrast, in an off-resonant cavity, the mode density is strongly decreased and the emission is inhibited. The spontaneous emission rate is thus not constant, but depends on its surrounding. Cavities provide a way to actively control the emission properties.

The spontaneous emission coupling factor or more simple the collection efficiency β is another useful parameter to characterize the influence of a cavity. It is equal to the fraction of the photons emitted into the cavity mode compared to the total number of emitted photons. For a lossless cavity, i.e. $Q_{\text{cav}} \to \infty$, the collection efficiency equals unity. In practice, however, a certain amount of photons will always be emitted into non-resonant modes, decreasing β. The collection efficiency is given by the decay rate

into the cavity divided by the total decay rate:

$$\beta = \frac{W_{\mathrm{cav}}}{W_{\mathrm{cav}} + W_{\mathrm{fs}}} = \frac{C}{C+1}, \tag{4.28}$$

where Eq. 4.23 has been applied. Consequently, β approaches unity for large Purcell factors.

The first experimental demonstration of modified spontaneous emission was however not achieved with a cavity, but by means of a one-sided reflecting surface. By placing an emitter in close proximity to a mirror, its directly emitted radiation pattern interferes with the reflected one, as described for example in [339, 349, 350, 351]. Constructive and destructive interference of the emission pattern results in the oscillation of the spontaneous emission rate around its free space value as a function of the distance between the emitter and the mirror. In the late 1970s, Drexhage *et al.* investigated the fluorescence decay of dye molecules placed in films at varied distances from a metal mirror and directly showed both inhibition and enhancement of spontaneous emission [230, 231, 352]. In very similar experiments but much later, Amos *et al.* determined the dependence of the spontaneous emission rate of Eu^{3+} ions upon both the distance from and the thickness of a silver film [353]. Chew showed that the transition rates of atoms inside and outside dielectric spherical particles can also be strongly modified [354, 65]. This effect should be kept in mind, when dealing with color centers embedded in small NDs.

The inhibition of microwave transitions of Rydberg atoms passing through a cavity was shown in 1985 by Hulet *et al.* [355], after a proposal by Kleppner [356]. In 1987 Jhe *et al.* could show the same effect for a transition in the near infrared [357]. Already in 1983, Goy *et al.* had reported enhanced spontaneous emission, i.e. a reduced lifetime, in a resonant cavity. They made use of a millimeter-wave transition of Rydberg atoms crossing a resonant superconducting high-Q cavity. In 1986, enhanced and inhibited spontaneous emission with cavities in the optical domain was first demonstrated by Heinzen *et al.* [358, 359].

2. Bad emitter regime

Having derived the standard case of a narrow-band emitter coupled to cavity with a relatively wide resonance, the opposite situation is straightforward. If the cavity resonance is much more narrow than the emitter's emission spectrum, the cavity density of states is modeled as a delta function centered at the frequency of the cavity resonance $\rho(\omega) = \delta(\omega - \omega_{\mathrm{c}})$. The density of states of the emitter is approximated by a Lorentzian function

$$\Lambda(\omega) = \frac{1}{\pi\delta\omega_0} \frac{\delta\omega_0^2}{(\omega - \omega_0)^2 + \delta\omega_0^2}, \tag{4.29}$$

with the emitter's angular transition frequency ω_0 and linewidth $\delta\omega_0$ (HWHM). Altogether, Fermi's Golden Rule (Eq. 4.14) yields

$$W_{\mathrm{cav}}(\omega_{\mathrm{c}}) = \frac{2}{\hbar\epsilon_0}\mu_{12}^2\xi^2\frac{Q_{\mathrm{em}}}{V}\frac{\delta\omega_0^2}{(\omega_{\mathrm{c}}-\omega_0)^2+\delta\omega_0^2}, \tag{4.30}$$

where the quality factor of the emitter

$$Q_{\mathrm{em}} = \frac{\omega_0}{2\delta\omega_0} \tag{4.31}$$

has been introduced. For broad-band emitters, like the NV center, Q_{em} can be estimated from the linewidth of the emission spectrum. The so-called effective Purcell factor is then given by

$$C_{\mathrm{eff}} = \frac{3}{4\pi^2}\left(\frac{\lambda}{n}\right)^3\frac{Q_{\mathrm{em}}}{V}\cdot\xi^2\frac{\delta\omega_0^2}{(\omega_c-\omega_0)^2+\delta\omega_0^2}. \tag{4.32}$$

In comparison with the original Purcell factor (Eq. 4.24), the quality factor of the emitter Q_{em} replaces the cavity quality factor Q and the Lorentzian function is centered at the emitter frequency ω_0. Consequently, the modification of the spontaneous emission rate now depends on both cavity and emitter properties, i.e. the cavity mode volume and the linewidth of the emitter. Note that it does however not depend on the quality factor of the cavity. Experimentally, this case is realized by coupling an NV center at room temperature to a high-Q cavity, for instance.

3. Emitter and cavity with comparable linewidth

At last, the general case is discussed, when the linewidth of the emitter is comparable to that of the cavity resonance. Both the emitter's and the cavity's density of states are now approximated by Lorentzian functions. Starting once more with Fermi's Golden Rule (Eq. 4.14), the integral over both Lorentzians and the matrix element has to be solved. As explained in more detail in [27], the modified spontaneous emission rate then results in

$$W_{\mathrm{cav}}(\omega_0,\omega_{\mathrm{c}}) = \frac{1}{\hbar\epsilon_0}\mu_{12}^2\xi^2\frac{1}{V}\frac{\omega_0\kappa+\omega_{\mathrm{c}}\delta\omega_0}{(\omega_0-\omega_{\mathrm{c}})^2+(\kappa+\delta\omega_0)^2}. \tag{4.33}$$

This relation includes the two previously derived emission rates Eqs. 4.22 and 4.30, as special cases for $\omega_{\mathrm{c}}=\omega_0$, $\delta\omega_0=0$ and $\omega_0=\omega_{\mathrm{c}}$, $\kappa=0$, respectively. For negligible detuning of the cavity resonance with respect to the emission frequency $\omega_{\mathrm{c}}=\omega_0$, Eq. 4.33 can be transformed into the simple representation

$$W_{\mathrm{cav}}(\omega_0=\omega_{\mathrm{c}}) = \frac{2}{\hbar\epsilon_0}\mu_{12}^2\xi^2\frac{Q_{\mathrm{eff}}}{V}. \tag{4.34}$$

Here, the effective quality factor [26]

$$Q_{\mathrm{eff}} = \left(\frac{1}{Q_{\mathrm{cav}}}+\frac{1}{Q_{\mathrm{em}}}\right)^{-1}, \tag{4.35}$$

combines the quality factor of the cavity (Q_{cav}) and the emitter (Q_{em}). Applying the original definition of the Purcell factor Eq. 4.23 with the free space spontaneous emission rate Eq. 4.12, the effective Purcell factor is obtained

$$C_{\mathrm{eff}} = \frac{3}{4\pi^2}\left(\frac{\lambda}{n}\right)^3 \frac{Q_{\mathrm{eff}}}{V}. \tag{4.36}$$

This is a maximal value for ideal dipole orientation, $\xi = 1$, and perfect overlap of the cavity resonance and the emission. The effective quality factor is plotted for different scenarios in Fig. 4.1(b). In contrast to the ideal Purcell factor (Fig. 4.1(a)), the effective Purcell factor saturates for large values of the cavity quality factor and its maximally achievable value critically depends on the quality factor of the emitter. In analogy to Eq. 4.28, the collection efficiency is given by

$$\beta = \frac{C_{\mathrm{eff}}}{C_{\mathrm{eff}} + 1}. \tag{4.37}$$

4.3.3. Rate Model

Previously, the emission spectrum was modeled as a single transition with a large effective linewidth, in order to simplify the analysis. However, in a more accurate picture, the emission spectrum may also comprise individual transitions, with different rates. For example, the fluorescence spectrum of the NV center features several PSB transition besides the ZPL, as schematically shown in Fig. 2.3(c). The dissipative James-Cummings theory including excessive dephasing provides a way to treat the coupled system [26, 360]. The dynamics can be described by the coherent coupling rate g_0, the cavity decay rate κ, the decay rate of the emitter γ_0, and the excessive dephasing rate γ^*. The dipole matrix element $\vec{\mu}$ is now distributed between the ZPL and individual sideband transitions that arise due to the coupling to phonons. The treatment of the phonon side band is simplified by applying a single phonon mode model where the k-th phonon sideband is approximated by a Lorentzian function with an effective width γ_k^* and a transition strength ζ_k. Thus, the ZPL ($k = 0$) and the sideband (1,2,...,n) can be treated in the same way. Inhomogeneous broadening in an emitter ensemble, like spectral diffusion, may be a source of additional dephasing. However, this mechanism is expected to have a minor effect compared to phonon induced broadening in the sideband. After all, the coupling rate of a single emitter and the individual, k-th-phonon-sideband transition is determined by

$$g_{0k} = \frac{\vec{\mu_k} \cdot \vec{E_k}}{\hbar} = \sqrt{\frac{3\pi c^3}{2\omega_k^2 V}\zeta_k \eta_{E,k} \gamma_0}\cos\theta, \tag{4.38}$$

with the dipole matrix element $\vec{\mu_k}$, the local electric field $\vec{E_k}$, the angular transition frequency ω_k, the cavity mode volume V, the angle between the cavity mirror plane and the dipole axis θ, the speed of light c, and the factor $\eta_{E,k} = (E_k/E_0)^2$, as a correction for the emitter not being placed directly in the field maximum E_0 of the standing-wave field antinode. The energy decay rate of the cavity at a particular transition frequency

is given by $\kappa_k = \pi c/2d\mathcal{F}_k$ (Eq. 4.5), where the finesse $\mathcal{F}_k$ is in general a function of the transition frequency.

Adapting the results from [26] to a series of transitions coupled to the cavity, the total emission rate of an emitter into a single cavity mode at the frequency ω_c is given by

$$R(\omega_\mathrm{c}) = \sum_k \frac{4g_{0k}^2\Gamma_k}{\Gamma_k^2 + 4\Delta_k^2}. \tag{4.39}$$

The contributing transitions are at frequencies ω_k, with coupling strengths g_{0k} and total incoherent rates $\Gamma_k = \kappa_k + \gamma_0 + \gamma_k^*$. The cavity detunings are $\Delta_k = \omega_c - \omega_k$. Finally, the effective Purcell factor can be expressed as

$$C_\mathrm{eff}(\omega_\mathrm{c}) = \frac{R(\omega_\mathrm{c})}{\gamma_0} \tag{4.40}$$

Hence, Purcell enhancement becomes independent of the decay rate of the cavity κ_k, if dephasing is dominant, i.e. $\gamma_k^* \gg \kappa_k$. This finding agrees with the previous results for the bad emitter regime where it was shown that the Purcell factor is independent of the cavity quality factor.

Furthermore, the quantity R can be considered as effective coupling rate between the atom and the cavity mode. As seen from the perspective of the atom, the cavity mode constitutes an additional loss channel, whose effective rate is given by

$$R_\mathrm{eff} = \frac{R2\kappa}{R + 2\kappa}, \tag{4.41}$$

with the cavity decay rate κ (here, HWHM). Note that this is the final outcoupling rate and for small cavity decay rates, the photons are not emitted fast enough out of the cavity and can be reabsorbed. The outcoupling efficiency can then be written as

$$\beta = \frac{R_\mathrm{eff}}{\gamma_0 + R_\mathrm{eff}}. \tag{4.42}$$

5. Fiber-based Fabry-Pérot microcavities

In this chapter, fiber-based Fabry-Pérot cavities (FFPCs) will be discussed. The common architecture of Fabry-Pérot cavities, as introduced in chapter 3, is defined by two opposing mirrors forming an optical resonator. While the cavity mirrors of typical Fabry-Pérot cavities are macroscopic, in the case of FFPCs, at least one of the often concave cavity mirrors is fabricated directly on the microscopic endfacet of an optical fiber, as illustrated in Fig. 5.1. The manufacturing process of such a cavity fiber involves microstructuring of its end face, e.g. by CO_2-laser machining or focused ion beam milling [361, 32], followed by the application of a mirror coating.

The main motivation for FFPCs is their potential for very small cavity mode volumes down to $V \sim \lambda^3$ and mode field radii w_0 on the micron scale. As discussed in chapter 4, the effective Purcell factor $C_{\text{eff}} \sim 1/V$ (Eq. 4.36) is independent of the cavity finesse for broad-band emitters like the NV center at room temperature, even though the finesse determines the cavity linewidth. A small cavity mode volume is therefore of prime importance, when aiming at large effective Purcell factors. Yet, the strong spatial confinement of the cavity mode of FFPCs can be accompanied with a very large finesse. Values of up to $1.9 \cdot 10^5$ have been reported [54]. This makes FFPCs likewise attractive for the coupling of narrrow-band emitters like atoms or NV centers at cryogenic temperatures, when the Purcell enhancement scales as $C_0 \sim Q_{\text{cav}}/V \sim \mathcal{F}/w_0^2$ (Eq. 4.26).

The feasibility of very small mode volumes and mode field radii is based on the micron-scale dimensions of the concave mirror structure on the end face of the fiber, along with the ability to bring the cavity mirrors extremely close together. The mode volume and the mode field radius of a plane-concave cavity are proportional to $V \sim d^2\sqrt{R/d-1}$

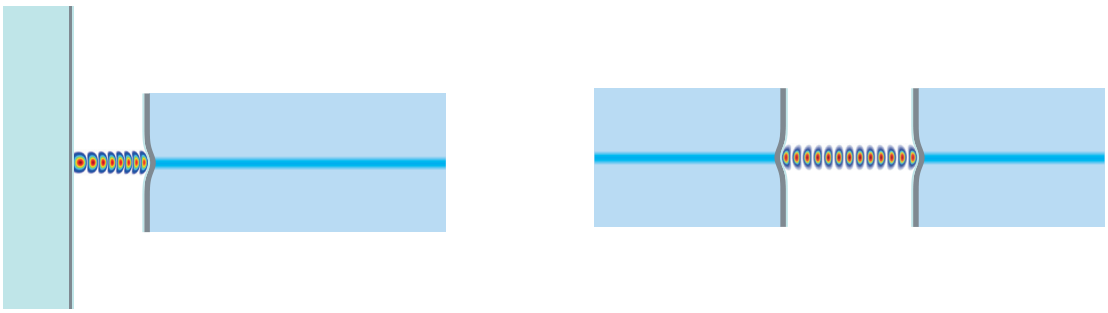

(a) (b)

Figure 5.1.: Schematic of fiber-based Fabry-Pérot cavities: (a) Geometry with one fiber and one planar mirror substrate and (b) two single-mode fibers.

(Eq. 3.43) and $w_0 \sim \sqrt{d\sqrt{R/d-1}}$ (Eq. 3.41), respectively, illuminating the dominant dependence on the cavity length d, compared to that on the mirror radius R. A mode volume of λ^3 is, for example, obtained for a cavity length of $d = \lambda/2$ and a radius of curvature of $R = 127.5\lambda \approx 80\,\mu\text{m}$, such that a single field antinode builds up between the mirrors. To ultimately decrease the cavity length to a few hundred nanometers, requires to shape the fiber tip profile on a ten nanometer scale, which can be achieved by advanced laser machining. The mirror coating that is deposited on the microstructure can be both dielectric, allowing for low-loss and customized transmission and reflection bands, and metallic, which is advantageous, when penetration into the mirror stack needs to be minimized.

In combination with technical advantages, among them the intrinsic fiber coupling, good accessibility of the open mode volume, free tunability, different opportunities for stabilization of the cavity length [362, 56], and operability in various environments (e.g. at cryogenic temperatures), FFPCs are beneficial for a broad range of experiments. For instance, coupling of various kinds of solid-state emitters to FFPCs has been demonstrated, including quantum dots [363, 364, 365], quantum wells [366], molecules [60, 367] and NV centers [78, 79, 32, 31, 73]. Direct application of solid-state emitters to a cavity mirror with a matched spacer layer enables the robust coupling to an antinode of the cavity's electric field, for instance, when color centers in NDs are used.

As an example for the outstanding performance of FFPC, coherent light-matter interaction in the optical domain has been achieved for atoms and cavities with dielectric low-loss mirror coatings. Neutral atoms can be coupled to FFPCs with extremely large and well-controllable coupling rates and Purcell factors larger than 10^2 [368]. This has lead to remarkable achievements like single atom preparation and high-fidelity readout [58], measurement of the internal state of a single atom without energy exchange, observation of the quantum Zeno effect [59], and creation of multiparticle entanglement with more than 40 atoms [369, 370].

In contrast to neutral atoms, the strong coupling regime has not been reached for charged particles, yet. Combining ion traps with small-mode-volume, high-finesse cavities is tricky, because dielectric mirrors tend to charge up and deteriorate the trapping potential. This can easily result in the loss of the trapped particles for small mirror distances. Therefore, the Purcell factors have remained about two orders of magnitude below that of neutral atoms [190]. Due to their small dimensions, FFPCs might overcome the problems encountered for macroscopic dielectric mirrors. First attempts with FFPCs have already yielded a dramatic decrease of the cavity mode volume and hold promise for the realization of the strong coupling regime with ions [188, 189, 190, 191].

Moreover, FFPCs have successfully been applied in the field of cavity optomechanics [371, 372, 373, 374, 375, 376] and provide a way for imaging applications with cavity-enhanced sensitivity [60, 61, 62, 63].

In the beginning of this chapter, microstructuring of the end face of optical fibers by CO_2-laser machining is presented. The first sections provide basic insight into the ablation process, the range of feasible mirror geometries, and the technical realization of

the micromachining procedure. An overview of produced structures follows. In order to realize FFPCs with ultimately short mirror spacing, the edges of the fibers have to be cropped. The technical implementation of mechanical and laser-induced fiber cropping is explained next. The mirror coating plays a crucial role for the cavity performance, especially with respect to the finesse and the minimally achievable mode volume, which is affected by the penetration of the electric field into the coating stack. The subsequent section thoroughly studies the features of dielectric and silver coatings, together with a characterization of the produced mirrors. Next, we discuss practical limitations particular to FFPCs, including the coupling efficiency from the cavity to the fiber mode, clipping loss due to the finite size of the micromirror, and mode mixing as a consequence of its finite, non-ideal shape. The chapter is finished with a short excursion to the history of fiber optic communication.

5.1. CO_2-laser machining

CO_2-laser light having a wavelength in the band from 9.4 to 10.6 µm is strongly absorbed by fused silica. At moderate laser intensities, it can thus be applied to superficially melt glass within a layer of a few microns. Advantageously, the surface roughness of this layer is strongly reduced by the surface tension of the molten glass. Laser polishing of optical surfaces is known to be an effective technique to achieve sub-nanometer surface roughness (σ_{rms}) [377, 378], which is an ideal basis for the construction of mirrors featuring very low scattering loss $S \approx (4\pi\sigma_{\mathrm{rms}}/\lambda)^2$ (Eq. 3.17), as low as a few parts per million (ppm).

However, when the laser penetrates deeper into the material and a larger glass volume is melted, minimization of the surface tension results in the creation of convex structures. This has for example been utilized for the manufacturing of microlenses [379, 380] or high-Q whispering gallery mode resonators like microspheres [381, 382] and microtoroids [383]. This effect is detrimental for surface polishing and in particular for the creation of concave structures. For increased laser intensities, ablation of glass by thermal evaporation takes place.

The machining of concave microstructures with focused CO_2-laser pulses succeeds in a parameter regime where evaporation is dominant, while melting is limited to a thin superficial layer [53]. The formation of a micron-scale depression with very low surface roughness is then feasible within a single machining step. Note that the material removal rate scales nonlinear with the temperature [53] and is thus extremely sensitive to the laser intensity, a parameter that must be well controlled to obtain reproducible structures. Laser ablation in the discussed domain has been fruitfully applied to micromachine the cleaved end face of optical fibers [51, 52, 54, 56, 57], as well as to planar fused silica substrates [384, 385, 386].

The transverse Gaussian intensity profile of the laser pulse transfers into a temperature profile in the substrate and via thermal evaporation into a likewise-shaped depth profile. Cuts through the resulting depression are fitted acceptably with a Gaussian curve of the form $z(\rho) = t \cdot \exp(-(2\rho/D)^2)$, with the profile depth t and the $1/e$-diameter D, as shown in Fig. 5.2. The central part of the profile is well approximated by a sphere. Its radius

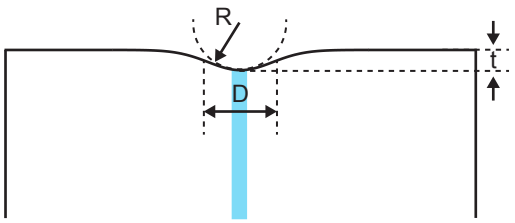

Figure 5.2.: Machined fiber end face with concave depression.

of curvature can be inferred from the simple relation applicable to Gaussian curves:

$$R \approx \frac{D^2}{8t} \tag{5.1}$$

The parameters R and D serve as good estimates for the radius of curvature and the usable diameter of the mirror, respectively.

Based on the relation between the geometrical parameters, the minimal mode radius w_0 (Eq. 3.41) and mode volume V (Eq. 3.43) can be evaluated that are in principle achievable with a plane-concave cavity with one laser-machined micromirror with structure depth t and diameter D, as shown in Fig. 5.3(a,b). The structure depth sets a lower bound to the minimal cavity length $d \geq t$. For a cavity resonant with light at a given wavelength λ, the minimal mode order consistent with the structure depth is given by $q = \lceil t/(\lambda/2) \rceil$, where $\lceil x \rceil = \min\{n \in \mathbb{Z} | n \geq x\}$ denotes the smallest following integer or the ceiling of x. For each of the steps that are visible in both plots, the cavity length is then given by $d = q \cdot \lambda/2$, for $\lambda = 700\,\mathrm{nm}$. The parameter regime is restricted by the stability condition, requiring that the cavity length is smaller than the radius of curvature of the concave mirror $d \leq R$. The deeper the structures for a given diameter and mode order, the smaller its radius of curvature and therefore also the mode radius and mode volume.

5.1.1. Setup

The laser-machining technique applied to optical fibers was originally developed in the group of Prof. Jakob Reichel, now at E.N.S. in Paris [387, 388, 51, 53]. The first microstructured fibers for this work were produced in Paris in 2011, using the setup of his group at the Laboratoire Kastler Brossel, which is extensively described in [388, 53]. Therefore, the following brief description will be restricted to a setup, which was later installed in our group in Munich, in order to produce structures with even smaller dimensions. It is similar to the advanced Paris setup, which is described in [57].

A sketch of the experimental layout is shown in Fig. 5.4(a). The RF-pumped CO_2-laser[1] provides a nominal power of 40 W at a wavelength of 10.6 µm. Choosing a laser with larger output power than actually necessary is motivated by its better power stability, an extremely critical parameter for the ablation process. The pumping and thus the output power is pulsed at 5 kHz corresponding to a pulse length of 50 µs. The average

[1] Synrad firestar v40

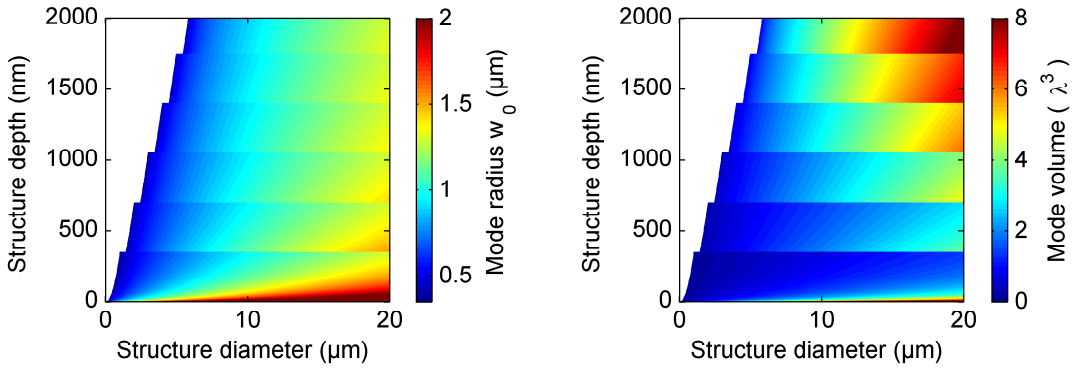

(a) (b)

Figure 5.3.: (a) Mode waist w_0 on the planar mirror and (b) mode volume V as a function of the structure diameter D and depth t for a plano-concave cavity resonant with light at $\lambda = 700\,\mathrm{nm}$.

power can be adjusted by the duty cycle. At a duty cycle of 40%, an output power of 25 W was measured for our laser. The power stability after half an hour warm-up time is a few percent. The beam passes through an acousto-optic modulator[2] (AOM) that is controlled by a voltage. By applying a radio frequency to the AOM, the first diffraction order is guided into the optical path towards the fiber, while it hits a beam dump, when the voltage is off. This allows for fast switching and thus, the formation of pulse trains with well-controllable power and duration. In this optical configuration, the laser is steadily running, which is beneficial concerning its power stability. A polarizer and a quarter-waveplate act as optical isolator reducing back-reflections into the laser. To enable smaller foci, the beam diameter is increased with a beam expander[3] before it gets focused onto the end face of the fiber with a zinc selenide (ZnSe) aspheric lens with a focal length of one inch or alternatively half an inch. The laser power for different AOM voltages at a duty cycle of 30% is given in Fig. 5.4(b), with the measurement being performed between the quarter-waveplate and the telescope. The laser pulse trains applied to the fiber typically have a power of some hundred mW and a duration of up to a few ten ms. The fibers to be machined are mounted on a three axes positioning stage[4] with a repetition accuracy of 100 nm and a travel range of 52x52x300 mm. Translation along the axis with the longest travel range allows to move the fibers directly into the focus of either a white light interferometer (WLI) based on a Mireau objective[5] and a blue LED[6] or a simple microscope. The fiber end face can therefore be inspected in between different machining steps without taking the fiber out of its holder and loosing

[2] Gooch and Housego
[3] Ronar-Smith 2x-8x
[4] PI miCos, PLS-85 and LS-180 step motors with linear scale LS-012
[5] Mireau objective Nikon CF IC Epi Pan DI, 20X, NA 0.4
[6] Central wavelength $\lambda = 463.25\,\mathrm{nm}$ and spectral width $\Delta\lambda = 19.99\,\mathrm{nm}$

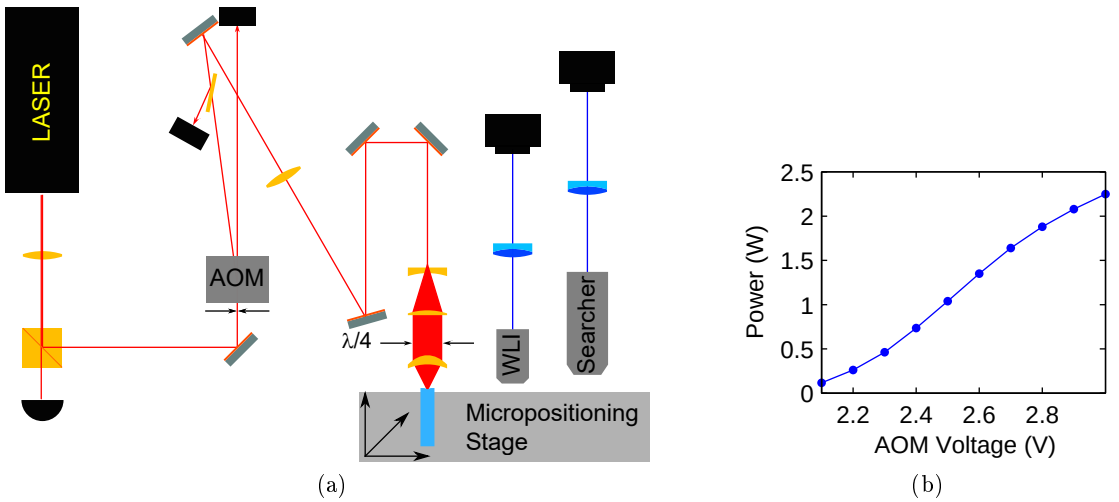

Figure 5.4.: (a) CO_2-laser setup used for microstructuring of optical fiber end faces. (b) Laser power at 30% duty cycle measured for different AOM control voltage between quarter-waveplate and telescope.

the positioning relative to the CO_2-laser focus. The microscope serves to first locate the fiber in its holder. Once its relative position has been set, the fiber is moved to the WLI where its end face is examined. Cracks or parasitic particles are straightforward to detect. The interferometric measurement yields sub-Å height resolution and a lateral resolution of around 400 nm. An excellent three dimensional (3D) reconstruction of the laser-machined structures can be obtained by phase-shifting interferometry, where a series of images with shifted interferograms is evaluated. For this purpose, the Mireau objective can be moved with a piezoelectric nanopositioner[7].

5.1.2. Fibers machined with the setup in Paris

In collaboration with C. Deutsch, S. Stapfner and D. Hunger about 180 fibers were laser-machined in Paris. Two types of SM fibers[8] and one type of gradient-index multi-mode (MM) fiber[9] were used. These fibers have a standard cladding diameter of 125 µm. Fibers with a metallic coating (e.g. copper, aluminum, gold) are expedient to prevent outgassing in vacuum environments, e.g. when a low-loss dielectric mirror coating by ion-beam sputtering is envisaged.

To prepare the unprocessed fibers for laser machining, the fiber coating is stripped over a length of some ten millimeters, first. The commonly-used copper coating is removed with an etching solution of iron(III) chloride, for instance. Next, the stripped fiber is cleaved and checked with a WLI. Fibers with an end facet exhibiting cracks or centrally positioned glass remains are discarded. The cleave quality is highly correlated to the used

[7] Npoint nPFocus Objective Stage
[8] Oxford Electronics SM800-125CB, Fiberguide Industries ASI^{TM} 633
[9] Oxford Electronics GI50-125CB

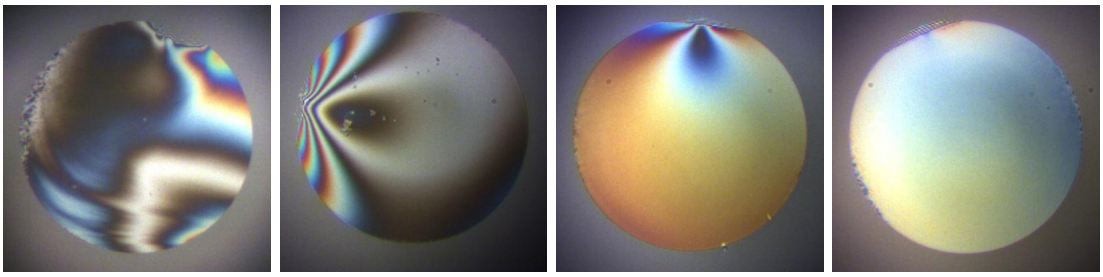

(a) (b) (c) (d)

Figure 5.5.: WLI images of fiber end faces before laser-machining. The quality of the fiber cleave is increasing from (a) to (d). The fiber diameter is 125 µm.

fiber cleaver. The best results regarding the planarity of the cleave have been obtained with a surprisingly simple model[10]. Different types of optical fibers have a noticeable but minor effect on the cleave. Any protrusion from the fiber's end face, including kinks or glass remains, limit the minimally achievable cavity length, pointing out the importance of a clean and plane fiber cleave. Figures 5.5(a-d) show examples for different cleave qualities: (a) Discard (b) The glass pieces are unproblematic for further machining, since they are far from the center. They can become hindering for short cavities, however. (c) The kink, here on the top, is characteristic for most cleaves. The imaging method cannot clarify whether it is a depression or protrusion. A protrusion potentially limits the minimally achievable cavity length. The planarity is very good. (d) Perfect cleave.

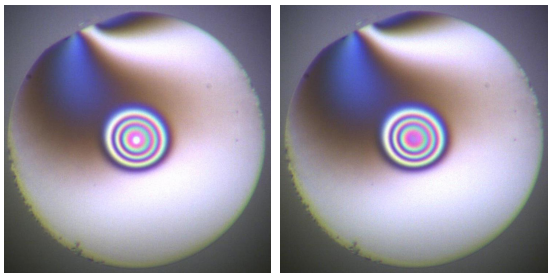

(a) (b)

Figure 5.6.: Laser-machined fiber (a) with and (b) without illuminated fiber core.

Finally, the end face of the fiber is laser machined and recorded once more with a WLI. Note that the WLI was not directly integrated into the machining setup, here, making a control more cumbersome. The earlier apparatus did not yet allow for 3D reconstruction, neither. The alignment of the structure relative to the fiber core is checked by shining light into the back of the fiber. The fiber core appears as a bright spot in the WLI image. As illustrated in Fig. 5.6(a,b) very good alignment is feasible. The center of the concave

[10]Corning Precision Diamond Cleaver FBC-006

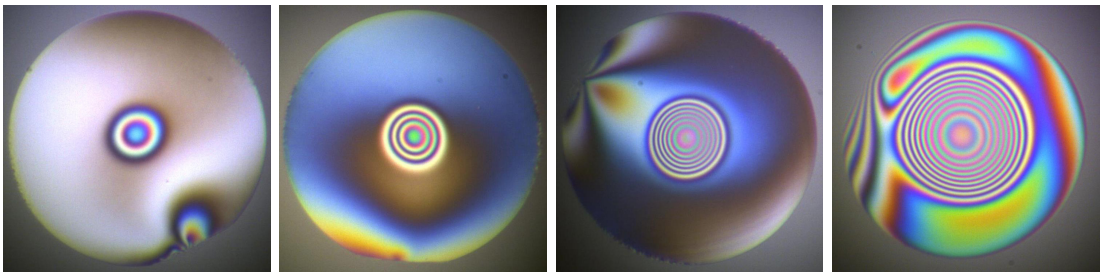

(a) $t = 0.53\,\mu m$, $D = 20\,\mu m$, $R = 95\,\mu m$, $P = 430\,mW$, $T = 16\,ms$, $w = 27\,\mu m$

(b) $t = 0.90\,\mu m$, $D = 22\,\mu m$, $R = 67\,\mu m$, $P = 490\,mW$, $T = 16\,ms$, $w = 27\,\mu m$

(c) $t = 1.86\,\mu m$, $D = 23\,\mu m$, $R = 36\,\mu m$, $P = 430\,mW$, $T = 16\,ms$, $w = 27\,\mu m$

(d) $t = 2.78\,\mu m$, $D = 56\,\mu m$, $R = 121\,\mu m$, $P = 620\,mW$, $T = 21\,ms$, $w = 50\,\mu m$

Figure 5.7.: Selection of WLI images showing different structure geometries produced with the Paris setup. The fiber diameter is 125 µm.

structure typically deviated less than a fiber core radius of 3.5 µm from the core.

The irradiation power of the laser P ranged from 0.48 to 0.65 W, the pulse length T from 16 to 23 ms and the beam width w was set to 27 or 50 µm by the choice of the focusing lens. Some of the fibers were irradiated with a short afterpulse of 8 ms expected to further smoothen the surface by melting a superficial layer before ablation sets in. The geometric parameters of the produced structures are depths t between 0.5 and 3 µm, diameters D from 20 to 60 µm, and radii of curvature R from 35 to 200 µm. A selection of machined structures is shown in Fig. 5.7. Please note the remarkable difference between the machining of SM and MM fibers. For identical laser setting, the structure on a MM fiber gets more than three times deeper than that on a SM fiber (compare Fig. 5.7(a,c)). This can be attributed to different types of glass used for the fiber core and cladding. Presumably, the core material ablates faster. Due to the much larger core diameter of the MM fiber ($\varnothing = 50\,\mu m$), the structure size increases. In general, the laser power has to be fine-tuned for every type of substrate.

Another detail worth mentioning is the apparent ellipticity of the structures. It is caused by the polarization of the CO_2 laser itself, as well as by aberrations introduced by the optical elements. It can be reduced by careful alignment. According to Uphoff *et al.* [54], the elliptic geometry of laser-machined Fabry-Pérot cavities is the main reason for the frequency splitting of the polarization eigenmodes of the fundamental transverse mode.

After laser machining, the surface roughness of the microstructures is controlled with an atomic force microscope[11] (AFM) using a special fiber holder. Square areas with an edge length of 0.5 µm were scanned. The standard deviation from a line-wise polynomial fit of second order yields the root mead square (rms) surface roughness. The average over

[11] Digital Instruments Dimension 3100

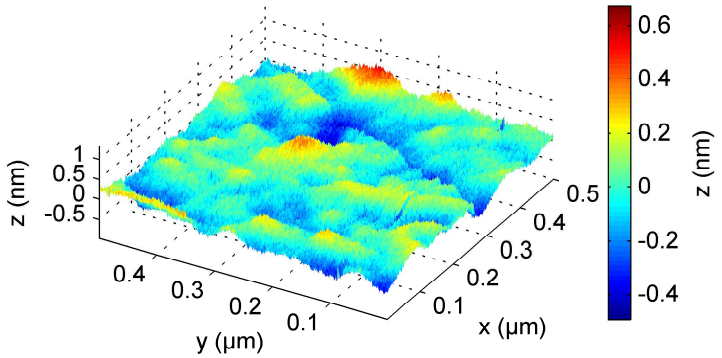

Figure 5.8.: AFM measurement of a laser-machined fiber surface after subtraction of linewise polynomial fits of second order.

ten measurements of a fiber machined with a smoothing afterpulse resulted in an rms surface roughness of $\sigma = (0.14 \pm 0.01)\,\mathrm{nm}$, close to the resolution limit of the AFM. Under the assumption that the mirror coating does not introduce additional surface roughness, the corresponding scattering loss amounts to $S = 5 \cdot 10^{-6}$ at $\lambda = 780\,\mathrm{nm}$, in short 5 ppm (see Equ. 3.17). Figure 5.8 displays the surface roughness after subtraction of the polynomial fit curves.

5.1.3. Fibers machined with the setup in Munich

As a result of the optimized focusing optics[12] and the ability for fast inspection of the produced features, particularly small and shallow structures become feasible with the advanced setup: Profile diameters D down to about 4 µm, radii of curvature R as small as 5 µm and depths t from some ten nanometers to 3 µm were created, which is substantially smaller than the structures produced in Paris (see Table 5.1). Note, that these values do not represent an ultimate limit; in general the setup enables smaller structures.

Setup	D (µm)	R (µm)	t (µm)
Paris	20-60	35-200	0.5-3
Munich	$\gtrsim 4$	$\gtrsim 5$	0.01-3

Table 5.1.: Overview of produced structures

Before laser machining takes place, the optical fibers are prepared as described above (see Section 5.1.2). Pulse sequences with large variability are feasible using the AOM. A typical pulse train applied to create the central depression involves three consecutive pulses at a laser duty cycle of 60% and an AOM voltage of 2.7 V. This pulse train is used up to five times, until the desired structure depth is reached, which is checked with

[12] A beam expander (Ronar-Smith 2x-8x) is used before focusing with an aspheric lens having a focal length of one inch

the WLI integrated into the setup. The fiber core is directly made visible in the WLI image, by illuminating the fiber from the other end with an LED. This enables the in situ control of the positioning of the structure, yielding an accuracy of typically less than one micron. The central feature is in most cases created after the edges of the end facet have been cropped by laser machining to allow for shorter mirror distances. The cropping procedure is subsequently explained in more detail (see Section 5.2).

An example of a readily machined and silver coated end face of a fiber[13] is shown in Fig. 5.9. The 3D reconstruction obtained with the WLI, provides an excellent impression of the surface topography. A Gaussian fit curve is in very good agreement with a cut through the profile and results in $D = 7\,\mu\text{m}$, $R = 90\,\mu\text{m}$, and a depth t below 100 nm. The radius of curvature can also be obtained from a parabolic fit to the central part of the depression. Using this fiber, the realization of a plano-concave cavity with a $\lambda/2$ mirror separation, i.e. a cavity with a single field antinode, is indeed possible, as presented in Section 7.2. The theoretically expected clipping loss and coupling efficiency for this geometry are displayed in Fig. 5.25.

5.2. Fiber cropping

Mechanical contact of the mirrors of FFPCs limits the minimally achievable mirror distance and thus the cavity length. The main reason preventing smaller distances is the imperfect planarity of the fiber cleave, which is typically around one micron for standard optical fibers having a cladding diameter of 125 µm. Moreover, the cleave can result in an end facet, which is tilted with respect to the optical axis of the fiber and the mirror structure created later on. Kinks or glass remains on the end facet originating from the cleaving procedure represent further potential protrusions, which can however be avoided in most cases.

The difficulty of reaching sub-micron mirror distances is easily illustrated, by considering the involved geometrical dimensions: Imagine a plane-concave cavity that is resonant with the fundamental oscillation of an electromagnetic wave, i.e. the cavity length equals $\lambda/2$, with $\lambda = 700\,\text{nm}$, here. Assuming that the emitter is placed in the field maximum and that the concave structure is as shallow as $t = 100\,\text{nm}$, the gap between the mirrors amounts to roughly 75 nm, three order of magnitudes smaller than the cladding diameter. Due to the limited planarity or a tilt of the cleave, the fiber establishes contact with the plane mirror before this cavity length is reached in practice. It hence seems natural to crop the edges of the fiber, to remove all protrusions from its end facet and allow for more alignment freedom, as illustrated in Fig. 5.10. Using optical fibers with a reduced cladding diameter from the beginning (if available for the desired type) cannot directly solve the issue, since laser machining of their end facet is expected to easily result in the formation of convex structures.

Two different cropping techniques have been established throughout the scope of this thesis: The fiber edges can either be removed by mechanical polishing or by a more controlled method based on laser ablation.

[13] Optical fiber type: Thorlabs S405-XP

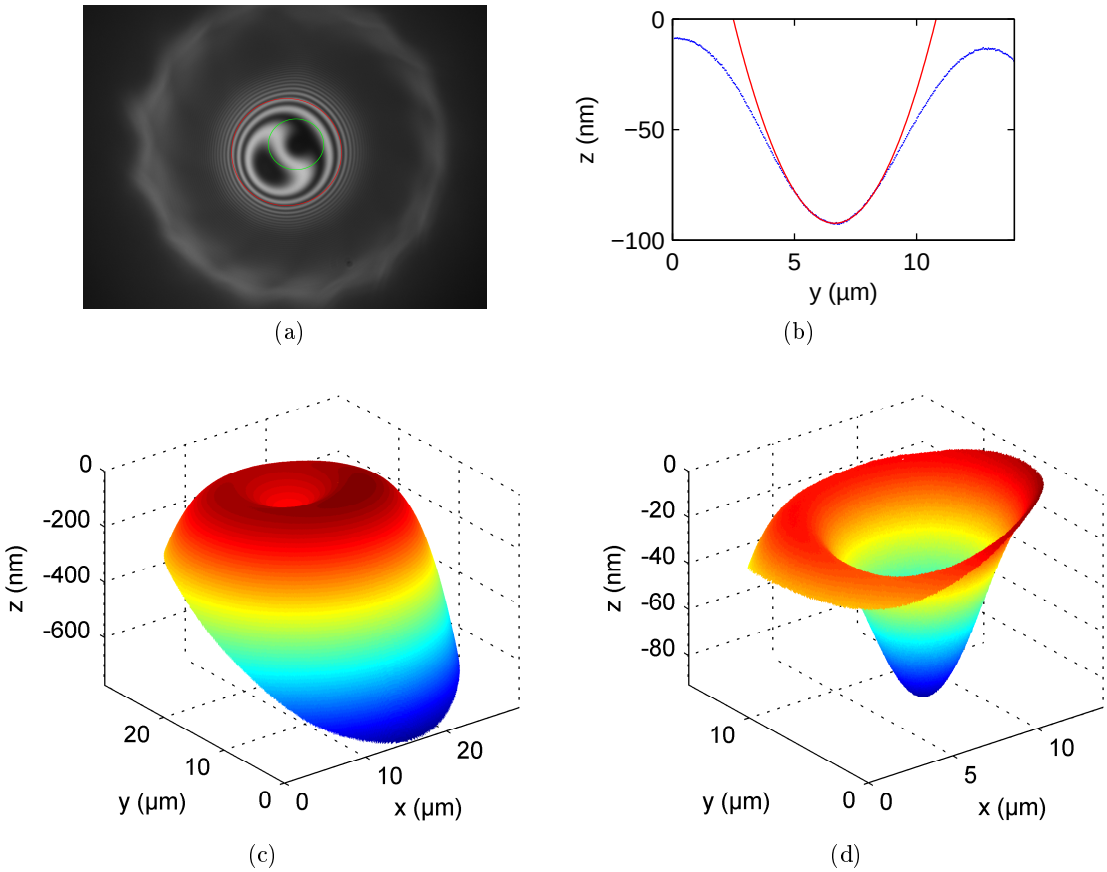

Figure 5.9.: (a) WLI image of a readily machined and silver coated fiber end face with laser-cropped edges. The outer circular transition from bright to dark marks the fiber edge ($\varnothing = 125\,\mu m$) located behind the focus. Figure 5.12(c) provides the corresponding side view. (c,d) Topography obtained from the areas marked in (a) by red and green circles, respectively. The edge length of the protrusion is below 20 µm. (b) Cut through the profile shown in (d) (blue dots) together with a parabolic fit (red line).

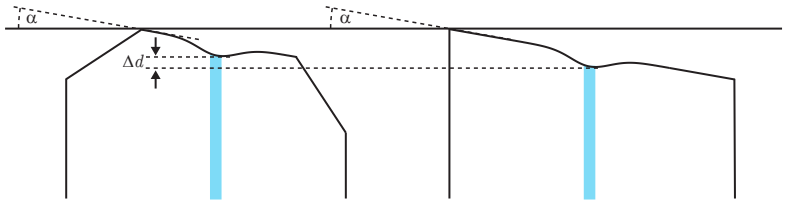

Figure 5.10.: For the same angular tilt α the cropped fiber (left) gets closer to the plane mirror than the unmachined fiber (right). In other words, the gained alignment freedom of the cropped fiber allows shorter cavities.

5.2.1. Mechanical fiber cropping

The edges of the fiber end facet can be removed with minor experimental overhead by mechanical polishing. This method is usually applied before the central feature is produced by laser machining, since the delicate procedure involves a non-vanishing risk to break the fiber. However, it is noteworthy that even already machined and dielectrically-coated fibers survived the treatment without noticeable damage to the micromirror, which was proven by an unchanged finesse.

Starting with an unmachined fiber, the first steps involve stripping and cleaving. Next, some millimeters of the fiber are coated with polymethylmethacrylat (PMMA) to protect its end face from glass and dirt particles created throughout polishing. Subsequently, the fiber is fixed in a custom holder, such that its tip is upside down and touches a piece of polishing sheet[14] under an adjustable angle. The mounting of the fiber allows a backlash in the direction of the fiber optical axis of a few millimeters, in order to prevent breakage of the glass fiber by excessive stress. The polishing sheet underneath the fiber tip is slowly pulled from one side to the other for a few times, removing a first part of the outer edge. This step is repeated three more times after the mount has been rotated by ninety degrees around the fiber axis. For the rotation of the mount, the fiber is withdrawn from the sheet. In the end, the PMMA layer is dissolved in acetone in an ultrasonic bath. Directly after taking the fiber out of the acetone, it is rinsed with isopropanol and deionized water, leaving behind a clear fiber end face without glass particles. The resulting and intermediate end face geometry are examined with the WLI. As shown in Fig. 5.11(b), the remaining plateau is immaculate and almost quadratic, with an edge length of some ten micrometers. Side views can be obtained with an optical microscope, as depicted in Fig. 5.11(a).

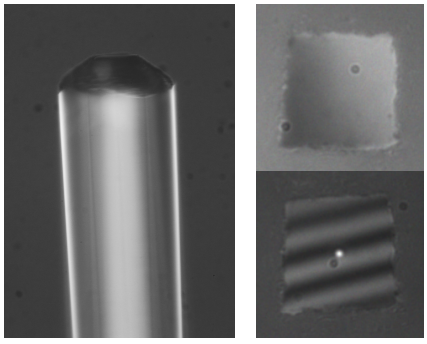

(a) (b)

Figure 5.11.: Fiber cropped by polishing. (a) Microscopic side view. The cladding diameter is 125 µm. The remaining protrusion has an edge length of $\approx 40\,\mu m$ (b) Corresponding WLI images of the end face. The well-centered fiber core is illuminated in the lower figure. The black spots are imaging artifacts.

[14]Thorlabs LFG1P Aluminum Oxide or LF1D Diamond Lapping (Polishing) Sheet 1 µm Grit

5.2.2. Fiber cropping by laser ablation

CO_2-laser ablation can be utilized to crop the edges of the end facet of an optical fiber, in order to shape the fiber tip roughly like a flat top cone. To this end, multiple laser pulse sequences are applied to its edge in circular patterns, to crop the outer part of the end facet. This results in a protruding plateau with diameters of typically below 20 µm. Microscopic side views of such fibers are shown in Fig. 5.12. Note that laser cropping may leave behind some glass debris on the now protruding fiber plateau. By applying a few weak laser pulses, the plateau can be polished by melting a thin surface layer. Laser cropping can be performed with the unaltered laser setup described in Section 5.1.1 and can thus be applied directly before or after the central structure has been created.

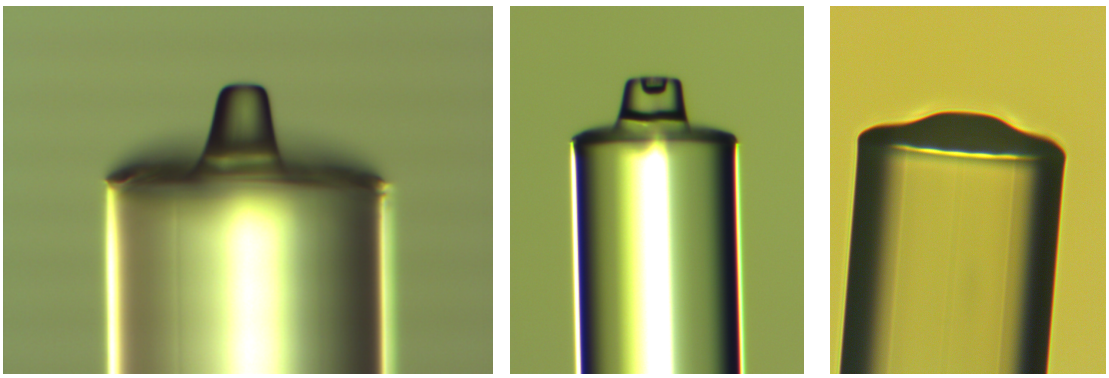

(a) (b) (c)

Figure 5.12.: Side view of different laser-cropped fibers taken with a microscope (magnifications 10-20x). The cladding diameter of all fibers is 125 µm. In (b) the deep central structure machined into the mesa structure is visible.

To obtain a planar protrusion with steep edges, a cropping procedure based on a multitude of laser pulses is used. Inspection of the end face after each step with the WLI is essential to prepare a viable pulse protocol. A typical pulse sequence is specified in Table 5.2, together with a schematic illustration of the positioning of the applied pulses. For each step, a number of equidistant sites are defined, which lie on a circle with a fixed radius centered around the fiber core. A number of consecutive pulses is applied to each of these sites. The more pulses, the more material is removed. A smooth transition from the edges to the center of the fiber is achieved by reducing the number of sites and pulses with decreasing radius. For this example, the duty cycle of the laser was kept constant at 60% for all pulses, the AOM voltage was at 3.4 V. An aspheric lens with a focal length of half an inch was used for focusing.

The circular cropping sequence can result in a profile covered with a thin layer of debris and a slightly protruding rim. By applying a melting sequence, the debris and the bulgy edges are smoothened. For this purpose, the end face of the fiber is moved 500 µm out of focus to achieve a more homogeneous illumination. Using very low laser

Step	Radius (µm)	Sites	Pulses
1 (red)	62	31	4
2 (green)	52	26	4
3 (blue)	40	20	3
4 (yellow)	32	16	2
5 (magenta)	26	13	1

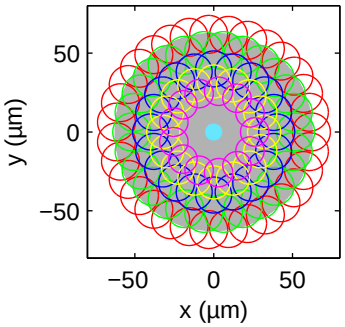

Table 5.2.: Typical pulse sequence for laser cropping. The figure on the right illustrates how this sequence acts on the end face of the optical fiber.

power but increasing the number of pulses to 6000 assures that only a thin surface layer is melted and prevents the collapse into a convex shape. The melting sequence is applied several times until the protruding plateau has reached a planarity better than about 100 nm. Compared to the cropping sequence, the duty cycle is increased to 98.75%, the AOM voltage is reduced to 2.3 V. The fiber is now ready to create the central feature, as already described in Section 5.1. The profile of a fully machined and coated fiber is shown in Fig. 5.9(c,d).

5.3. Mirror coating

After laser machining, a mirror coating is applied to the end face of the optical fibers. Different coating materials and techniques are available. Throughout the scope of this thesis, dielectric, as well as, silver coatings were used. Dielectric coatings are composed of multiple, thin, dielectric layers with alternating high and low refractive index. The simulation of multilayer coatings based on the matrix method has already been discussed in Section 3.2. The wavelength dependent reflectivity of such a coating system can be designed with a high degree of freedom by the accurate choice of the coating materials, the layer thicknesses and the number of layers. For example, cavity mirrors are feasible that exhibit a very large reflectivity at the wavelength of the fluorescence from an emitter, while they transmit the excitation light at the same time. Very large reflectivities exceeding 0.99999 can be realized, using low-loss materials [335]. Dielectric mirrors are the first choice, when a high cavity finesse takes priority, for example for the coupling of narrow-band emitters like atoms or when photons with a high spectral purity are desired.

However, electric fields impinging on dielectric mirrors penetrate some hundred nanometers to a few micrometers into the layer stack, which sets a lower bound to the minimally achievable mode volume. When aiming at ultra-low mode volume cavities, metallic mirrors represent an attractive alternative, since the penetration depth amounts to only a few ten nanometers, here. Yet, the comparatively large absorption loss of metals limits the reflectivity of metal mirrors. Silver, for instance, exhibits an absorption of roughly

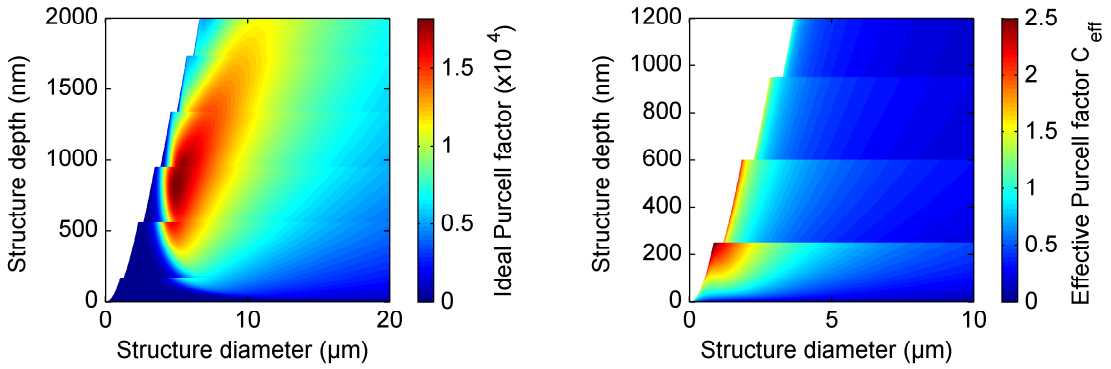

(a) (b)

Figure 5.13.: (a) Ideal Purcell factor C_0 as a function of the structure diameter D and depth t for $\lambda = 780\,\mathrm{nm}$, $d_{\mathrm{pen}} = 610\,\mathrm{nm}$, $\mathcal{F} = 150\,000$, including clipping loss and a reduction of the finesse for structures with steep sidewalls. (b) Effective Purcell factor C_{eff} for $\lambda = 700\,\mathrm{nm}$, $d_{\mathrm{pen}} = 100\,\mathrm{nm}$, $\mathcal{F} = 40$, $Q_{\mathrm{em}} = 8$, including clipping loss.

3% and a reflectivity of more than 95% for wavelengths larger than 500 nm. The finesse of a Fabry-Pérot cavity with silver mirrors can therefore not exceed values of around 100. This is however more than sufficient to achieve Purcell enhancement with NV centers coupled to ultra-small mode volume cavities at ambient conditions. As discussed in Section 4.3, finesse values around 20 are for instance optimal, when aiming at maximal photon count rates.

In short, cavities with metal mirrors allow for extremely small mode volumes at moderate finesse, while dielectric mirrors enable a superior finesse at slightly larger mode volumes. Two scenarios for the Purcell enhancement achievable with plano-concave cavities are given in Fig. 5.13(a,b). First, the ideal Purcell factor is evaluated for a high-finesse cavity with dielectric mirrors, which is the relevant figure of merit for the coupling of narrow-bandwidth emitters. In contrast, the effective Purcell factor prevails for the second scenario, where a broadband emitter, like the NV center, is coupled to an ultra-small mode volume cavity with silver mirrors.

The calculation of the ideal Purcell factor for the cavity with dielectric mirrors is based on a nominal finesse of 150 000 at $\lambda = 780\,\mathrm{nm}$ and a total penetration depth of 610 nm, resulting in peak values on the order of $1 \cdot 10^4$. The optimum is reached for structures with a diameter $\approx 5\,\mu\mathrm{m}$ and a depth $\approx 800\,\mathrm{nm}$, for the fourth mode order. The latter is now given by $q = \lceil (t + d_{\mathrm{pen}})/(\lambda/2) \rceil$, with the penetration depth d_{pen}. The ideal Purcell factor is proportional to the ratio $\mathcal{F}/w_0^2$. While diffraction limits the minimally achievable mode radius w_0, the nominal cavity finesse $\mathcal{F}$ is reduced by clipping loss (see Section 5.4) for very small structures. Furthermore, for an increasing ratio of structure depth to diameter, the sidewalls of the mirror get more and more inclined. Since the reflectivity of the coating stack is optimized for normal angle of incidence, the cavity

finesse deteriorates for mirrors with steep surfaces.

The effective Purcell factor, which scales with Q_{eff}/V, is illustrated for an emitter with a quality factor $Q_{\text{em}} = 8$ at $\lambda = 700\,\text{nm}$. The total penetration depth into the glass capped silver mirrors is set to 100 nm, the maximal cavity finesse to $\mathcal{F} = 40$. Maximal effective Purcell factors are obtained for small mode volumes, i.e. for small and shallow structures, and mode order $q = 1$. However, clipping loss sets a lower limit to the beneficial effect of a small mode volume.

In the following, a more detailed characterization of dielectric and silver coatings is given.

5.3.1. Dielectric coating

Dielectric mirrors are distributed Bragg reflectors consisting of several thin layers of materials with alternating high and low refractive indices. When a light wave is incident on the layer system, each layer boundary gives rise to a partial reflection. The transmission and reflection behavior is a result of multi-beam interference. Constructive interference is obtained by adjusting the layer thicknesses appropriately, e.g. when the optical thickness of the layers is equal to one fourth of the wavelength of the incident light. The overall reflectivity increases with the amount of layer pairs. This enables the design of highly reflective mirrors with controllable spectral response. The larger the difference between the refractive indices of the involved materials, the larger the mirror reflectivity and the larger the bandwidth for a given number of layers. The spectral window, for which the mirror is reflective, is called stopband. By finishing the mirror stack with a low-refractive index layer with an optical thickness equal to $\lambda/4$, the antinode of an impinging electric field can be positioned slightly above the mirror. In this way, the cavity coupling to an emitter that is directly placed on such a mirror can be optimized.

Among the various deposition methods for dielectric mirror coatings, ion beam sputtering (IBS) is arguably the most advanced and yields the lowest absorption loss. Mirror coatings produced by IBS are commercially available from several companies[15]. By way of example, a mirror coating produced by Advanced Thin Films (ATF) on fibers machined in Paris is discussed more thoroughly.

Mirror transmission

For the coating produced by ATF, a mirror transmission of $T = 12\,\text{ppm}$ at $\lambda = 780\,\text{nm}$ was targeted, which constitutes a compromise between a large cavity finesse and a reasonable amount of light leaving the cavity. This requirement is met by choosing the transmission about equal to the sum of scattering and absorption loss, such that around every second photon exits the resonator via the cavity mode before being lost. Assuming that the coating does not introduce additional surface roughness, the scattering loss of

[15] Advanced Thin Films, Boulder, CO 80301, USA
Laseroptik GmbH, 30826 Garbsen, Germany
Laser Zentrum Hannover e.V., 30419 Hannover, Germany
Layertec optische Beschichtungen GmbH, 99441 Mellingen, Germany

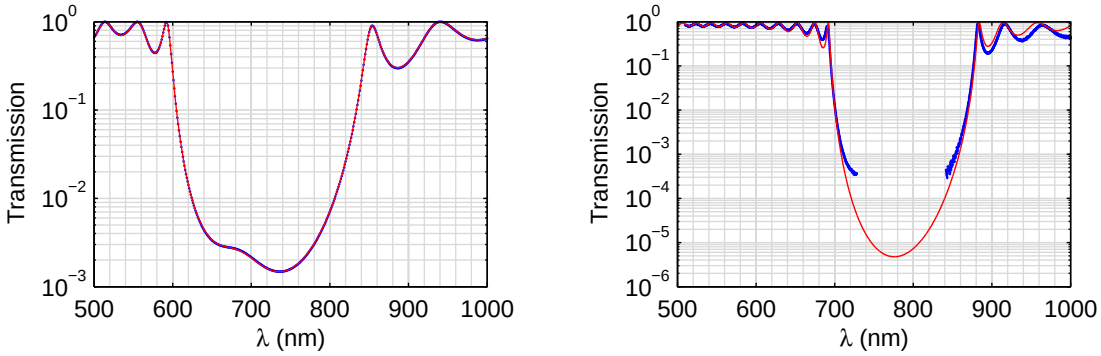

(a) (b)

Figure 5.14.: Comparison of measured (blue dots) and simulated (red line) coating transmission. (a) Coating with a target transmission of 1500 ppm at 740 nm (Laseroptik Garbsen). Simulation based on complete knowledge of the layer system. Data provided by manufacturer. (b) Coating with a target transmission of 12 ppm at 780 nm (ATF). Measurements were performed with a grating spectrometer able to resolve transmission values down to roughly $1 \cdot 10^{-3}$. Simulation based on a $\lambda/4$-layer stack approximation.

the fibers machined in Paris amounts to approximately $S = 5$ ppm (see Section 5.1.2). According to the manufacturer, absorption loss is on the order of $A = 6$ ppm. In total, the loss of a single mirror adds up to 23 ppm, corresponding to a cavity finesse of roughly 140 000 (see Eq. 3.20).

The target transmission is achieved with a mirror coating consisting of about 30 alternating layers of silicon dioxide (SiO_2) and tantalum pentoxide (Ta_2O_5) having refractive indices of $n_L = 1.46$ and $n_H = 2.1$, respectively. The coating stack is finished with a high-refractive-index layer. The transmission spectrum of the mirror is measured and provided by the manufacturer. It can also be simulated with the help of the matrix method (Section 3.2). Knowledge of the exact thicknesses and refractive indices of all coating layers enables an accurate prediction of the transmission spectrum, as shown for a different coating in Fig. 5.14(a). However, details about the layer system are in general not disclosed by the companies. In this case, the coating stack is approximated by choosing the layer thicknesses such that the optical path length matches a quarter of the wavelength to be reflected. Adjusting the amount of layer pairs leads to qualitative agreement to measured transmission curves, as shown for the ATF coating in Fig. 5.14(b). For this example, the simulated transmission has been fitted to the wings of the stop band, rather than precisely matching the target transmission of 12 ppm, illustrating the limits of this approximation. Once the layer stack of one mirror is modeled, it can be easily combined with that of a second mirror, to yield the transmission of a complete cavity. The specifications of the dielectric mirror coatings applied throughout this work are listed in the following.

Mirror specifications

Advanced Thin Films (ATF)

- Designed transmission $T = 12\,\text{ppm}$ at 780 nm, measured transmission $T = 7.3\,\text{ppm}$ at 780 nm
- applied in [362]

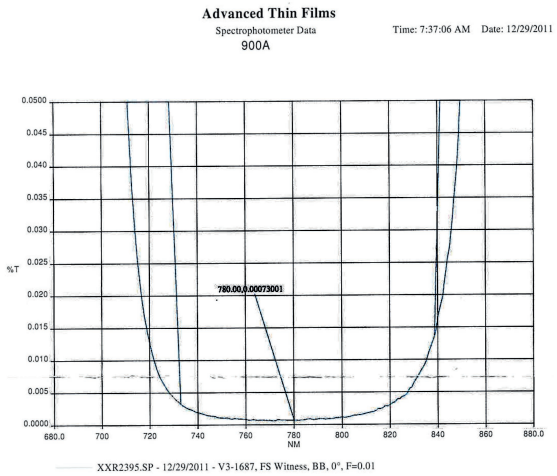

Figure 5.15.: ATF coating: Transmission spectrum measured by the manufacturer yielding $T = 7.3\,\text{ppm}$ at 780 nm

Laser Zentrum Hannover (LZH)

- Designed for $T = 34\,\text{ppm}$ at 780 nm
- 14 layers of SiO_2 with $n_{SiO_2} = 1.455$, 15 layers of TaO5 with $n_{TaO_5} = 2.105$
- Measured scattering loss at 633 nm, AOI 0°: 70-80 ppm
- Measured absorption loss at 1064 nm, AOI 0°: 100-120 ppm
- detailed description in [51]

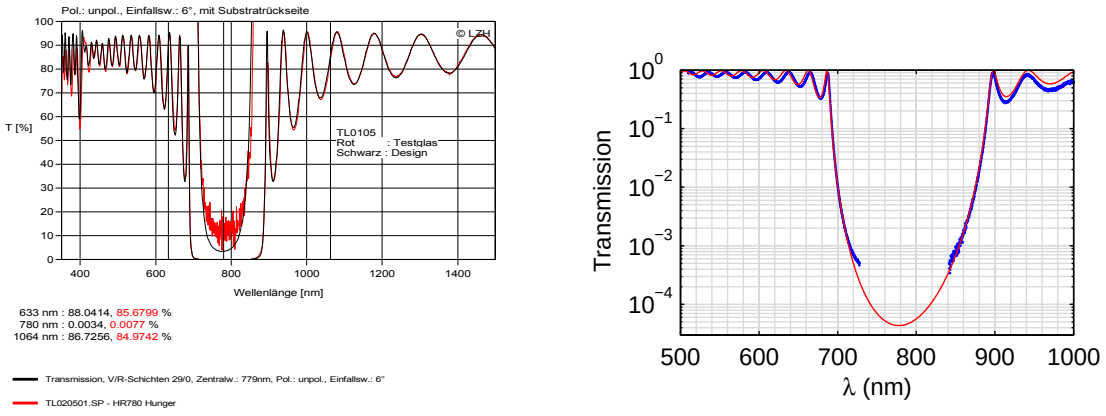

(a) (b)

Figure 5.16.: LZH coating: (a) Manufacturer specifications providing the measured (red) and theoretically expected (black) transmission spectrum. (b) Measured (blue dots) and simulated (red line) mirror transmission.

Layertec

- Designed for $T = 60\,\text{ppm}$ at 780 nm
- Anti-reflection coating for 532 nm ($R(0°, 532\,\text{nm}) < 10\%$)
- SiO_2 spacer layer to move emitter into field maximum
- Back side with anti-reflection coating AR(0°,650-780 nm)<0.4% + AR(0°,532 nm)<1%

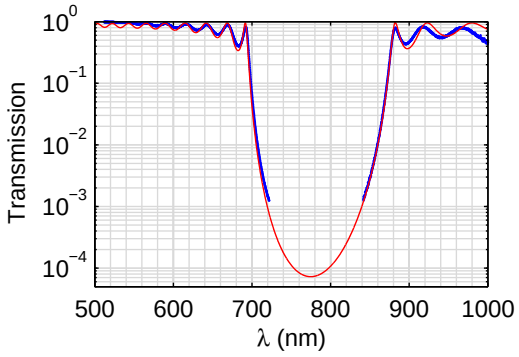

Figure 5.17.: Layertec coating: Measured (blue dots) and simulated (red line) mirror transmission.

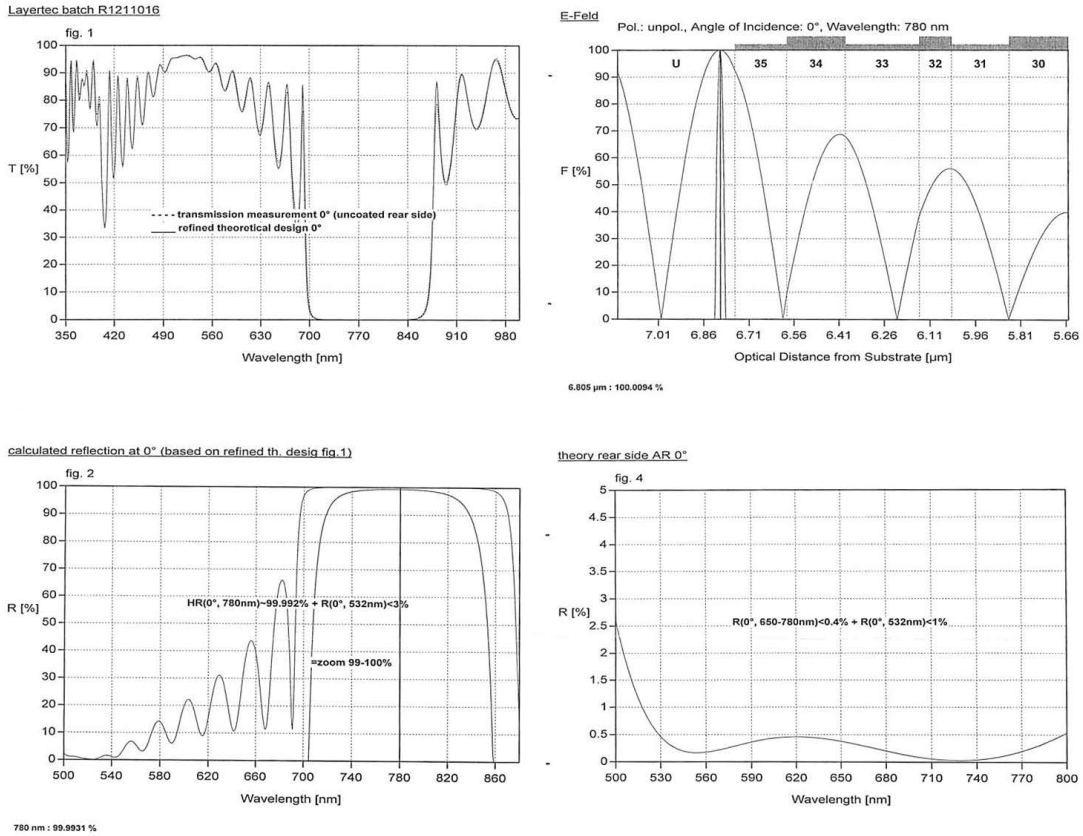

Figure 5.18.: Layertec coating manufacturer specifications.

Cavity finesse

The cavity finesse is directly connected to the total loss introduced by the contributing mirrors. Different experimental methods for its determination exist. The approach applied here, is based on the individual measurement of the cavity linewidth $\delta\nu$ and the free spectral range ν_F, whose ratio yields the finesse (see Eq. 3.13). The corresponding setup is sketched in Fig. 5.19(a). For this example, the FFPC consists of a SM and a MM fiber. For the cavity alignment, the two fibers are mounted on a piezo-actuated, linear three-axis translation stage and a manual pitch and yaw stage, respectively.

The cavity linewidth is determined with a narrow-band diode laser[16] operating at 780 nm. A fiber-coupled electro-optic modulator[17] (EOM) is used to imprint sidebands at a preset microwave frequency onto the laser by phase modulation. The modulated light is directly coupled into the back side of the SM cavity fiber. The light, which is transmitted through the cavity, is coupled out through the MM fiber and detected by a photo diode. The signal is recorded, while the cavity length is swept over the cavity resonance for the central laser frequency and its two sidebands, here at ± 4 GHz. The sidebands serve as a frequency ruler for the precise determination of the resonance linewidth.

For the measurement of the free spectral range, a superluminescent diode[18] (SLED) replaces the diode laser. The light of the SLED has a spectral width of roughly 60 nm centered around 760 nm and is coupled into the SM fiber. The phase modulation of the laser light, as well as the length modulation of the cavity are meanwhile switched off. The transmitted light is recorded with a grating spectrometer. The free spectral range is defined by the spectral distance of two neighboring resonances in the cavity-transmitted SLED spectrum in the frequency domain. Furthermore, the spectral position of the two resonances yields the cavity length (see Eq. 3.4).

Combining the two measurements, the finesse can be determined. An example for the finesse measured for different cavity lengths is shown in Fig 5.19(b), for cavity mirrors with the previously discussed ATF coating. A maximal finesse of $140\,000 \pm 10\,000$ is reached for a cavity length of 6.9 µm, in very good agreement with the expected value inferred from the total loss. For larger mirror spacing, the finesse deteriorates. While it is still around 90 000 for a cavity length of 55 µm, there is a sharp drop towards the stability limit of the cavity.

Even larger values of up to $172\,000 \pm 10\,000$ have been measured for a plane-concave cavity at a length of 7.5 µm using one fiber of the same batch and a macroscopic mirror [362]. The increased finesse might stem from the reduction of absorption loss by annealing, which is able to resolve defects in the coating layers. Possibly, local annealing has happened while stabilizing the cavity length on resonance. The small mode waist ($w_0 \simeq 2\,\mu$m) and the high finesse yield large intracavity intensities, even for moderate incoupling powers P_i. Assuming ideal fiber coupling and mode matching, the intracavity power is given by $P_\mathrm{c} = P_\mathrm{i} T\,(\mathcal{F}/\pi)^2$, where T is the mirror transmission (Eq. 3.25). For

[16] Toptica DL100
[17] Photline NIR-MPX800-LN-10
[18] Exalos EXS7505-8411

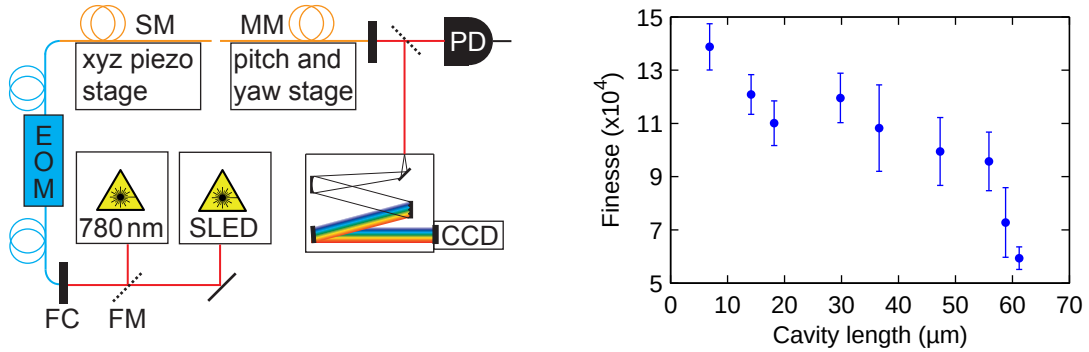

(a) (b)

Figure 5.19.: (a) Setup used to determine the cavity finesse. FM: flip mirror, FC: fiber coupler, PD: photo diode (b) Finesse measurement for different cavity lengths resulting in a maximal value of $140\,000 \pm 10\,000$ at a cavity length of 6.9 µm.

$P_\mathrm{i} = 1\,\mathrm{mW}$, the intracavity power amounts to about 36 W and the peak intensity

$$I_\mathrm{max} = \frac{8P_c}{\pi w_0^2} \tag{5.2}$$

may reach values of $2\,\mathrm{GW/cm^2}$, which is on the order of the damage threshold of low-loss coatings. To my knowledge, the largest finesse of FFPCs published so far is $190\,000 \pm 10\,000$ for a mirror transmission of 2.9 ppm [54].

The measured finesse of 172 000 corresponds to a total loss per mirror of roughly 18 ppm, which is distributed between transmission, absorption and scattering loss. The target transmission for this coating is 12 ppm and absorption loss after annealing can be as low as 3 ppm according to the manufacturer. Hence, scattering loss amounts to roughly 3 ppm, corresponding to a surface roughness of only 0.1 nm (Eq. 3.17). This is comparable to the surface roughness of standard super-polished mirror substrates typically specified as better than 0.2 or 0.1 nm. Table 5.3 provides the theoretically achievable cavity finesse for a few values of the scattering loss and the transmission. The absorption loss is fixed at 6 ppm.

σ_rms (nm) / S (ppm)	T =2 ppm	T =5 ppm	T =10 ppm
0.1 / 2.6	300 000	230 000	170 000
0.14 / 5.1	240 000	200 000	150 000
0.2 / 10	170 000	150 000	120 000

Table 5.3.: Finesse in dependence of surface roughness σ_rms, scattering loss S, and transmission T for fixed absorption loss $A = 6$ ppm.

Penetration of the electric field into the mirror stack

A major drawback of dielectric coatings compared to metallic mirrors is the rather large penetration of the electric field into the mirror stack. If the high and low refractive indices n_{H} and n_{L} of the two coating materials are known, the geometrical penetration depth can be calculated following [389]. The adapted expressions valid for a dielectric mirror in air are given by

$$L_{\mathrm{H}} = \frac{\lambda}{4\bar{n}\Delta n}, \tag{5.3}$$

if the mirror is finished with a high-refractive-index layer and

$$L_{\mathrm{L}} = \frac{\lambda\bar{n}}{4\Delta n} + \frac{\lambda\Delta n}{2\pi^2\bar{n}}, \tag{5.4}$$

if finished with a low-refractive-index layer, where

$$\bar{n} = 2\left(\frac{1}{n_{\mathrm{H}}} + \frac{1}{n_{\mathrm{L}}}\right)^{-1}, \tag{5.5}$$

and

$$\Delta n = n_{\mathrm{H}} - n_{\mathrm{L}}. \tag{5.6}$$

For the typical coating materials, SiO_2 and Ta_2O_5, having refractive indices $n_{\mathrm{L}} = 1.46$ and $n_{\mathrm{H}} = 2.1$, respectively, the electric field geometrically penetrates $L_{\mathrm{H}} = 177\,\mathrm{nm}$ and $L_{\mathrm{L}} = 539\,\mathrm{nm}$ into the mirror stack. Assuming that the optical path length of the layers equals a quarter wavelength, here $\lambda = 780\,\mathrm{nm}$, the layers have geometrical thicknesses of $d_{SiO_2} = 134\,\mathrm{nm}$ and $d_{Ta_2O_5} = 93\,\mathrm{nm}$, respectively. Evidently, the field penetrates a few layers into the mirror stack before being stopped.

More significant than the geometrical penetration depth is the optical penetration depth, which is estimated by

$$d_{\mathrm{H,L}} = \bar{n}L_{\mathrm{H,L}}, \tag{5.7}$$

and amounts to $d_{\mathrm{H}} = 305\,\mathrm{nm}$ and $d_{\mathrm{L}} = 929\,\mathrm{nm}$, here. These values increase for wavelengths differing from the design wavelength. The total (optical) penetration depth d_{pen} of a cavity is given by the sum of the penetration depths of all involved cavity mirrors. The mirrors coated by ATF are finished with a high refractive index material. Hence, a Fabry-Pérot cavity with two of these mirrors experiences a total penetration depth of about 610 nm, which critically limits the minimally achievable mode volume.

For the coupling of an emitter to the field maximum of the cavity mode, it is advantageous to place the emitter on a mirror with a suitably sized, low-refractive-index spacer layer. In this case, the total penetration depth is closer to 1.2 µm. The enlarged mode volume can be approximated by replacing the cavity length d in Eq. 3.43 by the effective cavity length

$$d_{\mathrm{eff}} = d + d_{\mathrm{pen}}, \tag{5.8}$$

while assuming that the mode width w_0 does not change.

5.3.2. Silver coating

Compared to low-loss dielectric mirrors composed of a multitude of layers, metal coatings are rather simple systems and can be produced with minor experimental overhead. Silver mirrors, for instance, can be prepared by applying a thin film of some ten to hundred nanometers of the metal onto a substrate like a macroscopic glass cover slip or the microscopic end facet of an optical fiber. To prevent oxidation, a protective glass layer is usually coated on top. Additionally, the glass cap may serve to position the maximum of the electric field slightly above the mirror surface, to optimize the coupling to directly attached emitters. Silver stands out against other metals due to its large reflectivity and low fluorescence in the visible. The principal motivation for metal coatings is the minor penetration of electric fields into the mirror, which enables FFPCs with ultra-small mode volumes. As subsequently explained in more detail, the mirror transmission depends on the thickness of the silver layer, which can be optimized for different coupling scenarios with broad-band emitters. On the one hand, a maximal effective Purcell factor is obtained for maximal cavity finesse, i.e. cavity mirrors with lowest transmission, which is obtained for large silver layer thickness. On the other hand, the photon rate is maximized for a cavity where one mirror has a slightly larger transmission, i.e. a thinner silver layer, such that the light can be efficiently coupled out and collected. These scenarios will be thoroughly discussed in Section 7.2.

Penetration depth and mirror transmission

The $1/e$-penetration depth of the electric field into metals with a complex refractive index $n' = n - \mathrm{i}k$ is given by [390]

$$\delta = \frac{\lambda}{2\pi k}. \tag{5.9}$$

For silver, the extinction coefficient k continuously increases from about 3 to 7 for wavelengths from 500 to 1000 nm, which results in penetration depths between 28 and 22 nm. Silver mirrors with a layer thickness, which is comparable to the penetration depth, are semitransparent. As shown in Fig. 5.20(a), the mirror transmission decreases exponentially with the thickness of the silver layer. The calculation is based on the matrix method (Section 3.2) for normal incidence of the light wave on the mirror. It is confirmed by an additional finite difference time domain (FDTD) simulation[19].

Table 5.4 summarizes simulated and measured parameters for the mirrors used in the experiments described in Section 7.2. For better illustration, two mirror coatings denominated M1 and F1 are now discussed in more detail:

Mirror M1 A typical mirror coating applied to a planar glass cover slip consists of a silver layer of 33 nm capped with 20 nm of glass. The wavelength-dependent transmission (T), reflectivity (R) and absorption (A) of this mirror is simulated with the matrix method (Section 3.2) for normal angle of incidence, as shown in Fig. 5.20(b). At a

[19] Lumerical FDTD Solutions

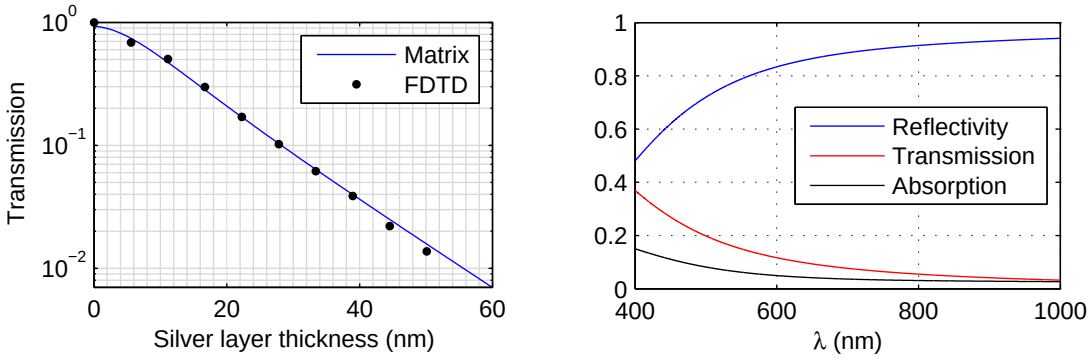

(a) (b)

Figure 5.20.: (a) Transmission of an individual silver layer on a glass substrate at $\lambda = 700\,\text{nm}$ as a function of the layer thickness, simulated with the matrix method (blue line). It is in very good agreement with FDTD simulations (black dots). (b) Reflectivity (blue), transmission (red) and absorption (black) of a silver layer of 33 nm thickness, capped with 20 nm of glass as a function of the wavelength.

Name	r	Ag	SiO_2	λ	T_{exp}	T_{th}	R_{exp}	R_{th}	A_{th}	$\mathcal{F}_{exp}$	$\mathcal{F}_{th}$
M1	∞	33 nm	20 nm	532 nm	0.15	0.16		0.77	0.07	21	18
				692 nm		0.08		0.88	0.04	42	37
F1	90 µm	60 nm	20 nm	532 nm	0.06	0.02	0.93	0.92	0.06		
				692 nm		0.008		0.96	0.03		
M2	∞	33 nm	60 nm	532 nm	0.24	0.24		0.66	0.10		
				633 nm	0.16	0.15				18	21
				692 nm		0.11		0.83	0.05		28
F2	∞	60 nm	20 nm	532 nm	0.06	0.02	0.93	0.92	0.06		
				692 nm		0.008		0.96	0.03		

Table 5.4.: Measured (exp) and simulated (th) parameters of typical silver mirror coatings. The cavity finesse is given for the combination of these mirrors (M1 with F1 and M2 with F2). r: radius of curvature of the mirror, λ: wavelength

wavelength of 692 nm, values of $R_{\mathrm{th}} = 88.7\,\%$, $T_{\mathrm{th}} = 7.7\,\%$ and $A_{\mathrm{th}} = 3.6\,\%$ are expected. The reflectivity increases with the wavelength, while the transmission and absorption decrease. This general behavior is independent of the silver layer thickness and a direct consequence of the wavelength dependence of the refractive index of silver. The glass cap has a minor effect. For a pure silver layer the values change only slightly ($R_{\mathrm{th}} = 90.0\,\%$, $T_{\mathrm{th}} = 6.8\,\%$, and $A_{\mathrm{th}} = 3.2\,\%$). The transmission of this mirror is checked experimentally by measuring the power of a laser before and behind the mirror. At a wavelength of 532 nm, the measurement yields a transmission of $T_{\mathrm{exp}} = (15 \pm 2)\,\%$, while the predicted value amounts to $T_{\mathrm{th}} = 16\%$. The quoted errors are obtained from measurements at different mirror locations typically yielding moderate variations of the transmission.

Mirror F1 The second mirror to be considered is coated with 60 nm of silver and capped with 20 nm of glass. This coating is typically applied to the end face of fibers. When fibers are used as substrates, the transmission cannot be determined straightforward, since the coupling efficiency into the fiber is not known very accurately. Therefore, the transmission is usually determined for glass substrates coated in parallel to the fibers. Due to the larger thickness of the silver layer, the mirror transmission is lower than a few percent. For mirrors with a low transmission, the determination of the reflectivity is more precise. Here, the reflectivity amounts to $R_{\mathrm{exp}} = (93 \pm 2)\,\%$ at 532 nm, close to the predicted value of $R_{\mathrm{th}} = 92\%$. In general, very good agreement to the values obtained with the matrix method were found.

Cavity transmission and finesse

The cavity finesse that is achievable with silver mirrors is limited to values of around 100, as a consequence of absorption loss within the silver films, which is on the order of 3-4%. Thus, for decreasing mirror transmission, i.e. increasing silver layer thicknesses, the finesse starts to saturate, as displayed in Fig. 5.21(a). For the shown example, the silver layer thickness of the first mirror is fixed to 100 nm, while it is varied from 0 to 100 nm for the second one. The glass capping is 20 nm for both mirrors. The determination of the finesse is based on the calculation of the individual mirror reflectivities with the matrix method for normal angle of incidence and applying Eq. 3.18.

Cavity consisting of mirrors M1 and F1 Now, the two previously discussed mirrors are combined as Fabry-Pérot cavity. The transmission behavior of this cavity is simulated with the matrix method, with an air spacer layer of 4 µm in between the two mirrors. As shown in Fig. 5.21(b), three neighboring resonances are present in a spectral window from 600 to 800 nm. Due to the asymmetric transmission of the mirrors, the photons would predominantly leave the cavity through the thinner mirror, enabling large collection efficiency in the experiment. According to Eq. 3.22, the probability of a photon to leave the resonator through the thinner mirror amounts to 51%, compared to only 5% through the thicker one.

The cavity finesse is also measured. While the first mirror (M1) is deposited on a

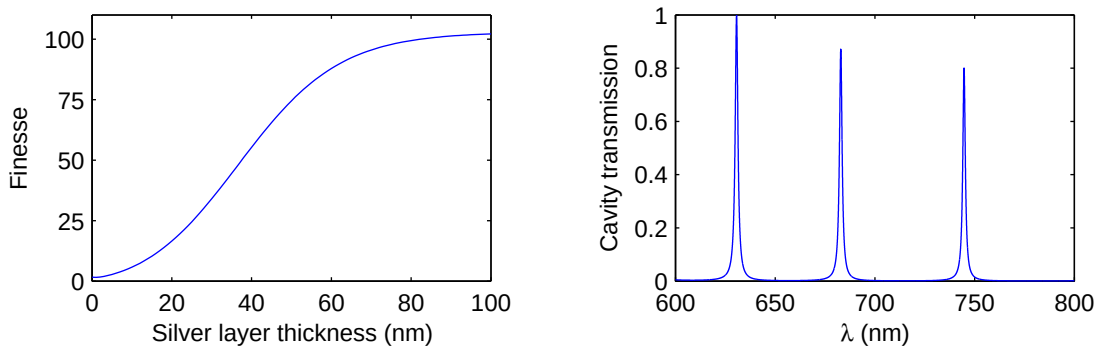

(a) (b)

Figure 5.21.: (a) Cavity finesse as a function of the silver layer thickness of one of the mirrors. (b) Normalized cavity transmission of two glass capped silver mirrors (M1 and F1) at a mirror spacing of 4 µm.

macroscopic planar glass substrate, the second (F1) is on a fiber end facet with a concave laser-machined structure. A narrow-band laser is coupled into the fiber end and the cavity transmission is detected behind the macroscopic mirror with a photo diode, while the cavity length is swept over a little more than one free spectral range with a piezoelectric actuator. Fibers with a concave profile yield stable spatial cavity modes that can be directly focused onto the detector. In contrast, plane-plane cavities require spatial filtering. Only the central feature of the interference pattern, known as Newton's rings, is used.

Figure 5.22 shows transmission measurements of the plane-concave cavity having a length of around 10 µm for two different wavelengths (532 nm and 692 nm). The finesse is obtained by fitting Eq. 3.11 to the transmission data, resulting in values of $\mathcal{F}_{\mathrm{exp}} = 21 \pm 1$ at 532 nm and $\mathcal{F}_{\mathrm{exp}} = 42 \pm 1$ at 692 nm. This is slightly larger than the theoretically expected values of $\mathcal{F}_{\mathrm{th}} = 18$ and $\mathcal{F}_{\mathrm{th}} = 37$, respectively. The excess can be explained by thicker than assumed silver layers, if the sputtering rate (see below) differed from the expected value. In this case, the individual mirror transmission would be lowered and the finesse increased. However, the measured transmission being in good agreement to theory, contradicts this assumption. It is hence not clear, why the finesse is larger than expected. In conclusion, the finesse is acceptably close to its target value. Scattering loss is negligible, as will be shown subsequently.

Manufacturing procedure

Silver mirrors can be self-manufactured with reasonable effort. The mirrors prepared for this work were produced in the clean room of the chair of solid state physics at the Ludwig-Maximilians University, Munich. The facility offers two different coating devices

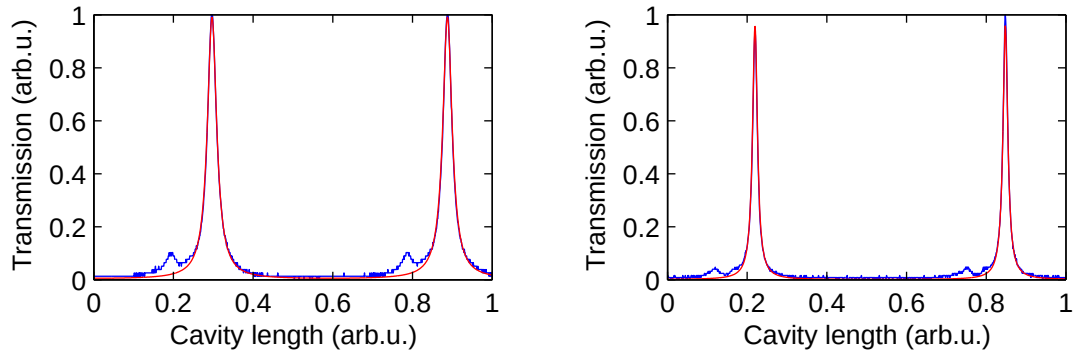

(a) (b)

Figure 5.22.: Transmission of a cavity, whose length is modulated around 10 µm (blue dots) together with a fit (red line) yielding a cavity finesse $\mathcal{F}_{\text{exp}} = 21 \pm 1$ at 532 nm (a) and $\mathcal{F}_{\text{exp}} = 42 \pm 1$ at 692 nm (b). The comparison illustrates the much narrower resonances at the larger wavelength.

based on electron beam physical vapor deposition (EBPVD)[20] and magnetron sputter deposition (MSD)[21], respectively. Both apparatuses can be equipped with Ag and SiO_2 targets. The MSD device offers easier access to a larger sample space, which is crucial for fiber coating. Thus, fibers were exclusively coated by sputter deposition. The same method was predominantly applied, when using cover slips as mirror substrates, even though EBPVD yields good results, as well.

A brief protocol of MSD follows: At first, the fibers and substrates to be coated are placed inside the vacuum chamber. Four available slots allow individual coatings. The vacuum chamber is evacuated for some ten minutes to about an hour until it reaches a few $1 \cdot 10^{-6}$ mbar. Longer evacuation times yield pressures saturating at a few $1 \cdot 10^{-7}$ mbar. Next, an argon flow into the chamber is established and the argon pressure is regulated to $2 \cdot 10^{-2}$ mbar. An electric DC field is applied between the silver target and the sample holder. At electric powers starting at about 3 W, an argon plasma ignites and the sputtering process is triggered. Electrons and argon ions are accelerated towards the sample and the target, respectively. When the argon ions hit the target, they release silver particles that are deposited on the sample. Thus, increasing the power results in larger deposition rates. The power can be ramped up to about 50 W. For a power value set to 3 W (30 W), the applied voltage between target and sample amounts to 240 V (350 V) at a current of 15 mA (85 mA). Coating of the sample is initiated by removing an intermediate screen between target and sample, after about ten minutes of pre-sputtering, in order to remove residues from the target, as well as to thermalize the system to obtain stable deposition rates. For a fixed power, the layer thickness is controlled by the coating

[20] UHV vapor deposition system from Bestec with electron beam source Telemark 271/277-32
[21] Von Ardenne Magnetron Sputter System LS 320 S

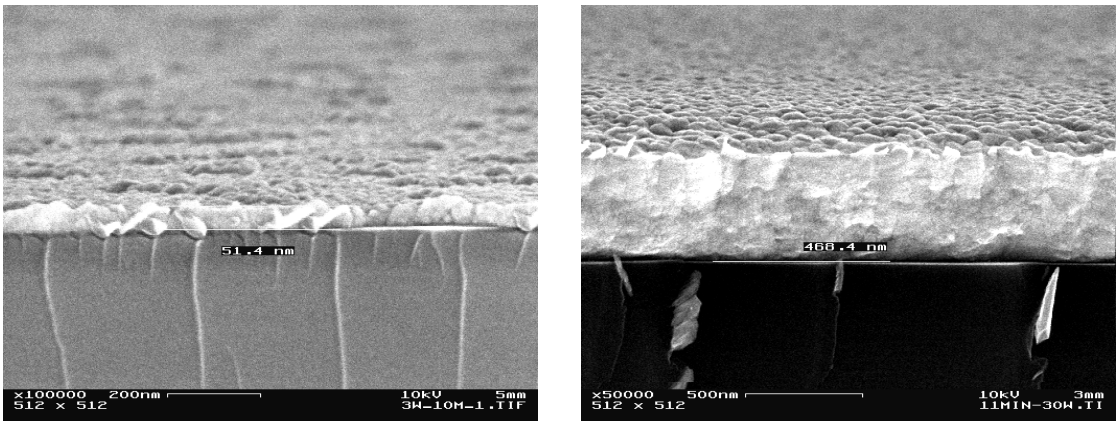

(a) (b)

Figure 5.23.: SEM images of a silver film sputtered on a silicon substrate. The crack offers a clear view on the silver layer. The grainy structure of the layer is characteristic for silver. (a) Sputtering at 3 W for 10 minutes leading to a layer thickness of about 51 nm. (b) Sputtering at 30 W for 11 minutes leads to a layer thickness of about 470 nm.

time. For the production of silver films of a few ten nanometers, it proved beneficial to keep the power as low as 3 W, such that the deposition time is on the order of some minutes. The deposition onto the sample is blocked, when the intermediate screen is moved in again. Subsequently, the electric field is switched off. In a second, analogue step, a glass capping layer is deposited on top of the silver film, without breaking the vacuum. Since SiO_2 is dielectric, an AC field is applied instead of a DC field, which prevents charge build-up. An electric RF power of 50 W leads to convenient deposition rates.

Unfortunately, no quartz crystal microbalance is included into the MSD device, such that the deposition rate cannot be controlled in situ, but has to be determined in auxiliary measurements. The sputtering rate for silver is determined by measuring the thickness of a silver film on a silicon substrate, by scanning electron microscopy (SEM). If the silicon substrate is broken after the deposition process, the crack offers a clear view on the silver film and its thickness can be measured straightforward, as shown in Fig. 5.23. Assuming that the thickness of the deposited material increases linearly with time, a silver deposition rate of about $6\,\mathrm{nm\,s^{-1}}$ at a sputtering power of 3 W was found. The thickness of a SiO_2-layer on a silicon substrate is determined by ellipsometry, yielding a deposition rate of about $4\,\mathrm{nm\,s^{-1}}$ at a sputtering power of 50 W.

Surface quality

SEM images offer a fast impression of the deposited films, regarding their coherence and overall morphology, as shown in Fig. 5.23. AFM measurements can additionally

provide precise information about the surface roughness, which eventually defines the scattering loss. The surface roughness is obtained by subtracting line-wise polynomial fits of second order from the raw data, as already discussed for laser machined glass fibers in Section 5.1.

The tested samples consist of silver films without glass capping, deposited on silicon wafers. The bare wafers exhibit an rms surface roughness of about 0.2 nm. The roughness of the silver films reached from 1.6 nm for a sputtering power of 3 W, up to 5.2 nm for 30 W, as displayed in Fig. 5.24. The expected scattering loss at a wavelength of 700 nm spans from roughly 1‰ to 1%. Compared to absorption, scattering loss thus plays a minor role and is negligible for the films sputtered with a power of 3 W.

The silver mirrors applied for the actual experiments are either deposited on low fluorescence quartz glass[22] or laser-machined fibers, for which surface roughness values down to 0.5 nm and 0.14 nm were measured, respectively (see Section 5.1). Consequently, these substrates have a minor effect on the roughness of the deposited silver films. The glass cap of usually 20 nm that finishes the mirrors, is not expected to change the surface quality considerably, either.

[22] Heraeus Suprasil

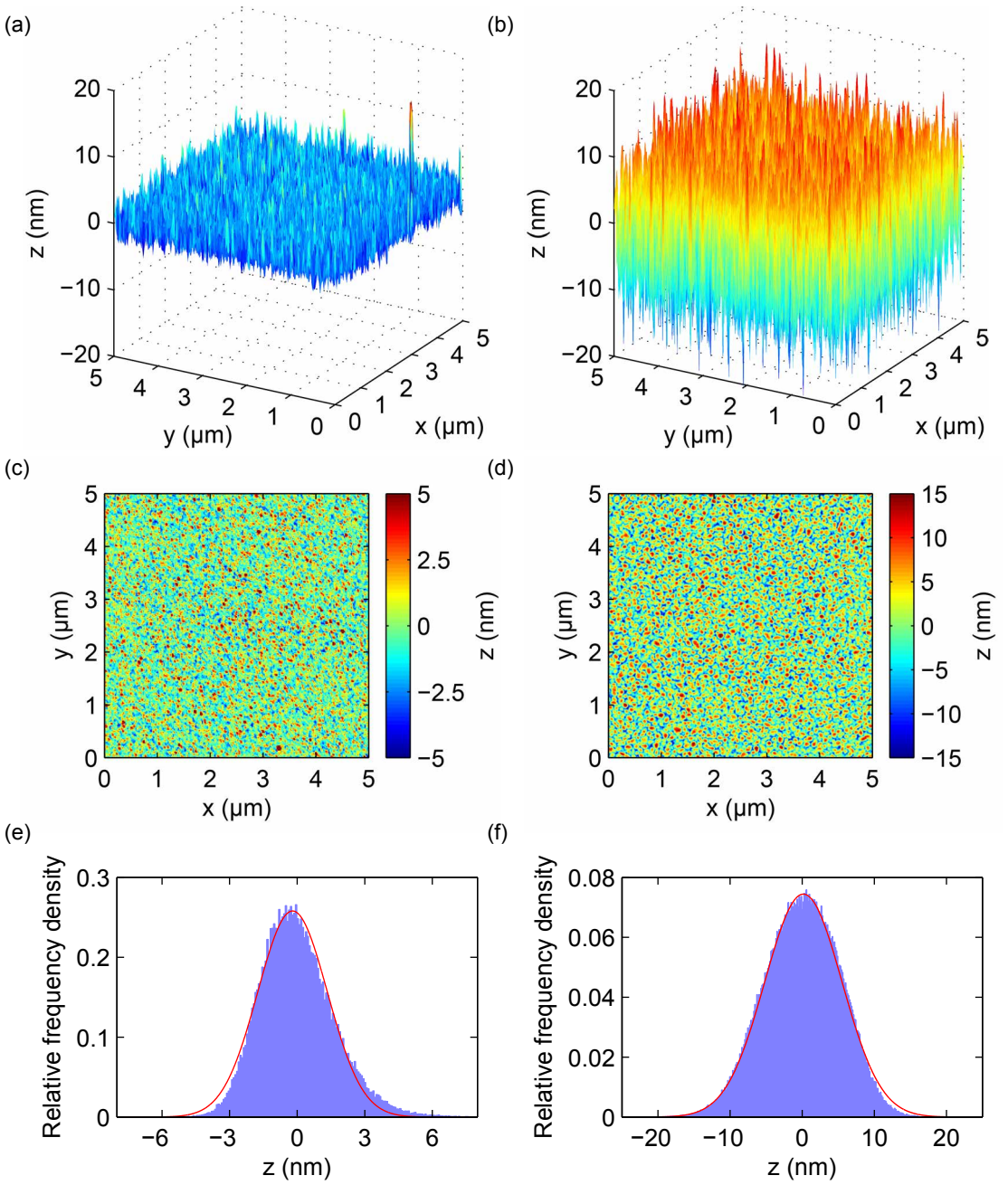

Figure 5.24.: AFM measurements of silver layers sputtered with powers of 3 W (a,c,e) and 30 W (b,d,f). Comparison of the 3D surface roughness (a,b) with the corresponding 2D plots (c,d) show that both the peak amplitude and the grain diameter is noticeably smaller for the silver layer sputtered with lower power. (e,f) Relative frequency density of all roughness values (purple) together with a Gaussian distribution fit (red). The standard deviation or equivalently the rms roughness amounts to 1.6 nm and 5.2 nm, respectively.

5.4. Limiting parameters: Fiber coupling, clipping loss, mode mixing

Coupling efficiency

Complex experimental settings can strongly benefit from the robust, intrinsic in- and out-coupling of the cavity mode to the fiber mode. The coupling efficiency is directly defined by the mode matching between the fiber and the cavity mode and can be approximated by the overlap integral of these modes, when the phase mismatch is neglected. For negligible transverse and angular misalignment between the fiber core and the imprinted structure, the power coupling efficiency to a single mode (SM) fiber can be estimated by

$$\tilde{\epsilon} \approx \left(\frac{2 w_\mathrm{f} w_\mathrm{m}}{w_\mathrm{f}^2 + w_\mathrm{m}^2} \right)^2 , \tag{5.10}$$

with the radius of the mode that is guided in the fiber core w_f and the cavity mode radius at the position of the mirror w_m [51]. If the wavefront curvature and the lensing effect is furthermore included, the coupling efficiency is given by

$$\epsilon = \frac{4}{\left(\frac{w_\mathrm{f}}{w_\mathrm{m}} + \frac{w_\mathrm{m}}{w_\mathrm{f}} \right)^2 + \left(\frac{\pi n_\mathrm{f} w_\mathrm{f} w_\mathrm{m}}{\lambda R} \right)^2}, \tag{5.11}$$

where n_f denotes the refractive index of the fiber core and R is the radius of curvature of the mirror [51]. Misalignment between the machined mirror structure and the fiber core, which is neglected here, reduces the coupling efficiency further. However, very good centering of the structure with respect to the fiber core is feasible in practice. For the derivation of the general case including transverse and angular misalignment consult [391].

Consider a cavity consisting of a planar macroscopic mirror and a concave mirror on the end facet of an optical fiber having a radius of curvature $R = 90\,\mu\mathrm{m}$ and a diameter $D = 7\,\mu\mathrm{m}$ (see Fig. 5.9). These parameters correspond to the actual experimental setting that will be discussed in Section 7.2.1. The mode radius on the planar mirror w_0 and on the fiber w_m are given by Eqs. 3.41 and 3.42, respectively. As shown in Fig. 5.25(a), for a wavelength of $\lambda = 700\,\mathrm{nm}$, the mode radius on the planar mirror takes a maximum of around $3.2\,\mu\mathrm{m}$ in the middle of the stability range, i.e. at a cavity length of $d = R/2 = 45\,\mu\mathrm{m}$. On the contrary, the mode radius on the fiber diverges, when getting closer to the stability limit $d = R$.

The obtained values for the mode radii w_0 and w_m are now used to evaluate the coupling efficiency ϵ as a function of the cavity length, for a standard SM fiber with $n_\mathrm{f} = 1.45$ and $w_\mathrm{f} = 2\,\mu\mathrm{m}$. As shown in Fig. 5.25(b), the maximal coupling efficiency of 98% is reached for a cavity length $d = 3.2\,\mu\mathrm{m}$, when the cavity mode on the concave mirror is approximately equal to mode guided in the fiber core $w_\mathrm{m} = w_\mathrm{f}$. The mirror curvature prevents perfect alignment. Even for the fundamental resonance, where the cavity length is roughly given by $d = \lambda/2 = 350\,\mathrm{nm}$ (neglecting phase shifts and penetration into the

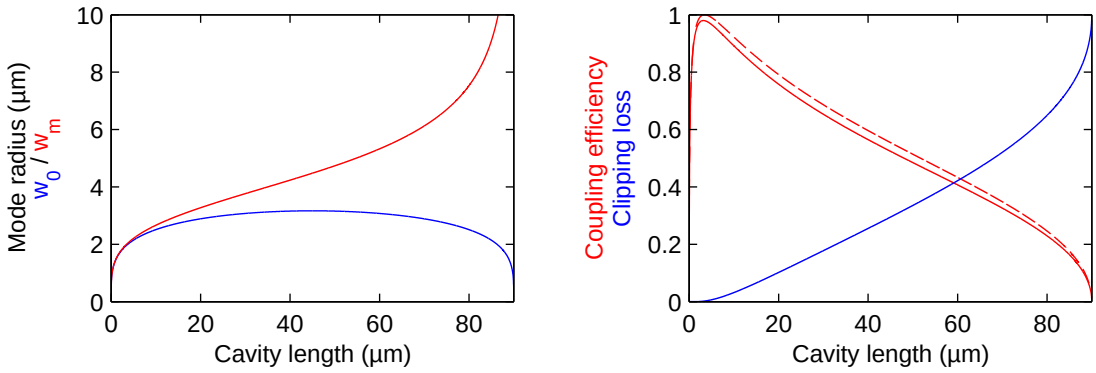

(a) (b)

Figure 5.25.: Parameters for a plane-concave cavity with one macroscopic plane mirror and machined fiber mirror with diameter $D = 7\,\mu\text{m}$ and radius of curvature $R = 90\ \mu\text{m}$. (a) Mode radii as a function of the cavity length. While the mode radius on the plane mirror w_0 (blue line) is bounded above, the mode radius on the fiber mirror w_m (red line) diverges for long cavities. (b) Coupling efficiency ϵ (red line), $\tilde{\epsilon}$ (red dashed line), and clipping loss (blue line).

mirror coating), the coupling efficiency is still larger than about 70%. It drops for long cavities, since the cavity mode on the fiber mirror w_m gets increasingly larger than the fiber mode. The simple approximation $\tilde{\epsilon}$ deviates less than 10% from the more precise expression ϵ.

Clipping loss

The lateral extension of the concave mirror structures are on the order of some microns. With increasing cavity length, the mode waist on the mirror can get comparable to the structure size, leading to additional loss. A conservative estimate for the so-called clipping loss is established by comparing the size of a Gaussian cavity mode to the finite diameter of the micromirror. The loss for a single reflection on a mirror of diameter D is then given by

$$L_\text{cl} = e^{-2(D/2)^2/w_\text{m}^2}, \tag{5.12}$$

with the mode radius on the mirror w_m. The clipping loss for the same cavity parameters that have been used for the evaluation of the coupling efficiency, is illustrated in Fig. 5.25(b). For increasing cavity length, the mode radius on the fiber and hence the clipping loss increases. For cavities shorter than $d = 10\,\mu\text{m}$, the clipping loss is below 4%. In this work, the cavity length is chosen as short as possible and clipping loss is expected to play a minor role, for the chosen structure diameters. As a rule of thumb, the mode radius should be at least three (better four) times smaller than the $1/e$-radius of the mirror structure, to avoid noticeable clipping loss.

Mode mixing

Note that the finite mirror size and non-ideal shape of laser-machined micromirrors furthermore results in (near-)resonant coupling between different transverse cavity modes. The impact of mode mixing for FFPCs has been thoroughly studied by Benedikter *et al.* [392]. Admixed higher order transverse modes that suffer from diffraction loss, as a consequence of their extended size may open a loss channel to the fundamental mode. This behavior gives rise to distinct drops of the cavity finesse at certain cavity lengths. However, this effect is not very pronounced for short cavities, when the fundamental cavity mode is close to a Gaussian cavity mode. Furthermore, for mirrors with a small diameter, the finesse already deteriorates for mirror separations that are shorter than what is expected from the stability range, which is given by the radius of curvature of the mirror.

5.5. A brief history of fiber-optic communication

The intrinsic fiber coupling of FFPCs is a great advantage over other resonator geometries suffering from poor coupling efficiency. Optical fibers provide a practical way for low-loss optical interconnection based on a sophisticated and well-established technique. This would be of great benefit, for instance for the direct implementation of FFPC-coupled quantum systems into existing communication structures. In this way, it might become possible to harness the quantum properties of light over long distances some day [393]. To get an idea of the technological advances of optical communication, the history of fiber optics is briefly sketched in the following.

The backbone of our contemporary telecommunication system relies on a gigantic network of glass fibers. The information to be sent is encoded with light signals traveling through the fibers with a velocity of roughly 200 000 km/s, corresponding to five times around the earth in one second. Due to a radially decreasing refractive index of the applied fiber material, light is guided within its core by total internal reflection. Different wavelengths constitute independent transmission channels within a single fiber, also known as wavelength division multiplexing, resulting in an enormous bandwidth. Furthermore, the attenuation of present-day optical fibers is much lower than that of electrical cables, allowing signals to travel over tens of kilometers before they need to be amplified.

In fact, the reduction of loss was one of the keys towards the practical application of fiber networks [394]. In 1966 Charles K. Kao and Geroge A. Hockham gave a detailed analysis of the potential of dielectric fibers used as waveguides at optical frequencies [395]. They concluded that the information capacity of dielectric fibers outperformed that of the existing coaxial-cable and radio systems at presumably lower material costs. However, the success crucially depended on the development of low-loss dielectric materials, requiring to reduce loss from common values at that time of about 1 dB/m to around 20 dB/km. Convinced that there was no fundamental, physical loss mechanism contradicting the feasibility of such fibers, their work stimulated new material research. And indeed, in

1970 Robert D. Maurer, Donald Keck and Peter C. Schultz demonstrated a single-mode fiber meeting the desired requirements at a wavelength of 633 nm. Their breakthrough was based on the dramatic reduction of material impurities by using highly purified fused silica. By adding precisely monitored amounts of dopants, they were able to induce a slightly increased refractive index of the fiber core with respect to the cladding that gives rise to mode guidance, without increasing the attenuation decisively. In 2009, Kao, sometimes referred to as the "Father of Fiber Optics" received the Nobel prize "for groundbreaking achievements concerning the transmission of light in fibers for optical communication"[23].

A second crucial step in the success story of optical communication was the realization of erbium-doped fiber amplifiers in the end of the 1980s. These novel amplifiers enabled all-optical amplification, without the need to convert optical to electrical signals, amplify them, and convert them back again. Signals at different wavelengths transmitted through a single fiber can be amplified in parallel, establishing the practical use of wavelength division multiplexing. This meant a major simplification over existing systems and boosted the transmission capacity per fiber. Furthermore, the invention of various sophisticated light sources contributed to the prospering field decisively. In particular, semiconductor laser diodes play an important role. The emitted radiation can be coupled into fibers with a high efficiency, its modulation is fast and easy.

[23] http://www.nobelprize.org/nobel_prizes/physics/laureates/2009/index.html

6. Experimental methods

In the beginning of this chapter, a detailed description of the experimental setup is given. Next, the studied samples of fluorescent nanodiamonds (FNDs) are introduced. The preparation of the diamond nanocrystals on a substrate or mirror is described and the distribution of the crystal size is discussed. Finally, the characterization of NV centers by confocal microscopy is presented, applying a set of standard measurements.

6.1. Integrated fiber cavity - confocal microscope setup

The core part of the experimental setup is the optical cavity assembled of a planar macroscopic mirror and a concave mirror on the end face of an optical fiber, shown in Fig. 6.1(a). Nanodiamonds containing NV centers in an aqueous solution are directly applied onto the planar mirror. The cavity is embedded into a confocal microscope enabling simultaneous excitation of and light collection from the emitters through the planar mirror with a high numerical aperture (NA) objective[1] (Fig .6.1(b) and Fig. 6.2). The latter is mounted on a piezoelectric positioning system[2] for fine adjustment of the focus with a range of 100 µm. Alternatively, excitation is performed through the cavity fiber, while still collecting with the objective. Light collection with the cavity fiber is in principle possible, as well. However, this optical path was not used, to avoid loss due to imperfect mode matching to the fiber mode. The mirror coatings can be designed asymmetrically, such that the photons predominantly escape the cavity through the planar mirror. After the fluorescence is collected with the objective, it is first spectrally filtered with a dichroic mirror (DM), a long-pass (LP), and a notch filter (NF)[3], then spatially filtered with a pinhole in between two achromatic lenses[4], and finally detected with a grating spectrometer[5] or two avalanche photo diodes (APDs)[6] in a HBT setup with a 50-50 beamsplitter [113]. Lifetime and autocorrelation measurements can be carried out using time recording electronics[7] that process the signals from the APDs.

The planar mirror is fixed inside a gimbal mirror mount[8] that is attached to a three-

[1] Carl Zeiss LD Plan-Neofluar 63x/0.75 Korr, magnification 63X, NA=0.75 or Mitutoyo Plan Apo Infinity Corrected Long WD Objective, magnification 50X, NA=0.55
[2] PI P-721.SL2
[3] Semrock Di02-R594-25x36, BLP01-594R-25, Thorlabs NF533-17 or Thorlabs DMLP657, FEL0600, FES0850, NF533-17
[4] Thorlabs AC254-100-A-ML, 50 µm Pinhole P50S
[5] Princeton Instruments Acton SP2500 with Andor iKon-M 934 (A-DU934N-BRDD) connected via optical fiber Thorlabs HPSC-25 or SM600
[6] Excelitas SPCM-AQRH-12-TR or Laser Components Count-50
[7] PicoQuant PicoHarp 300 or qutools quTau
[8] Newport U50-G21

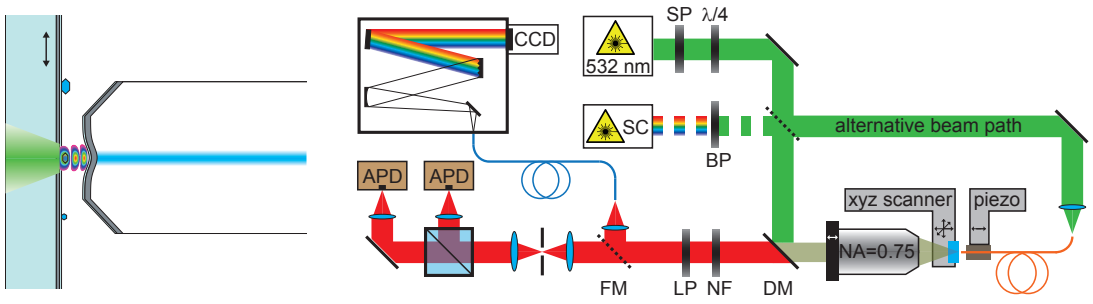

Figure 6.1.: (a) Schematic drawing of the microcavity consisting of a micropatterned and mirror-coated end facet of an optical fiber and a macroscopic planar mirror. (b) Combined cavity and confocal microscope setup (FM: flip mount)

axis slip-stick positioner[9]. Thus, the mirror can be scanned transversely through the microscope focus in order to locate suitable emitters. The critical angular alignment of the cavity is performed with the gimbal mirror mount. The fiber is stably mounted on a stacked piezoelectric actuator[10] aligned with the cavity axis, enabling precise tuning and stabilization of the cavity length within a range of about one FSR. For stabilization, we use the modulated excitation light transmitted through the cavity, which is reflected from the DM. A cavity-length-dependent feedback signal is generated and fed to the stacked piezoelectric actuator that controls the fiber position. Furthermore, the fiber can be completely withdrawn and the setup then serves as conventional confocal microscope, for instance for preparative sample characterization.

In an earlier setup, the planar mirror was mounted rigidly in a two-axis piezoelectric positioning stage[11]. The cavity length was tuned by moving the entire stage in direction of the cavity axis with a piezoelectric actuator. For the alignment of the cavity, the fiber was mounted on a five-axis manual positioner[12]. Based on the experiences with this setup, the advanced concept was improved decisively. Much better passive mechanical stability is achieved by a rigid design with small dimensions. Additionally, the stability profits from reduced degrees of freedom, at the cost of a more sophisticated cavity alignment procedure. The new closed-loop piezoelectric positioner enables to translate the mirror by a large travel range of up to 20 mm in three directions, while the old device restricted scanning to 100 µm in the two lateral dimensions. Moving the mirror in the direction of the cavity axis in a more controlled way, proves beneficial for fast switching between pre-characterization of the sample by confocal microscopy and the measurements with the cavity. Automatic stabilization of the cavity length with a piezoelectric actuator is now possible by moving only the fiber and leaving the mirror in a fixed position.

[9] Stack of three Attocube ECS3030 positioners
[10] PI PL033.31
[11] PI 541.2 SL
[12] Elliot Scientific MDE122, MDE185

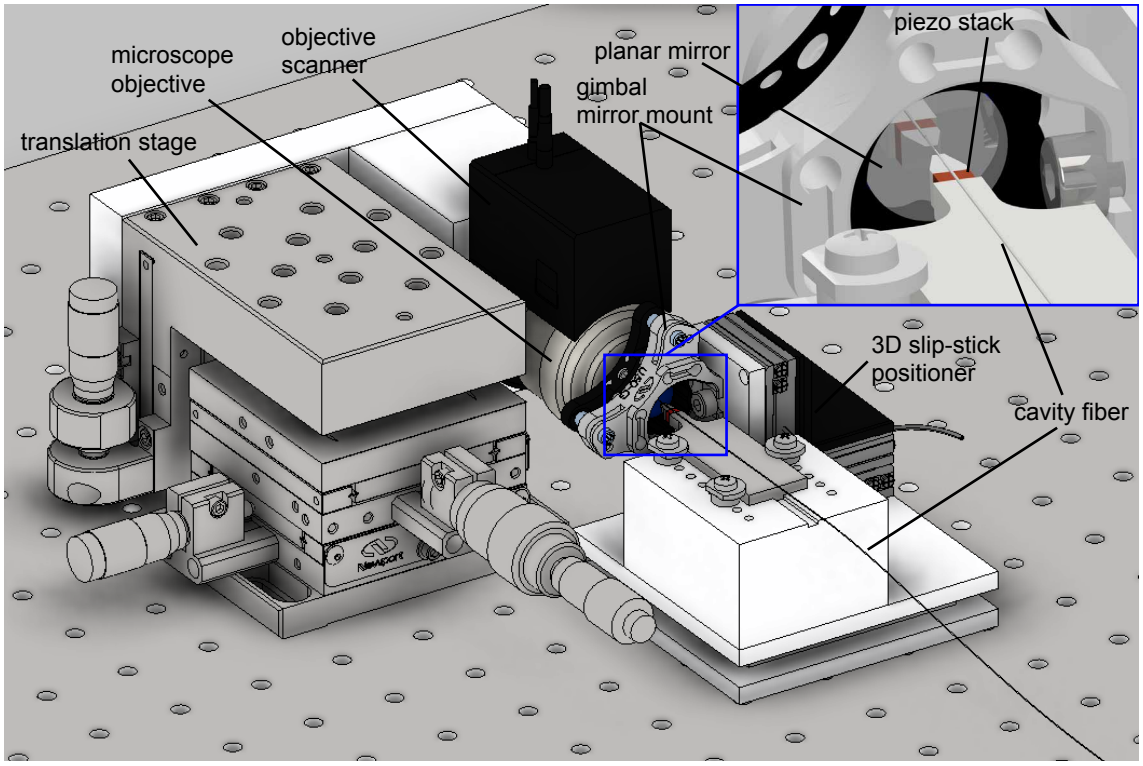

(a)

Figure 6.2.: Technical drawing of the setup

Two light sources are used for excitation. First, a continuous wave (cw), narrow-band laser with a wavelength of 532 nm[13]. The light it provides is spatially filtered by a SM optical fiber[14] and spectrally filtered by a short pass (SP) or band pass (BP) filter[15], to remove fluorescence created in the fiber. A quarter wave plate ($\lambda/4$) serves to obtain circularly polarized light. For the measurement of the excited state lifetime, a supercontinuum (SC) laser is used, which generates picosecond pulses with up to 20 MHz repetition rate[16]. Its emission, spanning from about 460 to 2000 nm, is spectrally filtered to a region around 532 nm, either by several interference filters[17], or with an acousto-optic tunable filter (ATOF) allowing to select a tunable wavelength channel with a spectral bandwidth of 2-7 nm. In addition, the SC source serves to record broad band cavity transmission spectra, to calibrate the cavity length. To this end, an emission spectrum from roughly 600 to 800 nm is selected with another set of interference filters[18].

[13] Cobolt Samba, 150 mW
[14] Thorlabs P3-488-FC-5
[15] Thorlabs FES0550, SemRock FF01-510/84-25
[16] Fianium SC450-2-PP with AOTF-VIS
[17] SemRock FF01-950/SP-25, FF01-550/49-25
[18] e.g. SemRock BLP01-594R-25, FF01-950/SP-25

Detection efficiency

The overall optical detection efficiency of the setup behind the first lens is inferred from the total transmission of the detection path and the quantum efficiency of the APDs. The transmission is determined experimentally by coupling a narrow-band diode laser, operating at 691.5 nm, into the back of the cavity fiber. The transmitted power is measured directly behind the objective and directly in front of the APDs, i.e. after transmission through all optical elements including the pinhole. A maximal fraction of 67% of the light is transmitted for a cavity length of 1 µm, for which the collection optics has been optimized (Fig.6.3). For an increasing cavity length, the transmission decreases to about 40% at 20 µm. Including the quantum efficiency of the APDs of 65% at 650 nm, an upper bound of the total detection efficiency of 43% at 690 nm results.

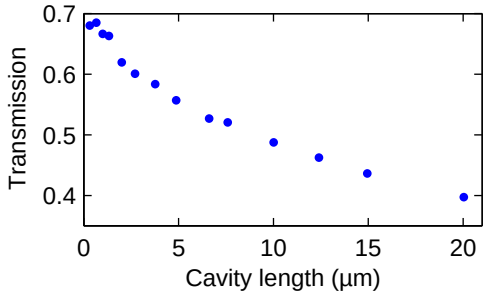

Figure 6.3.: Transmission of the detection path as a function of the cavity length, not including the quantum efficiency of the APDs.

6.2. Fluorescent nanodiamonds

Nanodiamonds are commercially available[19], since they are of great use for mechanical polishing applications. Polycrystalline diamond powder can, for instance, be formed by explosion synthesis that is followed by a grinding procedure[20]. Alternatively, the high-pressure high-temperature (HPHT) synthesis provides monocrystalline diamond particles. Chemical vapor deposition (CVD) constitutes a further way to manufacture synthetic NDs with high purity. Nanodiamonds created by impact processes induced by meteorites are rather exotic [396]. A few different ND samples were applied for this work, primarily differing in the crystal size and the amount of contained NV centers. All samples were preserved in an aqueous colloidal solution.

The first set of FNDs was provided by courtesy of H.-C. Chang from the Academia Sinica in Taipei, Taiwan and comprised two samples with size distributions expected to peak at 35 and 100 nm, respectively, abbreviated as **Tai35** and **Tai100**. These diamonds were irradiated with helium ions to increase the concentration of NV centers

[19] ...for example from Microdiamant, Element Six or VanMoppes

[20] http://www.microdiamant.com/products/micron-diamond-powder/
http://www.tagblatt.ch/nachrichten/wirtschaft/Detonationen-und-Diamanten;art123834,2871621

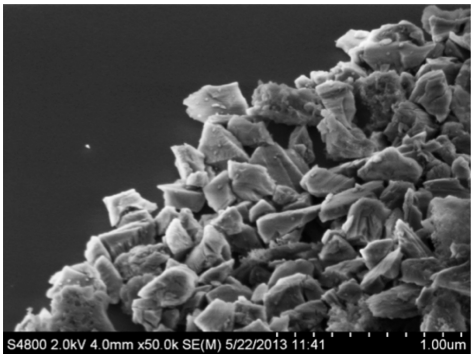

Figure 6.4.: SEM image of diamond sample STG100

[397, 398]. Surface treatment with acids and thermal oxygen etching removed surface shells of graphite and other contaminants. The resulting surfaces are predominantly oxygen terminated, favoring the negative charge state of the NV center [399, 400]. While single NV centers can be found in Tai35, Tai100 contains ensembles with up to a few hundreds of emitters per crystal. The declared mass concentration of the aqueous diamond solution was 0.1% w/v (mass/volume) for both Tai35 and Tai100.

Additionally, a sample by courtesy of H. Fedder and R. Reuter from the University of Stuttgart was used. Starting with a product[21] containing crystal sizes of up to 200 nm, more than roughly 80% of the small diamonds were removed from the sample by centrifugation. Therefore, FNDs showing stable and bright fluorescence are expected to have sizes distributed between 100 and 200 nm. The shape of the NDs is nonuniform and rather chip-shaped, as shown in the SEM image in Fig. 6.4. These FNDs predominantly contain single NV centers and will be referred to as **STG100**. The aqueous solution had a diamond concentration of 0.5 mg/ml.

Sample preparation

Two different preparation methods were applied to attach the FNDs to glass cover slips or cavity mirrors: Spin coating and drop casting. For the samples from Taiwan spin coating according to the following procedure was carried out. In a first step, the diamond solution is thoroughly mixed in an ultrasonic bath. Subsequently, the original solution is diluted in deionized water at a ratio of 1:10 000. Roughly 40 µl of an aqueous solution of 0.5% polyvinylacetat (PVA) is added to 1 ml of diamond solution, for better attachment of the crystals to the substrate's surface. Finally, about 200 µl of the final solution are dropped onto substrates with diameters on the order of 10 mm. Immediately afterwards, spin coating with around 2000 rounds per minute for 270 s is initialized. This recipe yields a suitable concentration of bright FNDs on the substrate that is both large enough to find

[21] Presumably, the starting material was a Syndia® SYP or SYP GAF submicron diamond powder with a median size of 90 or 125 nm supplied by Van Moppes. This is fractured monocrystalline diamond produced by the HPHT method. For further details consult the datasheet http://www.vanmoppes.ch/phocadownload/EN-Micron/SubMicron-GAF_EN.pdf

several emitters in a area of $(100\,\mu m)^2$, but at the same time low enough to address them individually by confocal microscopy. For the Stuttgart sample, reasonable concentrations of FNDs were obtained by directly drop casting about 10 µl of the original solution onto the substrates.

Pre-characterization measurements of the FNDs were performed with low auto-fluorescence fused silica substrates[22]. Before applying a diamond solution, they were cleaned chemically[23] and, in some cases, additionally by plasma cleaning[24].

Diamond crystal size determination

The size distribution of the diamond crystals was checked with a scanning electron microscope (SEM) for Tai35 and Tai100. For better contrast, the diamonds were spin coated onto silicon wavers following the standard preparation method. The diameter distribution was obtained by fitting circles to the encountered crystals, as shown in Fig 6.5. The determined mean diameter for Tai35 is slightly larger than the expected value of 35 nm. This might be due to the fact that it is much easier to find larger objects with the SEM, when approaching the resolution limit of the device. In the case of Tai100, this constraint can be ruled out. While most of the emitters exhibit diameters around 100 nm, a considerable amount of crystals with diameters of up to 400 nm can be encountered.

6.3. Sample characterization by confocal microscopy

STG100 sample

Prior to investigating FNDs inside the cavity, the prepared sample is characterized in the confocal microscope, i.e. the side of the substrate that supports the diamonds, faces the objective. The first confocal scan reveals, whether the prepared diamond solution yields an appropriate concentration of FNDs. Ideally, around ten emitters are found in a scan area of about $(50\,\mu m)^2$, as shown in Fig. 6.6(a), for a STG100 sample on a glass cover slip. Then, single FNDs can be addressed individually and characterized by means of a few standard measurements yielding the spectrum, lifetime, autocorrelation, and saturation behavior.

By way of example, a set of measurements for a single NV center is now discussed in more detail (NV1 shown in Fig. 6.6(a)). The recorded spectrum[25] features a broad PSB and a distinct ZPL around 640 nm confirming that the observed fluorescence is indeed originating from an NV center and no other color center (Fig. 6.6(b)). Next, the lifetime is determined by TCSPC under pulsed excitation[26]. The corresponding histogram is

[22] Hellma 665.000-QS

[23] In a solution of 1-2% Hellmanex II in deionized water, at 70-80°C for 20 minutes in the ultrasonic bath

[24] Lab-Ash 100, 180 s at 55W/2W

[25] Excitation with cw laser ligth at 532 nm with a power of 4 mW. The exposure time was 100 s.

[26] The supercontinuum source is driven at 100% with 10 MHz repetition rate. A spectral band of a few nanometeres around 532 nm is selected with the AOTF operated at maximal efficiency. The total excitation power is on the order of 1 mW. Ten data sets with an acquisition time of 10 s each were averaged for the histogram.

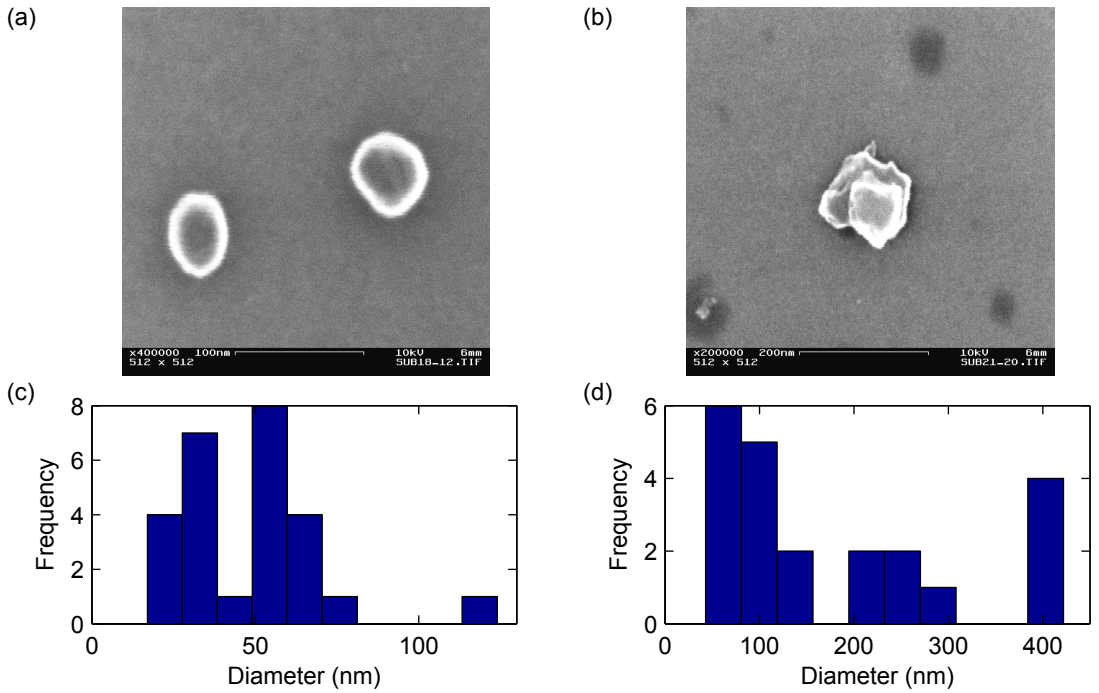

Figure 6.5.: SEM images and size distribution of diamond nanocrystals on a silicon waver of (a,c) Tai35 and (b,d) Tai100.

displayed in Fig. 6.6(c). A monoexponential fit is in very good agreement with the data and results in an observed excited state lifetime of $\tau = (32 \pm 1)\,\mathrm{ns}$. This is a first hint that the observed NV center is possibly a single emitter, since ensembles typically exhibit multi-exponential decays. The prompt peak in the beginning of the decay stems from short-lived background fluorescence. To unambiguously prove single emitter behavior, the $g^{(2)}$-function is measured[27]. Figure 6.6(d) displays the data featuring pronounced antibunching at $\tau = 0$ and correlated emission around the dip. This behavior agrees well with the theoretically expected curve for a three level model (Eq. 2.58). The exact fit function is given by

$$g^{(2)}(\tau) = 1 + p\left\{b\mathrm{e}^{-|\tau|/\tau_2} - (1+b)\,\mathrm{e}^{-|\tau|/\tau_1}\right\}, \tag{6.1}$$

where the parameter p accounts for background light. The fit results in $g^{(2)}(0) = 0.11$, an excited state lifetime of $\tau_2 = 25\,\mathrm{ns}$, and a decay time from the intermediate state of $\tau_1 = 160\,\mathrm{ns}$. The non-zero value of $g^{(2)}(0)$ is attributed to parasitic background fluorescence created in the glass cover slip.

[27] Excitation with cw laser at 532 nm at a power of 1 mW, 120 s acquisition time

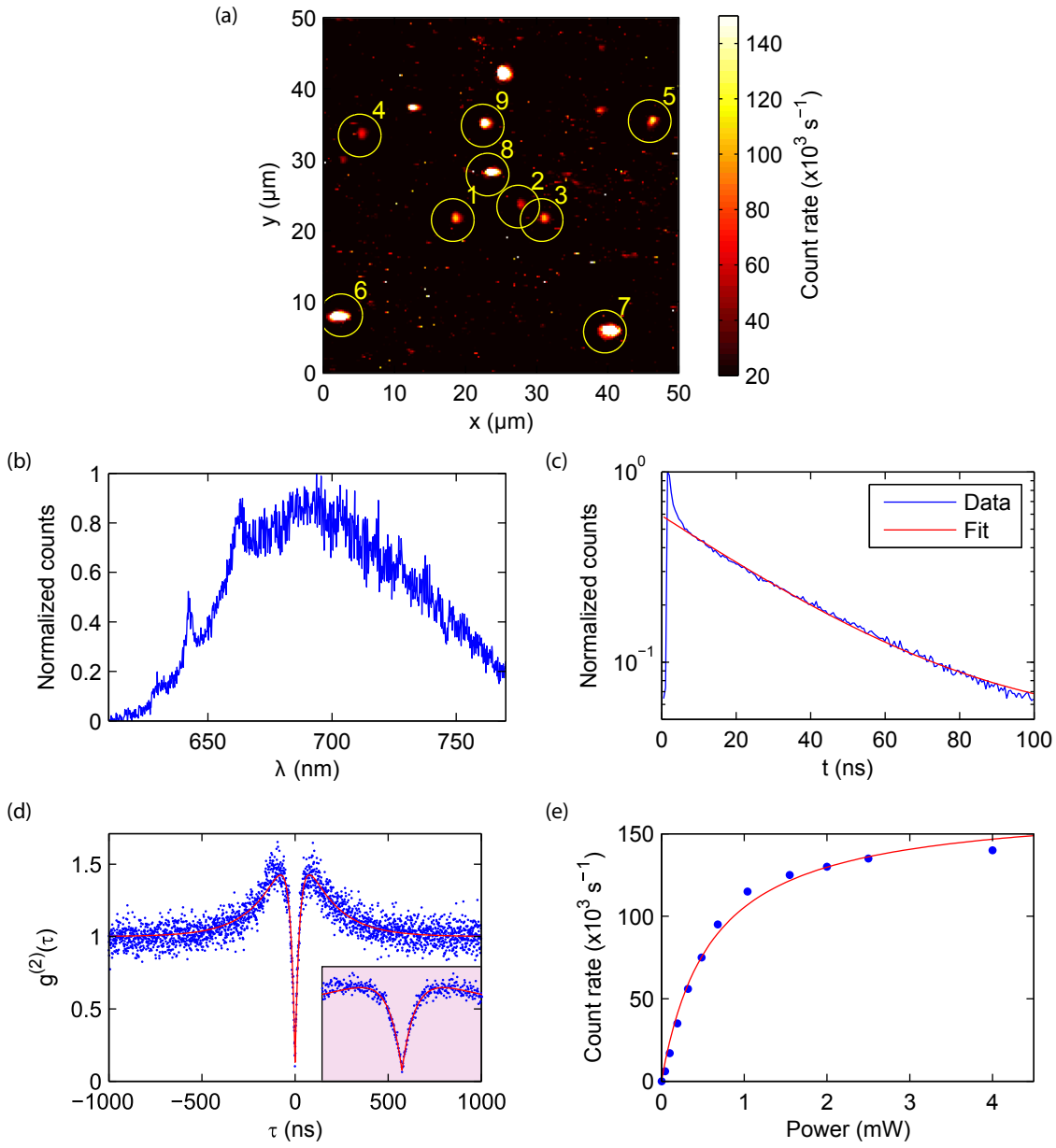

Figure 6.6.: (a) Confocal microscope scan of STG100 sample on a glass substrate. The marked FNDs are single NV centers (1-5) and emitter ensembles (6-9). Characterization measurements for NV1: (b) Fluorescence spectrum featuring a clear ZPL around 640 nm and a broad PSB typical of NV centers. (c) TCSPC histogram (blue) to determine the lifetime with a monoexponential fit (red) in good agreement, yielding $\tau = (32 \pm 1)$ ns (d) Second-order autocorrelation function (blue) with fit based on three-level model (red), resulting in $g^{(2)}(0) = 0.11$. The inset shows the time span from -150 to 150 ns in more detail. (e) Count rate as a function of the excitation power, yielding an uncorrected saturation count rate of $(1.7 \pm 0.1) \cdot 10^5\, s^{-1}$.

In order to determine the saturation count rate of the emitter, the collected photon rate is measured for varied excitation power of the cw laser with $\lambda = 532\,\mathrm{nm}$. The uncorrected count rate as a function of the excitation power P in front of the objective (NA=0.75) is shown in Fig 6.6(e). The applied fit function is derived from the expected rate of either a two- or three-level system (Eq. 2.32, Eq. 2.36)

$$R(P) = \frac{R_\infty P}{P_{\mathrm{sat}} + P}, \tag{6.2}$$

yielding $R_\infty = (1.7 \pm 0.1) \cdot 10^5\, s^{-1}$ and $P_{\mathrm{sat}} = 0.60\,\mathrm{mW}$. A linear term accounting for background does not influence the fit significantly and is therefore omitted, here.

To gain insight into the statistical distribution of the main properties of the diamond sample (single-photon purity, saturation count rate, lifetime), about 20 NV centers were analyzed. This is an important step for the later comparison with NV centers inside the cavity, since the same emitters cannot be analyzed in free space. In Fig. 6.7, the saturation count rate is plotted as a function of the single-photon purity $g^{(2)}(0)$, in order to infer the average rate of photons that is emitted per NV center. An ensemble of n NV centers inside an FND is expected to emit n times as many photons as a single NV center, i.e. the saturation count rate scales as

$$R_{\infty,n} = n \cdot R_{\infty,1}. \tag{6.3}$$

The number of emitters within an ensemble can be inferred from $g^{(2)}(0)$ (Eq. 2.55), by making use of the relation

$$n = \lfloor 1/(1 - g^{(2)}(0)) \rfloor + 1, \tag{6.4}$$

where $\lfloor x \rfloor$ symbolizes the largest previous integer or simply the floor of x. This expression for n predicts single emitters for all $0 \leq g^{(2)}(0) < 1/2$, two emitters for $1/2 \leq g^{(2)}(0) < 2/3$, and so forth. It takes account for the background fluorescence that increases $g^{(2)}(0)$. With these relations, the data can be fitted, resulting in a saturation count rate for a single NV center of $(1.5 \pm 0.1) \cdot 10^5\, s^{-1}$.

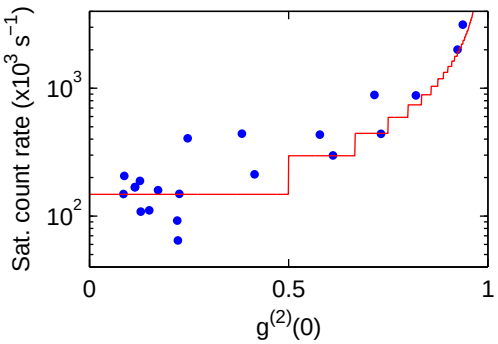

Figure 6.7.: Detected saturation count rate as a function of the single-photon purity $g^{(2)}(0)$ (blue dots), together with a fit (red line).

The observed excited state lifetimes are summarized in a histogram, as shown in Fig. 6.8. The detected lifetimes exhibit a rather broad distribution ranging from 6 to almost 36 ns, centered around 17 ns. For comparison, the same diamond sample is investigated on a mirror coated with 33 nm of silver and 20 nm of glass. Here, the liftetimes span from 4 to 24 ns, centered around 13 ns. This corresponds to a lifetime reduction by a factor of 1.3 ± 0.3 with respect to the sample on the glass substrate, as a consequence of self-interference of the dipole emission on the mirror. Note that the maximal lifetime reduction on a perfect metal mirror amounts to 1.25, when averaging over different dipole orientations [339].

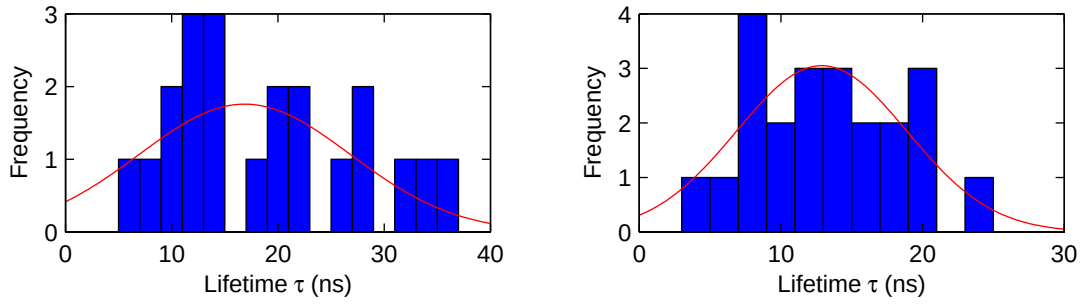

Figure 6.8.: Histogram of lifetimes τ obtained by monoexponential fits (blue), together with fits (red) for a STG100 sample on (a) a glass substrate and (b) a silver mirror.

Tai35 and Tai100 sample

In order to infer the amount of NV centers within an FND, its saturation count rate can be compared to that of single emitters. Here, we relate the count rates obtained from FNDs of the Tai100 sample, which contain emitter ensembles, to that of Tai35, which mostly contain single emitters. Two samples with either Tai35 or Tai100 NDs are first prepared on glass substrates by spin coating. Subsequently, the samples are investigated by confocal microscopy. Second-order autocorrelation measurements of the Tai35 sample reveal that more than 10% of the FNDs contain single emitters. By comparing their average saturation count rate with the fluorescence yield of Tai100 FNDs, an approximate number of 30-300 NV centers per Tai100-nanocrystal is estimated. Furthermore, the presence of negatively charged NV centers is confirmed by recording spectra. The latter do not show significant contribution of fluorescence from NV^0 for neither of the two samples. The mean excited state lifetime of Tai100 on a glass sample was determined by TCSPC under pulsed excitation resulting in $\tau = (20 \pm 4)$ ns.

7. Results

In this chapter, the experimental realization of coupling NV center fluorescence to FFPCs is discussed for two different approaches. In a first experiment, the PSB fluorescence of NV center ensembles is coupled to a high finesse cavity with dielectric mirrors in the bad emitter regime. This concept provides insight into the scaling laws of Purcell enhancement by varying both the mode volume and the quality factor over a large range. A second, complementary approach relies on NV centers coupled to utra-small mode volume FFPCs with silver mirrors, to enhance the single-photon count rate and to directly demonstrate modifications of the spontaneous emission lifetime. Finite-difference time-domain (FDTD) simulations and an analytical model shed light on the role of the ND that can provide additional field confinement and boost the obtainable Purcell enhancement. At last, cavity-enhanced fluorescence lifetime imaging is briefly presented.

7.1. Nitrogen-vacancy center ensembles in a high finesse dielectric cavity

Characterization of the setup

The cavity applied in this setup, consists of the dielectrically-coated, concave end face of a SM fiber and a dielectric, planar, macroscopic mirror coated with Tai100 NDs. The laser-machined profile on the fiber has an effective radius of curvature of $R = 100\,\mu\text{m}$ at the center of the structure. The mode waist of the cavity is $w_0 = 2.2\,\mu\text{m}$ and the effective cavity length is as small as $d_{\text{eff}} = 4.3\,\mu\text{m}$, including penetration into the dielectric coating stack. As a result, the minimal mode volume amounts to 16 μm^3 ($47\,\lambda^3$). The dielectric coatings for the fiber and the macroscopic mirror were supplied by Laser Zentrum Hannover (LZH) and by Layertec, respectively. The detailed mirror specifications can be found in Section 5.3.1. The mirror coating has been designed for maximal reflectivity for light at 780 nm. At this wavelength, the cavity finesse is as large as 30 000 for small mirror distances. Increasing the cavity length to $d_{\text{eff}} = 39\,\mu\text{m}$, reduces the finesse to 20 000. For even larger distances, the finesse drops faster, probably owing to diffraction loss, as a consequence of the finite mirror diameter. The largest quality factor is achieved at $d_{\text{eff}} = 39\,\mu\text{m}$ and reaches $Q = 2 \cdot 10^6$.

Nanodiamonds of the Tai100 sample containing bright NV center ensembles are spread on the macroscopic mirror by spin coating. The concentration of FNDs is rather low ($<0.01\,\mu\text{m}^{-2}$), to be able to address individual nanocrystals with the cavity mode. By terminating the planar mirror with a $\lambda/4$-layer of SiO_2, the maximum of the electric field is shifted slightly above the surface, to optimize the coupling of the emitter to the cavity.

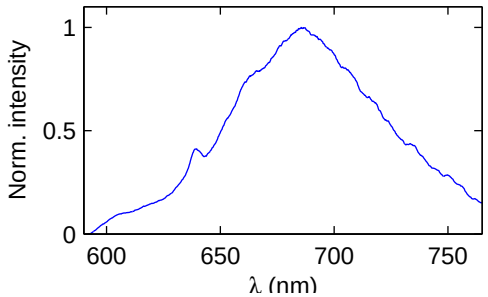

Figure 7.1.: Spectrum of the NV center at room temperature

See the specifications in Section 5.3.1 for the electric field as a function of the optical distance from the mirror substrate.

The NV fluorescence spectrum is characterized by a ZPL at 637 nm with a linewidth of about 2 THz at room temperature [29] and a broad PSB stemming from the coupling to a phonon continuum with a clear maximum of the coupling strength at a phonon frequency of around 16 THz [247]. The PSB comprises several transitions. The strength of the integrated kth sideband is given by the Frank-Condon factors for displaced harmonic oscillator states $\zeta_k = \mathrm{e}^{-D} D^k/k!$, with the Huang-Rhys factor $D = 3.2$ for NV centers in bulk diamond. The experimentally observed fluorescence spectrum of the NV center ensemble is peaking at 690 nm with a FWHM of about 70 nm, as shown in Fig. 7.1.

The applied cavity coating splits the emission spectrum into two regions: The mirrors are transmissive for wavelengths shorter than 690 nm, and the emission is affected only weakly by the cavity, i.e. close to free-space fluorescence is present. For increasing wavelengths, the mirrors become more and more reflective and cavity enhancement sets in, yielding emission into sharp resonances. Being able to observe both free-space and cavity enhanced emission at the same time, the effect of the cavity enhancement can be evaluated within a single measurement, by comparison of the two regions. An additional advantage of this approach is the much simplified search for NV centers inside the cavity, because a large part of their fluorescence is transmitted through the mirror. Furthermore, the coating of the outcoupling mirror has been designed for low reflectivity at 532 nm, $R < 3\%$, such that the excitation light experiences almost constant conditions for varied cavity length. Asymmetric mirror coatings serve to optimize the outcoupling efficiency into the detection path. To this end, the transmission of the planar mirror ($T = 60$ ppm at 780 nm) is chosen about twice as large as that of the fiber mirror ($T = 34$ ppm). Last but not least, the large variation of the reflectivity across the NV emission spectrum enables the investigation of the cavity enhancement as a function of the quality factor.

Confocal microscopy

In a first step, the sample is characterized by confocal microscopy through the rear side of the planar mirror, while the cavity fiber is still withdrawn (see Section 6.1). Confocal microscopy through the partially transparent planar mirror serves to localize

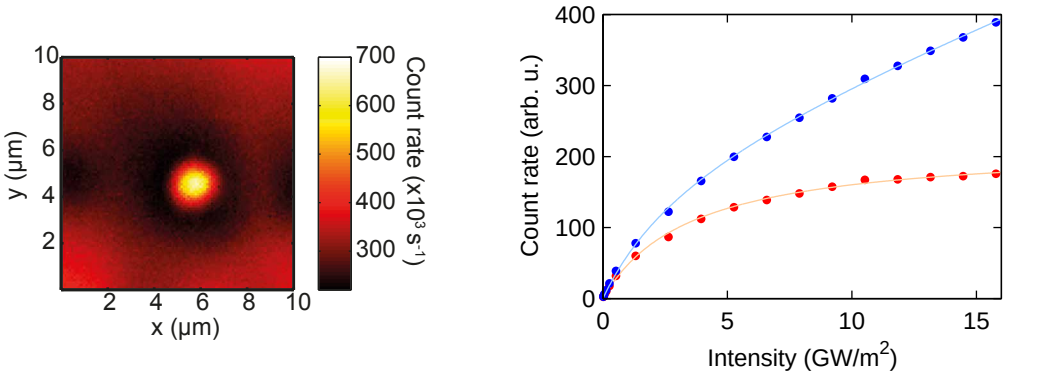

(a) (b)

Figure 7.2.: (a) Confocal scan of an individual FND with $I = I_{\mathrm{sat}}/2$. The mirror background is visible in the corners of the scan, whereas it has been bleached in the area around the emitter. (b) Saturation measurement of the free-space NV center fluorescence (blue dots), in comparison with the background corrected behavior (red dots). The fits based on the saturation model are indicated by the lines.

individual FNDs, as shown in Fig. 7.2(a). Fitting of the recorded point spread function of a single FND with a Gaussian function yields a $1/e^2$-radius of 1.1 µm, slightly larger than the value of 0.75 µm obtained when the sample faces the objective. This is a result of the reduced effective numerical aperture NA' $\approx$ NA$/n_{\mathrm{m}}$, encountered when focusing through the planar mirror, which acts as a dielectric medium with refractive index n_{m}. Furthermore, a strong contribution of background light is observed within the spectral detection window, which is presumably originating from fluorescence created in the coating stack of the mirror and the fiber, as well as from Raman scattering in the fiber. Thus, emitter ensembles (Tai100) with an increased fluorescence yield are applied to achieve a reasonable signal to background ratio. However, note that a large part of the background fluorescence can be prevented, by designing the reflectivity of the fiber coating such that excitation light does not enter the cavity fiber. In this way, single emitter experiments are feasible [78, 79]. The amount of background light can be evaluated by saturation measurements. Here, an FND with roughly 50 NV centers is chosen. The measured intensity dependence exhibits a saturation part and a linear part, originating from background fluorescence, as shown in Fig. 7.2(b). Thus, the fit function based on Eq. 6.2 includes an additional linear term:

$$R(I) = \frac{R_\infty I}{I_{\mathrm{sat}} + I} + aI. \tag{7.1}$$

The intensity $I = 2P/\pi w_{\mathrm{ex}}^2$ is inferred from the measured excitation mode waist $w_{\mathrm{ex}} = 1.5\,\mu\mathrm{m}$ and the applied excitation power P. The excitation mode waist is determined by scanning an FND through the focus, while recording the fluorescence without spatial

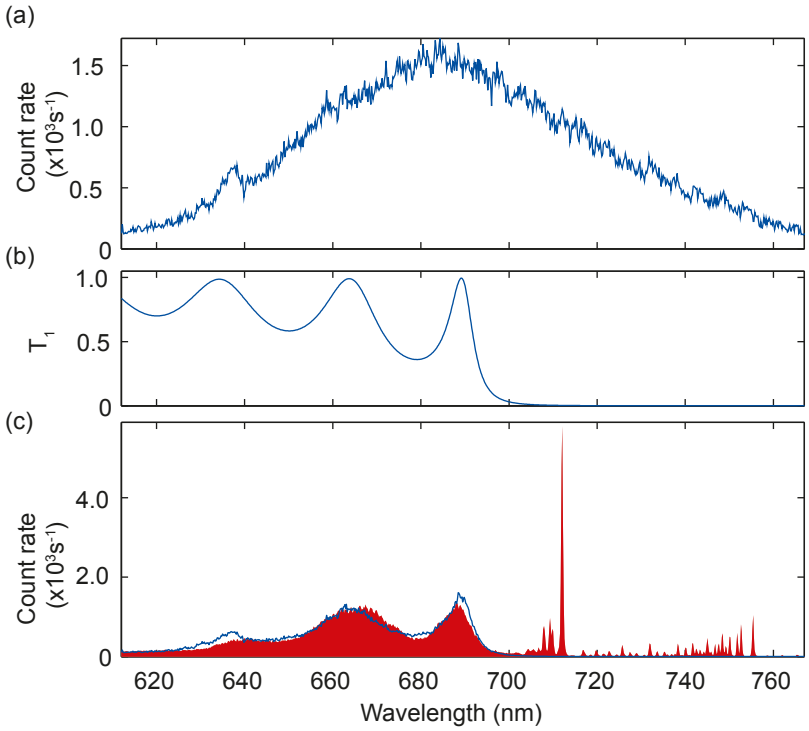

Figure 7.3.: (a) Free-space spectrum of an NV center ensemble (Tai100) on a glass substrate (b) Calculated transmission spectrum of the planar macroscopic mirror (c) Emission spectrum of an FND inside the cavity (red). The transmissive part can be understood as the product of the free-space spectrum and the mirror transmission (blue).

filtering. The fit results in a saturation intensity of $I_{\mathrm{sat}} = 3.5\,\mathrm{GWm}^{-2}$, agreeing with typical literature values [221], and a background ratio of 20% in the regime where the fluorescence increases linearly with the excitation intensity. The subsequent measurements have been background corrected. Finally, the fluorescence lifetime of FNDs is investigated by TCSPC under pulsed excitation. Values ranging from 16 to 23 ns are measured, which is rather short for NDs, but can be attributed to a reduced lifetime due to a modified density of states on the mirror. In summary, the spectra, saturation, and lifetime measurements assure that it is indeed NV center fluorescence that is coupled to the cavity.

Cavity measurements

In a next step, the modified emission spectrum of an FND inside the cavity is studied. To this end, the ensemble with about 50 NV centers is studied once more. After positioning the FND into the focus of the objective, the cavity fiber is aligned for optimal overlap of the fundamental cavity mode with the emitter. A spectrum characteristic

for this situation is displayed in Fig. 7.3(c), together with a free-space spectrum taken on a glass substrate with negligible background (Fig. 7.3(a)), and the calculated transmission curve of the outcoupling mirror $T_1(\lambda)$ (Fig. 7.3(b)). Multiplying the free-space spectrum with $T_1(\lambda)$ and scaling with a constant factor, provides a good approximation to the short-wavelength part of the emission spectrum modulated by the cavity. Enhanced emission into sharp cavity resonances is observed within the stop band of the mirror coating. Two neighboring fundamental modes at $\lambda_1 = 715\,\mathrm{nm}$ and $\lambda_2 = 755\,\mathrm{nm}$ dominate the spectrum. Furthermore, a series of weak higher-order transverse modes show up. The effective cavity length is determined by the position of the fundamental modes $d_{\mathrm{eff}} = \lambda_1\lambda_2/\left[2(\lambda_2 - \lambda_1)\right] = 6.75\,\mu\mathrm{m}$ and includes the penetration of the cavity mode into the coating stack. A simulation based on the matrix method predicts an overall penetration into the coating at the denominated wavelengths that adds up to $1.5\,\mu\mathrm{m}$. The separation of the higher-order transverse modes can be harnessed to evaluate the effective radius of curvature of the concave fiber mirror using the relation $\Delta\lambda_{nm} = \lambda^2 \arccos\left(\sqrt{1 - d_{\mathrm{eff}}/R}\right) / \left(2\pi d_{\mathrm{eff}}\right)$ [50]. A value of $R = 100\,\mu\mathrm{m}$ is inferred, which is in good agreement with measurements of the fiber profile by white light interferometry. With the knowledge of the effective radius, the mode waist and volume can be calculated within the paraxial approximation (Eqs. 3.41 and 3.43). Because the effective cavity length is much smaller than the effective radius $d_{\mathrm{eff}} \ll r$ and $w_0 \gg \lambda/2$, the approximation exhibits a high precision.

Effective Purcell factor

The experimental setting corresponds to emitter-cavity coupling in the bad emitter regime. In this situation, the emission is distributed over a broad spectrum $S(\lambda)$, with the spectral width $\delta\lambda_{\mathrm{em}}$ being much larger than the cavity full linewidth $\delta\lambda$. Thus, only a fraction of $\delta\lambda/\delta\lambda_{\mathrm{em}}$ of the emission couples to the cavity. In this limit, the effective Purcell factor (inferred from Eq. 4.32) is governed by the quality factor of the emitter, as can be easily seen from

$$C_{\mathrm{eff}} \approx \eta_\lambda \frac{\delta\lambda}{\delta\lambda_{\mathrm{em}}} C = \frac{3\lambda_0^3}{4\pi^2} \frac{Q_{\mathrm{em}}}{V} \eta_\lambda \left| \frac{\vec{\mu}\vec{E}(\lambda_0)}{\mu E_0(\lambda_0)} \right|^2 , \tag{7.2}$$

with the wavelength of the cavity resonance λ_0 and $\eta_\lambda = S(\lambda_0)/\max(S)$ accounting for the detuning from the maximum of the spectrum.

The effective Purcell factor is determined experimentally by comparison of three background corrected spectra:

1. A typical free-space reference spectrum $S_0(\lambda)$ that is recorded for FNDs on a glass sample facing the objective

2. A spectrum that is emitted from the investigated FND on the planar cavity mirror facing the cavity fiber $S_{\mathrm{m}}(\lambda)$

3. A spectrum of the same emitter inside the cavity $S_{\mathrm{c}}(\lambda)$

The expected free-space spectrum of the studied FND is approximated by a scaled reference spectrum $S_{\mathrm{fs}}(\lambda) \approx b \cdot S_0(\lambda)$. The scaling factor b is determined by least square fitting of the spectrum recorded through the mirror $S_{\mathrm{m}}(\lambda)$ to $b \cdot T_1(\lambda) S_0(\lambda)$. The transmission of the planar mirror $T_1(\lambda)$ is obtained from a direct measurement and is additionally simulated by the matrix method. The total emission into the strongest cavity resonance $P_{\mathrm{c}} = \int_{\lambda_0-\Delta}^{\lambda_0+\Delta} S_{\mathrm{c}}(\lambda)\mathrm{d}\lambda$ can then be compared to the integrated emission expected in free space $P_{\mathrm{fs}} = \int_{\lambda_1}^{\lambda_2} S_{\mathrm{fs}}(\lambda)\mathrm{d}\lambda$, with an integration range Δ of three resonance linewidths (FWHM) around the resonance peak, and choosing $\lambda_1 = 590\,\mathrm{nm}$, $\lambda_2 = 770\,\mathrm{nm}$ to integrate over the entire NV spectrum.

Since the Purcell factor relates the emission into a particular cavity mode to the free-space emission into the whole solid angle, it is necessary to account for the varied collection efficiency in each case. To evaluate the free-space emission, it has to be considered that the presence of the Bragg mirror and the substrate modify the emission pattern. This is a result of self-interference of the emitting dipole. Analytical and FDTD simulations are applied to account for this effect. Increased emission into the dielectric medium which is beyond the critical angle is not collected, since no immersion liquid is used in this experiment. For the transmissive part of the spectrum, the angular distribution of the emission within the NA (0.55) of the objective is hardly affected by the refraction through the mirror stack and the substrate. The averaged excited state lifetime does not change considerably, either. As a result, the collection efficiency is estimated from the free-space dipole emission pattern, the effective solid angle of the objective inferred from the observed point spread function, and the angle dependent transmission coefficient. Weighting with a distribution of dipole orientations, which will be explained in more detail below, results in an overall collection efficiency of $\eta_\Omega = 0.05$.

Next, the probability of a photon emitted into the cavity to leave through the macroscopic mirror (see Eq. 3.22) is evaluated at the spectral position of the resonance $\lambda_0 = 710\,\mathrm{nm}$. The measured values for the mirror loss $L_1 = 23\,\mathrm{ppm}$, $L_2 = 71\,\mathrm{ppm}$, and the transmission $T_1(\lambda_0) = 1900\,\mathrm{ppm}$, $T_2(\lambda_0) = 810\,\mathrm{ppm}$ obtained from the coating simulation, yield a probability of $\eta_{\mathrm{c}} = 0.68$. Additional loss in the detection path, as well as the detection efficiency is assumed to be equal for the free-space and cavity setup and thus cancel out in the comparison.

In total, the effective Purcell factor is experimentally determined by

$$C_{\mathrm{eff}}(\lambda_0) = \frac{P_{\mathrm{c}}(\lambda_0)}{P_{\mathrm{fs}}} \frac{\eta_\Omega}{\eta_{\mathrm{c}}}. \tag{7.3}$$

A value of $C_{\mathrm{eff}} = (6 \pm 2) \cdot 10^{-3}$ is evaluated from the spectra shown in Fig. 7.4(a). The error is determined from systematic uncertainties of the applied evaluation method, predominantly owing to a variation of the spectra of different FNDs and to an alignment and wavelength dependent collection efficiency. Due to the low effective Purcell factor, TCSPC under pulsed excitation with and without the cavity did not show significant modifications of the excited state lifetime.

For comparison of the experimentally determined value (Eq. 7.3) to theory (Eq. 7.2),

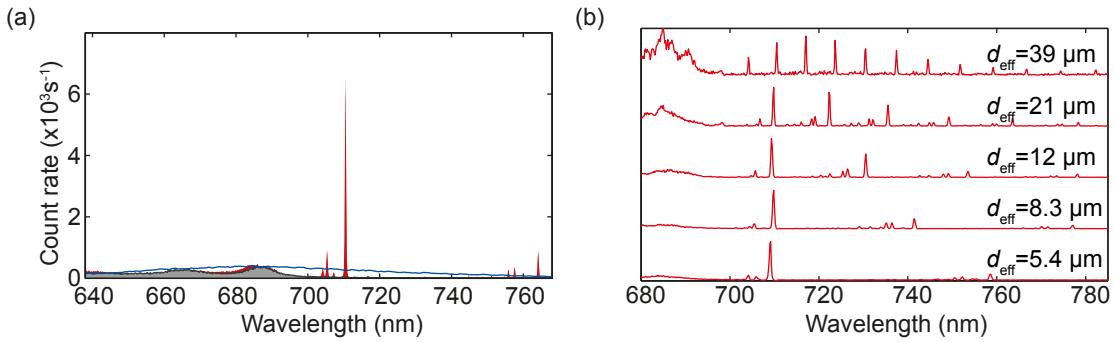

Figure 7.4.: (a) Comparison of spectra of an FND, inferred for free-space conditions (S_{fs}, blue), through the mirror (S_{m}, gray), and inside the cavity with $d_{\mathrm{eff}} = 5.0\,\mu\mathrm{m}$ (S_{c}, red). (b) Series of normalized sample spectra for decreasing cavity length from $d_{\mathrm{eff}} = 39\,\mu\mathrm{m}$ (top) to $d_{\mathrm{eff}} = 5.4\,\mu\mathrm{m}$ (bottom).

the influence of the term $\eta_\lambda \left|\vec{\mu}\vec{E}(\lambda_0)/\mu E_0(\lambda_0)\right|^2$ is estimated. The detuning from the maximum of the NV spectrum results in a decreased coupling by a factor $\eta_\lambda = 0.75$, which is determined from the reference spectrum. In the investigated spectral region, the spatial position of the standing-wave maximum shifts from the position of the emitters at the center wavelength towards the mirror coating for shorter wavelengths. Consequently, the coupling is reduced, especially close to the edge of the stop band of the mirror where the dispersive character of the coating results in a phase shift. At the position of the resonance, at $\lambda_0 = 710\,\mathrm{nm}$, the coating parameters yield $\eta_E = (E/E_0)^2 = 0.55$. Furthermore, the effect of the fixed but randomly oriented dipoles is considered. The excitation was performed by using circularly polarized light and below-saturation power. Thus, the angle dependence of the excitation probability $\left(\vec{\mu}\vec{E}\right)^2 \propto \cos^2(\theta)$ results in a normalized distribution $p(\theta) = 3/2\,\cos^2(\theta)$, with the angle between the dipole axis and the mirror θ. The observed average enhancement is therefore reduced by a factor $\eta_\theta = \int p(\theta)\cos^2(\theta)\cos(\theta)\mathrm{d}\theta = 0.8$. Altogether, Eq. 7.2 is modified to

$$C_{\mathrm{eff}} = \frac{3\lambda_0^3}{4\pi^2}\frac{Q_{\mathrm{em}}}{V}\eta_\lambda\eta_\theta\eta_E, \tag{7.4}$$

to match the experimental conditions. With the parameters of this measurement, i.e. $V = 19\,\mu\mathrm{m}^3$, $Q_{\mathrm{em}} \approx 10$, the theoretical value of the effective Purcell factor amounts to $C_{\mathrm{eff}} = (5 \pm 2)\cdot 10^{-3}$, in good agreement with the experimental finding.

The scaling behavior of the effective Purcell factor is explicitly demonstrated as a function of the mode volume. To this end, its value is determined for the strongest cavity resonance for varied cavity length in a set of measurements like the one shown in Fig. 7.4(a). Some sample spectra are displayed in Fig. 7.4(b). The result of the full data set is summarized in Fig. 7.5, illustrating the very good agreement with the theory according to Eq. 7.2. The theoretical curve predicts significant Purcell enhancement,

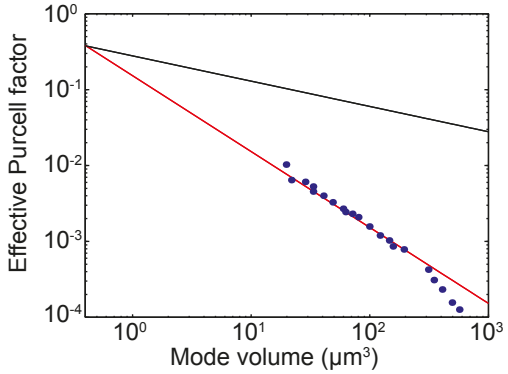

Figure 7.5.: Effective Purcell factor as a function of the mode volume illustrating the scaling behavior in the bad emitter regime. The experimental values (blue dots) stemming from the strongest cavity resonance at $\lambda_0 = 710\,\mathrm{nm}$ are in good agreement with theory (red line). For comparison, the ideal Purcell factor (Eq. 4.32) divided by a factor 100 is added (black line).

i.e. $C_{\mathrm{eff}} \approx 1$, for mode volumes on the order of $1\lambda^3$ ($\approx 0.34\,\mu m^3$). This is exactly the regime that is investigated with the ultra-small mode volume silver cavities discussed in Section 7.2.

Ideal Purcell factor

Opposed to the moderate effective Purcell factors achievable for this system, the ideal Purcell factors can be formidable. Only a small fraction of the totally emitted fluorescence is coupled to the resonator. However, the spectral density of light emitted into the cavity resonance is strongly enhanced. The ideal Purcell factor C is directly given by the ratio of the spectral density for the cavity and the free-space situation. This can be imagined as resonantly coupling a spectral element of the emission with Fourier-limited width to the cavity, which consequently experiences the full (ideal) Purcell enhancement. Due to the large variation of the mirror coating transmission across the emission spectrum, the enhancement can be investigated in dependence of the quality factor of the cavity. By varying the cavity length, the cavity resonance can be positioned at any wavelength, resulting in a modification of the quality factor over almost three orders of magnitude.

Example spectra for the stepwise tuning of the cavity length over one free spectral range are shown in Fig. 7.6(a). Here, the cavity length was at its minimum $d_{\mathrm{eff}} = 4.3\,\mu\mathrm{m}$, corresponding to the longitudinal cavity mode with eight antinodes between the mirrors. In addition, a single spectrum is shown in Fig. 7.6(b) that illustrates the situation for the same cavity geometry and excitation conditions, but a larger cavity length with $d_{\mathrm{eff}} = 39\,\mu\mathrm{m}$. In this case, several neighboring fundamental modes between 700 and 800 nm are visible within the stop band of the mirror, which sample different quality factors within a single measurement.

The ideal Purcell factor is evaluated by comparison of the maximal spectral density on

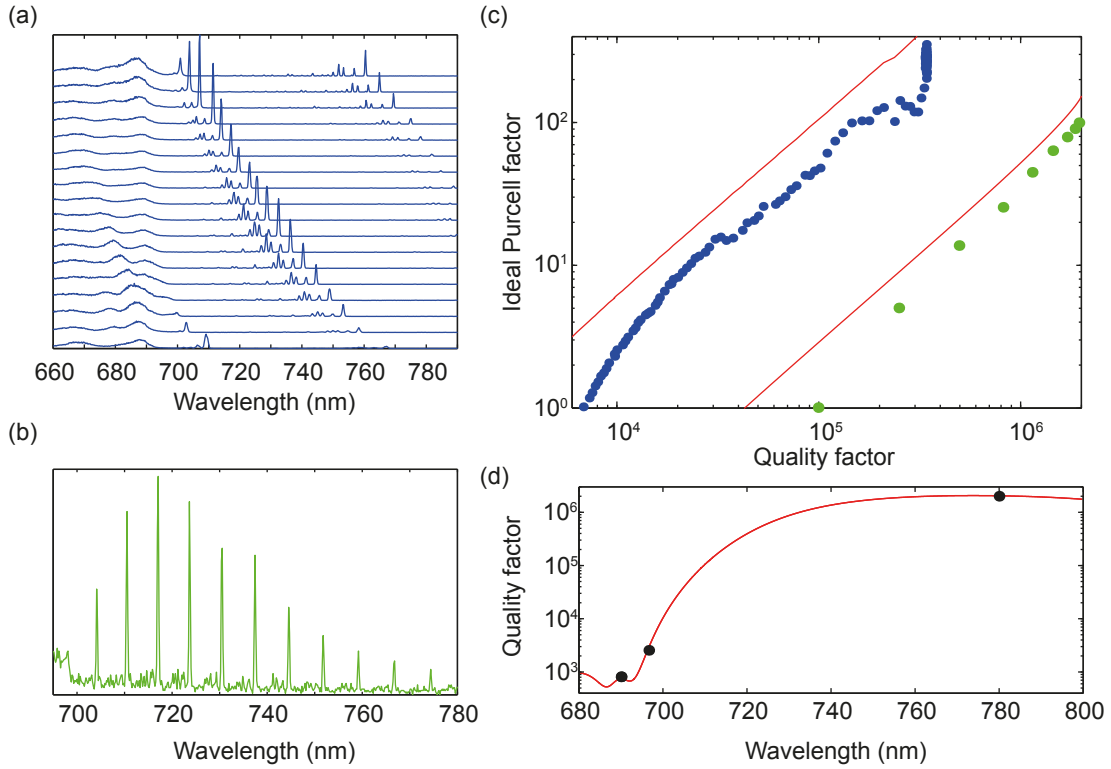

Figure 7.6.: (a) Spectra containing a single resonance tuned across the accessible NV spectrum, starting at the minimal cavity length $d_{\text{eff}} = 4.3\,\mu\text{m}$ (top). (b) Cavity spectrum with several resonances recorded for $d_{\text{eff}} = 39\,\mu\text{m}$. (c) Scaling of the ideal Purcell factor as a function of the quality factor for the data sets partially shown in (a) (blue dots) and (b) (green dots), together with the theoretical predictions of Eq. 4.32 (red lines). (d) Measured (black dots) and calculated (red line) quality factor as a function of the wavelength for $d_{\text{eff}} = 39\,\mu\text{m}$.

resonance $S_{\mathrm{c,max}}(\lambda_0)$ with the free-space value at the identical wavelength $S_{\mathrm{fs}}(\lambda_0)$. The linewidth of the cavity resonance is beyond the spectral resolution of the spectrometer. Therefore, the peak spectral density is inferred from the integrated emission into the resonance P_{c}, by assuming a Lorentzian resonance shape, yielding $S_{\mathrm{c,max}} = 2P_{\mathrm{c}}/\pi\delta\lambda$. The cavity linewidth is given by $\delta\lambda = \lambda_0^2 (T_1 + T_2 + L_1 + L_2)/4\pi d\sqrt{R_1 R_2}$, with the reflectivity $R_i = 1 - T_i - L_i$. It is determined with a simulation of the wavelength-dependent coating transmission and by several measurements. For instance, for maximal finesse, at $\lambda_0 = 780\,\mathrm{nm}$, the cavity linewidth, and thus the quality factor $Q = \lambda_0/\delta\lambda$, is measured with a narrow-band diode laser. Lower quality factors are determined by using broad band light and the spectrometer. The quality factor $Q(\lambda)$ predicted by the simulation is in good agreement with the measured values, as shown in Fig. 7.6(d). The free-space spectrum and the corrections accounting for the collection efficiency and the mirror loss are treated in analogy to the calculus of the effective Purcell factor. In summary, the ideal Purcell factor is experimentally obtained from the relation

$$C = \frac{S_{\mathrm{c,max}}}{S_{\mathrm{fs}}} \frac{\eta_\Omega}{\eta_{\mathrm{c}}}. \tag{7.5}$$

The inferred values of the ideal Purcell factor as a function of the quality factor are shown in Figure 7.6(c), comprising the data points evaluated from the spectra of Fig 7.6(a,b). Like before, the theory includes η_E and η_θ. The detuning factor η_λ cancels out, since both spectral densities $S_{\mathrm{c,max}}$ and S_{c} are evaluated at the identical wavelength. At minimal cavity length $d_{\mathrm{eff}} = 4.3\,\mu\mathrm{m}$ where $Q = (3.5 \pm 0.3) \cdot 10^5$, the measurements result in a maximal Purcell factor of 300 ± 100, which is among the largest reported values. Remarkably, the maximal cavity finesse, and thus the quality factor, is only slightly distorted ($<20\%$) by the presence of a nanocrystal, as can been seen in Fig. 7.7.

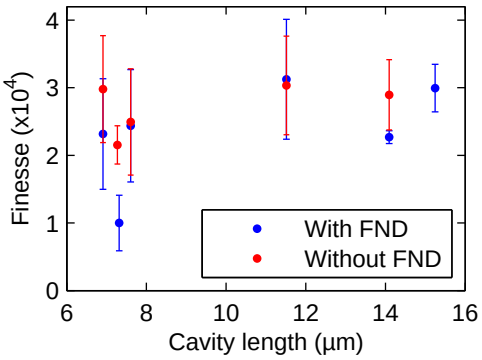

Figure 7.7.: Cavity finesse measured with (blue) and without (red) FND inside the cavity.

Rate Model

For a coherent ensemble, the individual emitters form a collective dipole, increasing the collective coupling strength to $g_N = \sqrt{N} g_0$, with the number of emitters N. However,

for the present situation, the coupling of multiple emitters to the cavity does not yield a modified coupling rate. Strong dephasing limits the collective enhancement that can be quantified by the figure of merit $\alpha = NR/\gamma^*$, which compares the enhanced emission rate under ideal conditions with the dephasing rate [401]. Dynamics are modified for $\alpha > 0.1$. Since we evaluate $\alpha \sim 10^{-3}$ for the parameters of this experiment, no collective effects are expected.

In order to model our experiments more accurately, the free-space spectrum $S_0(\omega)$ is now fitted by a sum of Lorentzians with effective widths γ_k^* and transition strengths ζ_k, based on the theoretical considerations of Section 4.3.3. All other quantities are determined by measurements. The fit yields $\zeta_k = [0.02, 0.25, 0.44, 0.24, 0.06, 0.01]$ THz and $\gamma_k^* = 2\pi \cdot [3, 23, 25, 29, 34, 40]$ THz, with $\omega_k = 2\pi(470 - k \cdot 16)$ THz. Contributions for transitions for $k > 5$ are negligible. The large discrepancy between the dephasing rates of the ZPL and the PSB stems from different phonon interaction mechanisms. While the ZPL interacts with thermally excited low-frequency phonons, the PSB transitions couple to a structured phonon continuum extending up to the cutoff at ~ 40 THz [247]. In addition, the width of the bands grows with k, as a result of the increasing possible phonon decay paths.

Applying the experimental parameters corresponding to Fig. 7.4(a) to the model, yields an effective Purcell factor of $C_{\text{eff}} = (6 \pm 2) \cdot 10^{-3}$ (according to Eq. 4.40). This is in good agreement with the value previously determined from the data. The deviation of the fitted transition strengths from the Frank-Condon factors might partially be due to a wavelength dependent collection efficiency of the setup. This may involve an error of up to 20% for the Purcell factors determined by the experiment and both theoretical models.

In conclusion, the description of the Purcell enhancement based on the rate model proves that the simple treatment based on the effective quality factor that is limited by the emitter (Eq. 7.2), is a valid approximation, as long as the effective dephasing is dominant over all other rates, i.e. the structure of the phonon sideband stays obscured. Furthermore, the model illuminates the effect of different transition branching and dephasing.

7.2. Nitrogen-vacancy centers in ultra-small mode volume silver cavities

The effective quality factor and thus the Purcell factor is bounded above by the lower of the two quality factors Q_{cav} and Q_{em}, as discussed in Section 4.3. For broad-band emitters with low Q_{em}, it is thus unrewarding to use high-Q cavities, when aiming at large Purcell enhancement. When Q_{cav} surpasses Q_{em}, the increasing density of state of the cavity is nullified by the decreasing spectral band that gets enhanced. Even though the spectral purity of the photons leaving the cavity increases, the effective Purcell enhancement stagnates. This behavior is illustrated in Fig. 7.8(a) where the effective Purcell factor is given as a function of the quality factor of the cavity for different values of the mode volume spanning from $0.2\lambda^3$ to $2\lambda^3$. For this example, $Q_{\mathrm{em}} = 8$, as estimated from the linewidth of the emission spectrum of the NV center at room temperature (see Fig. 1.1(b)). While the mode volume has a dramatic effect on the effective Purcell factor, the influence of an increasing cavity quality factor becomes negligible for values larger than about 50. To boost the Purcell enhancement of broad-band emitters, cavities with ultra-small mode volumes are therefore required. The cavity quality factors can be chosen moderate.

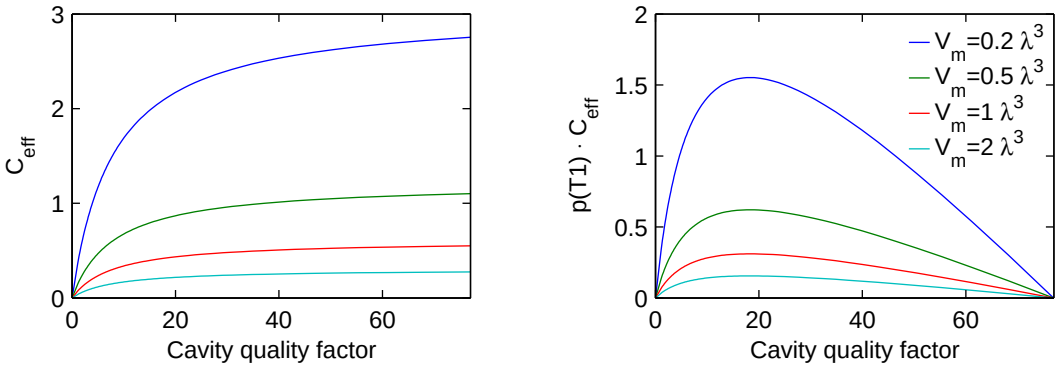

(a) (b)

Figure 7.8.: (a) Effective Purcell factor and (b) effective Purcell factor multiplied with the probability of a photon to leave through the mirror as a function of the cavity quality factor for different mode volumes (legend see (b)).

However, for practical applications like single-photon sources, large photon rates are often prioritized to large effective Purcell factors. The photon rate that is coupled out from a Fabry-Pérot resonator is proportional to the product $C_{\mathrm{eff}} \cdot p(T_1)$, i.e. to the effective Purcell factor and the probability to transmit through the outcoupling mirror, which decreases with increasing cavity quality factor (Eq. 3.22). Thus, there is a clear maximum of the photon rate, when evaluated as a function of the cavity quality factor. This is shown in Fig. 7.8(b), for the same parameters as before. The maximal photon rate is obtained for quality factors around 20. Note, that the quality factor is equal to the

cavity finesse for the fundamental cavity resonance with longitudinal mode order $q = 1$ (Eq. 3.27).

7.2.1. Plane-concave silver cavity

Cavity characterization

The microcavity used in this experiment is assembled of a laser machined, silver-coated fiber and a macroscopic, plane silver mirror with STG100 NDs. The fiber tip is tapered to allow for sub-micron mirror distances and has a concave profile with a radius of curvature $R = 90\,\mu\text{m}$, a diameter $D = 7\,\mu\text{m}$ and a depth t below 100 nm (see Fig. 5.12(c) and Fig. 5.9). To realize minimal mode volumes, a compromise has to be made between the size of the radius of curvature and the smallest achievable mirror separation, since a small radius requires a deep profile. To be able to study the regime where the diamond crystal provides additional field confinement, small mirror separation is prioritized, making a compromise on the radius of curvature. The mirror is prepared on a fused silica substrate coated with 33 nm of silver and capped with 20 nm of glass to prevent oxidation. A transmission T_1 of 15% at 532 nm is measured, in good agreement to a value of 16 % simulated with the matrix method. The latter furthermore yields $T_1 = 8\%$, $R_1 = 88\%$, and $A_1 = 4\%$ at 692 nm, The silver coating of the fiber has a thickness of 60 nm and is also capped with 20 nm of glass. A reflectivity of $(92 \pm 2)\%$ is measured at 532 nm, compared to a theoretical value of 92%. Simulations result in $R_2 = 96\%$, $T_2 = 0.8\%$, and $A_2 = 3\%$ at 692 nm. These parameters amount to expected finesse values of 18 at 532 nm and 37 at 692 nm, slightly below the measured values of 21 ± 1 and 42 ± 1, respectively (see Fig. 5.22). The probability of a photon to leave the cavity through the planar mirror is $p(T_1) = 51\%$ at a wavelength of 692 nm.

To determine the mode volume $V = \pi w_0^2 d/4$, the optical cavity length d and the mode waist w_0 are measured individually. The optical cavity length of a plano-concave cavity is given by $d = (q + \zeta/\pi)\,\lambda/2 \approx q\lambda/2$, for a radius of curvature $R \gg d$ (Eq. 3.49), where q denotes the longitudinal mode order and $\zeta = \arccos\left(\sqrt{1 - d/R}\right)$ the Gouy phase. By recording the cavity transmission under broadband illumination with the spectrometer, d is obtained from the separation and location of the resonances, as shown in Fig. 7.9. The mode order can be determined, for instance, from the change of the resonance wavelength $\Delta\lambda$, when the cavity length is shifted by Δz, by means of the simple relation $q = 2\Delta z/\Delta\lambda$. In this way, it is confirmed that the shortest possible cavity length $d = \lambda_0/2$ is actually reached without touching the planar mirror with the fiber tip, i.e. full tunability is preserved even for the fundamental resonance, with the longitudinal mode order $q = 1$.

Note that the geometrical mirror separation $d_0 = [q + (\zeta - \phi)/\pi]\,\lambda/2$ is shorter than the optical cavity length d, since the field penetrates into the glass capping layer and the silver mirror featuring a finite conductivity. An average deviation of the reflection phase from π, $\phi = \pi - (\phi_1 + \phi_2)/2$ may take this into account. For the mirrors used here, $\phi_1 \approx \phi_2 \approx 0.72\pi$ at $\lambda = 700$ nm [402], such that the air gap amounts to $d_0 \approx 260$ nm for $q = 1$. Certainly, this value is reduced further, as a result of an increased effective refractive index, when a ND is located inside the cavity mode.

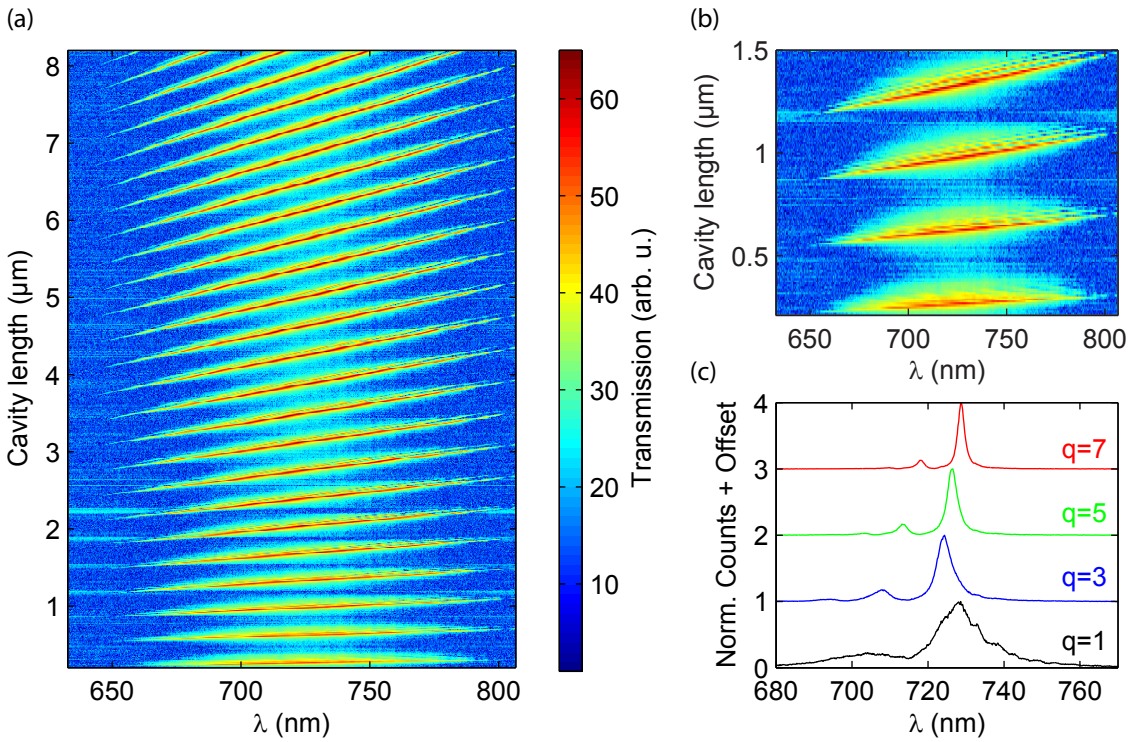

Figure 7.9.: (a) Series of cavity transmission spectra as a function of the cavity length obtained under broadband illumination. (b) Close-up of the last four resonances in (a) illustrating tunability down to $\lambda_0/2$. (c) Individual spectra from (a) for different longitudinal mode orders q.

The mode waist $w_0 = \sqrt{\lambda/\pi \cdot \sqrt{Rd - d^2}}$ (Eq. 3.41) is inferred from the observed size of the point spread function w_{det} in a cavity-enhanced fluorescence image which is obtained by scanning the cavity over a point-like object, such as a single NV center and collecting the fluorescence emitted into the cavity (Fig. 7.10(a,b)). The point spread function is the product of the cavity mode for emission w_0 and excitation $w_{\mathrm{ex}} = \sqrt{\lambda_{\mathrm{ex}}/\lambda}\, w_0$. The $1/e^2$-radius of the point spread function is determined by $w_{\mathrm{det}} = w_{\mathrm{ex}} w_0 / \sqrt{w_{\mathrm{ex}}^2 + w_0^2}$, providing a way to evaluate w_0. The excitation was performed at $\lambda_{\mathrm{ex}} = 532\,\mathrm{nm}$ through the cavity fiber, the collected fluorescence from the NV center is distributed around $\lambda = 690\,\mathrm{nm}$. The size of the point spread function was measured for different cavity lengths spanning from around 1 to 9 µm, yielding the mode waist and volume. Comparison with the values for w_0 and $V = \lambda d\sqrt{dR - d^2}/4$ expected from the previously determined radius of curvature of the concave fiber mirror are in good agreement to the data (Fig. 7.10(c)), and strongly suggests that a minimal mode volume $V = 1.0\,\lambda_0^3 = 0.34\,\mu\mathrm{m}^3$ and mode waist $w_0 = 1.1\,\mu\mathrm{m}$ are realized at $d = \lambda_0/2$.

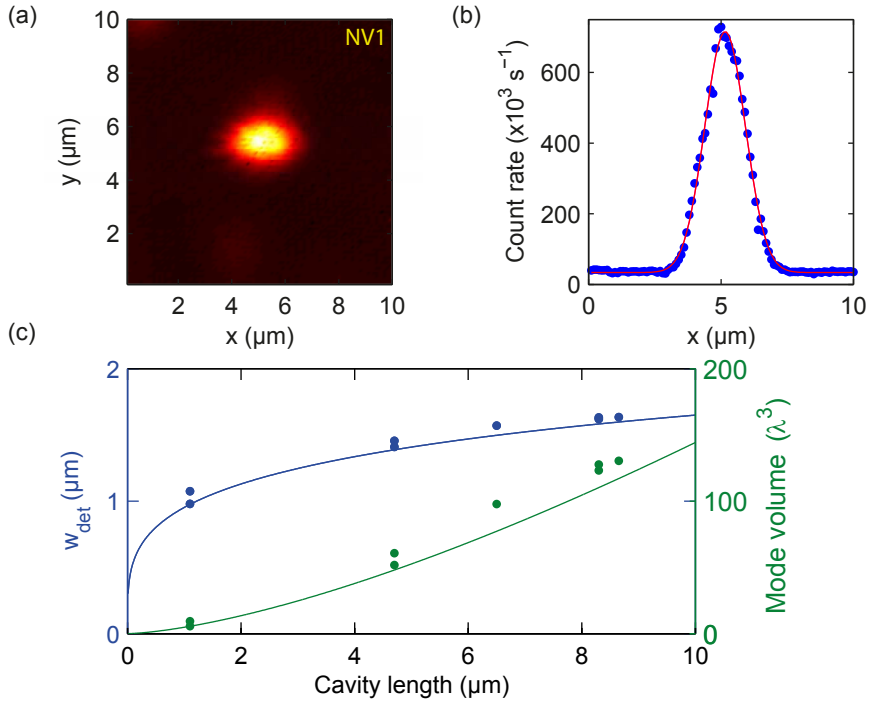

Figure 7.10.: (a) Cavity-enhanced fluorescence scan at a cavity length of 1.1 µm, showing a single NV center. (b) Vertical cut through the scan in (a), together with a Gaussian fit, resulting in $w_{\mathrm{det}} = 1.1\,\mu\mathrm{m}$. Note the large uncorrected peak count rate. (c) Measured width of the point spread function w_{det} (blue dots) as a function of the cavity length and thereof derived mode volume (green dots), together with the theoretical values obtained from the radius of curvature of the fiber mirror (lines).

Simulation of the expected count rate as function of the cavity length

The number of photons emitted into the cavity mode critically depends on the cavity length d, since both fluorescence and excitation light are subject to cavity modulation, for our experimental configuration. Thus, the normalized expected count rates are evaluated as a function the cavity length, as shown in Fig. 7.11(a) where the parameters of the currently discussed cavity-emitter system[1] have been used. The NV center spectrum is approximated by a Gaussian distribution whose width is given by the emitter quality factor Q_{em}, as shown in Fig. 7.11(b). The transmission of the Fabry-Pérot cavity is modeled as a sum of individual Lorentzians, located at $\lambda_i = 2d/i$, with $i = 1, 2, ..., 20$, and their width is determined by the cavity quality factor $Q_i = 2\mathcal{F}d/\lambda_i$. The product of the NV center spectrum with the cavity transmission yields the collectable emission spectrum, and the integration over the whole spectral band gives a measure for the relative count rates for constant excitation power. In practice, the excitation light will also be subject to cavity modulation. The modulation of the excitation power is implemented by weighting the sum over the emission spectrum with the cavity transmission at a certain excitation wavelength or with the cavity transmission integrated over a spectral excitation band. Purcell enhancement can be included by multiplication with the effective Purcell factor C_{eff}, according to Eq. 4.36. Altogether, three different cases are considered: Excitation at a single wavelength, broad-band excitation, and excitation with constant power, as it would be the case if the cavity mirrors would not affect the excitation light, at all.

For excitation at a single wavelength, here $\lambda = 532\,\mathrm{nm}$, the largest count rate is not obtained for the shortest cavity length, because the excitation light is then blocked by the cavity. A clear count rate maximum appears at a cavity length of $d = 1.1\,\mu\mathrm{m}$, which is the shortest mirror spacing where both excitation (longitudinal mode order $q = 4$) and fluorescence ($q = 3$) are in resonance with the cavity. In contrast, for broad-band excitation spanning from $\lambda = 525$ to $575\,\mathrm{nm}$, the largest count rates are expected at shortest cavity length, as a result of the growing influence of Purcell enhancement. However, count rates for $q = 2$ are still low. For ideally constant excitation, the count rate maxima continously increase with decreasing cavity length.

Single emitter photon count rate measurements

After characterization of the spatial mode of the cavity and calibrating its length, the search for single NV centers is initiated. To this end, a cavity-enhanced fluorescence scan of a larger area is performed. The excitation light is introduced through the cavity fiber. The cavity length is stabilized to a mirror separation of roughly $10\,\mu\mathrm{m}$ where both the excitation and fluorescent light are resonant with the cavity. The excitation power was kept at $3.6\,\mathrm{mW}$ at $532\,\mathrm{nm}$. Figure 7.12 displays a scan over an area of $(50\,\mu\mathrm{m})^2$, with about 50 visible emitters. The saturation behavior, as well as the second order correlation function $g^{(2)}(\tau)$ to prove single-emitter behavior was recorded for five emitters marked with a circle (NV2-NV6). For these measurements, the cavity length was stabilized at

[1] Plane-concave cavity with finesse $\mathcal{F} = 42$, emitter quality factor $Q_{\mathrm{em}} = 8$, central emitter wavelength $\lambda_0 = 690\,\mathrm{nm}$, radius of curvature $R = 90\,\mu\mathrm{m}$.

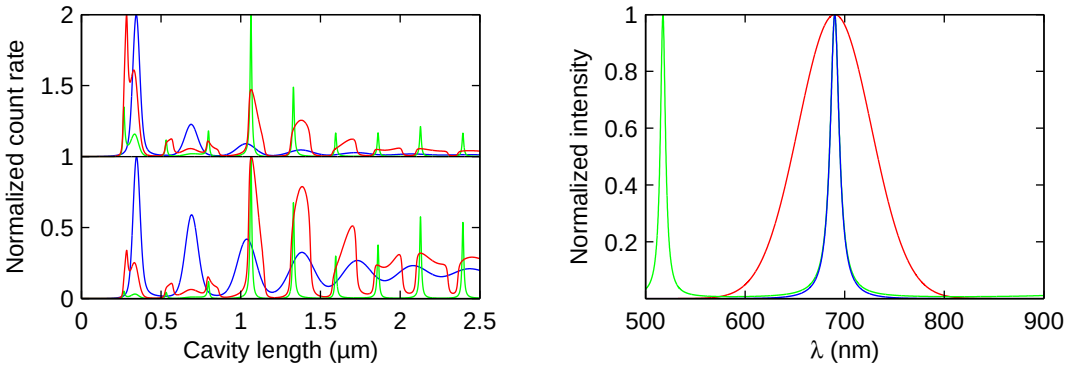

(a) (b)

Figure 7.11.: (a) Calculated count rate into the cavity mode for constant excitation power (blue), excitation at 532 nm (green) and excitation in a spectral band from 525 to 575 nm (red), including (upper panel) and not including (lower panel) Purcell enhancement. (b) Approximated spectrum of the NV center (red), together with the Fabry-Pérot cavity transmission (green) and their product (blue) at a cavity length of 1.1 µm and for a cavity finesse of 42.

the shortest possible cavity length $d = 1.1\,\mu\text{m}$ for which the excitation and fluorescent light is simultaneously in resonance with the cavity, as illustrated in Fig. 7.11. Due to significant Purcell enhancement, the largest signal to background ratio is obtained at this "sweet spot" where the longitudinal mode orders are $q = 3$ for $\lambda_0 = 690\,\text{nm}$ and $q = 4$ for $\lambda_{\text{ex}} = 532\,\text{nm}$.

The corresponding setup has already been used for the measurement of one data point of the point spread function, on the basis of the more isolated emitter (NV1), shown in Fig. 7.10(a,b). In this case, a spatial resolution of 1.1 µm, an uncorrected peak count rate exceeding $6 \cdot 10^5\,s^{-1}$, a signal to background ratio larger than 20, and clear antibunching with $g^{(2)}(0) = 0.21$ was measured. The large signal to background ratio suggests the feasibility of clean single-photon emission. However, the value for $g^{(2)}(0)$ indicates that there is some additional background from the nanocrystal itself. The simultaneous enhancement of the excitation and fluorescence, and the emission into the well-collectable cavity mode, result in enhanced photon count rates and enable spatial and spectral filtering at the same time. As a consequence, cavity-enhanced scanning fluorescence microscopy holds promise for improved net signal compared to confocal microscopy.

To give an example for the cavity-enhanced single-photon emission, the results for one NV center (NV2) are now discussed in more detail. The $g^{(2)}$-function measured for low excitation power is shown in Fig. 7.13(a), together with a fit based on the theory for a three-level system (Eq. 6.1). The fit value $g^{(2)}(0) = 0.27$ proves that is indeed a single emitter. The fact that it does not drop to zero is primarily attributed to autofluorescence created in the mirror coating at this location. The excitation intensity dependent photon count rate is displayed in Fig. 7.13(b). The earlier applied fit function including a linear

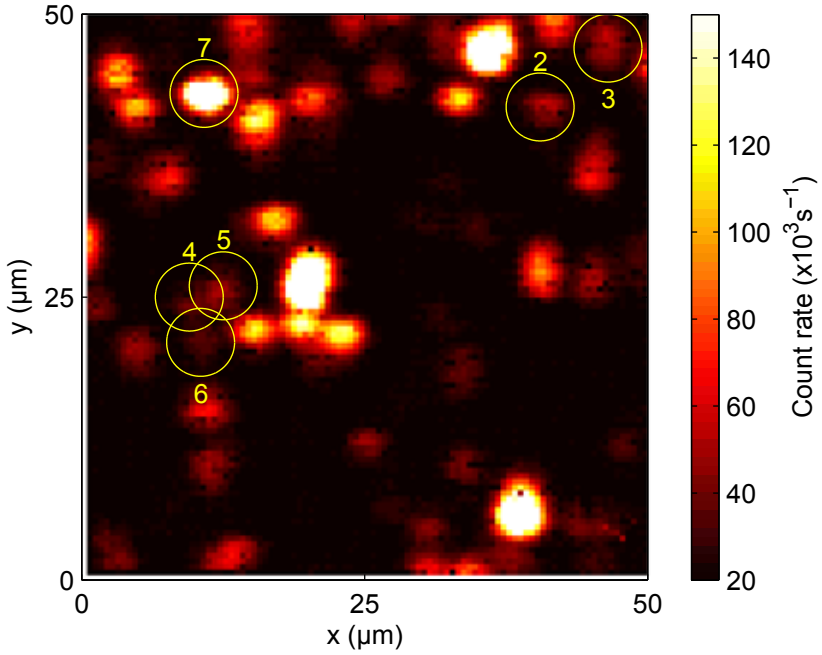

Figure 7.12.: Cavity-enhanced fluorescence scan with 6 marked NV centers, five of which are single emitters (NV2-NV6) and one a bright emitter ensemble (NV7).

term accounting for background is applied: $R(I) = R_\infty I/(I_{\text{sat}} + I) + aI$ (Eq. 7.1). For the presented data sets, the excitation was performed through the cavity fiber, yielding slightly better signal to background ratios than for the excitation through the microscope objective. Here, the intensity denotes the intra-cavity value, which is related to the transmitted power P_t, the transmission of the outcoupling mirror T_1, and the evaluated excitation mode waist w_{ex} by

$$I = \frac{8P_\text{t}}{\pi w_{\text{ex}}^2 T_1}. \tag{7.6}$$

The fit yields a collected saturation count rate $R_\infty = 6.9 \cdot 10^5\, s^{-1}$, a saturation intensity $I_{\text{sat}} = 0.49 \cdot 10^9\,\text{Wm}^{-2}$, and a linear background parameter $a = 1.0 \cdot 10^5\, s^{-1}/10^9\,\text{Wm}^{-2}$. Additionally, the intensity dependent background count rate is measured at a mirror location without any emitter. The observed slope is equal to the value a, indicating that the nanocrystal is not contributing notably to the background, in this case. The stated count rates are the uncorrected rates detected with the APDs. The overall detection efficiency of the setup amounts to 43% (see Section 6.1). Accordingly, a total saturation count rate of $1.6 \cdot 10^6$ photons per second is collected by the first lens, i.e. the objective.

In order to quantify the emission enhancement induced by the cavity, several single emitters (NV1-NV6) are investigated inside the cavity and compared to the confocal measurements of an STG100 sample on a glass substrate (see Section 6.3). For both situations, the saturation count rate R_∞ and $g^{(2)}(0)$ are determined for each emitter.

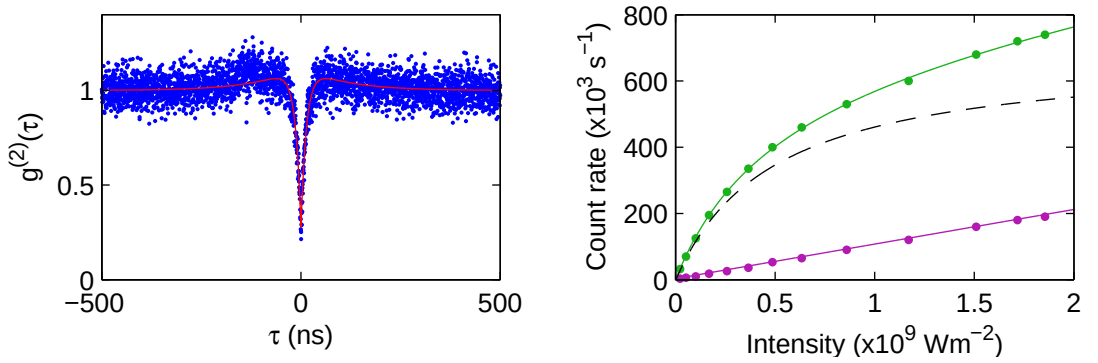

(a) (b)

Figure 7.13.: Results for NV2: (a) Measured $g^{(2)}$-function (blue dots), together with fit (red line), yielding $g^{(2)}(0) = 0.27$. (b) Saturation curve, displaying the uncorrected count rate as a function of the intra-cavity intensity, yielding a saturation count rate of $6.9 \cdot 10^5\, s^{-1}$.

By plotting R_∞ versus $g^{(2)}(0)$ the cavity emission can be compared to the free-space-like emission, as shown in Fig. 7.14. In the cavity case, the lowest measured value of $g^{(2)}(0)$ was around 0.2, as a result of background fluorescence created in the silver mirror. We thus expect all NV centers with $g^{(2)}(0) \lesssim 0.7$ to be single emitters. Averaging over the saturation count rates of the NV centers inside the cavity yields $R_\infty = (5.7 \pm 0.6) \cdot 10^5\, s^{-1}$, in comparison to $(1.5 \pm 0.1) \cdot 10^5\, s^{-1}$ on the glass substrate. This corresponds to an average enhancement factor of 3.8.

Single emitter lifetime measurements

In a next step, the modification of the excited-state lifetime inside the cavity is investigated to directly demonstrate the Purcell effect. To this end, we perform time-correlated single-photon counting under pulsed excitation for varied mirror spacings [77]. For a cavity length $d > 0.8\,\mu m$, no significant lifetime modification can be noticed. In contrast, the lifetime is reduced considerably for $d = \lambda_0/2$. For NV2, the lifetime amounts to $\tau = (11 \pm 0.5)$ ns at $d = 2\,\mu m$ and reduces to $\tau_c = (7 \pm 1.5)$ ns at $d = \lambda_0/2$, as shown in Fig. 7.14(b). However, as a result of the excitation light being off-resonant with the cavity at $d = \lambda_0/2$, the signal-to-background ratio is low for this cavity length, and the lifetime value can only be determined with a large uncertainty. The decay of the background includes nonmonoexponential contributions that are accounted for by error bars by trying out different fit domains.

The situation for the large mirror spacing at $d = 2\,\mu m$ actually corresponds to a "half cavity" with one mirror only. For this setting, the emission lifetime is always biased by the sample mirror. In conclusion, we compare the lifetime within a full cavity at shortest mirror spacing to the lifetime on a single silver mirror in this measurement.

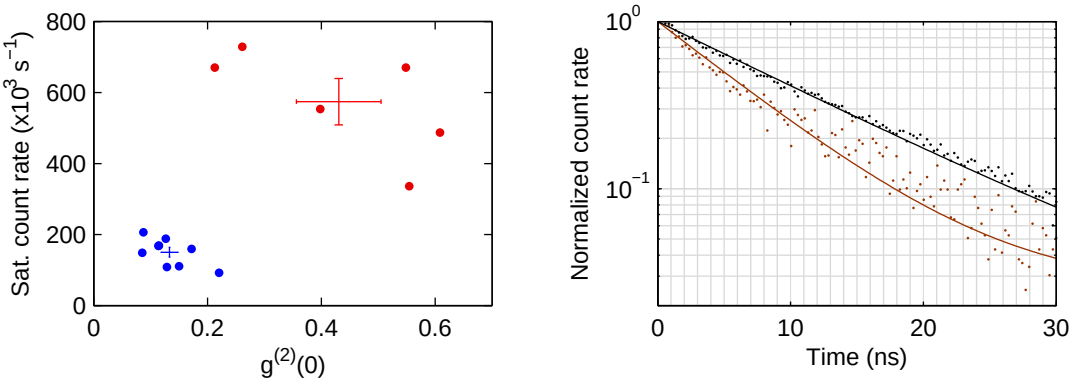

(a) (b)

Figure 7.14.: (a) Saturation count rate versus single-photon purity $g^{(2)}(0)$ for single NV centers inside the cavity (red dots) and on a glass substrate (blue dots), together with the averaged values (crosses), indicating cavity enhancement by a factor of 3.8. (b) Lifetime measurement for NV 2 at $d = 2\,\mu\text{m}$ (black) and $d = \lambda_0/2$ (brown), together with monoexponential fits.

An additional statistical comparison between the lifetimes on a silver mirror and on a glass substrate yields a reduction by a factor of 1.3 ± 0.3 (Fig. 6.8). Furthermore, a FDTD simulation averaged over dipole orientations results in a reduction factor of 1.8 (Section 7.2.2) implying a free-space lifetime of up to $\tau_0 = 20\,\text{ns}$. Based on this estimate, the effective Purcell factor can be derived: $C_{\text{eff}} = [(\tau_0/\tau_c) - 1]/\text{QE} = 2 \pm 0.6$, for a quantum efficiency of $\text{QE} = 1$ and correspondingly larger values for $\text{QE} < 1$.

For a short review of the quantum efficiency of NV centers embedded in NDs see Section 2.2.4.2. In the next paragraph, the experimental results will be compared to theoretical expectations. Some more insight into the influence of the QE is given further below.

Comparison to theory

An increased count rate at $d = 1.1\,\mu\text{m}$, as well as a decreased lifetime at $d = \lambda_0/2$ have been observed for single NV centers inside the cavity. The experimentally determined enhancement is now compared to a theoretically expected factor. At first, the count rate enhancement at $d = 1.1\,\mu\text{m}$ is evaluated by comparing the photon rate of an NV center inside the cavity to the rate obtained on a glass substrate.

The rate of photons coupled out of the cavity is determined by

$$R_c = C_{\text{eff}} \gamma_r p(T_1), \tag{7.7}$$

with the radiative decay rate of the excited state γ_r and the probability of a photon to leave the cavity through the outcoupling mirror $p(T_1)$. For the present setup, $p(T_1) = 0.51$. The cavity mode is fully collected by the microscope objective. The effective Purcell

factor, given by Eq. 4.36, amounts to $C_{\text{eff}} \sim 0.12$, for the experimental parameters used here, i.e. for the longitudinal mode order $q = 3$, yielding $V = 5\lambda^3$, $Q_{\text{c}} = q \cdot 42 = 126$, and $Q_{\text{em}} = \lambda_0/\Delta\lambda \approx 8$, being derived from the center wavelength of the emission spectrum $\lambda_0 = 690$ and its full-width at half-maximum $\Delta\lambda = 90\,\text{nm}$.

In order to determine the ratio of photons collected from an NV center on the glass substrate, it is necessary to integrate the emission pattern over the solid angle collected by the microscope objective. The radiation pattern of a dipole on a glass substrate is non-trivial, because it is influenced by the air-glass interface [349, 350]. Calculations result in a total collection efficiency of $\eta_\Omega = 0.16$, for the objective used here (NA=0.75). The total rate of collected photons on the glass substrate amounts to

$$R_{\text{glass}} = \gamma_{\text{r}} \eta_\Omega. \tag{7.8}$$

If the detection efficiency behind the objective is assumed to be equal for both cases, the theoretical enhancement factor is expected to be

$$\frac{R_{\text{c}}}{R_{\text{glass}}} = C_{\text{eff}} \frac{p(T_1)}{\eta_\Omega} = 0.38, \tag{7.9}$$

opposed to an experimental value of 3.8.

For the lifetime measurement at $d = \lambda_0/2$, the theoretical enhancement factor amounts to $C_{\text{eff}} = 0.6$, for the parameters $V = 1\lambda_0^3$, $Q_{\text{c}} = 42$, and $Q_{\text{em}} = 8$. This is once more substantially smaller than the experimentally determined value. The strong contrast to the experimental findings suggests that the simplified model based on the effective Purcell factor is not applicable in this situation. The latter is derived on the supposition that the cavity subtends a negligible solid angle and that the emitting dipole remains far from any surface. However, the spontaneous emission is affected by three main aspects lying beyond this approach.

1. The close proximity of the emitter to the mirror surface results in self-interference of the emission pattern over a large angular distribution. Furthermore, near-field coupling is possible [349, 350]. FDTD simulations for an orientation-averaged dipole in a ND that is placed on a silver mirror result in a lifetime reduction by a factor of 1.8 with respect to a setting without the mirror (see Section 7.2.2). Furthermore, the contribution of nonradiative decay is shown to be less than 10%.

2. The simple picture that only the fundamental mode is influenced by the cavity, while all other modes are unaltered is unsustainable. Since the cavity mirrors subtend a large solid angle, the cavity influences the mode structure in a more general way, for instance leading to inhibited decay into certain modes [339, 364].

3. For very small mirror distances and certain diamond crystal sizes, the ND can give rise to additional, lateral field confinement of the optical mode.

These issues can be resolved by FDTD simulations, which will be discussed in more detail in Section 7.2.2. A simulation of an emitter coupled to a cavity, accounting for all aspects

at the same time, yields an effective Purcell factor of $C_{\text{eff}} = 1.4$ at $d = 1.1\,\mu\text{m}$, comparing the cavity-enhanced emission rate to the one in free space. In this case, the effective Purcell factor for a dipole in parallel to the mirror surface is simulated, since dipoles with normal orientation are excited and collected only very weakly. In conclusion, the theoretical enhancement factor is corrected to a value of $R_c/R_{\text{glass}} = 4.5$, only about 20% larger than determined experimentally. At $d = \lambda_0/2$ the simulation predicts $C_{\text{eff}} = 11$, which would correspond to a much larger lifetime reduction than observed experimentally. The simulated large Purcell enhancement presumably originates from mode confinement by the diamond nanocrystal.

The discrepancy to the experimentally observed values can be attributed to a reduced coupling strength originating from a non-ideal dipole orientation and a displacement of the emitter with respect to the field maximum of the cavity. In addition, the lifetime modification might be mitigated by the finite QE. As shown in the next paragraph, the issue would be resolved for QE = 0.2, according to Eq. 7.13.

Quantum efficiency

The efficient generation of single photons depends crucially on a large QE, which can be significantly diminished by absorptive media in close proximity to the emitter. In fact, using silver mirrors, having a refractive index with a large imaginary part, involves the danger of quenching the fluorescence of a nearby NV centers. The QE is defined by

$$\text{QE} = \frac{\gamma_r}{\gamma_r + \gamma_{nr}}, \tag{7.10}$$

where γ_r and γ_{nr} are the radiative and nonradiative decay rates, respectively. The excited state decay rate is then given by

$$\frac{1}{\tau_0} = \gamma_0 = \gamma_r + \gamma_{nr}. \tag{7.11}$$

Ideally, the intrinsic quantum efficiency of the NV center sample could be inferred from a comparison of the measured lifetime changes with simulations. However, there would be a large uncertainty due to several unknown contributions. Thus, the quantum efficiency of a dipole is studied in dependence of the distance from a silver mirror with FDTD simulations.

The mirror is modeled as a 33 nm thick silver layer on top of a glass substrate, capped with a glass layer of variable thickness. A dipole oriented in parallel to the mirror surface is located at the center of a diamond cube with 30 nm edge length, which is positioned directly on the glass capping layer. A series of simulations yields the quantum efficiency as a function of the thickness of the capping layer, as shown in Fig 7.15. The onset of nonradiative decay is located at a thickness of around 20 nm where the quantum efficiency amounts to about 0.8. For larger layer thicknesses the quantum efficiency quickly approaches unity. Since the used mirrors have glass capping layers with a minimal thickness of 20 nm and the applied diamonds are typically larger than roughly 100 nm, nonradiative decay is expected to be less than 10% in the presented experiments. In the

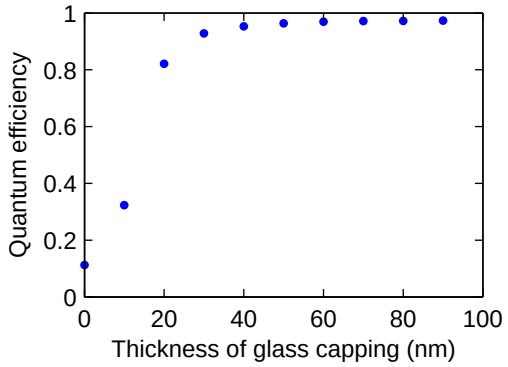

Figure 7.15.: Quantum efficiency as a function of the thickness of the glass capping layer. For thicknesses larger than 30 nm the quantum efficiency exceeds 90%.

evaluation of the effective Purcell factor it is thus assumed that the nonradiative rate in the cavity does not change: $\gamma_{\mathrm{nr}}^{\mathrm{c}} = \gamma_{\mathrm{nr}}$.

Note that Purcell enhancement can increase the QE in the cavity, which is given by

$$\mathrm{QE}^{\mathrm{c}} = \frac{(C_{\mathrm{eff}} + 1)\,\gamma_{\mathrm{r}}}{(C_{\mathrm{eff}} + 1)\,\gamma_{\mathrm{r}} + \gamma_{\mathrm{nr}}^{\mathrm{c}}}. \tag{7.12}$$

In contrast, the lifetime modification by the cavity is mitigated by a finite QE:

$$\frac{\tau_0}{\tau_{\mathrm{c}}} = \mathrm{QE} \cdot C_{\mathrm{eff}} + 1. \tag{7.13}$$

Since the saturation count rates in free space and in the cavity depend only on the radiative decay rates γ_{r} and $C_{\mathrm{eff}}\gamma_{\mathrm{r}}$, respectively, they are independent of the QE.

Lifetime measurements with emitter ensembles

Lifetime variations could be observed for single NV centers. However, the measured lifetime is strongly influenced by background fluorescence created in the mirror. The latter depends on the excitation power, which is itself subject to cavity modulations. The desired fluorescence signal from the NV centers is thus obscured significantly by cavity-length dependent background.

The STG100 sample predominantly contains single NV centers and small emitter ensembles. A few ensembles with some ten or more emitters have also been observed. The increased brightness can be harnessed to demonstrate cavity-length-dependent lifetime modulations, as shown for an ensemble of roughly 50 NV centers in Fig. 7.16 (NV7 of Fig. 7.12).

Since the distribution of dipole orientations and locations of the individual NV centers inside the ND leads to a nonuniform coupling strength to the cavity, a multi-exponential function (stretched exponential) [403]

$$I(t) = \exp\left[-\left(t/\tau_0\right)^{\beta}\right] \tag{7.14}$$

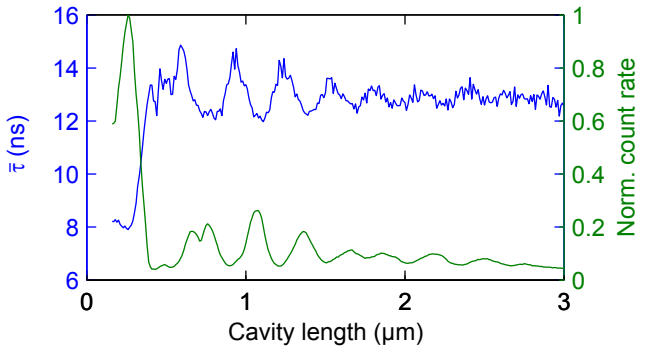

Figure 7.16.: Mean lifetime $\bar{\tau}$ (blue) and the normalized photon count rate (green) as a function of the cavity length for an ensemble of about 50 emitters. A clear drop of the liftime together with an increase in the count rate for a very short cavity length hints at additional field confinement provided by the diamond nanocrystal.

is applied to fit each TCSPC histogram and to determine the mean lifetime

$$\bar{\tau} = \tau_0 \frac{\Gamma(2/\beta)}{\Gamma(1/\beta)}, \tag{7.15}$$

where Γ denotes the gamma function.

While the modification of the excited state lifetime remains moderate for larger mirror distances, a strong decrease for a cavity length below about 0.5 µm is observed. Here, the mean lifetime drops by about 40% from 13 to 8 ns. At the same time the photon count rate increases by about a factor of 20, confirming that the lifetime reduction is not a pure result of quenching the radiative transition. This behavior hints at additional field confinement provided by the diamond crystal at ultimately short mirror distances. The effect of the optical mode being guided by the ND is analyzed in more detail in the following section, where a bright NV center ensemble is coupled to a plane-parallel FFPC.

7.2.2. Plane-parallel silver cavity with NV center ensembles

In the previous section, a lifetime reduction and count rate increase have been demonstrated for single NV centers in a plane-concave FFPC. The strong Purcell enhancement at very short mirror separation encourages the notion that a Fabry-Pérot mode is combined with additional lateral field confinement by a suitably sized diamond nanocrystal, here. Measurements with small NV center ensembles supported this idea.

In this section, measurements and simulations are presented that give further insight into the occurrence of such a nanodiamond-induced waveguide mode. A Fabry-Pérot cavity with plane-parallel architecture facilitates the separation of the waveguide effect from the transversal mode confinement by the cavity mirrors. Thus, a cavity fiber with a cleaved planar end face with mechanically polished edges is applied that enables ultimately short mirror spacings. For this experiment, we furthermore use bright NV center ensembles providing an increased signal-to-background ratio, in order to minimize the influence of distant-dependent background fluorescence on the lifetime modulation by the cavity. To this end, NDs of the Tai100 sample embedding some hundred NV centers are spin coated onto the planer outcoupling mirror. For details about the NDs and the sample preparation see Section 6.2. Since collective effects are expected to be irrelevant, the theoretical treatment is in analogy to single emitters.

Cavity characterization

The fiber used here, has a cleaved, planar endfacet with mechanically polished edges. This geometry does not necessitate laser machining and can therefore be fabricated with minor experimental overhead. Furthermore, the simple plane-plane cavity architecture facilitates the direct comparison with FDTD simulations. The mirror parameters of this experiment are given by an outcoupling mirror with 33 nm of silver, capped with 60 nm of glass and a fiber mirror with 60 nm of silver and 20 nm of glass. Note that the only difference to the plane-concave silver cavity is an increased glass capping of the outcoupling mirror, resulting in a slightly larger mirror transmission. Measurements with narrow-band lasers yield $T_1 = 24\%$ at 532 nm and $T_1 = 16\%$ at 633 nm, respectively. This is in good agreement with values of 24% and 15%, respectively, calculated with the matrix method. A simulated transmission of $T_1 = 11\%$ and absorption of $A_1 = 5\%$ at 692 nm amount to an expected probability of a photon to leave the cavity through this mirror of $p(T_1) = 0.11/(0.11 + 0.05 + 0.008 + 0.03) = 0.56$. A finesse of $\mathcal{F} = 18$ is measured at 633 nm, slightly lower than the evaluated value of 21, increasing to $\mathcal{F} = 28$ at 700 nm.

Modulation of the excited state lifetime

The experimental setting is similar to the one described by Chizhik *et al.* [404, 77], where the lifetime of single molecules is probed with a tunable microresonator. In our case, the fluorescence lifetime of an NV center ensemble is measured by TCSPC for different cavity lengths. The mirror spacing is varied with a piezoelectric actuator. The

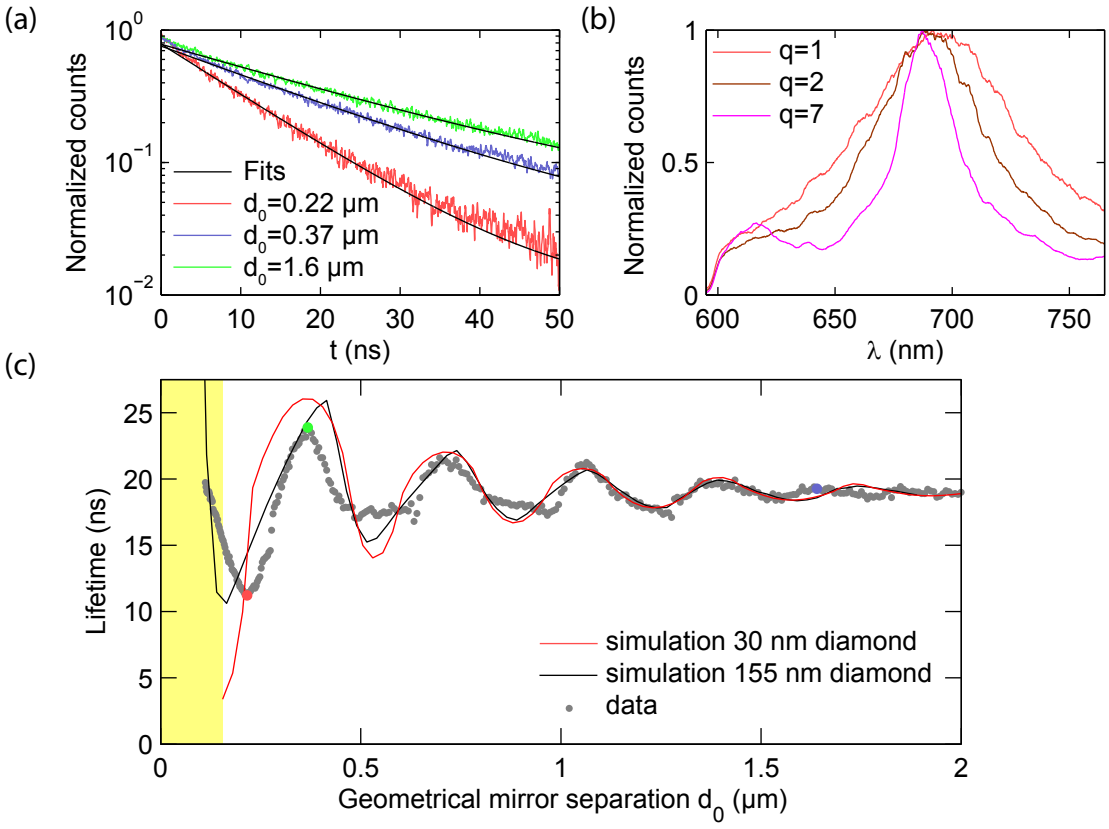

Figure 7.17.: (a) TCSPC histogram for three different cavity lengths (indicated by the dots in (c) with corresponding color code), together with mono-exponential fits (red: $\tau = 11.2\,\text{ns}$, blue: $\tau = 19.3\,\text{ns}$, green: $\tau = 23.9\,\text{ns}$). (b) Cavity emission spectra at resonances with longitudinal mode orders $q = 1, 2, 7$. (c) Comparison of measured lifetime as a function of the mirror separation $\tau(d_0)$ with FDTD simulations for a dipole oriented in parallel to the mirror surface inside a diamond cube of edge length 30 nm and 155 nm. The yellow area indicates the distance range, at which the fiber touches the larger diamond.

geometrical mirror distance d_0 and the optical cavity length d are calibrated by analyzing fluorescence spectra. For geometrical mirror distances below about 500 nm, a deviation of the actual cavity length from the expected value is observed, which is most probably a result of the cavity fiber touching the macroscopic mirror with one of its edges. Thus, the distance calibration is adjusted for $d \lesssim 500\,\mathrm{nm}$, to restrict the cavity length to values $d > 100\,\mathrm{nm}$. For each cavity length, a TCSPC histogram is recorded and fitted with a mono-exponential decay curve[2] providing the lifetime $\tau(d_0)$, as shown for three different mirror separations in Fig. 7.17(a). The resulting diagram with the fitted lifetimes as a function of the cavity length is displayed in Fig. 7.17(c) for one NV center ensemble. It is compared to FDTD simulations for a diamond cube with an edge length of 30 nm and alternatively 155 nm (see next section). Additionally, fluorescence spectra filtered by the cavity are recorded, demonstrating that the resonance linewidth scales inversely with the mirror separation, see Fig. 7.17(b). However, the spectral resonance width does not allow to directly infer the cavity quality factor, because the resonance wavelength of plane-parallel cavities is angle dependent and a large angular range is collected indeed.

When the mirror separation is below about 2 µm, noticeable lifetime modifications are observed. Whenever the cavity is resonant (off-resonant) with the fluorescence emission, the lifetime is reduced (increased), due to the modification of the local density of states. The minimal (maximal) measured lifetime of $\tau_\mathrm{c} = 11.2\,\mathrm{ns}$ (23.9 ns) corresponds to a reduction (enlargement) of the the lifetime of 40% (25%) with respect to the lifetime of $\tau_\mathrm{m} = 18.9\,\mathrm{ns}$ detected when the fiber is withdrawn, i.e. the lifetime measured for the NV center ensemble in the ND on the outcoupling mirror alone. Yet, the lifetime on the mirror is already reduced compared to free space. This effect is assessed by a statistical comparison (see Fig. 6.8) yielding a reduction factor of 1.3 ± 0.3, as well as by FDTD simulations yielding a dipole-orientation-averaged reduction factor of 1.8. The latter suggests a free-space lifetime of up to $\tau_0 = 34\,\mathrm{ns}$. Consequently, an upper bound for the effective Purcell factor of $C_\mathrm{eff} = \left(\frac{\tau_0}{\tau_\mathrm{c}} - 1\right)/\mathrm{QE} = 2.0$ is inferred for $\mathrm{QE} = 1$.

By investigating several FNDs in an analogous way, a shortest lifetime of $\tau_\mathrm{c} = 6.7\,\mathrm{ns}$ is observed with similar relative lifetime changes. Moreover, an increase of the integrated fluorescence signal by up to a factor of 40 is detected, when the cavity length is reduced from around 2 µm to $d = \lambda/2$, as shown in Fig. 7.18. The reasoning for the count rate enhancement is as follows: For large mirror separations, the influence of the cavity is negligible and only the fluorescence transmitted through the planar mirror ($T_1 = 0.11$) is collected by the objective (NA=0.55) with a small efficiency. On the contrary, for short cavities, the fluorescence is predominantly emitted into the cavity mode, as a result of Purcell enhancement. The outcoupling probability through the macroscopic mirror amounts to $\eta = 0.56$, and the cavity mode is entirely collected by the objective due to its small divergence angle.

[2] In general, a multi-exponential decay is expected for an emitter ensemble where the distribution of dipole orientations and positions of the individual NV centers inside the ND leads to a nonuniform coupling strength to the cavity [403]. Fitting with this function results in larger lifetime modulations, such that mono-exponential fitting, which is applied here, constitutes a conservative estimate.

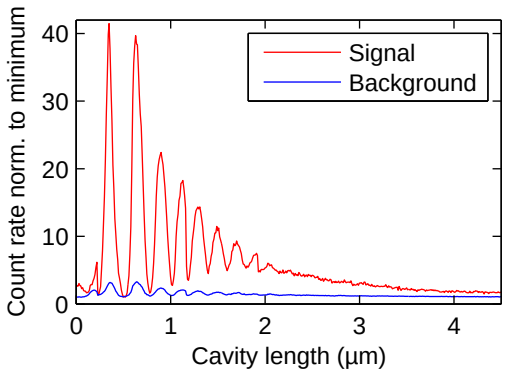

Figure 7.18.: Modulation of the detected signal and background count rates as a function of the cavity length normalized to their minimum.

Simulation of the spontaneous emission modification by the cavity

In order to model the modification of the spontaneous emission behavior of an NV center coupled to a Fabry-Pérot microcavity, FDTD simulations based on Maxwell's equations are performed. FDTD simulations constitute a powerful method to predict the time-dependent behavior of electromagnetic fields in complex material environments. Compared to analytic solutions for a certain setting [405, 406, 407, 351, 408, 409, 410, 411, 412, 413], the numerical approach provides more flexibility to implement customized geometries. For instance, it is straightforward to introduce a diamond nanocrystal into the cavity.

The commercial software Lumerical is applied to simulate the emission behavior of an electrical dipole inside a ND, coupled to a plane-parallel Fabry-Pérot microcavity with silver mirrors. The ND is implemented as cube with a refractive index of 2.4 and an edge length of 155 nm and alternatively 30 nm, for comparison. An electric dipole source with a Gaussian spectrum peaking at a wavelength of 690 nm with a $1/e$-width of 100 nm is located at its center. The diamond is positioned directly on top of the outcoupling mirror that consists of a glass substrate with a 33 nm thick silver layer finished with a glass capping of 60 nm. The thickness of the glass capping is chosen such that the dipole is positioned at an antinode of the electric field inside the cavity. This parameter was optimized for the diamond with an edge length of 155 nm. Adjusting the thickness for the smaller diamond in a range from 60 to 120 nm did not change the effective emission rate modulation significantly. Thus, the same value was chosen for this case. The second mirror, i.e. the fiber mirror in the experiment, is composed of a silver layer with a thickness of 60 nm and a glass capping of 20 nm. These coating parameters correspond to the actually applied mirrors of the experiment.

Figure 7.19(a) shows a cross section of the simulated geometry together with the intensity distribution for a central dipole oriented parallel to the mirror surface. Note the logarithmic scaling. For this instance, the shortest possible cavity length is chosen for the diamond cube with an edge length of 155 nm. A strong confinement of the intensity to

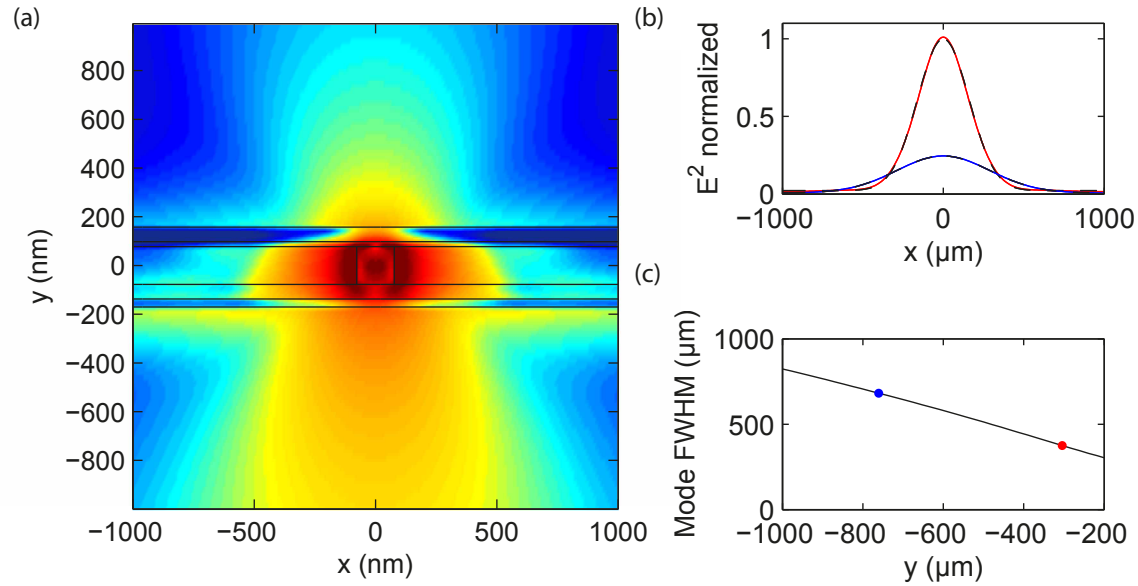

Figure 7.19.: (a) Simulation of the intensity distribution of a dipole oriented along the x-axis located at the origin (logarithmic scale, red: high, blue: low). The intensity is confined between the two silver mirrors (horizontal black lines, including the spacer layers) and localized to the nanocrystal (black square). Outcoupling occurs predominantly through the thinner bottom mirror. (b) Two horizontal cuts (blue, red lines) through (a), together with Gaussian fits (black dashed lines), illustrating the shape of the outcoupled mode. (c) Width of the Gaussian fits to the mode as a function of the vertical distance y. The red and blue dots indicate the position of the horizontal cuts in (b).

the diamond crystal is apparent, just like the directional outcoupling through the lower mirror. Horizontal cuts through the intensity map reveal that the outcoupled mode has an almost perfect Gaussian shape, as shown for two examples at different distances from the dipole in Fig. 7.19(b). A series of Gaussian fits to the mode profiles furthermore demonstrates that the width of the outcoupled mode increases approximately linearly with the propagation away from the diamond, as displayed in Fig. 7.19(c). The inferred divergence of the mode corresponds to an NA of 0.27, or 0.38 after the refraction at the glass-air interface of the mirror substrate. Therefore, the outcoupled mode can be easily collected by an objective.

To study the cavity-length-dependent modification of the spontaneous emission lifetime inside the resonator, the mirror distance is varied, starting from the setting where both mirrors touch the diamond crystal to a distance of about 2 µm. Dipole orientations parallel and normal to the mirror surface are simulated. For each cavity length, the ideal Purcell factor is determined as a function of the wavelength $C(\lambda)$, quantifying the emission rate enhancement inside the cavity with respect to the situation where the

dipole is embedded in the ND in vacuum[3]. To obtain the effective Purcell factor that is expected for the NV center, the ideal Purcell factor is averaged over the NV center's emission spectrum $S(\lambda)$, which is modeled as a Gaussian distribution with a central wavelength of 690 nm and a FWHM of 90 nm:

$$C_{\text{eff}} = \frac{\int_{-\infty}^{\infty} C(\lambda) S(\lambda) \mathrm{d}\lambda}{\int_{-\infty}^{\infty} S(\lambda) \mathrm{d}\lambda}. \tag{7.16}$$

For better comparability with the experimental data, the Purcell factor $C(\lambda)$ is normalized to the Purcell factor $C_{\text{m}}(\lambda)$ that is obtained when the upper (fiber) mirror is removed and we average over the emission spectrum of the NV center $S(\lambda)$. The effective lifetime change can then be expressed as

$$\frac{\tau_{\text{m}}}{\tau_{\text{c}}} = \frac{\int_{-\infty}^{\infty} \left[C(\lambda)+1\right] \left[C_{\text{m}}(\lambda)+1\right]^{-1} S(\lambda) \mathrm{d}\lambda}{\int_{-\infty}^{\infty} S(\lambda) \mathrm{d}\lambda}. \tag{7.17}$$

The simulated lifetime in the cavity τ_{c} for parallel dipole orientation is in good agreement with the data, as shown in Fig. 7.17(c). Since, the normal dipole component is only weakly excited and coupled to the cavity mode, it does not contribute significantly. An interesting feature is observed, when comparing the theoretically expected enhancement for the two simulated diamond sizes at shortest mirror distances. While the simulated lifetime for the smaller diamond has a minimal value of roughly 11 ns, it drops below 4 ns, for the larger crystal, indicating strong Purcell enhancement. This is a hint for additional mode confinement provided by the larger nanocrystal at short mirror distances.

A clearer picture of this effect is obtained by directly investigating the effective Purcell factor C_{eff} as a function of the cavity length and the ideal Purcell factor $C(\lambda)$ at the location of maximal effective Purcell factor. As shown in Fig. 7.20(a), the effective Purcell factor of dipoles oriented in parallel to the mirror surface experiences significant cavity-length-dependent modulation, while dipoles with normal orientation are only slightly affected. For parallel dipoles, the modulation amplitude increases with decreasing cavity length and is approximately equal for the different diamond sizes for mirror distances larger than $\lambda/2$. However, for the resonance with longitudinal mode order $q = 1$, the effective Purcell factor C_{eff} increases to a value above 10 for the larger ND, while it remains below 3 for the smaller one. We thus conclude that only the larger crystal is able to support additional mode confinement. This finding is confirmed by Fig. 7.20(b), where the ideal Purcell factor for $q = 1$ is shown plotted as a function of the wavelength $C(\lambda)$. The larger diamond exhibits a pronounced resonance with a peak ideal Purcell factor above 62. The full potential of this large enhancement factor could be harnessed with emitters having a narrow emission spectrum, such as the SiV center, for instance. In contrast, the ideal Purcell factor remains small and without resonance for the smaller crystal. It is worth mentioning that the analytical calculation of a dipole at the center of

[3] In fact, the simulation determines the Purcell enhancement inside the cavity with respect to a dipole embedded in bulk diamond, first. Thus, a normalization to a dipole located in a ND in vacuum is performed to obtain the actual Purcell factor.

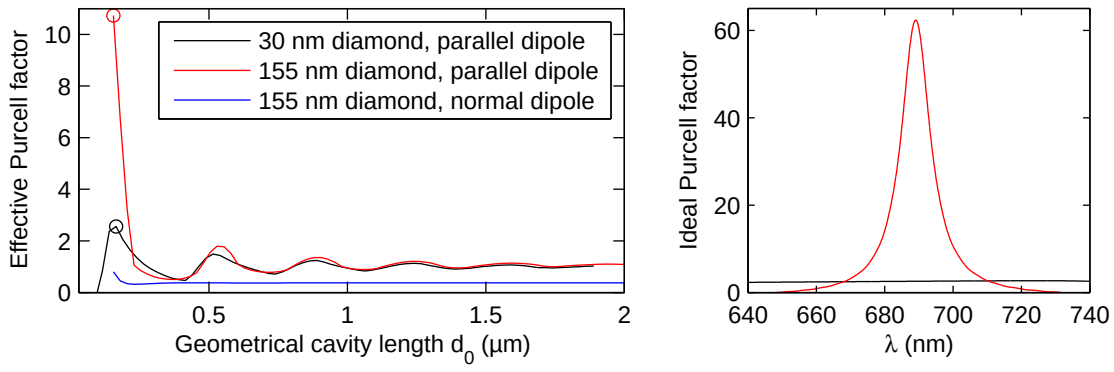

(a) (b)

Figure 7.20.: (a) Effective Purcell factor C_{eff} as a function of the geometrical cavity length d_0 for dipole orientations parallel and normal to the mirror surface and diamond sizes of 30 nm and 155 nm. (b) Ideal Purcell factor as a function of the emission wavelength λ at the cavity length indicated by the circles in (a) for diamond sizes of 30 nm (black line) and 155 nm (red line).

a plane-parallel cavity with lossless mirrors, but without the diamond nanocrystal results in an ideal Purcell factor of only 2 [339]. This value is close to the one obtained for the ND with 30 nm edge length.

Waveguide effect

A simple model serves to illustrate the origin and consequences of mode confinement by a ND of suitable size that enables large Purcell enhancement. To this end, the diamond crystal is modeled as a simple cylindrical waveguide [225] with refractive index $n = 2.4$ and radius b. The parametrization of the refractive index is given by

$$n_{\text{r}} = \begin{cases} n & |r| \leq b \\ 1 & |r| > b \end{cases}, \tag{7.18}$$

with the radial coordinate r. The waist w_0 and the effective refractive index n_{eff} of the propagating waveguide mode can then be estimated as a function of the diameter of the waveguide, by solving the Helmholtz equation for the electric field in one dimension

$$\left(\nabla^2 + k^2\right) E = 0, \tag{7.19}$$

where $k = 2\pi n_{\text{r}}/\lambda$. As shown in Fig. 7.21(a), the maximal confinement is expected for a particle diameter around 140 nm, where a minimal $1/e^2$ mode radius of 160 nm and an effective refractive index of 1.9 is obtained.

The model is furthermore adjusted to the experimentally encountered situation by introducing such a diamond waveguide into a planar Fabry-Pérot cavity with a mirror

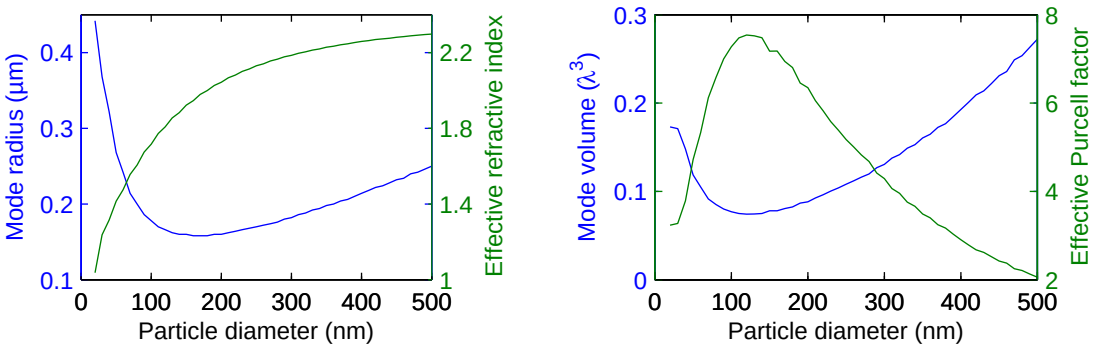

(a) (b)

Figure 7.21.: (a) Mode waist and effective refractive index as a function of the particle diameter. (b) Mode volume and effective Purcell factor as a function of the particle diameter. For the evaluation of the Purcell factor, the quality factors of the cavity and the emitter are set to $Q_c = 28$ and $Q_{em} = 10$, respectively.

separation of $d = \lambda/2n_{eff}$. Here, n_{eff} represents the refractive index that the propagating mode experiences. This leads to a cavity mode with a volume as low as $V = \pi w_0^2 \lambda/8n_{eff} = 0.07\,(\lambda/n_{eff})^3$, which constitutes a dramatic decrease compared to the values achievable with Fabry-Pérot cavities with curved mirrors (see Fig. 7.21(b)). Assuming an effective quality factor $Q_{eff} = 10$, the effective Purcell factor amounts to $C_{eff} \sim 8$, in reasonable agreement with the FDTD simulations. The simulations are however closer to the experimental scenario and indicate maximal Purcell enhancement for a diamond cube with a diameter around 155 nm. For crystals smaller than 140 nm, the enhancement decreases quickly and there is no additional field confinement any more for an edge length of 30 nm.

The measurements show a moderate signature of mode confinement by the ND. Due to experimental imperfections including averaging over dipole orientations and a deteriorated quantum efficiency of the emitters, the amplitude of the lifetime variations is expected to be reduced with respect to theory. This behavior is indeed observed in Fig. 7.17(c), for example for the lifetime minima at the resonances $q = 2$ or $q = 3$ where the measured lifetime is not reduced as much as the simulation for both diamond sizes predicts. However, for $q = 1$, at the presumed onset of additional mode confinement, the lifetime reduction in the data is comparable with the ideally expected variation for the 30 nm diamond. This suggests Purcell enhancement larger than simulated to compensate for experimental imperfection that diminish the lifetime reduction. It should be noted that a small amount of parasitic lifetime modulation seems to affect the data, as well. It is most probably originating from cavity-modulated excitation light leading to variable contributions of the background fluorescence created in the mirrors. This effect can be noticed for larger mirror separations $d > 1.3\,\mu m$, with a periodicity of around 270 nm.

Simulation of the lifetime reduction of a dipole on a silver mirror

The simulations of the effective Purcell factor furthermore yield the lifetime reduction of an emitter on the outcoupling mirror alone, compared to free space[4]. At $d \sim 2\,\mu\text{m}$, the lifetime modification is negligible and effective Purcell factors of $C_{\text{eff},\parallel} = 1.07$ and $C_{\text{eff},\perp} = 0.37$ are obtained for parallel and normal dipoles, respectively (see Fig. 7.20(a)). Averaging over the dipole orientations yields $C_{\text{eff,m}} = \frac{2}{3} \cdot C_{\text{eff},\parallel} + \frac{1}{3} \cdot C_{\text{eff},\perp} = 0.8$, resulting in a total reduction of the lifetime on the mirror by a factor of 1.8.

7.2.3. Cavity-enhanced fluorescence lifetime imaging with a plane-concave silver-dielectric cavity

Fluorescence lifetime imaging microscopy (FLIM) is a powerful method for the investigation of fluorescent samples. FLIM allows to observe photophysical events that are difficult or impossible to observe on the basis of the fluorescence intensity [414]. In contrast to the fluorescence intensity, the fluorescence lifetime is more stable against all kinds of parasitic variations of the collected photon flux, originating from modifications of the excitation power, photo bleaching, scattered light, etc.. FFPCs provide a way for an efficient implementation of this technique, and hold promise for both a high spatial resolution, as well as a cavity-enhanced sensitivity [61, 63].

Here, cavity-enhanced fluorescence lifetime imaging is demonstrated with a hybrid microcavity consisting of a planar silver mirror and a dielectrically coated fiber with a concave profile[5]. The cavity is embedded into the standard confocal microscope setup described in Section 6.1. Dielectric coatings offer the possibility for a large transmission at the wavelength of the excitation light, such that the excitation power can be reduced to a minimum, and the intra-cavity power is only slightly influenced by length changes of the cavity. Thus, the amount of background fluorescence created in the fiber or the mirror stack is reduced considerably, resulting in an increased signal-to-noise ratio, which is beneficial for both intensity-based confocal microscopy and FLIM.

At the same time, the reflectivity at the emitter wavelength can be very large for dielectric mirrors, such that the cavity finesse is only limited by the reflectivity of the silver mirror[6]. Note that the penetration of the electric cavity field into the metallic mirror is negligible compared to the penetration into the dielectric mirror. The latter slightly increases the minimal achievable mode volume[7]. In summary, the hybrid silver-dielectric cavity design offers the flexibility of dielectric coating designs in combination with an ultra-small mode volume.

Nanodiamonds (STG100) on the planar mirror serve as fluorescent sample. Pulsed

[4] For a theoretical description of the behavior of the decay rate of a dipole in front of a planar mirror consult for instance [339].

[5] Radius of curvature $R = 50\,\mu\text{m}$, determined by white light interferometry

[6] The finesse obtained from spectra is $\mathcal{F} = 32 \pm 1$ at $\lambda = 700\,\text{nm}$ for this setting.

[7] For this microcavity, the shortest cavity length resonant with NV center fluorescence is at $d = \lambda$, limited to almost equal parts by the profile depth $t \sim 200\,\text{nm}$ and the penetration depth into the dielectric mirror $d_{\text{pen}} = 220\,\text{nm}$. The expected smallest achievable mode volume amounts to $2.1\,\lambda^3$.

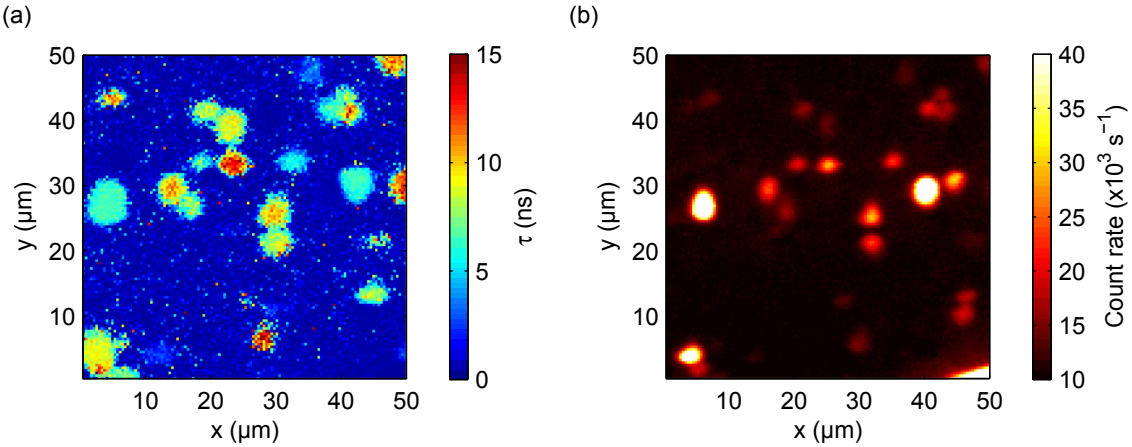

Figure 7.22.: (a) FLIM map of an NV center sample inside a hybrid silver-dielectric cavity. (b) Fluorescence intensity scan of the same region.

excitation with a broad-band light source[8] is performed through the cavity fiber, while the planar mirror is scanned through the cavity mode. Fluorescence collection[9] is performed via the microscope objective. For each mirror position, a TCSPC histogram is recorded and fitted with a mono-exponential decay, yielding the decay time τ.

Figure 7.22(a) shows an example of a FLIM image of an area of $(50\,\mu m)^2$, for an excitation power of 2 mW. It contains several emitters of variable lifetimes ranging from about 5 to 15 ns. The short values might be explained by a reduced lifetime due to self-interference of the emission on the silver mirror. The cavity length was set to around 8 µm, such that several nearby cavity resonances sample the fluorescence spectrum. For this rather large mirror distance and broad-band excitation, variations in the cavity length, originating from the lateral stepping motion, hardly affect the fluorescence lifetime. Thus, stabilization of the cavity length is not necessary. The spatial resolution is given by the cavity mode width, which is slightly larger than the one achieved for standard confocal microscopy, in this case. It can however be improved by reducing the cavity length. Furthermore, higher order transversal modes can serve to additionally boost the spatial resolution [61]. The same region is imaged by recording the fluorescence intensity for excitation with 1 mW of cw laser light at 532 nm through the cavity fiber, as shown in Fig. 7.22(b). To average over intensity fluctuations induced by changes of the cavity length[10], the latter was actively modulated around 10 µm at 20 Hz with the stacked piezoelectric actuator. The comparison of the two imaging methods highlights the better contrast achieved by FLIM.

[8] The SC source is filtered to a spectral band spanning from roughly 525 to 575 nm with a set of interference filters (Semrock FF01-550/49-25, FF01-650/SP-25, FF01-950/SP-25)

[9] For better contrast, the fluorescence is spectrally filtered with a long pass (Thorlabs FEL0650)

[10] The applied stacked piezoelectric stepper motors inevitably induce fluctuations of the cavity length.

8. Conclusion and outlook

The coupling of NV centers to microcavities holds a lot of promise for the practical implementation of fundamental quantum information processing concepts, and in particular for bright single-photon sources and efficient spin-readout at ambient conditions. In this thesis, we have investigated the coupling of the fluorescence of NV centers to fiber-based Fabry-Pérot microcavities at room temperature. Ultra-small mode volumes and a very high finesse are achievable with this cavity design that furthermore combines several advantageous features, among them intrinsic fiber-coupling, open access to the mode volume, tunabilty over a wide range, as well as the possibility to stabilize the cavity length.

The Fabry-Pérot-type cavities were realized with a planar macroscopic mirror and a microscopic mirror on the end face of an optical fiber. We made use of advanced CO_2-laser micromachining to manufacture concave profiles with very low surface roughness on the fiber tip. Nanodiamonds containing single NV centers or emitter ensembles are directly placed on the macroscopic mirror, allowing for excellent coupling to the cavity mode. By scanning the macroscopic mirror through the cavity mode, different emitters can be studied with a single cavity.

A first set of cavity fibers was produced in collaboration with the group of Prof. Jakob Reichel at ENS Paris. Mirror structures with diameters between 20 and 60 µm, radii of curvature between 35 and 200 µm, and depths between 0.5 and 3 µm were manufactured. Measurements of the surface roughness of the yet uncoated fibers, resulted in values as low as 0.14 nm, such that scattering loss due to the mirror substrate is negligible. To demonstrate the feasibility of high-finesse fiber-based cavities, some of these fibers have been coated with low-loss, dielectric mirrors with a transmission of 10 ppm. A finesse of up to 170 000 was measured for a test cavity consisting of one single-mode and one multi-mode fiber at a cavity length of 6.9 µm.

With an advanced CO_2-laser setup that was later installed in Munich, we manufactured a series of fibers having mirror profiles with diameters as small as 4 µm, radii of curvature as low as 5 µm, and structure depths between 0.01 and 3 µm. Furthermore, the fiber edges were cropped by laser machining to enable ultimately short mirror spacings. The penetration depth into the mirrors was reduced dramatically by using silver instead of a dielectric coating. These modifications resulted in the realization of fiber-based cavities with ultra-small mode volumes, as small as $1\lambda^3$. Resonances with a single antinode of the electromagnetic field were observed, while full tunability was sustained.

Two complementary concepts for the coupling of NV centers to fiber-based Farby-Pérot cavities were realized. In a first approach, the scaling laws for the cavity enhancement of broadband emitters have been experimentally verified using a high-finesse cavity with

dielectric mirror coatings. By direct comparison of free-space and cavity enhanced emission spectra, the effective and ideal Purcell factors were determined for a large range of quality factors ($Q = 6 \cdot 10^3 - 2 \cdot 10^6$) and mode volumes ($V = 16 - 600\,\mu m^3$). The effective Purcell factor remains small, because the narrow cavity resonance couples only to a small fraction of the broad phonon sideband emission spectrum of the NV center. In contrast, the emission spectral density could be increased by up to a factor of 300, corresponding to the ideal Purcell factor achievable with this resonator. It is worth mentioning that the finesse of $\mathcal{F} = 30\,000$ is preserved, even when rather large diamond nanocrystals are introduced into the cavity mode.

These results may pave the way for the implementation of efficient, widely-tunable, narrow-band single-photon sources at room temperature. Even the generation of indistinguishable single photons with solid-state emitters that are subject to strong dephasing seems in reach, as proposed by Grange *et al.* [322]. Furthermore, coupling of the ZPL of the NV center at cryogenic temperatures to high-finesse fiber-based Fabry-Pérot cavities holds out the prospect of reaching the strong coupling regime. These aspects are discussed in more detail below.

A second approach was based on NV centers coupled to ultra-small mode volume cavities with silver mirrors. We have demonstrated that efficient extraction of single photons is feasible even for quantum systems with a broad emission spectrum. Purcell enhancement combined with a large coupling efficiency into a well-collectable mode leads to net count rates surpassing free-space rates. Up to $1.6 \cdot 10^6$ photons per second were collected from a single NV center. In addition, the tunable modification of the spontaneous emission lifetime of NV center ensembles provided direct evidence of the Purcell effect, and we found an effective Purcell factor of up to 2. The large variation in the spontaneous lifetime points to the reduction of the mode volume due to the build-up of a transversal waveguide-like mode in diamond nanocrystals with appropriate dimensions, in addition to the Fabry-Pérot cavity mode. We have performed FDTD simulations resulting in effective Purcell factors of up to 11 for NV centers and of up to 63 for SiV centers, supporting our notion of the waveguide effect. The collection efficiency β would then amount to 0.91 (NV) and 0.98 (SiV), respectively. Furthermore, the background fluorescence would be reduced dramatically. Source efficiencies $\beta\eta_c$ of 76% (NV), and 82% (SiV), respectively, could be obtained for optimized mirror coatings, restricted by the finite absorption loss of silver. The controlled fabrication of diamond nanostructures [20, 415, 416] might allow to optimally exploit the waveguide effect and lead to bright single-photon sources and highly efficient single-spin-readout at ambient conditions. Even without additional mode confinement by the ND, SiV centers coupled to fiber-based cavities with ultra-small mode volume and high finesse have the potential for efficient single-photons sources operating at rates surpassing 1 GHz [320].

Generation of indistinguishable single photons at room temperature

Indistinguishable single photons are a key requirement for the implementation of various quantum information processing protocols, including linear optical quantum computing [101] or long-distance quantum teleportation [417]. Indistinguishable photons are photons with a Fourier-transform-limited linewidth with identical frequency and polarization. Whether a pair of photons is indistinguishable in deed, can be tested experimentally by investigating their quantum mechanical interference behavior, harnessing the Hong-Ou-Mandel effect [325].

The intrinsic degree of indistinguishability of the photons from a quantum emitter can be defined by $I = \gamma/(\gamma+\gamma^*)$ (Eq. 2.67), with the population decay rate γ and the pure dephasing rate γ^* [322]. For typical solid-state emitters at room temperature like the NV center, the pure dephasing rate is orders of magnitude larger than the population decay rate. Consequently, the intrinsic indistinguishability is practically zero.

To enable a larger degree of indistinguishability one may spectrally filter the photons after being emitted. However, the efficiency drops with the narrowing of the filter, such that a reasonable degree of indistinguishability results in a very low efficiency. By coupling the emitter to an optical resonator, both a high degree of indistinguishability and efficiency can be achieved. For instance, a Purcell-enhanced spontaneous emission rate would lead to a larger γ and thus to a larger degree of indistinguishability. Yet, to obtain a considerable effect, it would be necessary to realize Purcell factors on the order of γ^*/γ, which is currently not in experimental reach.

Another approach seems more promising to obtain single photons with a high degree of indistinguishability from quantum emitters that exhibit strong dephasing: In an unconventional coupling regime, for moderate cavity-emitter coupling strengths and high cavity quality factors Q, the broad emission spectrum of a dissipative quantum system can be funneled into the narrow cavity resonance, such that the associated efficiency exceeds the effect of pure spectral filtering by far, even though the concept involves a general trade-off between the degree of indistinguishability and the efficiency [322]. This so-called incoherent good-cavity regime is characterized by a coherent coupling rate $2g \ll \kappa + \gamma + \gamma^*$ and a cavity decay rate $\kappa < \gamma + \gamma^*$. In this domain, the cavity is able to store photons for a period of time that is on the order of or longer than the dephasing time of the emitter, and the cavity itself acts as an effective emitter that is pumped incoherently by the quantum emitter.

The degree of indistinguishability is then given by

$$I = \frac{\gamma + \frac{\kappa R}{\kappa + R}}{\gamma + \kappa + 2R}, \tag{8.1}$$

where $R = 4g_0^2/(\kappa + \gamma + \gamma^*)$ denotes the effective transfer rate between the cavity and the emitter (Eq. 4.39). A large degree of indistinguishability is thus obtained for $\kappa < \gamma$ and $R < \gamma$, i.e. the cavity decay rate should be small enough to enable the generation of Fourier-transform limited photons by spectral filtering without influencing the emission dynamics of the quantum emitter significantly.

In the weak coupling regime, the probability to obtain a photon from the cavity mode per initial excitation, i.e. the efficiency, is given by

$$\beta = \frac{\kappa R}{\kappa R + \gamma\,(\kappa + R)}. \tag{8.2}$$

A large efficiency is found in the domain where $R > \gamma$ and $\kappa > R$, which is however not accompanied with a large degree of indistinguishability in the good-cavity regime. Yet, compared to linear spectral filtering, much larger values of the product of the efficiency and the indistinguishability βI can be realized.

If we assume a linear filter with a spectral width $\Delta\nu_\mathrm{f}$, to filter the emission of a broadband emitter with $\Delta\nu_\mathrm{f} \ll \gamma^*$, the source efficiency has an upper limit of $\beta \leq \Delta\nu_\mathrm{f}/\gamma^*$. Furthermore, the degree of indistinguishability is limited by $I_\mathrm{f} \leq \gamma/\Delta\nu_\mathrm{f}$, due to the Fourier-transform condition. In conclusion, linear spectral filtering results in a product $\beta_\mathrm{f} I_\mathrm{f} \leq \gamma/\gamma^*$.

For comparison of the performance of the presented cavity-based concept with the maximum value attainable by spectral filtering techniques, a cavity-funneling factor is now defined

$$F = \frac{\gamma}{\gamma^*}\beta I. \tag{8.3}$$

Values in excess of unity express a cavity-funneling effect, or in other words F can bee seen as the minimal enhancement ratio βI compared to spectral filtering. Since the cavity mode can be collected much more efficiently than spontaneous emission in free space, the benefit will be larger in fact.

To demonstrate that large funneling factors are compatible with a reasonable degree of indistinguishability in the incoherent good-cavity regime, we briefly discuss the model case of an SiV center coupled to a plano-concave cavity at room temperature. The fluorescence emission lifetime of the SiV center is around 1 ns, corresponding to a spontaneous decay rate of $\gamma/2\pi = 160\,\mathrm{MHz}$ (FWHM). At room temperature, SiV centers in NDs have shown an emission linewidth on the order of 1 nm [265]. We thus assume a dephasing rate $\gamma^*/2\pi = 550\,\mathrm{GHz}$ (FWHM). The cavity decay rate scales inversely proportional to the cavity finesse and the effective cavity length $\kappa \sim 1/\mathcal{F}d$ (Eq. 4.5). In order to meet the requirement for a sufficient degree of indistinguishability $\kappa < \gamma$, a concave mirror with a radius of curvature of $r = 100\,\mu\mathrm{m}$ is chosen, enabling rather large cavity lengths. However, since a larger mirror spacing results in a larger mode volume $V = \frac{\lambda}{4}d^2\sqrt{\frac{r}{d} - 1}$ (Eq. 3.43), the coherent coupling rate $g_0 = \sqrt{3c\lambda^2\gamma/4\pi V}$ (Eq. 4.13) decreases and may yield a lower effective coupling rate R, efficiency β and funneling ratio F at the same time.

To illustrate the full relation, the degree of indistinguishability and the funneling ratio are shown as a function of the effective cavity length and the cavity finesse in Figs 8.1(a,b). The necessary trade-off between the indistinguishability and the funneling ratio becomes evident. While the indistinguishability increases with growing finesse and cavity length, the funneling ratio is large for very short mirror spacing and a moderate finesse around 30 000. A good compromise is found for instance, for $d = 35\,\mu\mathrm{m}$ and $\mathcal{F} = 100\,000$, where

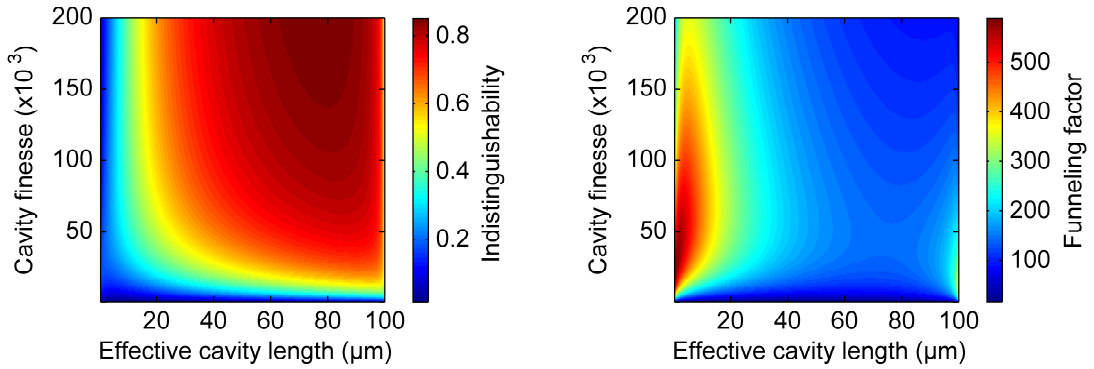

Figure 8.1.: (a) Indistinguishability I and (b) funneling factor F as a function of the effective cavity length and the cavity finesse for a plano-concave cavity with a radius of curvature of 100 µm, evaluated for an SiV center at room temperature.

$I = 0.70$, $\beta = 0.09$, and $F = 210$, representing the very efficient funneling of the emission spectrum into the well-collectable and narrow cavity mode with linewidth κ.

Cavity-coupling of the ZPL of NV centers at cryogenic temperatures

Coupling of the ZPL of the NV center to a high-finesse FFPC at cryogenic temperatures holds promise for the realization of coherent light-matter interaction. The strong coupling regime is reached when the coherent coupling rate $g_0 = \sqrt{3c\lambda^2\gamma_{0,\mathrm{ZPL}}/4\pi V}$ (Eq. 4.13) is larger than the cavity decay rate $\kappa = \pi c/2\mathcal{F}d$ (Eq. 4.5), the free-space spontaneous emission rate $\gamma_{0,\mathrm{ZPL}}$, and the dephasing rate γ^*, which is typically large for solid-state quantum emitters (see below). To find out when the cavity is in principle able to satisfy this tough requirement, we determine the ratio g_0/κ [51]. For a plano-concave cavity architecture, it is given by

$$g_0/\kappa = \frac{2\sqrt{3}}{\pi^{3/2}}\sqrt{\frac{\gamma_{0,\mathrm{ZPL}}\lambda}{c}}\frac{\mathcal{F}}{(r/d-1)^{1/4}}, \tag{8.4}$$

pointing out that the mirror radius of curvature R and the finesse $\mathcal{F}$ need to be optimized. Note that a larger cavity length d also leads to a larger ratio, but at the same decreases the absolute value of the coherent coupling rate g_0 due to the larger mode volume. This can be detrimental with respect to surpassing a large dephasing rate. Additionally, clipping loss and working close the stability range set practical limits to long cavities [51].

In this work, we have demonstrated that fiber-based Fabry-Pérot cavities with a finesse of 170 000 are feasible with dielectric mirrors. Furthermore, mirror profiles with radii of curvature $r \gtrsim 5$ µm have been manufactured. We expect that these properties can be combined in one cavity in order to reach the strong coupling regime. For the further

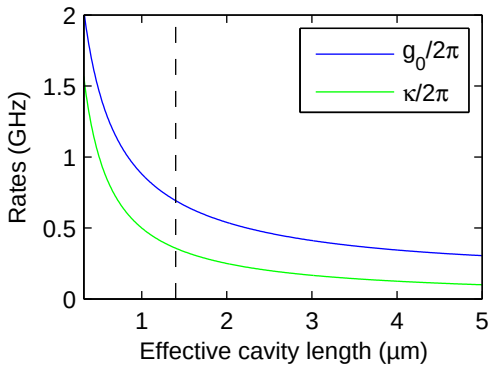

Figure 8.2.: Cavity decay rate κ and coherent coupling rate g_0 for the coupling of the NV center's ZPL to a FFPC at cryogenic temperatures. The effective cavity length is bounded below (black dashed line) by the profile depth and the penetration depth. To enter the strong coupling regime, the dephasing rate $\gamma^*/2\pi$ needs to stay below the coherent coupling rate $g_0/2\pi$.

estimation, we assume a plano-concave cavity with a mirror profile with a radius of curvature of $r = 10\,\mu\text{m}$. It is obtained for a structure with a diameter $D = 8\,\mu\text{m}$ and a depth $t = 800\,\text{nm}$, for instance. The maximum surface angle of a concave profile with these parameters is below 10°, such that additional loss due to an inclined coating stack is negligible. The structure diameter is still large enough to prevent notable clipping loss for short cavities, as well. Penetration into the mirror stack is approximately on the order of 600 nm. Additionally minding the structure depth, effective cavity lengths down to at least 2 µm are possible, corresponding to a cavity field with six antinodes, i.e. $6 \cdot \lambda/2$, for the wavelength of the ZPL $\lambda = 637\,\text{nm}$. The remaining distance of 600 nm between the protruding surface of the profile and the plane mirror enables sufficient freedom for alignment and tunability. We have demonstrated that cropping of the fiber edges by laser machining or mechanical polishing enables even shorter mirror distances, in practice. For a chosen finesse of 150 000, the cavity decay rate amounts to $\kappa/2\pi = 250\,\text{MHz}$ (HWHM), at an effective cavity length of 2 µm.

To evaluate the achievable coherent coupling strength, the branching ratio of the ZPL $\zeta_0 = 0.04$ has to be considered, as well as the splitting of the excited state into six fine-structure levels. For the transitions between the ground state $m_\text{s} = 0$ and the excited states E_x and E_y, a branching ratio of $\zeta_0(E_x, E_y) \approx 0.02$ is assumed for ideal state initialization [240]. An overall free-space spontaneous emission rate of $\gamma_{0,\text{ZPL}}/2\pi = \zeta_0(E_x, E_y) \cdot \gamma_0/2\pi \approx 80\,\text{kHz}$ (HWHM) is obtained for $2\gamma_0/2\pi = 8\,\text{MHz}$. This value corresponds to a lifetime $\tau = 1/2\gamma_0 = 20\,\text{ns}$, typically encountered for NV centers in NDs. The resulting coupling strength g_0 exceeds the cavity decay rate κ and the free-space rate $\gamma_{0,\text{ZPL}}$, as shown in Fig. 8.2.

Eventually, the achievable dephasing rate of the ZPL at low temperatures will be the limiting parameter with respect to realizing strong coupling. The broadening mechanism

of the ZPL of the NV centers has been thoroughly discussed in Section 2.2.4.2. Line broadening is dominated by dephasing due to the dynamic Jahn-Teller effect, as well as spectral diffusion resulting from fluctuations of the electrostatic environment. For ultra-pure synthetic bulk diamond grown by chemical vapor deposition, linewidths of a few hundred MHz have been demonstrated at cryogenic temperatures [254]. Even nearly lifetime-limited linewidths have been reported for both bulk diamond samples [29], and nanocrystals [68]. However, the abundance of NV centers exhibiting these superior properties in a ND sample is presumably very low. Dephasing rates of $\gamma^*/2\pi \approx 500\,\mathrm{MHz}$ (HWHM), would just suffice to enter the strong coupling regime, $g_0 > (\kappa, \gamma_0, \gamma^*)$, as noticeable in Fig. 8.2. The effective Purcell factor would then amount to roughly $C_{\mathrm{eff}} = 140$ at $d_{\mathrm{eff}} = 2\,\mu\mathrm{m}$. Alternatively, fabricated diamond nanostructures [20, 415, 416] or diamond membranes could be introduced into the cavity and provide preferable optical and spin properties.

In summary, realizing coherent light-matter interaction by coupling the ZPL of the NV center to fiber-based Fabry-Pérot cavities at cryogenic temperatures appears challenging but feasible. To this end, a suitable diamond sample is required where the broadening of the ZPL due to dephasing or spectral diffusion is low. This is achievable for ultra-pure synthetic diamond [418] and might even be encountered with sufficient abundance in NDs.

However, remember that strong coupling is not a mandatory demand for the successful implementation of most quantum information processing protocols based on solid-state emitters. The Purcell effect in the weak coupling regime can already lead to significantly enhanced fluorescence emission into the cavity mode, such that dephasing and spectral diffusion become effectively masked. Primarily, a large Purcell factor $C_{\mathrm{eff}} \gg 1$ is thus necessary to enable, for instance, efficient optical readout and initialization of the quantum states, efficient quantum gates [36], or entanglement [258]. Since the internal degrees of freedom of a quantum emitter like the NV center can be extremely sensitive to external physical parameters like nanoscale electromagnetic fields or temperature, their efficient readout would be highly beneficial for various sensing applications [39, 40, 20, 43]. To allow for fast optical retrieval of information from the quantum system, the decay rate of the cavity κ should be chosen rather large.

These requirements can be expressed more elegantly in terms of the effective transfer rate between the cavity and the emitter $R = 4g_0^2/(\kappa + \gamma_0 + \gamma^*)$ (Eq. 4.39) [26]. On resonance it is directly proportional to the effective Purcell factor $R = C_{\mathrm{eff}}\gamma_0$ (Eq. 4.40). In the bad cavity regime, i.e. $\kappa > R$, the parameter R takes the role of an effective spontaneous emission rate or spectral emission width. In conclusion, to maximize R and to obtain a high photon yield, "only" the coherent coupling rate needs to surpass the spontaneous emission rate of the emitter: $g_0 \gg \gamma_0$. Regarding both g_0 and κ, the cavity mode volume and length have to be chosen as small as possible. Note that this regime enables an outcoupling efficiency $\beta = \kappa R/[\kappa R + \gamma_0(\kappa + R)]$ close to unity and large effective outcoupling rates $R_{\mathrm{eff}} = R\kappa/(R + \kappa)$ [26].

The achievable domain of the effective coupling rate R is evaluated for the ZPL of the

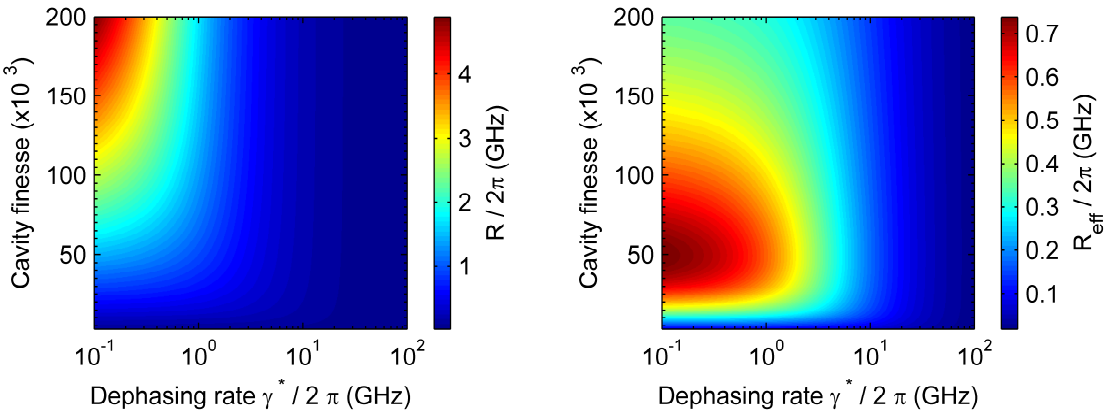

Figure 8.3.: (a) Effective spontaneous emission rate R and (b) effective outcoupling rate R_{eff} as a function of the dephasing rate $\gamma^*/2\pi$ in logarithmic scaling and the cavity finesse $\mathcal{F}$ in linear scaling.

NV center at cryogenic temperatures coupled to a plano-concave Fabry-Pérot cavity with an effective cavity length of 2 µm and a radius of curvature of $r = 10\,\mu\text{m}$, corresponding to a mode volume of approximately $V = 4.9\,\lambda^3$. We have demonstrated, that these cavity parameters are attainable, in practice. Like in the previous example, the free-space spontaneous emission rate of the ZPL is assumed to be on the order of $\gamma_{0,\text{ZPL}}/2\pi \approx 80\,\text{kHz}$, such that $g_{0,\text{ZPL}}/2\pi \approx 760\,\text{MHz}$.

In general, all involved transitions including the ZPL ($k = 1$), as well as the PSB ($k = 2, 3, ...$) have to be considered for the evaluation of the total effective transition rate $R = \sum_k R_k = \sum_k 4g_{0k}^2\Gamma_k / \left(\Gamma_k^2 + 4\Delta_k^2\right)$, with $\Gamma_k = \kappa_k + \gamma_0 + \gamma_k^*$ (see Eq. 4.39). However, at cryogenic temperatures, the PSB transitions have much larger dephasing rates γ_k^* than the ZPL. Thus, the dominant contribution to R is stemming from the coupling of the ZPL.

Figure 8.3 displays the behavior of the effective spontaneous emission rate R and the effective outcoupling rate R_{eff} as a function of the dephasing rate γ^* of the ZPL and the cavity finesse $\mathcal{F}$. In the current model, the dephasing rate γ^* is varied over large range from 100 MHz to 100 GHz to illustrate the influence of pure dephasing and spectral diffusion. If pure dephasing stemming from the dynamical Jahn-Teller effect [246] would be the dominant line broadening mechanism, these dephasing rates would be encountered at temperatures reaching from about 22 to 100 K (compare with Fig. 2.4). The cavity finesse is varied from 3 000 to 200 000. Since fiber-based Fabry-Pérot cavities are easily tunable, the cavity is assumed to be on resonance with the ZPL.

As shown in Fig. 8.3(a), a maximal effective spontaneous emission rate of almost 5 GHz is obtained for maximal cavity finesse and minimal dephasing. However, the efficient outcoupling of the photons via the cavity mode requires slightly larger cavity decay

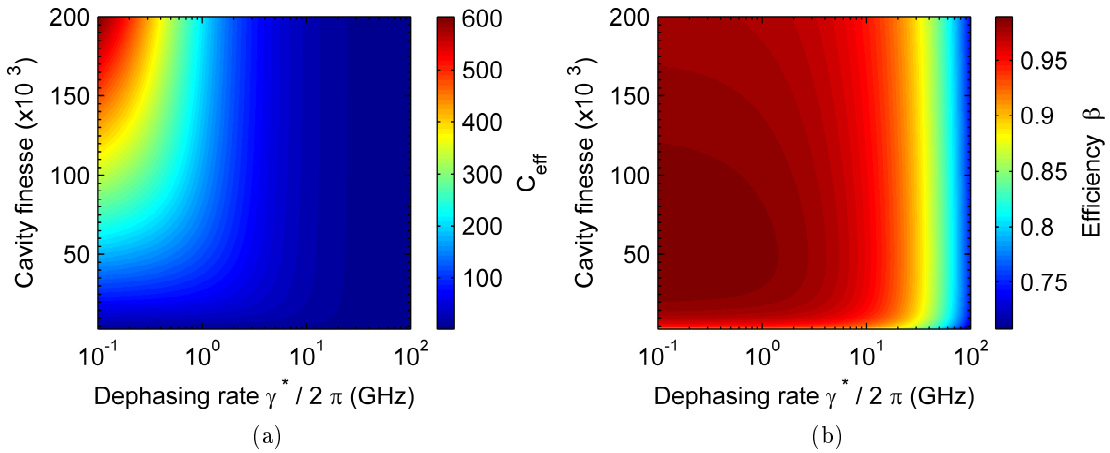

(a) (b)

Figure 8.4.: (a) Effective Purcell factor C_{eff} and (b) efficiency β as a function of the dephasing rate $\gamma^*/2\pi$ in logarithmic scaling and the cavity finesse $\mathcal{F}$ in linear scaling.

rates, i.e. a lower cavity finesse. This behavior is demonstrated in Fig. 8.3(b), where the effective outcoupling rate R_{eff} is shown for the same parameter range. The maximum of $R_{\text{eff}} \approx 740\,\text{MHz}$ is found for $\kappa/2\pi = 2g_0/2\pi = 1.5\,\text{GHz}$ (FWHM), corresponding to a moderate cavity finesse of about 50 000. As obvious from Fig. 8.4(a), the effective Purcell factor is directly proportional to the effective emission rate $C_{\text{eff}} = R/\gamma_0$, with a maximal value of $C_{\text{eff}} \approx 600$. Figure. 8.4(b) displays the efficiency β, which is larger than 0.7 over the whole parameter range with a maximum of 0.99.

To give an example for a rather large dephasing rate, we choose $\gamma^*/2\pi = 40\,\text{GHz}$, corresponding to the pure dephasing rate around the temperature of liquid nitrogen $T = 77\,\text{K}$. For a finesse of $\mathcal{F} = 50\,000$, the figures of merit amount to $R/2\pi = 57\,\text{MHz}$, $R_{\text{eff}}/2\pi = 55\,\text{MHz}$, $C_{\text{eff}} = 7.1$ and $\beta = 0.87$. Reducing the dephasing rate to $\gamma^*/2\pi = 5\,\text{GHz}$ would result in $R/2\pi = 360\,\text{MHz}$, $R_{\text{eff}}/2\pi = 290\,\text{MHz}$, $C_{\text{eff}} = 45$, and $\beta > 0.97$.

Besides the NV center, the SiV center constitutes a promising candidate for the coupling of a color center in diamond to microcavities. Owing to its quite exceptional split vacancy configuration, the SiV center exhibits inversion symmetry and its ZPL emission is thus more robust against electric charge fluctuations in its environment [263, 275]. As a result, negligible spectral diffusion and small inhomogeneous broadening have been observed [275, 274]. Besides in low-strain bulk diamond samples, excellent spectral properties have also been demonstrated for single SiV centers in NDs, i.e. nearly lifetime-limited linewidths on the order of 300 MHz [419], absolute photostability, and minimal spectral diffusion [70]. The beneficial features of the SiV center have already been harnessed to realize a quantum-optical switch at the single-photon level [106]. To this end, the color centers have been coupled to one-dimensional diamond waveguides and photonic-crystal microcavities with a mode volume $V \approx 2.5\,\lambda^3$ and a cavity quality factor $Q \approx 7200$ [420].

FFPC have the potential to even surpass these cavity parameters, while additionally being tunable. We have performed experiments with single SiV centers at room temperature coupled to a FFPC with a mode volume as small as $3.4\,\lambda^3$ and a cavity quality factor of $1.9 \cdot 10^4$. The observed effective Purcell factors of up to 9.2 hold a lot of promise [320]. Unfortunately, the excellent spin coherence encountered for NV centers has not yet been attained with the SiV center.

A. Abbreviations

AlAs	Aluminum arsenide
APD	Avalanche photo diode
BB84	Quantum key distribution scheme by C. Bennett and G. Brassard from 1984 [121]
CQED	Cavity quantum electrodynamics
DBR	Distributed Bragg reflector
EOM	Electro-optic modulator
Eq.	Equation
FDTD	Finite-difference time-domain
FFPC	Fiber Fabry-Pérot caviy
Fig.	Figure
FND	Fluorescent nanodiamond
FWHM	Full width at half maximum
GaAs	Gallium arsenide
HBT	Hanbury Brown and Twiss [321, 113]
HPHT	High-pressure high-temperature
HWHM	Half width at half maximum
InAs	Indium arsenide
LDOS	Local density of states
MM	Multi-mode
ND	Nanodiamond
PMMA	Polymethylmethacrylat
PSB	Phonon sideband

SEM	Scanning electron microscope
SLED	Superluminescent diode
SM	Single-mode
SPS	Single-photon source
STG100	Diamond sample with 100 nm crystals from Stuttgart
Tai35	Diamond sample with 30 nm crystals from Taiwan
Tai100	Diamond sample with 100 nm crystals from Taiwan
TCSPC	Time-correlated single-photon counting
QD	Quantum dot
QE	Quantum efficiency
QIP	Quantum information processing
qubit	Quantum bit
ZPL	Zero-phonon line

Bibliography

[1] G. Rempe, *Atoms in an optical cavity: Quantum electrodynamics in confined space*, Contemporary Physics **34**, 119 (1993).

[2] R. Miller, T. E. Northup, K. M. Birnbaum, A. Boca, A. D. Boozer, and H. J. Kimble, *Trapped atoms in cavity QED: coupling quantized light and matter*, Journal of Physics B: Atomic, Molecular and Optical Physics **38**, S551 (2005).

[3] H. Walther, B. T. H. Varcoe, B.-G. Englert, and T. Becker, *Cavity quantum electrodynamics*, Reports on Progress in Physics **69**, 1325 (2006).

[4] S. Haroche, *Nobel Lecture: Controlling photons in a box and exploring the quantum to classical boundary*, Rev. Mod. Phys. **85**, 1083 (2013).

[5] S. Haroche and J. M. Raimond, *Exploring the quantum*, Oxford Univ. Press, 2006.

[6] M. A. Nielsen and I. L. Chuang, *Quantum computation and quantum information*, Cambridge university press, 2010.

[7] K. Kupferschmidt, *Europe to bet up to Euro 1 billion on quantum technology*, Science (2016).

[8] P. W. Shor, *Polynomial-Time Algorithms for Prime Factorization and Discrete Logarithms on a Quantum Computer*, SIAM Review **41**, 303 (1999).

[9] N. Gisin, G. Ribordy, W. Tittel, and H. Zbinden, *Quantum cryptography*, Reviews of Modern Physics **74**, 145 (2002).

[10] N. Gisin and R. Thew, *Quantum communication*, Nature Photonics **1**, 165 (2007).

[11] E. M. Purcell, *Spontaneous Emission Probabilities at Radio Frequencies*, Physical Review- Proceedings of the American Physical Society **69**, 681 (1946).

[12] J. Vuckovic, D. Fattal, C. Santori, G. S. Solomon, and Y. Yamamoto, *Enhanced single-photon emission from a quantum dot in a micropost microcavity*, Applied Physics Letters **82**, 3596 (2003).

[13] J. Claudon, J. Bleuse, N. S. Malik, M. Bazin, P. Jaffrennou, N. Gregersen, C. Sauvan, P. Lalanne, and J.-M. Gerard, *A highly efficient single-photon source based on a quantum dot in a photonic nanowire*, Nat Photon **4**, 174 (2010).

[14] M. D. Birowosuto, H. Sumikura, S. Matsuo, H. Taniyama, P. J. van Veldhoven, R. Nötzel, and M. Notomi, *Fast Purcell-enhanced single photon source in 1,550-nm telecom band from a resonant quantum dot-cavity coupling*, Scientific Reports **2** (2012).

[15] O. Gazzano, S. Michaelis de Vasconcellos, C. Arnold, A. Nowak, E. Galopin, I. Sagnes, L. Lanco, A. Lemaitre, and P. Senellart, *Bright solid-state sources of indistinguishable single photons*, Nat Comms **4**, 1425 (2013).

[16] T. B. Hoang, G. M. Akselrod, and M. H. Mikkelsen, *Ultrafast Room-Temperature Single Photon Emission from Quantum Dots Coupled to Plasmonic Nanocavities*, Nano Letters **16**, 270 (2016).

[17] A. Young, C. Y. Hu, L. Marseglia, J. P. Harrison, J. L. O'Brien, and J. G. Rarity, *Cavity enhanced spin measurement of the ground state spin of an NV center in diamond*, New Journal of Physics **11**, 013007 (2009).

[18] L. Li, T. Schröder, E. H. Chen, M. Walsh, I. Bayn, J. Goldstein, O. Gaathon, M. E. Trusheim, M. Lu, J. Mower, and et al., *Coherent spin control of a nanocavity-enhanced qubit in diamond*, Nat Comms **6**, 6173 (2015).

[19] B. M. Chernobrod and G. P. Berman, *Spin microscope based on optically detected magnetic resonance*, Journal of Applied Physics **97**, 014903 (2005).

[20] P. Maletinsky, S. Hong, M. S. Grinolds, B. Hausmann, M. D. Lukin, R. L. Walsworth, M. Loncar, and A. Yacoby, *A robust scanning diamond sensor for nanoscale imaging with single nitrogen-vacancy centres*, Nature Nanotechnology **7**, 320 (2012).

[21] J. Wrachtrup and F. Jelezko, *Processing quantum information in diamond*, J. Phys.: Condens. Matter **18**, S807 (2006).

[22] M. Loncar and A. Faraon, *Quantum photonic networks in diamond*, MRS Bulletin **38**, 144 (2013).

[23] L. Childress and R. Hanson, *Diamond NV centers for quantum computing and quantum networks*, MRS Bulletin **38**, 134 (2013).

[24] I. Aharonovich and E. Neu, *Diamond Nanophotonics*, Advanced Optical Materials **2**, 911 (2014).

[25] T. Schröder, S. L. Mouradian, J. Zheng, M. E. Trusheim, M. Walsh, E. H. Chen, L. Li, I. Bayn, and D. Englund, *Quantum nanophotonics in diamond [Invited]*, J. Opt. Soc. Am. B **33**, B65 (2016).

[26] A. Auffeves, D. Gerace, J.-M. Gerard, M. F. Santos, L. C. Andreani, and J.-P. Poizat, *Controlling the dynamics of a coupled atom-cavity system by pure dephasing*, Physical Review B **81**, 245419 (2010).

[27] A. Meldrum, P. Bianucci, and F. Marsiglio, *Modification of ensemble emission rates and luminescence spectra for inhomogeneously broadened distributions of quantum dots coupled to optical microcavities*, Optics Express **18**, 10230 (2010).

[28] Y. Dumeige, R. Alleaume, P. Grangier, F. Treussart, and J.-F. Roch, *Controling the single-diamond nitrogen-vacancy color center photoluminescence spectrum with a Fabry-Perot microcavity*, New J. Phys. **13**, 025015 (2011).

[29] K.-M. C. Fu, C. Santori, P. E. Barclay, L. J. Rogers, N. B. Manson, and R. G. Beausoleil, *Observation of the Dynamic Jahn-Teller Effect in the Excited States of Nitrogen-Vacancy Centers in Diamond*, Physical Review Letters **103**, 256404 (2009).

[30] Y.-S. Park, A. K. Cook, and H. Wang, *Cavity QED with Diamond Nanocrystals and Silica Microspheres*, Nano Lett. **6**, 2075 (2006).

[31] H. Kaupp, C. Deutsch, H.-C. Chang, J. Reichel, T. W. Hänsch, and D. Hunger, *Scaling laws of the cavity enhancement for nitrogen-vacancy centers in diamond*, Physical Review A **88** (2013).

[32] R. Albrecht, *Coupling of a Single Nitrogen-Vacancy center in Diamond to a Fiber-based Microcavity*, PhD thesis, Universität des Saarlandes, 2014.

[33] C. K. Law and H. J. Kimble, *Deterministic generation of a bit-stream of single-photon pulses*, Journal of Modern Optics **44**, 2067 (1997).

[34] M. V. G. Dutt, L. Childress, L. Jiang, E. Togan, J. Maze, F. Jelezko, A. S. Zibrov, P. R. Hemmer, and M. D. Lukin, *Quantum Register Based on Individual Electronic and Nuclear Spin Qubits in Diamond*, Science **316**, 1312 (2007).

[35] P. Neumann, N. Mizuochi, F. Rempp, P. Hemmer, H. Watanabe, S. Yamasaki, V. Jacques, T. Gaebel, F. Jelezko, and J. Wrachtrup, *Multipartite Entanglement Among Single Spins in Diamond*, Science **320**, 1326 (2008).

[36] P. Neumann, R. Kolesov, B. Naydenov, J. Beck, F. Rempp, M. Steiner, V. Jacques, G. Balasubramanian, M. L. Markham, D. J. Twitchen, J. Pezzagna, S.and Meijer, J. Twamley, F. Jelezko, and J. Wrachtrup, *Quantum register based on coupled electron spins in a room-temperature solid*, Nature Physics **6**, 249 (2010).

[37] G. D. Fuchs, G. Burkard, P. V. Klimov, and D. D. Awschalom, *A quantum memory intrinsic to single nitrogen-vacancy centres in diamond*, Nature Physics **7**, 789 (2011).

[38] P. C. Maurer, G. Kucsko, C. Latta, L. Jiang, N. Y. Yao, S. D. Bennett, F. Pastawski, D. Hunger, N. Chisholm, M. Markham, and et al., *Room-Temperature Quantum Bit Memory Exceeding One Second*, Science **336**, 1283 (2012).

[39] G. Balasubramanian, I. Y. Chan, R. Kolesov, M. Al-Hmoud, J. Tisler, C. Shin, C. Kim, A. Wojcik, P. R. Hemmer, A. Krueger, T. Hanke, A. Leitenstorfer, R. Bratschitsch, F. Jelezko, and J. Wrachtrup, *Nanoscale imaging magnetometry with diamond spins under ambient conditions*, Nature **455**, 648 (2008).

[40] J. R. Maze, P. L. Stanwix, J. S. Hodges, S. Hong, J. M. Taylor, P. Cappellaro, L. Jiang, M. V. G. Dutt, E. Togan, A. S. Zibrov, A. Yacoby, R. L. Walsworth, and M. Lukin, *Nanoscale magnetic sensing with an individual electronic spin in diamond*, Nature **455**, 644 (2008).

[41] J. M. Taylor, P. Cappellaro, L. Childress, L. Jiang, D. Budker, P. R. Hemmer, A. Yacoby, R. Walsworth, and M. D. Lukin, *High-sensitivity diamond magnetometer with nanoscale resolution*, Nature Physics **4**, 810 (2008).

[42] F. Dolde, H. Fedder, M. W. Doherty, T. Nöbauer, F. Rempp, G. Balasubramanian, T. Wolf, F. Reinhard, L. C. L. Hollenberg, F. Jelezko, and J. Wrachtrup, *Electric-field sensing using single diamond spins*, Nature Physics **7**, 459 (2011).

[43] P. Neumann, I. Jakobi, F. Dolde, C. Burk, R. Reuter, G. Waldherr, J. Honert, T. Wolf, A. Brunner, J. H. Shim, H. Sumiya, J. Isoya, and J. Wrachtrup, *High-Precision Nanoscale Temperature Sensing Using Single Defects in Diamond*, Nano Lett. **13**, 2738 (2013).

[44] G. Kucsko, P. C. Maurer, N. Y. Yao, M. Kubo, H. J. Noh, P. K. Lo, H. Park, and M. D. Lukin, *Nanometre-scale thermometry in a living cell*, Nature **500**, 54 (2013).

[45] T. Plakhotnik, M. W. Doherty, J. H. Cole, R. Chapman, and N. B. Manson, *All-Optical Thermometry and Thermal Properties of the Optically Detected Spin Resonances of the NV Center in Nanodiamond*, Nano Lett. **14**, 4989 (2014).

[46] K. J. Vahala, *Optical microcavities*, Nature **424**, 839 (2003).

[47] J. Ward and O. Benson, *WGM microresonators: sensing, lasing and fundamental optics with microspheres*, Laser & Photonics Reviews **5**, 553 (2011).

[48] J. D. Joannopoulos et al., *Photonic crystals: putting a new twist on light*, Nature **386**, 143 (1997).

[49] M. Trupke, E. A. Hinds, S. Eriksson, E. A. Curtis, Z. Moktadir, E. Kukharenka, and M. Kraft, *Microfabricated high-finesse optical cavity with open access and small volume*, Applied Physics Letters **87**, 211106 (2005).

[50] T. Steinmetz, Y. Colombe, D. Hunger, T. W. Hänsch, A. Balocchi, R. J. Warburton, and J. Reichel, *Stable fiber-based Fabry-Perot cavity*, Applied Physics Letters **89**, 111110 (2006).

[51] D. Hunger, T. Steinmetz, Y. Colombe, C. Deutsch, T. W. Hänsch, and J. Reichel, *A fiber Fabry-Perot cavity with high finesse*, New J. Phys. **12**, 065038 (2010).

[52] A. Muller, E. B. Flagg, J. R. Lawall, and G. S. Solomon, *Ultrahigh-finesse, low-mode-volume Fabry-Perot microcavity*, Opt. Lett. **35**, 2293 (2010).

[53] D. Hunger, C. Deutsch, R. J. Barbour, R. J. Warburton, and J. Reichel, *Laser micro-fabrication of concave, low-roughness features in silica*, AIP Advances **2**, 012119 (2012).

[54] M. Uphoff, M. Brekenfeld, G. Rempe, and S. Ritter, *Frequency splitting of polarization eigenmodes in microscopic Fabry-Perot cavities*, New J. Phys. **17**, 013053 (2015).

[55] E. Janitz, M. Ruf, M. Dimock, A. Bourassa, J. Sankey, and L. Childress, *Fabry-Perot microcavity for diamond-based photonics*, Physical Review A **92**, 043844 (2015).

[56] J. Gallego, S. Ghosh, S. K. Alavi, W. Alt, M. Martinez-Dorantes, D. Meschede, and L. Ratschbacher, *High-finesse fiber Fabry-Perot cavities: stabilization and mode matching analysis*, Appl. Phys. B **122**, 47 (2016).

[57] K. Ott, S. Garcia, R. Kohlhaas, K. Schüppert, P. Rosenbusch, R. Long, and J. Reichel, *Millimeter-long fiber Fabry-Perot cavities*, Optics Express **24**, 9839 (2016).

[58] R. Gehr, J. Volz, G. Dubois, T. Steinmetz, Y. Colombe, B. L. Lev, R. Long, J. Esteve, and J. Reichel, *Cavity-Based Single Atom Preparation and High-Fidelity Hyperfine State Readout*, Physical Review Letters **104** (2010).

[59] J. Volz, R. Gehr, G. Dubois, J. Esteve, and J. Reichel, *Measurement of the internal state of a single atom without energy exchange*, Nature **475**, 210 (2011).

[60] C. Toninelli, Y. Delley, T. Stöferle, A. Renn, S. Götzinger, and V. Sandoghdar, *A scanning microcavity for in situ control of single-molecule emission*, Applied Physics Letters **97**, 021107 (2010).

[61] M. Mader, J. Reichel, T. W. Hänsch, and D. Hunger, *A scanning cavity microscope*, Nat Comms **6**, 7249 (2015).

[62] H. Kelkar, D. Wang, D. Martin-Cano, B. Hoffmann, S. Christiansen, S. Götzinger, and V. Sandoghdar, *Sensing Nanoparticles with a Cantilever-Based Scannable Optical Cavity of Low Finesse and Sub-λ^3 Volume*, Physical Review Applied **4** (2015).

[63] T. Hümmer, J. Noe, M. S. Hofmann, T. W. Hänsch, A. Högele, and D. Hunger, *Cavity-enhanced Raman microscopy of individual carbon nanotubes*, Nat Comms **7**, 12155 (2016).

[64] A. Beveratos, R. Brouri, T. Gacoin, J.-P. Poizat, and P. Grangier, *Nonclassical radiation from diamond nanocrystals*, Physical Review A **64** (2001).

[65] H. Chew, *Radiation and lifetimes of atoms inside dielectric particles*, Physical Review A **38**, 3410 (1988).

[66] F. Inam, M. Steel, and S. Castelletto, *Effects of the hosting nano-environment modifications on NV centres fluorescence emission*, Diamond and Related Materials **45**, 64 (2014).

[67] P. Tamarat, T. Gaebel, J. R. Rabeau, M. Khan, A. D. Greentree, H. Wilson, L. C. L. Hollenberg, S. Prawer, P. Hemmer, F. Jelezko, and J. Wrachtrup, *Stark Shift Control of Single Optical Centers in Diamond*, Physical Review Letters **97**, 083002 (2006).

[68] Y. Shen, T. M. Sweeney, and H. Wang, *Zero-phonon linewidth of single nitrogen vacancy centers in diamond nanocrystals*, Physical Review B **77**, 033201 (2008).

[69] G. Balasubramanian, P. Neumann, D. Twitchen, M. Markham, R. Kolesov, N. Mizuochi, J. Isoya, J. Achard, J. Beck, J. Tissler, V. Jacques, P. R. Hemmer, F. Jelezko, and J. Wrachtrup, *Ultralong spin coherence time in isotopically engineered diamond*, Nat Mater **8**, 383 (2009).

[70] K. Li, Y. Zhou, A. Rasmita, I. Aharonovich, and W. Gao, *Nonblinking Emitters with Nearly Lifetime-Limited Linewidths in CVD Nanodiamonds*, Physical Review Applied **6**, 024010 (2016).

[71] H. S. Knowles, D. M. Kara, and M. Atatüre, *Observing bulk diamond spin coherence in high-purity nanodiamonds*, Nature Materials **13**, 21 (2013).

[72] A. D. Greentree, *Nanodiamonds in Fabry-Perot cavities: a route to scalable quantum computing*, New J. Phys. **18**, 021002 (2016).

[73] H. Kaupp, T. Hümmer, M. Mader, B. Schlederer, J. Benedikter, P. Haeusser, H.-C. Chang, H. Fedder, T. W. Hänsch, and D. Hunger, *Purcell-Enhanced Single-Photon Emission from Nitrogen-Vacancy Centers Coupled to a Tunable Microcavity*, Physical Review Applied **6**, 054010 (2016).

[74] M. Steiner, F. Schleifenbaum, C. Stupperich, A. Failla, A. Hartschuh, and A. Meixner, *A new microcavity design for single molecule detection*, Journal of Luminescence **119-120**, 167 (2006).

[75] M. Steiner, A. Hartschuh, R. Korlacki, and A. J. Meixner, *Highly efficient tunable single photon source based on single molecules*, Applied Physics Letters **90**, 183122 (2007).

[76] M. Steiner, A. Virgilio Failla, A. Hartschuh, F. Schleifenbaum, C. Stupperich, and A. Johann Meixner, *Controlling molecular broadband-emission by optical confinement*, New J. Phys. **10**, 123017 (2008).

[77] A. I. Chizhik, A. M. Chizhik, D. Khoptyar, S. Bär, A. J. Meixner, and J. Enderlein, *Probing the Radiative Transition of Single Molecules with a Tunable Microresonator*, Nano Lett. **11**, 1700 (2011).

[78] R. Albrecht, A. Bommer, C. Deutsch, J. Reichel, and C. Becher, *Coupling of a Single Nitrogen-Vacancy Center in Diamond to a Fiber-Based Microcavity*, Physical Review Letters **110** (2013).

[79] R. Albrecht, A. Bommer, C. Pauly, F. Mücklich, A. W. Schell, P. Engel, T. Schröder, O. Benson, J. Reichel, and C. Becher, *Narrow-band single photon emission at room temperature based on a single nitrogen-vacancy center coupled to an all-fiber-cavity*, Applied Physics Letters **105**, 073113 (2014).

[80] S. Johnson, P. R. Dolan, T. Grange, A. A. P. Trichet, G. Hornecker, Y. C. Chen, L. Weng, G. M. Hughes, A. A. R. Watt, A. Auffeves, and J. M. Smith, *Tunable cavity coupling of the zero phonon line of a nitrogen-vacancy defect in diamond*, New J. Phys. **17**, 122003 (2015).

[81] S. Schietinger, T. Schröder, and O. Benson, *One-by-One Coupling of Single Defect Centers in Nanodiamonds to High-Q Modes of an Optical Microresonator*, Nano Lett. **8**, 3911 (2008).

[82] M. Gregor, R. Henze, T. Schröder, and O. Benson, *On-demand positioning of a preselected quantum emitter on a fiber-coupled toroidal microresonator*, Applied Physics Letters **95**, 153110 (2009).

[83] P. E. Barclay, K.-M. C. Fu, C. Santori, and R. G. Beausoleil, *Chip-based microcavities coupled to nitrogen-vacancy centers in single crystal diamond*, Applied Physics Letters **95**, 191115 (2009).

[84] P. E. Barclay, K.-M. Fu, C. Santori, and R. G. Beausoleil, *Hybrid photonic crystal cavity and waveguide for coupling to diamond NV-centers*, Optics Express **17**, 9588 (2009).

[85] C. Santori, P. E. Barclay, K.-M. C. Fu, R. G. Beausoleil, S. Spillane, and M. Fisch, *Nanophotonics for quantum optics using nitrogen-vacancy centers in diamond*, Nanotechnology **21**, 274008 (2010).

[86] P. E. Barclay, K.-M. C. Fu, C. Santori, A. Faraon, and R. G. Beausoleil, *Hybrid Nanocavity Resonant Enhancement of Color Center Emission in Diamond*, Physical Review X **1**, 011007 (2011).

[87] K.-M. C. Fu, P. E. Barclay, C. Santori, A. Faraon, and R. G. Beausoleil, *Low-temperature tapered-fiber probing of diamond nitrogen-vacancy ensembles coupled to GaP microcavities*, New J. Phys. **13**, 055023 (2011).

[88] A. Faraon, P. E. Barclay, C. Santori, K.-M. C. Fu, and R. G. Beausoleil, *Resonant enhancement of the zero-phonon emission from a colour centre in a diamond cavity*, Nature Photon **5**, 301 (2011).

[89] B. J. M. Hausmann, B. Shields, Q. Quan, P. Maletinsky, M. McCutcheon, J. T. Choy, T. M. Babinec, A. Kubanek, A. Yacoby, M. D. Lukin, and et al., *Integrated Diamond Networks for Quantum Nanophotonics*, Nano Lett. **12**, 1578 (2012).

[90] A. Faraon, C. Santori, Z. Huang, K.-M. C. Fu, V. M. Acosta, D. Fattal, and R. G. Beausoleil, *Quantum photonic devices in single-crystal diamond*, New J. Phys. **15**, 025010 (2013).

[91] J. Wolters, A. W. Schell, G. Kewes, N. Nüsse, M. Schoengen, H. Döscher, T. Hannappel, B. Löchel, M. Barth, and O. Benson, *Enhancement of the zero phonon line emission from a single nitrogen vacancy center in a nanodiamond via coupling to a photonic crystal cavity*, Applied Physics Letters **97**, 141108 (2010).

[92] D. Englund, B. Shields, K. Rivoire, F. Hatami, J. Vucovic, H. Park, and M. D. Lukin, *Deterministic Coupling of a Single Nitrogen Vacancy Center to a Photonic Crystal Cavity*, Nano Lett. **10**, 3922 (2010).

[93] T. van der Sar, J. Hagemeier, W. Pfaff, E. C. Heeres, S. M. Thon, H. Kim, P. M. Petroff, T. H. Oosterkamp, D. Bouwmeester, and R. Hanson, *Deterministic nanoassembly of a coupled quantum emitter-photonic crystal cavity system*, Applied Physics Letters **98**, 193103 (2011).

[94] A. Faraon, C. Santori, Z. Huang, V. M. Acosta, and R. G. Beausoleil, *Coupling of Nitrogen-Vacancy Centers to Photonic Crystal Cavities in Monocrystalline Diamond*, Physical Review Letters **109** (2012).

[95] B. J. M. Hausmann, B. J. Shields, Q. Quan, Y. Chu, N. P. de Leon, R. Evans, M. J. Burek, A. S. Zibrov, M. Markham, D. J. Twitchen, and et al., *Coupling of NV Centers to Photonic Crystal Nanobeams in Diamond*, Nano Lett. **13**, 5791 (2013).

[96] J. C. Lee, D. O. Bracher, S. Cui, K. Ohno, C. A. McLellan, X. Zhang, P. Andrich, B. Aleman, K. J. Russell, A. P. Magyar, and et al., *Deterministic coupling of delta-doped nitrogen vacancy centers to a nanobeam photonic crystal cavity*, Applied Physics Letters **105**, 261101 (2014).

[97] L. Li, T. Schröder, E. H. Chen, H. Bakhru, and D. Englund, *One-dimensional photonic crystal cavities in single-crystal diamond*, Photonics and Nanostructures - Fundamentals and Applications **15**, 130 (2015).

[98] J. Riedrich-Möller, L. Kipfstuhl, C. Hepp, E. Neu, C. Pauly, F. Mücklich, A. Baur, M. Wandt, S. Wolff, M. Fischer, S. Gsell, M. Schreck, and C. Becher, *One- and two-dimensional photonic crystal microcavities in single crystal diamond*, Nature Nanotechnology **7**, 69 (2011).

[99] J. Riedrich-Möller, C. Arend, C. Pauly, F. Mücklich, M. Fischer, S. Gsell, M. Schreck, and C. Becher, *Deterministic Coupling of a Single Silicon-Vacancy*

Color Center to a Photonic Crystal Cavity in Diamond, Nano Lett. **14**, 5281 (2014).

[100] J. Riedrich-Möller, S. Pezzagna, J. Meijer, C. Pauly, F. Mücklich, M. Markham, A. M. Edmonds, and C. Becher, *Nanoimplantation and Purcell enhancement of single nitrogen-vacancy centers in photonic crystal cavities in diamond*, Applied Physics Letters **106**, 221103 (2015).

[101] E. Knill, R. Laflamme, and G. J. Milburn, *A scheme for efficient quantum computation with linear optics*, Nature **409**, 46 (2001).

[102] J. L. OBrien, G. J. Pryde, A. G. White, T. C. Ralph, and D. Branning, *Demonstration of an all-optical quantum controlled-NOT gate*, Nature **426**, 264 (2003).

[103] J. L. O'Brien, *Optical Quantum Computing*, Science **318**, 1567 (2007).

[104] J. L. O'Brien, A. Furusawa, and J. Vucovic, *Photonic quantum technologies*, Nature Photon **3**, 687 (2009).

[105] J. Wolters, G. Kewes, A. W. Schell, N. Nüsse, M. Schoengen, B. Löchel, T. Hanke, R. Bratschitsch, A. Leitenstorfer, T. Aichele, and et al., *Coupling of single nitrogen-vacancy defect centers in diamond nanocrystals to optical antennas and photonic crystal cavities*, physica status solidi (b) **249**, 918 (2012).

[106] A. Sipahigil, R. E. Evans, D. D. Sukachev, M. J. Burek, J. Borregaard, M. K. Bhaskar, C. T. Nguyen, J. L. Pacheco, H. A. Atikian, C. Meuwly, and et al., *An integrated diamond nanophotonics platform for quantum-optical networks*, Science **354**, 847 (2016).

[107] J. C. Maxwell, *A Dynamical Theory of the Electromagnetic Field*, Philosophical Transactions of the Royal Society of London **155**, 459 (1865).

[108] M. Planck, *Zur Theorie des Gesetzes der Energieverteilung im Normalspectrum*, Verhandlungen der Deutschen Physikalischen Gesellschaft **2**, 237 (1900).

[109] A. Einstein, *Über einen die Erzeugung und Verwandlung des Lichtes betreffenden heuristischen Gesichtspunkt*, Annalen der Physik **322**, 132 (1905).

[110] G. N. Lewis, *The Conservation of Photons*, Nature **118**, 874 (1926).

[111] A. Zeilinger, G. Weihs, T. Jennewein, and M. Aspelmeyer, *Happy centenary, photon*, Nature **433**, 230 (2005).

[112] J. F. Clauser, *Experimental distinction between the quantum and classical field-theoretic predictions for the photoelectric effect*, Phys. Rev. D **9**, 853 (1974).

[113] R. H. Brown and R. Q. Twiss, *Correlation between Photons in two Coherent Beams of Light*, Nature **177**, 27 (1956).

[114] H. J. Carmichael and D. F. Walls, *A quantum-mechanical master equation treatment of the dynamical Stark effect*, J. Phys. B: At. Mol. Phys. **9**, 1199 (1976).

[115] H. J. Kimble and L. Mandel, *Theory of resonance fluorescence*, Physical Review A **13**, 2123 (1976).

[116] H. J. Kimble, M. Dagenais, and L. Mandel, *Photon Antibunching in Resonance Fluorescence*, Physical Review Letters **39**, 691 (1977).

[117] F. Diedrich and H. Walther, *Nonclassical radiation of a single stored ion*, Physical Review Letters **58**, 203 (1987).

[118] I. L. Chuang and Y. Yamamoto, *Simple quantum computer*, Physical Review A **52**, 3489 (1995).

[119] Q. A. Turchette, C. J. Hood, W. Lange, H. Mabuchi, and H. J. Kimble, *Measurement of Conditional Phase Shifts for Quantum Logic*, Physical Review Letters **75**, 4710 (1995).

[120] D. P. DiVincenzo, *The Physical Implementation of Quantum Computation*, Fortschritte der Physik **48**, 771 (2000).

[121] C. H. Bennett, *Quantum cryptography: Public key distribution and coin tossing*, in *International Conference on Computer System and Signal Processing, IEEE, 1984*, pages 175–179, 1984.

[122] E. Waks, K. Inoue, C. Santori, D. Fattal, J. Vuckovic, G. S. Solomon, and Y. Yamamoto, *Secure communication: Quantum cryptography with a photon turnstile*, Nature **420**, 762 (2002).

[123] J. Rarity, P. Owens, and P. Tapster, *Quantum Random-number Generation and Key Sharing*, Journal of Modern Optics **41**, 2435 (1994).

[124] T. Jennewein, U. Achleitner, G. Weihs, H. Weinfurter, and A. Zeilinger, *A fast and compact quantum random number generator*, Review of Scientific Instruments **71**, 1675 (2000).

[125] A. Stefanov, N. Gisin, O. Guinnard, L. Guinnard, and H. Zbinden, *Optical quantum random number generator*, Journal of Modern Optics **47**, 595 (2000).

[126] A. Einstein, B. Podolsky, and N. Rosen, *Can Quantum-Mechanical Description of Physical Reality Be Considered Complete?*, Physical Review **47**, 777 (1935).

[127] J. S. Bell, *On the Einstein-Podolsky-Rosen paradox*, Physics **1**, 195 (1964).

[128] S. J. Freedman and J. F. Clauser, *Experimental Test of Local Hidden-Variable Theories*, Physical Review Letters **28**, 938 (1972).

[129] A. Aspect, J. Dalibard, and G. Roger, *Experimental Test of Bell's Inequalities Using Time-Varying Analyzers*, Physical Review Letters **49**, 1804 (1982).

[130] G. Weihs, T. Jennewein, C. Simon, H. Weinfurter, and A. Zeilinger, *Violation of Bell's Inequality under Strict Einstein Locality Conditions*, Physical Review Letters **81**, 5039 (1998).

[131] M. A. Rowe, D. Kielpinski, V. Meyer, C. A. Sackett, W. M. Itano, C. Monroe, and D. J. Wineland, *Experimental violation of a Bell's inequality with efficient detection*, Nature **409**, 791 (2001).

[132] D. N. Matsukevich, P. Maunz, D. L. Moehring, S. Olmschenk, and C. Monroe, *Bell Inequality Violation with Two Remote Atomic Qubits*, Physical Review Letters **100** (2008).

[133] M. Ansmann, H. Wang, R. C. Bialczak, M. Hofheinz, E. Lucero, M. Neeley, A. D. O'Connell, D. Sank, M. Weides, J. Wenner, and et al., *Violation of Bell's inequality in Josephson phase qubits*, Nature **461**, 504 (2009).

[134] T. Scheidl, R. Ursin, J. Kofler, S. Ramelow, X.-S. Ma, T. Herbst, L. Ratschbacher, A. Fedrizzi, N. K. Langford, T. Jennewein, and et al., *Violation of local realism with freedom of choice*, Proceedings of the National Academy of Sciences **107**, 19708 (2010).

[135] J. Hofmann, M. Krug, N. Ortegel, L. Gerard, M. Weber, W. Rosenfeld, and H. Weinfurter, *Heralded Entanglement Between Widely Separated Atoms*, Science **337**, 72 (2012).

[136] M. Giustina, A. Mech, S. Ramelow, B. Wittmann, J. Kofler, J. Beyer, A. Lita, B. Calkins, T. Gerrits, S. W. Nam, and et al., *Bell violation using entangled photons without the fair-sampling assumption*, Nature **497**, 227 (2013).

[137] B. G. Christensen, K. T. McCusker, J. B. Altepeter, B. Calkins, T. Gerrits, A. E. Lita, A. Miller, L. K. Shalm, Y. Zhang, S. W. Nam, and et al., *Detection-Loophole-Free Test of Quantum Nonlocality, and Applications*, Physical Review Letters **111**, 130406 (2013).

[138] N. Brunner, D. Cavalcanti, S. Pironio, V. Scarani, and S. Wehner, *Bell nonlocality*, Rev. Mod. Phys. **86**, 419 (2014).

[139] B. Hensen, H. Bernien, A. E. Dreau, A. Reiserer, N. Kalb, M. S. Blok, J. Ruitenberg, R. F. L. Vermeulen, R. N. Schouten, C. Abellan, and et al., *Loophole-free Bell inequality violation using electron spins separated by 1.3 kilometres*, Nature **526**, 682 (2015).

[140] M. Giustina et al., *Significant-Loophole-Free Test of Bell's Theorem with Entangled Photons*, Physical Review Letters **115**, 250401 (2015).

[141] L. K. Shalm et al., *Strong Loophole-Free Test of Local Realism*, Physical Review Letters **115** (2015).

[142] D. Bouwmeester, J.-W. Pan, K. Mattle, M. Eibl, H. Weinfurter, and A. Zeilinger, *Experimental quantum teleportation*, Nature **390**, 575 (1997).

[143] T. Jennewein, C. Simon, G. Weihs, H. Weinfurter, and A. Zeilinger, *Quantum Cryptography with Entangled Photons*, Physical Review Letters **84**, 4729 (2000).

[144] M. D. Eisaman, J. Fan, A. Migdall, and S. V. Polyakov, *Invited Review Article: Single-photon sources and detectors*, Review of Scientific Instruments **82**, 071101 (2011).

[145] M. Oxborrow and A. G. Sinclair, *Single-photon sources*, Contemporary Physics **46**, 173 (2005).

[146] B. Lounis and M. Orrit, *Single-photon sources*, Reports on Progress in Physics **68**, 1129 (2005).

[147] C. Santori, D. Fattal, and Y. Yamamoto, *Single-photon devices and applications*, John Wiley and Sons, 2010.

[148] C. J. Chunnilall, I. P. Degiovanni, S. Kück, I. Müller, and A. G. Sinclair, *Metrology of single-photon sources and detectors: a review*, Opt. Eng **53**, 081910 (2014).

[149] W. Barnes, G. Björk, J. Gerard, P. Jonsson, J. Wasey, P. Worthing, and V. Zwiller, *Solid-state single photon sources: light collection strategies*, The European Physical Journal D - Atomic, Molecular and Optical Physics **18**, 197 (2002).

[150] C. Wang, *A solid-state single photon source based on color centers in diamond*, PhD thesis, Ludwig-Maximilians-Universität München, 2007.

[151] I. Aharonovich, S. Castelletto, D. A. Simpson, C.-H. Su, A. D. Greentree, and S. Prawer, *Diamond-based single-photon emitters*, Reports on Progress in Physics **74**, 076501 (2011).

[152] A. J. Shields, *Semiconductor quantum light sources*, Nature Photon **1**, 215 (2007).

[153] S. Buckley, K. Rivoire, and J. Vuckovic, *Engineered quantum dot single-photon sources*, Reports on Progress in Physics **75**, 126503 (2012).

[154] T. Schmitt-Manderbach, H. Weier, M. Fürst, R. Ursin, F. Tiefenbacher, T. Scheidl, J. Perdigues, Z. Sodnik, C. Kurtsiefer, J. G. Rarity, A. Zeilinger, and H. Weinfurter, *Experimental Demonstration of Free-Space Decoy-State Quantum Key Distribution over 144 km*, Physical Review Letters **98**, 010504 (2007).

[155] B. Y. Zel'Dovich and D. Klyshko, *Field statistics in parametric luminescence*, JETP Letters **9**, 40 (1969).

[156] D. C. Burnham and D. L. Weinberg, *Observation of Simultaneity in Parametric Production of Optical Photon Pairs*, Physical Review Letters **25**, 84 (1970).

[157] M. Houe and P. D. Townsend, *An introduction to methods of periodic poling for second-harmonic generation*, J. Phys. D: Appl. Phys. **28**, 1747 (1995).

[158] L. E. Myers, R. C. Eckardt, M. M. Fejer, R. L. Byer, W. R. Bosenberg, and J. W. Pierce, *Quasi-phase-matched optical parametric oscillators in bulk periodically poled $LiNbO_3$*, J. Opt. Soc. Am. B **12**, 2102 (1995).

[159] M. Förtsch, J. U. Fürst, C. Wittmann, D. Strekalov, A. Aiello, M. V. Chekhova, C. Silberhorn, G. Leuchs, and C. Marquardt, *A versatile source of single photons for quantum information processing*, Nature Communications **4**, 1818 (2013).

[160] G. Brida, I. P. Degiovanni, M. Genovese, F. Piacentini, P. Traina, A. Della Frera, A. Tosi, A. Bahgat Shehata, C. Scarcella, A. Gulinatti, and et al., *An extremely low-noise heralded single-photon source: A breakthrough for quantum technologies*, Applied Physics Letters **101**, 221112 (2012).

[161] P. G. Kwiat, K. Mattle, H. Weinfurter, A. Zeilinger, A. V. Sergienko, and Y. Shih, *New High-Intensity Source of Polarization-Entangled Photon Pairs*, Physical Review Letters **75**, 4337 (1995).

[162] R. Ursin, F. Tiefenbacher, T. Schmitt-Manderbach, H. Weier, T. Scheidl, M. Lindenthal, B. Blauensteiner, T. Jennewein, J. Perdigues, P. Trojek, and et al., *Entanglement-based quantum communication over 144 km*, Nature Physics **3**, 481 (2007).

[163] J. F. Clauser and A. Shimony, *Bell's theorem: Experimental tests and implications*, Reports on Progress in Physics **41**, 1881 (1978).

[164] A. Aspect, P. Grangier, and G. Roger, *Experimental Tests of Realistic Local Theories via Bell's Theorem*, Physical Review Letters **47**, 460 (1981).

[165] A. Aspect, P. Grangier, and G. Roger, *Experimental Realization of Einstein-Podolsky-Rosen-Bohm Gedankenexperiment: A New Violation of Bell's Inequalities*, Physical Review Letters **49**, 91 (1982).

[166] P. Grangier, G. Roger, and A. Aspect, *Experimental Evidence for a Photon Anticorrelation Effect on a Beam Splitter: A New Light on Single-Photon Interferences*, Europhys. Lett. **1**, 173 (1986).

[167] J. Kim, , O. Benson, H. Kan, and Y. Yamamoto, *A single-photon turnstile device*, Nature **397**, 500 (1999).

[168] T. Legero, T. Wilk, M. Hennrich, G. Rempe, and A. Kuhn, *Quantum Beat of Two Single Photons*, Physical Review Letters **93**, 070503 (2004).

[169] J. Beugnon, M. P. A. Jones, J. Dingjan, B. Darquie, G. Messin, A. Browaeys, and P. Grangier, *Quantum interference between two single photons emitted by independently trapped atoms*, Nature **440**, 779 (2006).

[170] P. Maunz, D. L. Moehring, S. Olmschenk, K. C. Younge, D. N. Matsukevich, and C. Monroe, *Quantum interference of photon pairs from two remote trapped atomic ions*, Nature Physics **3**, 538 (2007).

[171] D. L. Moehring, P. Maunz, S. Olmschenk, K. C. Younge, D. N. Matsukevich, L.-M. Duan, and C. Monroe, *Entanglement of single-atom quantum bits at a distance*, Nature **449**, 68 (2007).

[172] S. Gerber, D. Rotter, M. Hennrich, R. Blatt, F. Rohde, C. Schuck, M. Almendros, R. Gehr, F. Dubin, and J. Eschner, *Quantum interference from remotely trapped ions*, New J. Phys. **11**, 013032 (2009).

[173] M. Keller, B. Lange, K. Hayasaka, W. Lange, and H. Walther, *A calcium ion in a cavity as a controlled single-photon source*, New J. Phys. **6**, 95 (2004).

[174] A. Kuhn, M. Hennrich, T. Bondo, and G. Rempe, *Controlled generation of single photons from a strongly coupled atom-cavity system*, Applied Physics B **69**, 373 (1999).

[175] M. Hennrich, T. Legero, A. Kuhn, and G. Rempe, *Vacuum-Stimulated Raman Scattering Based on Adiabatic Passage in a High-Finesse Optical Cavity*, Physical Review Letters **85**, 4872 (2000).

[176] S. Brattke, B. T. H. Varcoe, and H. Walther, *Generation of Photon Number States on Demand via Cavity Quantum Electrodynamics*, Physical Review Letters **86**, 3534 (2001).

[177] A. Kuhn, M. Hennrich, and G. Rempe, *Deterministic Single-Photon Source for Distributed Quantum Networking*, Physical Review Letters **89**, 067901 (2002).

[178] J. McKeever, A. Boca, A. D. Boozer, J. R. Buck, and H. J. Kimble, *Experimental realization of a one-atom laser in the regime of strong coupling*, Nature **425**, 268 (2003).

[179] J. McKeever, A. Boca, A. D. Boozer, R. Miller, J. R. Buck, A. Kuzmich, and H. J. Kimble, *Deterministic Generation of Single Photons from One Atom Trapped in a Cavity*, Science **303**, 1992 (2004).

[180] M. Hijlkema, B. Weber, H. P. Specht, S. C. Webster, A. Kuhn, and G. Rempe, *A single-photon server with just one atom*, Nature Physics **3**, 253 (2007).

[181] M. Mücke, J. Bochmann, C. Hahn, A. Neuzner, C. Nölleke, A. Reiserer, G. Rempe, and S. Ritter, *Generation of single photons from an atom-cavity system*, Physical Review A **87**, 063805 (2013).

[182] J. I. Cirac, S. J. van Enk, P. Zoller, H. J. Kimble, and H. Mabuchi, *Quantum Communication in a Quantum Network*, Physica Scripta **T76**, 223 (1998).

[183] T. Wilk, S. C. Webster, A. Kuhn, and G. Rempe, *Single-Atom Single-Photon Quantum Interface*, Science **317**, 488 (2007).

[184] A. D. Boozer, A. Boca, R. Miller, T. E. Northup, and H. J. Kimble, *Reversible State Transfer between Light and a Single Trapped Atom*, Physical Review Letters **98**, 193601 (2007).

[185] H. J. Kimble, *The quantum internet*, Nature **453**, 1023 (2008).

[186] M. Keller, B. Lange, K. Hayasaka, W. Lange, and H. Walther, *Deterministic coupling of single ions to an optical cavity*, Applied Physics B: Lasers and Optics **76**, 125 (2003).

[187] M. Keller, B. Lange, K. Hayasaka, W. Lange, and H. Walther, *Continuous generation of single photons with controlled waveform in an ion-trap cavity system*, Nature **431**, 1075 (2004).

[188] M. Steiner, H. M. Meyer, C. Deutsch, J. Reichel, and M. Köhl, *Single Ion Coupled to an Optical Fiber Cavity*, Physical Review Letters **110**, 043003 (2013).

[189] H. Takahashi, A. Wilson, A. Riley-Watson, F. Orucevic, N. Seymour-Smith, M. Keller, and W. Lange, *An integrated fiber trap for single-ion photonics*, New J. Phys. **15**, 053011 (2013).

[190] B. Brandstätter, A. McClung, K. Schüppert, B. Casabone, K. Friebe, A. Stute, P. O. Schmidt, C. Deutsch, J. Reichel, R. Blatt, and et al., *Integrated fiber-mirror ion trap for strong ion-cavity coupling*, Review of Scientific Instruments **84**, 123104 (2013).

[191] M. Steiner, H. M. Meyer, J. Reichel, and M. Köhl, *Photon Emission and Absorption of a Single Ion Coupled to an Optical-Fiber Cavity*, Physical Review Letters **113**, 263003 (2014).

[192] T. Basche, W. E. Moerner, M. Orrit, and H. Talon, *Photon antibunching in the fluorescence of a single dye molecule trapped in a solid*, Physical Review Letters **69**, 1516 (1992).

[193] F. De Martini, G. Di Giuseppe, and M. Marrocco, *Single-Mode Generation of Quantum Photon States by Excited Single Molecules in a Microcavity Trap*, Physical Review Letters **76**, 900 (1996).

[194] C. Brunel, B. Lounis, P. Tamarat, and M. Orrit, *Triggered Source of Single Photons based on Controlled Single Molecule Fluorescence*, Physical Review Letters **83**, 2722 (1999).

[195] Y. L. A. Rezus, S. G. Walt, R. Lettow, A. Renn, G. Zumofen, S. Götzinger, and V. Sandoghdar, *Single-Photon Spectroscopy of a Single Molecule*, Physical Review Letters **108**, 093601 (2012).

[196] L. Fleury, J.-M. Segura, G. Zumofen, B. Hecht, and U. P. Wild, *Nonclassical Photon Statistics in Single-Molecule Fluorescence at Room Temperature*, Physical Review Letters **84**, 1148 (2000).

[197] B. Lounis and W. E. Moerner, *Single photons on demand from a single molecule at room temperature*, Nature **407**, 491 (2000).

[198] F. Treussart, R. Alleaume, V. Le Floch, L. T. Xiao, J.-M. Courty, and J.-F. Roch, *Direct Measurement of the Photon Statistics of a Triggered Single Photon Source*, Physical Review Letters **89**, 093601 (2002).

[199] A. Kiraz, M. Ehrl, T. Hellerer, . E. Müstecaplioglu, C. Bräuchle, and A. Zumbusch, *Indistinguishable Photons from a Single Molecule*, Physical Review Letters **94**, 223602 (2005).

[200] R. Lettow, V. Ahtee, R. Pfab, A. Renn, E. Ikonen, S. Götzinger, and V. Sandoghdar, *Realization of two Fourier-limited solid-state single-photon sources*, Optics Express **15**, 15842 (2007).

[201] V. Ahtee, R. Lettow, R. Pfab, A. Renn, E. Ikonen, S. Götzinger, and V. Sandoghdar, *Molecules as sources for indistinguishable single photons*, Journal of Modern Optics **56**, 161 (2009).

[202] R. Lettow, Y. L. A. Rezus, A. Renn, G. Zumofen, E. Ikonen, S. Götzinger, and V. Sandoghdar, *Quantum Interference of Tunably Indistinguishable Photons from Remote Organic Molecules*, Physical Review Letters **104**, 123605 (2010).

[203] J. P. Hadden, J. P. Harrison, A. C. Stanley-Clarke, L. Marseglia, Y.-L. D. Ho, B. R. Patton, J. L. OBrien, and J. G. Rarity, *Strongly enhanced photon collection from diamond defect centers under microfabricated integrated solid immersion lenses*, Applied Physics Letters **97**, 241901 (2010).

[204] P. Siyushev, F. Kaiser, V. Jacques, I. Gerhardt, S. Bischof, H. Fedder, J. Dodson, M. Markham, D. Twitchen, F. Jelezko, and et al., *Monolithic diamond optics for single photon detection*, Applied Physics Letters **97**, 241902 (2010).

[205] L. Marseglia, J. P. Hadden, A. C. Stanley-Clarke, J. P. Harrison, B. Patton, Y.-L. D. Ho, B. Naydenov, F. Jelezko, J. Meijer, P. R. Dolan, J. M. Smith, J. G. Rarity, and J. L. O'Brien, *Nanofabricated solid immersion lenses registered to single emitters in diamond*, Applied Physics Letters **98**, 133107 (2011).

[206] S. Castelletto, J. P. Harrison, L. Marseglia, A. C. Stanley-Clarke, B. C. Gibson, B. A. Fairchild, J. P. Hadden, Y.-L. D. Ho, M. P. Hiscocks, K. Ganesan, S. T.

Huntington, F. Ladouceur, A. D. Greentree, S. Prawer, J. L. OBrien, and J. G. Rarity, *Diamond-based structures to collect and guide light*, New J. Phys. **13**, 025020 (2011).

[207] T. Schröder, F. Gädeke, M. J. Banholzer, and O. Benson, *Ultrabright and efficient single-photon generation based on nitrogen-vacancy centres in nanodiamonds on a solid immersion lens*, New J. Phys. **13**, 055017 (2011).

[208] M. Leifgen, T. Schröder, F. Gädeke, R. Riemann, V. Metillon, E. Neu, C. Hepp, C. Arend, C. Becher, K. Lauritsen, and O. Benson, *Evaluation of nitrogen- and silicon-vacancy defect centres as single photon sources in quantum key distribution*, New Journal of Physics **16**, 023021 (2014).

[209] T. Gaebel, I. Popa, A. Gruber, M. Domhan, F. Jelezko, and J. Wrachtrup, *Stable single-photon source in the near infrared*, New Journal of Physics **6**, 98 (2004).

[210] J. R. Rabeau, Y. L. Chin, S. Prawer, F. Jelezko, T. Gaebel, and J. Wrachtrup, *Fabrication of single nickel-nitrogen defects in diamond by chemical vapor deposition*, Applied Physics Letters **86**, 131926 (2005).

[211] E. Wu, J. R. Rabeau, G. Roger, F. Treussart, H. Zeng, P. Grangier, S. Prawer, and J.-F. Roch, *Room temperature triggered single-photon source in the near infrared*, New Journal of Physics **9**, 434 (2007).

[212] T. Iwasaki, F. Ishibashi, Y. Miyamoto, Y. Doi, S. Kobayashi, T. Miyazaki, K. Tahara, K. D. Jahnke, L. J. Rogers, B. Naydenov, and et al., *Germanium-Vacancy Single Color Centers in Diamond*, Scientific Reports **5**, 12882 (2015).

[213] E. A. Ekimov, S. G. Lyapin, K. N. Boldyrev, M. V. Kondrin, R. Khmelnitskiy, V. A. Gavva, T. V. Kotereva, and M. N. Popova, *Germanium-vacancy color center in isotopically enriched diamonds synthesized at high pressures*, JETP Letters **102**, 701 (2015).

[214] F. Jelezko and J. Wrachtrup, *Single defect centres in diamond: A review*, physica status solidi (a) **203**, 3207 (2006).

[215] M. W. Doherty, N. B. Manson, P. Delaney, F. Jelezko, J. Wrachtrup, and L. C. Hollenberg, *The nitrogen-vacancy colour centre in diamond*, Physics Reports **528**, 1 (2013).

[216] V. M. Acosta, A. Jarmola, E. Bauch, and D. Budker, *Optical properties of the nitrogen-vacancy singlet levels in diamond*, Physical Review B **82**, 201202 (2010).

[217] M. W. Doherty, N. B. Manson, P. Delaney, and L. C. L. Hollenberg, *The negatively charged nitrogen-vacancy centre in diamond: the electronic solution*, New Journal of Physics **13**, 025019 (2011).

[218] A. Gruber, A. Dräbenstedt, C. Tietz, L. Fleury, J. Wrachtrup, and C. v. Borczyskowski, *Scanning Confocal Optical Microscopy and Magnetic Resonance on Single Defect Centers*, Science **276**, 2012 (1997).

[219] A. Dräbenstedt, L. Fleury, C. Tietz, F. Jelezko, S. Kilin, A. Nizovtzev, and J. Wrachtrup, *Low-temperature microscopy and spectroscopy on single defect centers in diamond*, Physical Review B **60**, 11503 (1999).

[220] R. Brouri, A. Beveratos, J.-P. Poizat, and P. Grangier, *Photon antibunching in the fluorescence of individual color centers in diamond*, Opt. Lett. **25**, 1294 (2000).

[221] C. Kurtsiefer, S. Mayer, P. Zarda, and H. Weinfurter, *Stable solid-state source of single photons*, Physical Review Letters **85**, 290 (2000).

[222] C.-H. Su, A. D. Greentree, and L. C. L. Hollenberg, *Towards a picosecond transform-limited nitrogen-vacancy based single photon source*, Optics Express **16**, 6240 (2008).

[223] A. T. Collins, M. F. Thomaz, and M. I. B. Jorge, *Luminescence decay time of the 1.945 eV centre in type Ib diamond*, Journal of Physics C: Solid State Physics **16**, 2177 (1983).

[224] E. Ampem-Lassen, D. A. Simpson, B. C. Gibson, S. Trpkovski, F. M. Hossain, S. T. Huntington, K. Ganesan, L. C. L. Hollenberg, and S. Prawer, *Nano-manipulation of diamond-based single photon sources*, Optics Express **17**, 11287 (2009).

[225] T. M. Babinec, B. J. M. Hausmann, M. Khan, Y. Zhang, J. R. Maze, P. R. Hemmer, and M. Loncar, *A diamond nanowire single-photon source*, Nature Nanotechnology **5**, 195 (2010).

[226] J. T. Choy, B. J. M. Hausmann, T. M. Babinec, I. Bulu, M. Khan, P. Maletinsky, A. Yacoby, and M. Loncar, *Enhanced single-photon emission from a diamond-silver aperture*, Nature Photon **5**, 738 (2011).

[227] L. Li, E. H. Chen, J. Zheng, S. L. Mouradian, F. Dolde, T. Schröder, S. Karaveli, M. L. Markham, D. J. Twitchen, and D. Englund, *Efficient Photon Collection from a Nitrogen Vacancy Center in a Circular Bullseye Grating*, Nano Lett. **15**, 1493 (2015).

[228] R. N. Patel, T. Schröder, N. Wan, L. Li, S. L. Mouradian, E. H. Chen, and D. R. Englund, *Efficient photon coupling from a diamond nitrogen vacancy center by integration with silica fiber*, Light: Science & Applications **5**, e16032 (2016).

[229] I. P. Radko, M. Boll, N. M. Israelsen, N. Raatz, J. Meijer, F. Jelezko, U. L. Andersen, and A. Huck, *Determining the internal quantum efficiency of shallow-implanted nitrogen-vacancy defects in bulk diamond*, Optics Express **24**, 27715 (2016).

[230] K. H. Drexhage, H. Kuhn, and F. P. Schäfer, *Variation of the Fluorescence Decay Time of a Molecule in Front of a Mirror*, Berichte der Bunsengesellschaft für physikalische Chemie **72**, 329 (1968).

[231] K. Drexhage, *Influence of a dielectric interface on fluorescence decay time*, Journal of Luminescence **1-2**, 693 (1970).

[232] A. Mohtashami and A. Femius Koenderink, *Suitability of nanodiamond nitrogen-vacancy centers for spontaneous emission control experiments*, New J. Phys. **15**, 043017 (2013).

[233] A. Beveratos, S. Kühn, R. Brouri, T. Gacoin, J.-P. Poizat, and P. Grangier, *Room temperature stable single-photon source*, The European Physical Journal D - Atomic, Molecular, Optical and Plasma Physics **18**, 191 (2002).

[234] H. Schniepp and V. Sandoghdar, *Spontaneous Emission of Europium Ions Embedded in Dielectric Nanospheres*, Physical Review Letters **89**, 257403 (2002).

[235] J. Storteboom, P. Dolan, S. Castelletto, X. Li, and M. Gu, *Lifetime investigation of single nitrogen vacancy centres in nanodiamonds*, Optics Express **23**, 11327 (2015).

[236] F. A. Inam, A. M. Edmonds, M. J. Steel, and S. Castelletto, *Tracking emission rate dynamics of nitrogen vacancy centers in nanodiamonds*, Applied Physics Letters **102**, 253109 (2013).

[237] F. A. Inam, M. D. W. Grogan, M. Rollings, T. Gaebel, J. M. Say, C. Bradac, T. A. Birks, W. J. Wadsworth, S. Castelletto, J. R. Rabeau, and et al., *Emission and Nonradiative Decay of Nanodiamond NV Centers in a Low Refractive Index Environment*, ACS Nano **7**, 3833 (2013).

[238] M. Berthel, O. Mollet, G. Dantelle, T. Gacoin, S. Huant, and A. Drezet, *Photophysics of single nitrogen-vacancy centers in diamond nanocrystals*, Physical Review B **91**, 035308 (2015).

[239] L. J. Rogers, S. Armstrong, M. J. Sellars, and N. B. Manson, *Infrared emission of the NV centre in diamond: Zeeman and uniaxial stress studies*, New Journal of Physics **10**, 103024 (2008).

[240] N. B. Manson, J. P. Harrison, and M. J. Sellars, *Nitrogen-vacancy center in diamond: Model of the electronic structure and associated dynamics*, Physical Review B **74**, 104303 (2006).

[241] L. Robledo, H. Bernien, T. v. d. Sar, and R. Hanson, *Spin dynamics in the optical cycle of single nitrogen-vacancy centres in diamond*, New Journal of Physics **13**, 025013 (2011).

[242] L. T. Hall, J. H. Cole, C. D. Hill, and L. C. L. Hollenberg, *Sensing of Fluctuating Nanoscale Magnetic Fields Using Nitrogen-Vacancy Centers in Diamond*, Physical Review Letters **103**, 220802 (2009).

[243] T. Gaebel, M. Domhan, I. Popa, C. Wittmann, P. Neumann, F. Jelezko, J. R. Rabeau, N. Stavrias, A. D. Greentree, S. Prawer, J. Meijer, J. Twamley, P. Hemmer, and J. Wrachtrup, *Room-temperature coherent coupling of single spins in diamond*, Nature Physics **2**, 408 (2006).

[244] L. Childress, M. V. Gurudev Dutt, J. M. Taylor, A. S. Zibrov, F. Jelezko, J. Wrachtrup, P. R. Hemmer, and M. D. Lukin, *Coherent Dynamics of Coupled Electron and Nuclear Spin Qubits in Diamond*, Science **314**, 281 (2006).

[245] L. Childress, J. M. Taylor, A. S. Sörensen, and M. D. Lukin, *Fault-Tolerant Quantum Communication Based on Solid-State Photon Emitters*, Physical Review Letters **96**, 070504 (2006).

[246] G. Davies, *The Jahn-Teller effect and vibronic coupling at deep levels in diamond*, Reports on Progress in Physics **44**, 787 (1981).

[247] G. Davies, *Vibronic spectra in diamond*, Journal of Physics C: Solid State Physics **7**, 3797 (1974).

[248] G. Davies and M. F. Hamer, *Optical Studies of the 1.945 eV Vibronic Band in Diamond*, Proceedings of the Royal Society of London A: Mathematical, Physical and Engineering Sciences **348**, 285 (1976).

[249] A. Gali, T. Simon, and J. E. Lowther, *An ab initio study of local vibration modes of the nitrogen-vacancy center in diamond*, New Journal of Physics **13**, 025016 (2011).

[250] J. Wolters, N. Sadzak, A. W. Schell, T. Schröder, and O. Benson, *Measurement of the Ultrafast Spectral Diffusion of the Optical Transition of Nitrogen Vacancy Centers in Nano-Size Diamond Using Correlation Interferometry*, Physical Review Letters **110**, 027401 (2013).

[251] T. A. Abtew, Y. Y. Sun, B.-C. Shih, P. Dev, S. B. Zhang, and P. Zhang, *Dynamic Jahn-Teller Effect in the NV-Center in Diamond*, Physical Review Letters **107**, 146403 (2011).

[252] L. C. Bassett, F. J. Heremans, C. G. Yale, B. B. Buckley, and D. D. Awschalom, *Electrical Tuning of Single Nitrogen-Vacancy Center Optical Transitions Enhanced by Photoinduced Fields*, Physical Review Letters **107**, 266403 (2011).

[253] J. Walker, *Optical absorption and luminescence in diamond*, Reports on Progress in Physics **42**, 1605 (1979).

[254] P. Siyushev, H. Pinto, M. Vörös, A. Gali, F. Jelezko, and J. Wrachtrup, *Optically Controlled Switching of the Charge State of a Single Nitrogen-Vacancy Center in Diamond at Cryogenic Temperatures*, Physical Review Letters **110**, 167402 (2013).

[255] V. M. Acosta, C. Santori, A. Faraon, Z. Huang, K.-M. C. Fu, A. Stacey, D. A. Simpson, K. Ganesan, S. Tomljenovic-Hanic, A. D. Greentree, and et al., *Dynamic Stabilization of the Optical Resonances of Single Nitrogen-Vacancy Centers in Diamond*, Physical Review Letters **108**, 206401 (2012).

[256] H. Bernien, L. Childress, L. Robledo, M. Markham, D. Twitchen, and R. Hanson, *Two-Photon Quantum Interference from Separate Nitrogen Vacancy Centers in Diamond*, Physical Review Letters **108**, 043604 (2012).

[257] A. Sipahigil, M. L. Goldman, E. Togan, Y. Chu, M. Markham, D. J. Twitchen, A. S. Zibrov, A. Kubanek, and M. D. Lukin, *Quantum Interference of Single Photons from Remote Nitrogen-Vacancy Centers in Diamond*, Physical Review Letters **108**, 143601 (2012).

[258] E. Togan, Y. Chu, A. S. Trifonov, L. Jiang, J. Maze, L. Childress, M. V. G. Dutt, A. S. Sorensen, P. R. Hemmer, A. S. Zibrov, and et al., *Quantum entanglement between an optical photon and a solid-state spin qubit*, Nature **466**, 730 (2010).

[259] J.-W. Pan, D. Bouwmeester, H. Weinfurter, and A. Zeilinger, *Experimental Entanglement Swapping: Entangling Photons That Never Interacted*, Physical Review Letters **80**, 3891 (1998).

[260] H. Bernien, B. Hensen, W. Pfaff, G. Koolstra, M. S. Blok, L. Robledo, T. H. Taminiau, M. Markham, D. J. Twitchen, L. Childress, and et al., *Heralded entanglement between solid-state qubits separated by three metres*, Nature **497**, 86 (2013).

[261] J. P. Goss, R. Jones, S. J. Breuer, P. R. Briddon, and S. Öberg, *The Twelve-Line 1.682 eV Luminescence Center in Diamond and the Vacancy-Silicon Complex*, Physical Review Letters **77**, 3041 (1996).

[262] A. Gali and J. R. Maze, *Ab initio study of the split silicon-vacancy defect in diamond: Electronic structure and related properties*, Physical Review B **88** (2013).

[263] C. Hepp, T. Müller, V. Waselowski, J. N. Becker, B. Pingault, H. Sternschulte, D. Steinmüller-Nethl, A. Gali, J. R. Maze, M. Atatüre, and et al., *Electronic Structure of the Silicon Vacancy Color Center in Diamond*, Physical Review Letters **112** (2014).

[264] L. J. Rogers, K. D. Jahnke, M. W. Doherty, A. Dietrich, L. P. McGuinness, C. Müller, T. Teraji, H. Sumiya, J. Isoya, N. B. Manson, and et al., *Electronic structure of the negatively charged silicon-vacancy center in diamond*, Physical Review B **89**, 235101 (2014).

[265] E. Neu, D. Steinmetz, J. Riedrich-Möller, S. Gsell, M. Fischer, M. Schreck, and C. Becher, *Single photon emission from silicon-vacancy colour centres in chemical vapour deposition nano-diamonds on iridium*, New J. Phys. **13**, 025012 (2011).

[266] E. Neu, M. Fischer, S. Gsell, M. Schreck, and C. Becher, *Fluorescence and polarization spectroscopy of single silicon vacancy centers in heteroepitaxial nanodiamonds on iridium*, Physical Review B **84**, 205211 (2011).

[267] C. Wang, C. Kurtsiefer, H. Weinfurter, and B. Burchard, *Single photon emission from SiV centres in diamond produced by ion implantation*, Journal of Physics B: Atomic, Molecular and Optical Physics **39**, 37 (2005).

[268] E. Neu, C. Arend, E. Gross, F. Guldner, C. Hepp, D. Steinmetz, E. Zscherpel, S. Ghodbane, H. Sternschulte, D. Steinmüller-Nethl, , Y. Liang, A. Krueger, and C. Becher, *Narrowband fluorescent nanodiamonds produced from chemical vapor deposition films*, Applied Physics Letters **98**, 243107 (2011).

[269] A. V. Turukhin, C.-H. Liu, A. A. Gorokhovsky, R. R. Alfano, and W. Phillips, *Picosecond photoluminescence decay of Si-doped chemical-vapor-deposited diamond films*, Physical Review B **54**, 16448 (1996).

[270] E. Neu, M. Agio, and C. Becher, *Photophysics of single silicon vacancy centers in diamond: implications for single photon emission*, Optics Express **20**, 19956 (2012).

[271] T. Feng and B. D. Schwartz, *Characteristics and origin of the 1.681 eV luminescence center in chemical-vapor-deposited diamond films*, Journal of Applied Physics **73**, 1415 (1993).

[272] E. Neu, C. Hepp, M. Hauschild, S. Gsell, M. Fischer, H. Sternschulte, D. Steinmüller-Nethl, M. Schreck, and C. Becher, *Low-temperature investigations of single silicon vacancy colour centres in diamond*, New J. Phys. **15**, 043005 (2013).

[273] K. D. Jahnke, A. Sipahigil, J. M. Binder, M. W. Doherty, M. Metsch, L. J. Rogers, N. B. Manson, M. D. Lukin, and F. Jelezko, *Electron-phonon processes of the silicon-vacancy centre in diamond*, New J. Phys. **17**, 043011 (2015).

[274] L. Rogers, K. Jahnke, T. Teraji, L. Marseglia, C. Müller, B. Naydenov, H. Schauffert, C. Kranz, J. Isoya, L. McGuinness, and et al., *Multiple intrinsically identical single-photon emitters in the solid state*, Nat Comms **5**, 4739 (2014).

[275] A. Sipahigil, K. D. Jahnke, L. J. Rogers, T. Teraji, J. Isoya, A. S. Zibrov, F. Jelezko, and M. D. Lukin, *Indistinguishable Photons from Separated Silicon-Vacancy Centers in Diamond*, Physical Review Letters **113**, 113602 (2014).

[276] T. Müller, C. Hepp, B. Pingault, E. Neu, S. Gsell, M. Schreck, H. Sternschulte, D. Steinmüller-Nethl, C. Becher, and M. Atatüre, *Optical signatures of silicon-vacancy spins in diamond*, Nat Comms **5**, 3328 (2014).

[277] L. J. Rogers, K. D. Jahnke, M. H. Metsch, A. Sipahigil, J. M. Binder, T. Teraji, H. Sumiya, J. Isoya, M. D. Lukin, P. Hemmer, and F. Jelezko, *All-Optical Initialization, Readout, and Coherent Preparation of Single Silicon-Vacancy Spins in Diamond*, Physical Review Letters **113**, 263602 (2014).

[278] B. Pingault, J. N. Becker, C. H. H. Schulte, C. Arend, C. Hepp, T. Godde, A. I. Tartakovskii, M. Markham, C. Becher, and M. Atatüre, *All-Optical Formation of Coherent Dark States of Silicon-Vacancy Spins in Diamond*, Physical Review Letters **113**, 263601 (2014).

[279] Z. Yuan, B. E. Kardynal, R. M. Stevenson, A. J. Shields, C. J. Lobo, K. Cooper, N. S. Beattie, D. A. Ritchie, and M. Pepper, *Electrically Driven Single-Photon Source*, Science **295**, 102 (2001).

[280] J. Y. Marzin, J. M. Gerard, A. Izrael, D. Barrier, and G. Bastard, *Photoluminescence of Single InAs Quantum Dots Obtained by Self-Organized Growth on GaAs*, Physical Review Letters **73**, 716 (1994).

[281] P. M. Petroff, *Semiconductor Self-Assembled Quantum Dots: Present Status and Future Trends*, Advanced Materials **23**, 2372 (2011).

[282] J. M. Gerard, D. Barrier, J. Y. Marzin, R. Kuszelewicz, L. Manin, E. Costard, V. Thierry-Mieg, and T. Rivera, *Quantum boxes as active probes for photonic microstructures: The pillar microcavity case*, Applied Physics Letters **69**, 449 (1996).

[283] G. S. Solomon, M. Pelton, and Y. Yamamoto, *Single-mode Spontaneous Emission from a Single Quantum Dot in a Three-Dimensional Microcavity*, Physical Review Letters **86**, 3903 (2001).

[284] E. Moreau, I. Robert, J. M. Gerard, I. Abram, L. Manin, and V. Thierry-Mieg, *Single-mode solid-state single photon source based on isolated quantum dots in pillar microcavities*, Applied Physics Letters **79**, 2865 (2001).

[285] M. Pelton, C. Santori, J. Vuckovic, B. Zhang, G. S. Solomon, J. Plant, and Y. Yamamoto, *Efficient Source of Single Photons: A Single Quantum Dot in a Micropost Microcavity*, Physical Review Letters **89**, 233602 (2002).

[286] C. Santori, D. Fattal, J. Vuckovic, G. S. Solomon, and Y. Yamamoto, *Single-photon generation with InAs quantum dots*, New J. Phys. **6**, 89 (2004).

[287] J. P. Reithmaier, G. Sek, A. Löffler, C. Hofmann, S. Kuhn, S. Reitzenstein, L. V. Keldysh, V. D. Kulakovskii, T. L. Reinecke, and A. Forchel, *Strong coupling in a single quantum dot-semiconductor microcavity system*, Nature **432**, 197 (2004).

[288] D. Press, S. Götzinger, S. Reitzenstein, C. Hofmann, A. Löffler, M. Kamp, A. Forchel, and Y. Yamamoto, *Photon Antibunching from a Single Quantum-Dot-Microcavity System in the Strong Coupling Regime*, Physical Review Letters **98**, 117402 (2007).

[289] H. Jayakumar, A. Predojevic, T. Huber, T. Kauten, G. S. Solomon, and G. Weihs, *Deterministic Photon Pairs and Coherent Optical Control of a Single Quantum Dot*, Physical Review Letters **110**, 135505 (2013).

[290] M. Müller, S. Bounouar, K. D. Jöns, M. Glässl, and P. Michler, *On-demand generation of indistinguishable polarization-entangled photon pairs*, Nature Photon **8**, 224 (2014).

[291] S. L. Portalupi, G. Hornecker, V. Giesz, T. Grange, A. Lemaitre, J. Demory, I. Sagnes, N. D. Lanzillotti-Kimura, L. Lanco, A. Auffeves, and P. Senellart, *Bright Phonon-Tuned Single-Photon Source*, Nano Lett. **15**, 6290 (2015).

[292] P. Michler, A. Kiraz, C. Becher, W. V. Schoenfeld, P. M. Petroff, L. Zhang, E. Hu, and A. Imamoglu, *A Quantum Dot Single-Photon Turnstile Device*, Science **290**, 2282 (2000).

[293] C. Santori, M. Pelton, G. Solomon, Y. Dale, and Y. Yamamoto, *Triggered Single Photons from a Quantum Dot*, Physical Review Letters **86**, 1502 (2001).

[294] A. Badolato, K. Hennessy, M. Atatüre, J. Dreiser, E. Hu, P. M. Petroff, and A. Imamoğlu, *Deterministic Coupling of Single Quantum Dots to Single Nanocavity Modes*, Science **308**, 1158 (2005).

[295] A. Högele, S. Seidl, M. Kroner, K. Karrai, R. J. Warburton, B. D. Gerardot, and P. M. Petroff, *Voltage-Controlled Optics of a Quantum Dot*, Physical Review Letters **93**, 217401 (2004).

[296] C. Santori, D. Fattal, J. Vuckovic, G. S. Solomon, and Y. Yamamoto, *Indistinguishable photons from a single-photon device*, Nature **419**, 594 (2002).

[297] A. J. Bennett, R. B. Patel, A. J. Shields, K. Cooper, P. Atkinson, C. A. Nicoll, and D. A. Ritchie, *Indistinguishable photons from a diode*, Applied Physics Letters **92**, 193503 (2008).

[298] E. Flagg, A. Muller, S. Polyakov, A. Ling, A. Migdall, and G. Solomon, *Interference of Single Photons from Two Separate Semiconductor Quantum Dots*, Physical Review Letters **104**, 137401 (2010).

[299] R. B. Patel, A. J. Bennett, I. Farrer, C. A. Nicoll, D. A. Ritchie, and A. J. Shields, *Two-photon interference of the emission from electrically tunable remote quantum dots*, Nature Photon **4**, 632 (2010).

[300] A. Faraon, I. Fushman, D. Englund, N. Stoltz, P. Petroff, and J. Vuckovic, *Coherent generation of non-classical light on a chip via photon-induced tunnelling and blockade*, Nature Physics **4**, 859 (2008).

[301] E. B. Flagg, A. Muller, J. W. Robertson, S. Founta, D. G. Deppe, M. Xiao, W. Ma, G. J. Salamo, and C. K. Shih, *Resonantly driven coherent oscillations in a solid-state quantum emitter*, Nature Physics **5**, 203 (2009).

[302] D. Englund, A. Majumdar, A. Faraon, M. Toishi, N. Stoltz, P. Petroff, and J. Vuckovic, *Resonant Excitation of a Quantum Dot Strongly Coupled to a Photonic Crystal Nanocavity*, Physical Review Letters **104**, 073904 (2010).

[303] M. Nomura, N. Kumagai, S. Iwamoto, Y. Ota, and Y. Arakawa, *Laser oscillation in a strongly coupled single-quantum-dot-nanocavity system*, Nature Physics **6**, 279 (2010).

[304] D. Fattal, K. Inoue, J. Vuckovic, C. Santori, G. S. Solomon, and Y. Yamamoto, *Entanglement Formation and Violation of Bell's Inequality with a Semiconductor Single Photon Source*, Physical Review Letters **92** (2004).

[305] R. M. Stevenson, R. J. Young, P. Atkinson, K. Cooper, D. A. Ritchie, and A. J. Shields, *A semiconductor source of triggered entangled photon pairs*, Nature **439**, 179 (2006).

[306] R. J. Young, R. M. Stevenson, P. Atkinson, K. Cooper, D. A. Ritchie, and A. J. Shields, *Improved fidelity of triggered entangled photons from single quantum dots*, New J. Phys. **8**, 29 (2006).

[307] C.-Y. Lu and J.-W. Pan, *Quantum optics: Push-button photon entanglement*, Nature Photon **8**, 174 (2014).

[308] D. Fattal, E. Diamanti, K. Inoue, and Y. Yamamoto, *Quantum Teleportation with a Quantum Dot Single Photon Source*, Physical Review Letters **92**, 037904 (2004).

[309] O. Fedorych, C. Kruse, A. Ruban, D. Hommel, G. Bacher, and T. Kümmell, *Room temperature single photon emission from an epitaxially grown quantum dot*, Applied Physics Letters **100**, 061114 (2012).

[310] A. Högele, C. Galland, M. Winger, and A. Imamoglu, *Photon Antibunching in the Photoluminescence Spectra of a Single Carbon Nanotube*, Physical Review Letters **100**, 217401 (2008).

[311] X. Ma, N. F. Hartmann, J. K. S. Baldwin, S. K. Doorn, and H. Htoon, *Room-temperature single-photon generation from solitary dopants of carbon nanotubes*, Nature Nanotechnology **10**, 671 (2015).

[312] S. Khasminskaya, F. Pyatkov, K. Slowik, S. Ferrari, O. Kahl, V. Kovalyuk, P. Rath, A. Vetter, F. Hennrich, M. M. Kappes, and et al., *Fully integrated quantum photonic circuit with an electrically driven light source*, Nature Photonics **10**, 727 (2016).

[313] J. Meijer, B. Burchard, M. Domhan, C. Wittmann, T. Gaebel, I. Popa, F. Jelezko, and J. Wrachtrup, *Generation of single color centers by focused nitrogen implantation*, Applied Physics Letters **87**, 261909 (2005).

[314] J. R. Rabeau, P. Reichart, G. Tamanyan, D. N. Jamieson, S. Prawer, F. Jelezko, T. Gaebel, I. Popa, M. Domhan, and J. Wrachtrup, *Implantation of labelled single nitrogen vacancy centers in diamond using* ^{15}N, Applied Physics Letters **88**, 023113 (2006).

[315] S. Pezzagna, D. Rogalla, H.-W. Becker, I. Jakobi, F. Dolde, B. Naydenov, J. Wrachtrup, F. Jelezko, C. Trautmann, and J. Meijer, *Creation of colour centres in diamond by collimated ion-implantation through nano-channels in mica*, physica status solidi (a) **208**, 2017 (2011).

[316] F. Dolde, I. Jakobi, B. Naydenov, N. Zhao, S. Pezzagna, C. Trautmann, J. Meijer, P. Neumann, F. Jelezko, and J. Wrachtrup, *Room-temperature entanglement between single defect spins in diamond*, Nature Physics **9**, 139 (2013).

[317] M. O. Scully and M. S. Zubairy, *Quantum optics*, Cambridge university press, 1997.

[318] R. Loudon, *The quantum theory of light*, OUP Oxford, 2000.

[319] X. T. Zou and L. Mandel, *Photon-antibunching and sub-Poissonian photon statistics*, Physical Review A **41**, 475 (1990).

[320] J. Benedikter, H. Kaupp, T. Hümmer, Y. Liang, A. Bommer, C. Becher, A. Krueger, J. M. Smith, T. W. Hänsch, and D. Hunger, *Cavity-Enhanced Single-Photon Source Based on the Silicon-Vacancy Center in Diamond*, Physical Review Applied **7** (2017).

[321] R. H. Brown and R. Twiss, *A new type of interferometer for use in radio astronomy*, The London, Edinburgh, and Dublin Philosophical Magazine and Journal of Science **45**, 663 (1954).

[322] T. Grange, G. Hornecker, D. Hunger, J.-P. Poizat, J.-M. Gerard, P. Senellart, and A. Auffeves, *Cavity-Funneled Generation of Indistinguishable Single Photons from Strongly Dissipative Quantum Emitters*, Physical Review Letters **114**, 193601 (2015).

[323] A. Kiraz, M. Atatüre, and A. Imamoglu, *Quantum-dot single-photon sources: Prospects for applications in linear optics quantum-information processing*, Physical Review A **69**, 032305 (2004).

[324] J. Bylander, I. Robert-Philip, and I. Abram, *Interference and correlation of two independent photons*, Eur. Phys. J. D **22**, 295 (2003).

[325] C. K. Hong, Z. Y. Ou, and L. Mandel, *Measurement of subpicosecond time intervals between two photons by interference*, Physical Review Letters **59**, 2044 (1987).

[326] R. Ghosh, C. K. Hong, Z. Y. Ou, and L. Mandel, *Interference of two photons in parametric down conversion*, Physical Review A **34**, 3962 (1986).

[327] Y. H. Shih and C. O. Alley, *New Type of Einstein-Podolsky-Rosen-Bohm Experiment Using Pairs of Light Quanta Produced by Optical Parametric Down Conversion*, Physical Review Letters **61**, 2921 (1988).

[328] R. Kaltenbaek, B. Blauensteiner, M. Zukowski, M. Aspelmeyer, and A. Zeilinger, *Experimental Interference of Independent Photons*, Physical Review Letters **96** (2006).

[329] L.-M. Duan and C. Monroe, *Colloquium: Quantum networks with trapped ions*, Rev. Mod. Phys. **82**, 1209 (2010).

[330] J. F. Mulligan, *Who were Fabry and Pérot?*, American Journal of Physics **66**, 797 (1998).

[331] B. E. Saleh, M. C. Teich, and B. E. Saleh, *Fundamentals of photonics*, volume 22, Wiley New York, 1991.

[332] M. Mader, *A cavity nanoscope*, Master's thesis, Ludwig-Maximilians-Universität München, 2012.

[333] S. A. Furman and A. V. Tikhonravov, *Basics of Optics of Multilayer Systems*, World Scientific Publishing, 1992.

[334] J. M. Bennett, *Recent developments in surface roughness characterization*, Meas. Sci. Technol. **3**, 1119 (1992).

[335] G. Rempe, R. Lalezari, R. Thompson, and H. Kimble, *Measurement of ultralow losses in an optical interferometer*, Optics Letters **17**, 363 (1992).

[336] M. Fox, *Quantum Optics An Introduction*, Oxford Univ. Press, 2006.

[337] A. Auffeves, B. Besga, J.-M. Gerard, and J.-P. Poizat, *Spontaneous emission spectrum of a two-level atom in a very-high- Q cavity*, Physical Review A **77**, 063833 (2008).

[338] A. Auffeves, J.-M. Gerard, and J.-P. Poizat, *Pure emitter dephasing: A resource for advanced solid-state single-photon sources*, Physical Review A **79**, 053838 (2009).

[339] E. Hinds, *Cavity Quantum Electrod Ynamics*, volume 28 of *Advances In Atomic, Molecular, and Optical Physics*, pages 237 – 289, Academic Press, 1990.

[340] E. Jaynes and F. Cummings, *Comparison of quantum and semiclassical radiation theories with application to the beam maser*, Proceedings of the IEEE **51**, 89 (1963).

[341] B. W. Shore and P. L. Knight, *The Jaynes-Cummings Model*, Journal of Modern Optics **40**, 1195 (1993).

[342] G. Rempe, R. J. Thompson, and H. J. Kimble, *Cavity quantum electrodynamics with strong coupling in the optical domain*, Physica Scripta **T51**, 67 (1994).

[343] H. J. Kimble, *Strong Interactions of Single Atoms and Photons in Cavity QED*, Physica Scripta **T76**, 127 (1998).

[344] D. Meschede, H. Walther, and G. Müller, *One-Atom Maser*, Physical Review Letters **54**, 551 (1985).

[345] G. Rempe, H. Walther, and N. Klein, *Observation of quantum collapse and revival in a one-atom maser*, Physical Review Letters **58**, 353 (1987).

[346] M. G. Raizen, R. J. Thompson, R. J. Brecha, H. J. Kimble, and H. J. Carmichael, *Normal-mode splitting and linewidth averaging for two-state atoms in an optical cavity*, Physical Review Letters **63**, 240 (1989).

[347] Y. Zhu, D. J. Gauthier, S. E. Morin, Q. Wu, H. J. Carmichael, and T. W. Mossberg, *Vacuum Rabi splitting as a feature of linear-dispersion theory: Analysis and experimental observations*, Physical Review Letters **64**, 2499 (1990).

[348] R. J. Thompson, G. Rempe, and H. J. Kimble, *Observation of normal-mode splitting for an atom in an optical cavity*, Physical Review Letters **68**, 1132 (1992).

[349] W. Lukosz and R. E. Kunz, *Light emission by magnetic and electric dipoles close to a plane interface. I. Total radiated power*, J. Opt. Soc. Am. **67**, 1607 (1977).

[350] W. Lukosz, *Light emission by magnetic and electric dipoles close to a plane dielectric interface. III. Radiation patterns of dipoles with arbitrary orientation*, J. Opt. Soc. Am. **69**, 1495 (1979).

[351] J. M. Wylie and J. E. Sipe, *Quantum electrodynamics near an interface*, Physical Review A **30**, 1185 (1984).

[352] K. H. Drexhage, *IV Interaction of Light with Monomolecular Dye Layers*, Progress in Optics **12**, 163 (1974).

[353] R. M. Amos and W. L. Barnes, *Modification of the spontaneous emission rate of Eu3+ ions close to a thin metal mirror*, Physical Review B **55**, 7249 (1997).

[354] H. Chew, *Transition rates of atoms near spherical surfaces*, J. Chem. Phys. **87**, 1355 (1987).

[355] R. G. Hulet, E. S. Hilfer, and D. Kleppner, *Inhibited Spontaneous Emission by a Rydberg Atom*, Physical Review Letters **55**, 2137 (1985).

[356] D. Kleppner, *Inhibited Spontaneous Emission*, Physical Review Letters **47**, 233 (1981).

[357] W. Jhe, A. Anderson, E. A. Hinds, D. Meschede, L. Moi, and S. Haroche, *Suppression of spontaneous decay at optical frequencies: Test of vacuum-field anisotropy in confined space*, Physical Review Letters **58**, 666 (1987).

[358] D. J. Heinzen, J. J. Childs, J. E. Thomas, and M. S. Feld, *Enhanced and inhibited visible spontaneous emission by atoms in a confocal resonator*, Physical Review Letters **58**, 1320 (1987).

[359] D. J. Heinzen and M. S. Feld, *Vacuum Radiative Level Shift and Spontaneous-Emission Linewidth of an Atom in an Optical Resonator*, Physical Review Letters **59**, 2623 (1987).

[360] E. del Valle and F. P. Laussy, *Regimes of strong light-matter coupling under incoherent excitation*, Physical Review A **84**, 043816 (2011).

[361] P. R. Dolan, G. M. Hughes, F. Grazioso, B. R. Patton, and J. M. Smith, *Femtoliter tunable optical cavity arrays*, Optics Letters **35**, 3556 (2010).

[362] J. F. S. Brachmann, H. Kaupp, T. W. Hänsch, and D. Hunger, *Photothermal effects in ultra-precisely stabilized tunable microcavities*, Optics Express **24**, 21205 (2016).

[363] A. Muller, E. B. Flagg, M. Metcalfe, J. Lawall, and G. S. Solomon, *Coupling an epitaxial quantum dot to a fiber-based external-mirror microcavity*, Applied Physics Letters **95**, 173101 (2009).

[364] Z. Di, H. V. Jones, P. R. Dolan, S. M. Fairclough, M. B. Wincott, J. Fill, G. M. Hughes, and J. M. Smith, *Controlling the emission from semiconductor quantum dots using ultra-small tunable optical microcavities*, New J. Phys. **14**, 103048 (2012).

[365] J. Miguel-Sanchez, A. Reinhard, E. Togan, T. Volz, A. Imamoglu, B. Besga, J. Reichel, and J. Esteve, *Cavity quantum electrodynamics with charge-controlled quantum dots coupled to a fiber Fabry-Perot cavity*, New J. Phys. **15**, 045002 (2013).

[366] B. Besga, C. Vaneph, J. Reichel, J. Esteve, A. Reinhard, J. Miguel-Sanchez, A. Imamoglu, and T. Volz, *Polariton Boxes in a Tunable Fiber Cavity*, Physical Review Applied **3** (2015).

[367] D. Wang, H. Kelkar, D. Martin-Cano, T. Utikal, S. Götzinger, and V. Sandoghdar, *Coherent Coupling of a Single Molecule to a Scanning Fabry-Perot Microcavity*, Physical Review X **7**, 021014 (2017).

[368] Y. Colombe, T. Steinmetz, G. Dubois, F. Linke, D. Hunger, and J. Reichel, *Strong atom-field coupling for Bose-Einstein condensates in an optical cavity on a chip*, Nature **450**, 272 (2007).

[369] A. Widera, *The Advantages of Extra Entanglement*, Science **344**, 160 (2014).

[370] F. Haas, J. Volz, R. Gehr, J. Reichel, and J. Esteve, *Entangled States of More Than 40 Atoms in an Optical Fiber Cavity*, Science **344**, 180 (2014).

[371] C. H. Metzger and K. Karrai, *Cavity cooling of a microlever*, Nature **432**, 1002 (2004).

[372] C. Metzger, I. Favero, A. Ortlieb, and K. Karrai, *Optical self cooling of a deformable Fabry-Perot cavity in the classical limit*, Physical Review B **78** (2008).

[373] I. Favero, S. Stapfner, D. Hunger, P. Paulitschke, J. Reichel, H. Lorenz, E. M. Weig, and K. Karrai, *Fluctuating nanomechanical system in a high finesse optical microcavity*, Optics Express **17**, 12813 (2009).

[374] N. E. Flowers-Jacobs, S. W. Hoch, J. C. Sankey, A. Kashkanova, A. M. Jayich, C. Deutsch, J. Reichel, and J. G. E. Harris, *Fiber-cavity-based optomechanical device*, Applied Physics Letters **101**, 221109 (2012).

[375] S. Stapfner, L. Ost, D. Hunger, J. Reichel, I. Favero, and E. M. Weig, *Cavity-enhanced optical detection of carbon nanotube Brownian motion*, Applied Physics Letters **102**, 151910 (2013).

[376] A. B. Shkarin, N. E. Flowers-Jacobs, S. W. Hoch, A. D. Kashkanova, C. Deutsch, J. Reichel, and J. G. E. Harris, *Optically Mediated Hybridization between Two Mechanical Modes*, Physical Review Letters **112** (2014).

[377] F. Laguarta, N. Lupon, and J. Armengol, *Optical glass polishing by controlled laser surface-heat treatment*, Applied Optics **33**, 6508 (1994).

[378] K. M. Nowak, H. J. Baker, and D. R. Hall, *Efficient laser polishing of silica micro-optic components*, Applied Optics **45**, 162 (2006).

[379] U. C. Paek and A. L. Weaver, *Formation of a Spherical Lens at Optical Fiber Ends with a CO2 Laser*, Applied Optics **14**, 294 (1975).

[380] M. Wakaki, Y. Komachi, and G. Kanai, *Microlenses and microlens arrays formed on a glass plate by use of a CO2 laser*, Applied Optics **37**, 627 (1998).

[381] L. Collot, V. Lefevre-Seguin, M. Brune, J. M. Raimond, and S. Haroche, *Very High-Q Whispering-Gallery Mode Resonances Observed on Fused Silica Microspheres*, Europhysics Letters (EPL) **23**, 327 (1993).

[382] D. W. Vernooy, A. Furusawa, N. P. Georgiades, V. S. Ilchenko, and H. J. Kimble, *Cavity QED with high-Q whispering gallery modes*, Physical Review A **57**, R2293 (1998).

[383] D. K. Armani, T. J. Kippenberg, S. M. Spillane, and K. J. Vahala, *Ultra-high-Q toroid microcavity on a chip*, Nature **421**, 925 (2003).

[384] R. J. Barbour, P. A. Dalgarno, A. Curran, K. M. Nowak, H. J. Baker, D. R. Hall, N. G. Stoltz, P. M. Petroff, and R. J. Warburton, *A tunable microcavity*, Journal of Applied Physics **110**, 053107 (2011).

[385] L. Greuter, S. Starosielec, D. Najer, A. Ludwig, L. Duempelmann, D. Rohner, and R. J. Warburton, *A small mode volume tunable microcavity: Development and characterization*, Applied Physics Letters **105**, 121105 (2014).

[386] L. Greuter, S. Starosielec, A. V. Kuhlmann, and R. J. Warburton, *Towards high-cooperativity strong coupling of a quantum dot in a tunable microcavity*, Physical Review B **92**, 045302 (2015).

[387] D. Hunger, *Herstellung und Charakterisierung von Faserresonatoren hoher Finesse*, Master's thesis, Ludwig-Maximilians-Universität München, 2005.

[388] C. Deutsch, *High Finesse Fabry-Perot resonators Production, characterization and applications*, Master's thesis, Ludwig-Maximilians-Universität München, 2008.

[389] L. Brovelli and U. Keller, *Simple analytical expressions for the reflectivity and the penetration depth of a Bragg mirror between arbitrary media*, Optics Communications **116**, 343 (1995).

[390] R. P. Feynman, R. B. Leighton, and M. Sands, *The Feynman Lectures on Physics - Volume II - Chapter 32-7*, Addison - Wesley, 1964.

[391] W. B. Joyce and B. C. DeLoach, *Alignment of Gaussian beams*, Applied Optics **23**, 4187 (1984).

[392] J. Benedikter, T. Hümmer, M. Mader, B. Schlederer, J. Reichel, T. W. Hänsch, and D. Hunger, *Transverse-mode coupling and diffraction loss in tunable Fabry-Pérot microcavities*, New Journal of Physics **17**, 053051 (2015).

[393] S. Ritter, C. Nölleke, C. Hahn, A. Reiserer, A. Neuzner, M. Uphoff, M. Mücke, E. Figueroa, J. Bochmann, and G. Rempe, *An elementary quantum network of single atoms in optical cavities*, Nature **484**, 195 (2012).

[394] J. Hecht, *City of light: the story of fiber optics*, Oxford University Press on Demand, 2004.

[395] K. Kao and G. A. Hockham, *Dielectric-fibre surface waveguides for optical frequencies*, Electrical Engineers, Proceedings of the Institution of **113**, 1151 (1966).

[396] C. Becher, *Fluorescent nanoparticles: Diamonds from outer space*, Nature Nanotechnology **9**, 16 (2014).

[397] S.-J. Yu, M.-W. Kang, H.-C. Chang, K.-M. Chen, and Y.-C. Yu, *Bright Fluorescent Nanodiamonds: No Photobleaching and Low Cytotoxicity*, Journal of the American Chemical Society **127**, 17604 (2005).

[398] N. Mohan, Y.-K. Tzeng, L. Yang, Y.-Y. Chen, Y. Y. Hui, C.-Y. Fang, and H.-C. Chang, *Sub-20-nm Fluorescent Nanodiamonds as Photostable Biolabels and Fluorescence Resonance Energy Transfer Donors*, Advanced Materials **22**, 843 (2010).

[399] L. Rondin, G. Dantelle, A. Slablab, F. Grosshans, F. Treussart, P. Bergonzo, S. Perruchas, T. Gacoin, M. Chaigneau, H.-C. Chang, V. Jacques, and J.-F. Roch, *Surface-induced charge state conversion of nitrogen-vacancy defects in nanodiamonds*, Physical Review B **82**, 115449 (2010).

[400] M. V. Hauf, B. Grotz, B. Naydenov, M. Dankerl, S. Pezzagna, J. Meijer, F. Jelezko, J. Wrachtrup, M. Stutzmann, F. Reinhard, and J. A. Garrido, *Chemical control of the charge state of nitrogen-vacancy centers in diamond*, Physical Review B **83**, 081304 (2011).

[401] V. V. Temnov and U. Woggon, *Superradiance and Subradiance in an Inhomogeneously Broadened Ensemble of Two-Level Systems Coupled to a Low-Q Cavity*, Physical Review Letters **95**, 243602 (2005).

[402] H. Becker, S. E. Burns, N. Tessler, and R. H. Friend, *Role of optical properties of metallic mirrors in microcavity structures*, Journal of Applied Physics **81**, 2825 (1997).

[403] M. N. Berberan-Santos, E. N. Bodunov, and B. Valeur, *Mathematical functions for the analysis of luminescence decays with underlying distributions 1. Kohlrausch decay function (stretched exponential)*, Chemical Physics **315**, 171 (2005).

[404] A. Chizhik, F. Schleifenbaum, R. Gutbrod, A. Chizhik, D. Khoptyar, A. J. Meixner, and J. Enderlein, *Tuning the Fluorescence Emission Spectra of a Single Molecule with a Variable Optical Subwavelength Metal Microcavity*, Physical Review Letters **102**, 073002 (2009).

[405] P. Stehle, *Atomic Radiation in a Cavity*, Physical Review A **2**, 102 (1970).

[406] M. R. Philpott, *Fluorescence from molecules between mirrors*, Chemical Physics Letters **19**, 435 (1973).

[407] R. R. Chance, A. Prock, and R. Silbey, *Decay of an emitting dipole between two parallel mirrors*, J. Chem. Phys. **62**, 771 (1975).

[408] G. Barton, *Quantum Electrodynamics of Atoms Between Parallel Mirrors*, Physica Scripta **T21**, 11 (1988).

[409] X.-P. Feng and K. Ujihara, *Quantum theory of spontaneous emission in a one-dimensional optical cavity with two-side output coupling*, Physical Review A **41**, 2668 (1990).

[410] X.-P. Feng, *Theory of short optical cavity with dielectric multilayer film mirrors*, Optics Communications **83**, 162 (1991).

[411] K. Ujihara, *Spontaneous Emission and the Concept of Effective Area in a Very Short Optical Cavity with Plane-Parallel Dielectric Mirrors*, Japanese Journal of Applied Physics **30**, L901 (1991).

[412] H. Benisty, H. De Neve, and C. Weisbuch, *Impact of planar microcavity effects on light extraction-Part I: basic concepts and analytical trends*, IEEE J. Quantum Electron. **34**, 1612 (1998).

[413] R. R. Chance, A. Prock, and R. Silbey, *Molecular Fluorescence and Energy Transfer Near Interfaces*, Advances in Chemical Physics **37**, 1 (2007).

[414] K. Suhling, L. M. Hirvonen, J. A. Levitt, P.-H. Chung, C. Tregidgo, D. A. Rusakov, K. Zheng, S. Ameer-Beg, S. Poland, S. Coelho, R. Henderson, and N. Krstajic, *Fluorescence Lifetime Imaging*, Handbook of Photonics for Biomedical Engineering (2015).

[415] S. A. Momenzadeh, R. J. Stöhr, F. F. de Oliveira, A. Brunner, A. Denisenko, S. Yang, F. Reinhard, and J. Wrachtrup, *Nanoengineered Diamond Waveguide as a Robust Bright Platform for Nanomagnetometry Using Shallow Nitrogen Vacancy Centers*, Nano Letters **15**, 165 (2015).

[416] C. Arend, P. Appel, J. N. Becker, M. Schmidt, M. Fischer, S. Gsell, M. Schreck, C. Becher, P. Maletinsky, and E. Neu, *Site selective growth of heteroepitaxial diamond nanoislands containing single SiV centers*, Applied Physics Letters **108**, 063111 (2016).

[417] H. de Riedmatten, I. Marcikic, W. Tittel, H. Zbinden, D. Collins, and N. Gisin, *Long Distance Quantum Teleportation in a Quantum Relay Configuration*, Physical Review Letters **92**, 047904 (2004).

[418] Y. Chu, N. de Leon, B. Shields, B. Hausmann, R. Evans, E. Togan, M. J. Burek, M. Markham, A. Stacey, A. Zibrov, and et al., *Coherent Optical Transitions in Implanted Nitrogen Vacancy Centers*, Nano Letters **14**, 1982 (2014).

[419] U. Jantzen, A. B. Kurz, D. S. Rudnicki, C. Schäfermeier, K. D. Jahnke, U. L. Andersen, V. A. Davydov, V. N. Agafonov, A. Kubanek, L. J. Rogers, and et al., *Nanodiamonds carrying silicon-vacancy quantum emitters with almost lifetime-limited linewidths*, New Journal of Physics **18**, 073036 (2016).

[420] M. J. Burek, Y. Chu, M. S. Z. Liddy, P. Patel, J. Rochman, S. Meesala, W. Hong, Q. Quan, M. D. Lukin, and M. Loncar, *High quality-factor optical nanocavities in bulk single-crystal diamond*, Nature Communications **5**, 5718 (2014).

Publications

- *Scaling laws of the cavity enhancement for nitrogen-vacancy centers in diamond*
  H. Kaupp, C. Deutsch, H.-C. Chang, J. Reichel, T. W. Hänsch, and D. Hunger
  Physical Review A **88**, 053812 (2013) [31]

- *Purcell-Enhanced Single-Photon Emission from Nitrogen-Vacancy Centers Coupled to a Tunable Microcavity*
  H. Kaupp, T. Hümmer, M. Mader, B. Schlederer, J. Benedikter, P. Haeusser, H.-C. Chang, H. Fedder, T. W. Hänsch, and D. Hunger
  Physical Review Applied **6**, 054010 (2016) [73]

- *Photothermal effects in ultra-precisely stabilized tunable microcavities*
  J. F. S. Brachmann, H. Kaupp, T. W. Hänsch, and D. Hunger
  Optics Express **24**, 21205 (2016) [362]

- *Cavity-Enhanced Single-Photon Source Based on the Silicon-Vacancy Center in Diamond*
  J. Benedikter, H. Kaupp, T. Hümmer, Y. Liang, A. Bommer, C. Becher, A. Krueger, J. M. Smith, T. W. Hänsch, D. Hunger
  Physical Review Applied **7**, 024031 (2017) [320]

Conference contributions

- *Cavity microscopy and strong light-matter interaction with fiber-based optical microcavities*
  Young Atom Opticians Conference
  Hannover, Germany, February 12-18, 2011

- *Cavity microscopy and strong light-matter interaction with fiber baser optical microcavities*
  476. WE-Heraeus-Seminar on Diamond: Spintronics, Photonics, Bio-Applications
  Bad Honnef, Germany, April 04-07, 2011

- *Coupling color centers in diamond to optical fiber microcavities*
  DPG Frühjahrstagung der Sektion AMOP
  Stuttgart, Germany, March 19-23, 2012

- *Coupling nanoscale solid state systems to optical fiber microcavities*
  DPG Frühjahrstagung der Sektion Kondensierte Materie
  Berlin, Germany, March 25-30, 2012

- *Coupling color centers in diamond to fiber-based Fabry-Pérot microcavities*
  23rd International Conference on Atomic Physics (ICAP)
  Palaiseau, France, July 23-27, 2012
  Poster awarded by the committee for the PAMO prize
  http://www-lpl.univ-paris13.fr/icap2012/submission.htm

- *Coupling color centers in diamond to fiber based Fabry-Pérot microcavities*
  DPG Frühjahrstagung der Sektion AMOP
  Hannover, Germany, March 18-22, 2013

- *Coupling color centers in diamond to fiber based Fabry-Pérot microcavities*
  Conference on Resonator QED
  Munich, Germany, September, 09-13, 2013
  http://www.ccqed.eu/conferences/munich2013/

- *Ultra-small mode volume cavities for the enhancement of NV center fluorescence*
  DPG Frühjahrstagung der Sektion AMOP
  Berlin, Germany, March 17-21, 2014

- *Ultra-small mode volume cavities for the enhancement of nitrogen-vacancy center fluorescence*
  Conference on Lasers and Electro-Optics (CLEO) Europe
  Munich, Germany, June 21-25, 2015

- *Ultra-small mode volume cavities for the enhancement of nitrogen-vacancy center fluorescence*
  DPG Frühjahrstagung der Sektion AMOP
  Heidelberg, Germany, March 23-27, 2015

- *Ultra-small mode volume cavities for the enhancement of nitrogen-vacancy center fluorescence*
  NIM Conference on Resonator QED
  Munich, Germany, August 03-07, 2015

Danksagung

Auf dem Weg zum Gelingen dieser Arbeit habe ich vielfache Förderung und Unterstützung erfahren und dabei einzigartigen Persönlichkeiten, mit denen ich forschen, leiden und begeistert sein durfte, kennengelernt. Ich empfinde eine tiefe Dankbarkeit, diese prägende Phase mit solch großartigen Mitstreitern verbracht zu haben. Erst durch die vielseitige freundschaftliche Zusammenarbeit konnte diese Arbeit entstehen.

Zuallererst möchte ich Herrn Professor Hänsch herzlich danken, mir die Möglichkeit gegeben zu haben, ein Teil in seinem exzellenten Team gewesen zu sein. Der freie Geist in Ihrer Arbeitsgruppe war stets anregend und begeisternd für mich. Ein besonderer Dank gilt David Hunger, der diese Arbeit initiiert hat. David, deine Geduld und Leidenschaft scheint grenzenlos. So halfen mir dein Optimismus und deine ermutigende Art auch bei zunächst aussichtslos erscheinenden Aufgaben hartnäckig und aufs Ziel gerichtet zu bleiben. Vielen herzlichen Dank für die fortwährende, umfassende und brillante Unterstützung, von den ersten gemeinsamen Experimenten im fast noch leeren Labor, bis zum Zusammenschreiben.

Erst die Kooperation mit internationalen Forschungsgruppen eröffnete manche Chance. So stellte uns Herr Professor Jakob Reichel am LKB in Paris das Setup zur Produktion meiner ersten mikrostrukturierten Fasern zur Verfügung. Durch die tatkräftige Unterstützung von Christian Deutsch, Sebastian Stapfner und David, konnten wir in einer Woche über einhundert Fasern "schießen" und sogar noch ein Gläschen Wein auf den Treppen des Mont Martre genießen. Vielen Dank für die intensiven und schönen Tage. Die Verspiegelung der Fasern lief dank den guten Vorbereitungen mit Sebastian ebenso reibungslos ab. Herrn Professor Chang von der Academia Sinica, sowie Helmut Fedder und Rolf Reuter von der Universität Stuttgart gilt mein Dank für die verschiedenen Nanodiamantproben, die sie uns unkompliziert bereit stellten.

Meinem Zimmerkollegen Matthias Mader möchte ich für seine originelle und stets besonders amüsante Gesellschaft danken. Dein Humor war mir stets eine große Freude, dein Fachwissen ersparte mir manche Recherche. Das Setup zur Faserbearbeitung, das du gemeinsam mit Benedikt Schlederer aufgebaut hast erwies sich als leistungsfähiges System zur Herstellung der kleinsten bisherigen Strukturen. Der großen Hilfsbereitschaft und Programmierkunst von Thomas Hümmer verdanke ich die Experimentsteuerung, herzlichen Dank für die tolle Unterstützung. Julia Benedikter danke ich für ihre Mithilfe bei den letzten Messungen. Durststrecken im Labor waren oft einmal zu überwinden. Hier konnte ich immer auf meine lieben Kollegen zählen, mit denen ich mich nicht nur über die Eigenheiten und Qualitäten der Fasercavities austauschen, sondern mit denen ich auch herzlich lachen konnte. Matthias, Thomas und Julia, die gemeinsame Zeit im Labor, wird mir stets in schöner Erinnerung bleiben, das ein oder andere Polt Zitat mit Sicherheit auch. Auch die gemeinschaftlichen Spaziergänge in die Mensa, während denen

es keineswegs nur um das vermeintliche Lieblingsthema Deutsche Bahn ging, sondern das Weltgeschehen insgesamt mit viel Witz diskutiert wurde, werden mir fehlen.

Des Weiteren durfte ich mich über den Beistand einiger erfahrener Postdoktoranden erfreuen, die mich direkt am Experiment oder durch ihre Expertise unterstützten. Mein Dank gilt insbesondere Louis Costa, Christian Deutsch, Tolga Bagci, Hannes Brachmann und Quirin Unterreithmeier. Ebenso herzlich bedanken möchte ich mich bei Philip Häusser, Benedikt Schlederer, Andreas Weissl und Michael Förg, die sich im Rahmen von Bachelor- und Masterarbeiten großartig engagierten.

Herrn Professor Weinfurter und seiner Arbeitsgruppe danke ich für die vielfältige Hilfe, zum Beispiel in Belangen der IT, beim Ausleihen von Gerätschaften und Literatur, sowie für die freundliche Aufnahme während der "einsamen" erste Tage der Doktorarbeit, insbesondere, Wenjamin Rosenfeld, Markus Weber, Daniel Schlenk, Michael Krug, Markus Rau, Lars Liebermeister, Norbert Ortegel, Daniel Burchhardt, Kai Redeker, Gwenelle Mélen und Martin Zeitlmeier

Auch durfte ich auf vielfältige technischen Unterstützung zählen. Philipp Altpeter möchte ich für die Assistenz im Reinraum am Lehrstuhl von Herrn Professor Jörg Kotthaus danken, den wir freundlicherweise umfangreich nutzen durften. Mein Dank geht auch an Toni Scheich, für die Hilfe in Fragen der Elektronik, an Nicole Schmidt, für die Betreuung der Chemie und Software, Herrn Aust, Herrn Großhauser und deren Team der mechanischen Werkstatt der LMU, sowie den Technikern am MPQ Charly Linner und Wolfgang Simon, für die Planung und Herstellung verschiedener Bauteile. Vielen herzlichen Dank auch an Frau Gabriele Gschwendtner und Frau Ingrid Hermann, die sich stets um vielerlei organisatorische Angelegenheiten gekümmert und mit großem Einsatz unsere Interessen vertreten haben.

Den fortwährende, großen Rückhalt meiner Familie kann ich nicht hoch genug einschätzen. Auch wenn die gemeinsame Zeit oft knapp war, wart ihr immer für mich da. Vielen Dank an meine Eltern, meine Oma und meine Schwester. Meiner Frau Dimitra möchte ich für ihre liebevollen Beistand und ihr Verständnis danken.